UQAC
Université du Québec
à Chicoutimi

In-depth study of ice nucleation and adhesion on structured hydrophobic and superhydrophobic surfaces

By

Samaneh Keshavarzi

Under supervision of Prof. Gelareh Momen and co-supervision of Prof. Reza Jafari

Manuscript-Based Thesis Presented to Université du Québec à Chicoutimi in Partial fulfillment of the Requirements for the Degree of Doctor of Philosophy (Ph.D.) in Engineering

BOARD OF EXAMINERS:

Professor Kadiata Ba, Department of Applied Sciences at UQAC, President of the Board

Professor David Seveno, Katholieke Universiteit Leuven (KU Leuven), External Member of the Board

Professor Éric Villeneuve, Department of Applied Sciences at UQAC, Internal Member of the Board

Professor Gelareh Momen, Department of Applied Sciences at UQAC, Internal Member of the Board

Professor Reza Jafari, Department of Applied Sciences at UQAC, Internal Member of the Board

Québec, Canada

RÉSUMÉ

La formation de glace et la nucléation de gouttelettes d'eau conduisant au givrage de surface posent des défis critiques dans diverses industries, notamment l'aérospatiale, les infrastructures extérieures, les transports et les systèmes énergétiques. Les méthodes de dégivrage actif conventionnelles présentent des limites telles qu'une consommation d'énergie élevée, un manque d'efficacité et des préoccupations environnementales, ce qui nécessite des approches plus efficaces.

Cette thèse de doctorat vise à relever ces défis en explorant les technologies passives de lutte contre le givrage, en se concentrant spécifiquement sur l'effet de la structure de surface pour développer des surfaces glaciophobes et atténuer la formation de givre sur celle-ci. La méthodologie de recherche implique la fabrication et la caractérisation de surfaces à la fois non ordonnées et ordonnées. L'impact de ces surfaces sur le comportement des gouttelettes d'eau, le temps de nucléation de la glace et la force d'adhérence de la glace est examiné en profondeur à l'aide de dispositifs expérimentaux et de techniques de pointe en apprentissage automatique.

Premièrement, cette étude se concentre sur l'amélioration de la répulsion de l'eau sur les surfaces qui ont été structures d'une façon non ordonnée à l'échelle micro pour prévenir la formation de glace en examinant le comportement des gouttelettes d'eau sur des surfaces en caoutchouc de silicone présentant différents niveaux de mouillabilité. La recherche explore la dynamique de l'impact des gouttelettes à différentes températures et évalue différents facteurs tels que l'angle de contact, la rugosité de surface, la taille des gouttelettes et la vitesse d'impact. Les effets de la température sur les surfaces microstructurées se révèlent minimes dans une large gamme de conditions. Les surfaces superhydrophobes présentant des propriétés spécifiques montrent l'amélioration la plus efficace du rebond des gouttelettes. La vitesse d'impact sur les surfaces rugueuses influence la probabilité d'éclaboussures. Dans notre étude, nous avons combiné des données expérimentales avec des techniques d'apprentissage automatique, telles que la régression logistique, les arbres de décision et les forêts aléatoires, pour prédire le comportement des gouttelettes en fonction des caractéristiques de surface, de la température et des paramètres des gouttelettes. Les résultats expérimentaux correspondent étroitement aux prédictions de l'apprentissage automatique, démontrant la précision de l'apprentissage automatique dans la prévision du mouvement des gouttelettes sur des surfaces hydrophobes et superhydrophobes à différentes températures.

Deuxièmement, cette recherche explore les surfaces superhydrophobes comme méthode passive pour prévenir la formation de givre en surface, en se concentrant sur le temps de nucléation de la glace en tant que facteur critique influencé par les propriétés du liquide, les conditions environnementales et les caractéristiques de la surface. L'analyse simultanée du temps de nucléation de la glace et de ses facteurs déterminants présente des défis. L'étude introduit deux approches, les tests expérimentaux et l'apprentissage automatique, pour analyser le temps de nucléation de la glace sur les surfaces non ordonnées exposées. Diverses surfaces hydrophobe/superhydrophobe en caoutchouc de silicone sont créées avec des paramètres de mouillabilité et de rugosité variables. Les surfaces

superhydrophobes, avec des paramètres de rugosité plus élevés et une distribution de rugosité gaussienne, montrent des temps de nucléation de la glace plus longs. Dans cette étude, nous avons utilisé des réseaux neuronaux pour développer un modèle corrélant le temps de nucléation de la glace avec les paramètres influents. Le modèle, entraîné avec des données expérimentales, prédit avec précision le temps de nucléation de la glace et identifie l'importance des paramètres de rugosité, de la mouillabilité de la surface, de la température et du volume des gouttelettes dans la détermination de la glaciophobicité de la surface.

Ainsi, nous avons étudié l'impact des surfaces géométriques microstructurées ordonnées basées sur une tranche de silicium sur le temps de nucléation de la glace, en utilisant à la fois des approches expérimentales et théoriques. Alors que les surfaces superhydrophobes offrent une solution passive pour atténuer la formation de givre, le défi réside dans les états intermédiaires de mouillage où les gouttelettes pénètrent partiellement dans les microstructures, compromettant leur efficacité anti-givrage. Nous avons examiné les effets d'un mouillage partiel à des températures sous refroidies en utilisant des structures de micropiliers. À mesure que la température diminue, le mouillage partiel dans la microstructure augmente, affectant la nucléation de la glace. En ajustant l'espacement et la hauteur des micropiliers, nous avons identifié les conditions qui optimisent les retards de nucléation de la glace. Les micropiliers plus hauts minimisent le contact gouttelette-solide, ce qui entraîne des retards de nucléation de la glace plus longs. Cette étude contribue à la conception de surfaces anti-givrantes superhydrophobes pour des scénarios impliquant un mouillage partiel.

Enfin, en plus de l'exploration complète de la nucléation de la glace, nous avons examiné systématiquement la force d'adhérence de la glace sur les surfaces de silicium hydrophobes et superhydrophobes dotées de micro-piliers cylindriques bien définis. En utilisant une méthode de test de micro-poussée personnalisée, nous avons mesuré quantitativement les forces de cisaillement requises pour détacher les gouttelettes d'eau gelée des surfaces. Cette approche permet une évaluation minutieuse de l'influence de la géométrie de surface sur l'adhérence de la glace. Les résultats révèlent une forte dépendance de la force d'adhérence de la glace aux paramètres géométriques, notamment l'espacement et la hauteur des piliers, ainsi qu'aux états de mouillage partiel à l'intérieur des structures à micro-piliers.

Mots-clés : Surface superhydrophobe, Surface hydrophobe, Paramètres de rugosité de surface, Topographie de surface, Mouillage partiel, Température, Impact de gouttelette, Nucléation hétérogène, Taux de nucléation, Temps de nucléation de la glace, Force d'adhérence de la glace, Glaciophobie, Apprentissage automatique, Zone de contact.

ABSTRACT

Ice formation and nucleation of water droplets leading to surface icing pose critical challenges in various industries, including aerospace, outdoor infrastructure, transportation, and energy systems. Conventional active de-icing methods have limitations such as high energy consumption, inefficiency, and environmental concerns, driving the need for more effective approaches.

This Ph.D. thesis aims to address these challenges by exploring passive anti-icing technologies, specifically focusing on the effect of surface structure to develop icephobic surfaces and mitigate surface icing. The research methodology involves fabricating and characterizing both non-ordered and ordered surfaces. The impact of these surfaces on water droplet behaviour, ice nucleation time, and ice adhesion strength is thoroughly investigated using experimental setups and cutting-edge machine learning techniques.

The initial phase of this study focuses on enhancing water repellency on non ordered surfaces to prevent ice formation by investigating how water droplets behave on silicone rubber surfaces with varying levels of hydrophobicity. The research explores droplet impact dynamics at different temperatures and evaluates factors like contact angle, surface roughness, droplet size, and impact velocity. The effects of temperature of microstructured surfaces are found to be minimal across a wide range of conditions. Superhydrophobic surfaces with specific properties show the most effective enhancement of droplet bouncing. The impact velocity on rough surfaces influences the likelihood of splashing. The study combines experimental data with machine learning techniques, such as logistic regression, decision trees, and random forests, to predict droplet behavior based on surface characteristics, temperature, and water droplet parameters. The results of the experiments align closely with the machine learning predictions, demonstrating the accuracy of machine learning in forecasting droplet motion on hydrophobic and superhydrophobic surfaces across different temperatures.

In the subsequent phase, building upon the groundwork of the first part, the research explores superhydrophobic surfaces as a passive method to prevent surface icing, focusing on ice nucleation time as a critical factor influenced by liquid properties, environmental conditions, and surface characteristics. Investigating ice nucleation time and its determining factors simultaneously presents challenges. The study introduces two approaches—experimental testing and machine learning—to analyze ice nucleation time on exposed non ordered surfaces. Various hydrophobic/superhydrophobic silicone rubber surfaces are created with varying wettability and roughness parameters. Surfaces with superhydrophobic properties, featuring higher roughness parameters and a Gaussian roughness distribution, exhibit longer ice nucleation times. The study employs neural networks to develop a model

correlating ice nucleation time with affecting parameters. The model, trained with experimental data, accurately predicts ice nucleation time, and identifies the significance of roughness parameters, surface wettability, temperature, and droplet volume in determining surface icephobicity.

The investigation then shifts to the impact of ordered microstructural geometric surfaces based on silicon wafer on ice nucleation time, utilizing both experimental and theoretical approaches. While superhydrophobic surfaces offer a passive solution for mitigating icing, the challenge lies in intermediate wetting states where droplets infiltrate microstructures, compromising their anti-icing efficacy. This study investigates the effects of such partial wetting at supercooled temperatures using micropillar structures. As temperature decreases, partial wetting within the microstructure increases, affecting ice nucleation. By adjusting micropillar spacing and height, the study identifies conditions that optimize ice nucleation delays. Higher micropillar heights minimize droplet-solid contact, resulting in longer ice nucleation delays. The study contributes to designing superhydrophobic anti-icing surfaces for scenarios involving partial wetting.

Lastly, in addition to the comprehensive exploration of ice nucleation, this study systematically investigates ice adhesion strength on hydrophobic and superhydrophobic silicon wafer surfaces featuring well-defined micro-cylindrical pillars. Employing a custom micro push-off test method, the research quantitatively measures the shear forces required to detach frozen water droplets from the surfaces. This approach allows for the meticulous assessment of how surface geometry influences ice adhesion. The results reveal a strong dependence of ice adhesion strength on geometric parameters, notably pillar spacing and height, as well as partial wetting states within the micro-pillar structures.

Keywords: Superhydrophobic surface, Hydrophobic surface, surface roughness parameters, Surface topography, Partial wetting, Temperature, Droplet impact, Heterogeneous nucleation, Nucleation rate, Ice nucleation time, Ice adhesion strength, Icephobicity, Machine learning, Contact area

Table of Contents

List of Figures

List of Tables

List of Abbreviations

ANN	Artificial Neural Network
CCD	Charged Coupled Device
CNT	Classical Nucleation Theory
DNN	Deep neural network
DT	Decision Trees
HTV	High-temperature vulcanized
Hetero-N	Heterogenous nucleation
Homo-N	Homogenous nucleation
LR	Logistic regression
MSE	Mean squared error
MAE	Mean of absolute error
MAPE	Mean of absolute percent error
PDMS	Polydimethylsiloxane
PCA	Principal Component Analysis
RMS	Root mean square
RF	Random Forest
SHAP	SHapley Additive exPlanations
Si	Silicon Wafer
SVM	Support Vector Machines
t-SNE	t-Distributed Stochastic Neighbor Embedding
WCA	Water contact angle

List of Symbols

A	Droplet-substrate contact area
β	Maximum spreading ratio
β_0	y-intercept
β_i	Parameters corresponding to the i^{th} class.
β_n	Coefficients associated with each independent variable
CAH	Contact angle hysteresis
CA	Contact angle
Ca	Capillary number
d	Thickness of the quasi-liquid layer
D	Deposition
D_0	Initial droplet diameter
D_{max}	Maximum spreading diameter
f	Effective wetting ratio in intermediate wetting
f	Interfacial correlation factor
F	Removal force
FB	Full bouncing
FN	Number of false negatives
FP	Number of false positives
γ_{LV}	Interface tensions of liquid/vapor
γ_{SV}	Interface tensions of solid/vapor
γ_{SL}	Interface tensions of the solid/liquid
h	Planck constant
J	Nucleation rate of ice embryos
k_B	Boltzmann's constant
$K\ (T)$	Diffusive flux of water molecules across the ice surface
m	Parameter represents the contact angle between ice nucleus and nucleating surface
μ	Liquid viscosity
μ_I	Chemical potential of ice
μ_M	Chemical potential of mother phase
n	Number density of water molecules at the ice nucleus/water interface
Oh	Ohnesorge number
P	Given pressure
P_0	Equilibrium pressure
PB	Partial bouncing
P_i	Empirical distribution of the i^{th} class
PS	Prompt splashing
R	Radius of curvature of solid particle or surface textures
Re	Reynolds number
RH	Relative humidity
r	Radius of an embryo
r^*	Critical radius of an embryo
S	Splashing
S_a	Arithmetical mean height
S_{al}	Autocorrelation length
S_{ku}	Kurtosis
S_q	Root mean square height
S_{sk}	Skewness
S_z	Ten point height
S_t	Maximum Height
u_0	Impact velocity

σ_I	Ice-air interfacial energy
σ_{ILL}	Surface energies of the interface between ice and the quasi-liquid layer
σ_{IW}	Surface energies of the interface between the ice and liquid
σ_{SLL}	Surface energies of the interface between the substrate and the quasi-liquid layer
σ_{SI}	Surface energies of the interface between the substrate and ice
σ_W	Water-air interfacial energy
T	Actual temperature
TP	Number of true positives
τ	Ice adhesion strength
T_m	Melting point temperature
θ_{adv}	Advancing contact angle
θ_{CB}	Cassie-Baxter contact angle
θ_{IW}	Contact angle of formed ice inside water droplet
θ_{PW}	Partial contact angle
θ_{rec}	Receding contact angle
θ_W	Wenzel contact angle
θ_Y	Young contact angle
V_I	Volume of solid phase
W_a	Work of adhesion
y	Predicted value
We	Weber number
x	Independent variable
ξ	Characteristic decay length,
Δh_{WI}	Enthalpy of melting
ΔT_m	Degree of supercooling
ΔG^*_{Hetero}	Critical heterogeneous nucleation barrier
ΔG^*_{Homo}	Critical homogenous nucleation barrier
ΔG^*	Critical energy barrier
ρ	Liquid density
Φ	Fraction of solid area

Dedication

This thesis is dedicated to my parents, [Farangis and Reza], my beloved sisters and brother, and my cherished nieces and nephews whose enduring love, support, and encouragement have been the driving force behind my academic journey. Your sacrifices, guidance, and belief in me have been my greatest source of strength and motivation. This accomplishment is as much yours as it is mine, and I am profoundly grateful for everything you have done for me. Thank you for being my source of support and for always believing in my dreams.

Acknowledgements

First and foremost, I would like to express my heartfelt gratitude to my research supervisor, *Prof. Gelareh Moman*, for her decisive role in my doctoral work. Her unwavering support, guidance, and kindness have been instrumental throughout my doctoral journey. The completion of this dissertation would not have been possible without her support and nurturing, and I am deeply thankful for her encouragement and patience throughout the duration of this research.

I also wish to express my deep appreciation to my co-supervisor, *Prof. Reza Jafari*, for his invaluable contributions to my project and his continuous involvement in overcoming the challenges I faced.

I extend my heartfelt appreciation to the members of my committee, *Prof. David Seveno*, *Prof. Éric Villeneuve, and Prof. Kadiata Ba* for their insightful guidance and support.

I would like to acknowledge and express my gratitude to *Carol Mercier*, the dedicated technician at the Anti-icing Materials International Laboratory (AMIL), UQAC. His unwavering support and expertise in setup fabrication were instrumental in the success of my experiments.

Furthermore, I want to thank *Graham Gibson* from Queen's University for his expertise in silicon wafer fabrication, and to *Khosrow Maghsoudi* for his expertise in creating structured silicone rubber surfaces. Their contributions significantly enhanced the quality of my research.

Additionally, I would like to thank *Patric Ebrel* for his guidance and contribution to my work. His insights have been invaluable to the success of my research.

I extend my sincere appreciation to Natural Sciences and Engineering Research Council of Canada (NSERC) for their invaluable financial support, as it has been the backbone of this research endeavor.

Lastly, I want to convey my deepest gratitude to my family and friends, especially *Mohammad Salsabili*, *Khatereh Seifaddini*, *Mahsa Mahdavirad*, *Arezou Anvari*, *Amir Azimi*, *Mohammad Bakhtiari*, *Kamal Pourkhorshid*, *Mohammadreza Mofarrehi, Farzaneh Aghamohammadi, Mohammad Khoshghadam*, and my fellow labmates for their love and support throughout my academic journey. Words cannot express how profoundly grateful I am to all of you.

INTRODUCTION

Problem definition

One of the serious challenges in many areas such as aerospace, outdoor infrastructure, transportation, power, refrigeration and energy systems is nucleation and freezing of water droplets that lead to lower efficiency, lower safety and economic damage (Figure 1) [1–3]. For example, the North American Ice Storm of 1998 severely destroyed numerous transmission towers and significant areas of Ontario and Quebec's electricity distribution infrastructure. More than 3.5 million consumers in total were affected, and some areas experienced power outages lasting up to a month [4]. Over 1 million people lost power as a result of the 2013 ice storm that hit eastern Canada, and the storm's insured losses were roughly CAD 200 million [5]. In April 2019, an ice storm cut off electricity to hundreds of thousands of Hydro-Québec customers, costing the provincial utility around $14 million [6]. In Oklahoma, the October 2020 Ice Storm broke more than 4200 power poles and left 300,000 people without electricity [7]. The most costly power outage in Texas history occurred in February 2021 due to severe winter storms that affected 4.5 million households and resulted in the deaths of over 200 persons [8].

Figure 1: Ice accumulation on different structures [9] *(Reprinted with permission).*

Therefore, effective measures would be taken to remedy these possible problems and remove ice or prevent its formation. These strategies can be divided into two categories: active de/anti-icing or passive de/anti icing methods. The conventional active methods can be classified into mechanical, chemical, and thermal approaches. In spite of the positive effects of these methods (the most tested, used, and reliable way to prevent icing effects [10]), using mechanical forces in mechanical approach, thermal electrical resistances in thermal methods, and anti-icing reagents in chemical technique make the measures energy consuming, often inefficient, expensive and environmentally unfriendly [11–13]. These potential drawbacks of active de-icing methods lead to a greater focus on more effective approaches based on passive anti-icing technology. The passive approaches aim to regulate and delay the formation of ice to minimize energy consumption and enhance system efficiency [14–16]. Various challenges and limitations also exist with passive anti-icing strategies. For instance, superhydrophobic surfaces may inadvertently strengthen ice adhesion due to interlocking effects between ice and their structures. Additionally, organic lubricating surfaces face issues like lubricant depletion, making them unsuitable for

prolonged use. While anti-icing gels are effective, their soft nature necessitates consideration of mechanical durability for real-world applications [17,18].

Given the drawbacks of both passive and active ice protection methods, there remains a serious need for the development of efficient, reliable, and durable ice protection systems. Hence, leveraging the strengths of both active and passive techniques while mitigating their weaknesses offers a more pragmatic solution. A hybrid approach that combines active and passive methods for preventing ice accumulation emerges as a promising strategy.

Therefore, development of high-performance anti-icing surfaces with extreme resistance to icing needs interdisciplinary knowledge such as micro-nano engineering, surface chemistry, interfacial thermodynamics and heat transfer [19]. Employing such knowledge to design anti-icing surfaces is a complicated and challenging task [20].

Icephobic surfaces and materials serve as passive anti-icing strategies relying on improved water repellency (droplet mobility) to remove water droplets before their freezing, hinder ice nucleation on the surface, reduce the ice adhesion force of the resulting ice accumulation with the surface, or a combination of these properties [19,21–24]. The development of high-performance anti-icing surfaces capable of extreme resistance to icing by enhancing water repellency, hindering ice nucleation and decreasing ice adhesion is crucial for ensuring the safe operation and protection of outdoor systems. To accomplish these goals, it is imperative to enhance our understanding of ice formation, nucleation, and adhesion processes, thereby facilitating the design of efficient and sustainable icephobic surfaces [25,26].

A fundamental aspect of designing icephobic surfaces lies in comprehensively understanding the underlying phenomena, including the dynamics of water droplets, ice formation mechanisms, and ice adhesion behavior. Comprehending nucleation is a crucial first step in the development of efficient icephobic surfaces [27,28]. Classical nucleation theory (CNT) is one of the most widely used approaches in ice nucleation process based on some parameters such as the Gibbs free energy barrier of freezing and the ice nucleation rate [12,14]. Using the principals of the theory, it is understated that the main determining factors contributing ice nucleation are degree of supercooling, geometrical features of nucleation surface such as ice/ water contact angle and surface structure [21,29–31].

In light of this knowledge, using surface structures to maximize the amount of trapped air inside structures and minimize the contact area between water droplet and surfaces under various degree of supercooling and their effect on droplet impact, freezing delay time and ice adhesion strength would determine the possibility of offering the best surface structure to enhance droplet mobility, the ice nucleation time and decrease the ice adhesion strength. The primary objective of this PhD project is to conduct a thorough examination of how surface structures impact ice formation. Specifically, we focus on their effects on water droplet behavior, freezing delay time, and the strength of ice adhesion. This will involve utilizing background theories and gaining a deep understanding of these phenomena by conducting experiments that study the impact of surface structures on water droplet impact, freezing delay time, and ice adhesion strength.

In addition to experimental investigations, a machine learning approaches are employed to establish correlations leading to design criteria for creating surfaces favoring droplet bouncing upon impact and enhanced freezing delay time. This correlation will depend

on surface characteristics, liquid properties, and environmental conditions. By exploring these associated parameters, we can advance the design of icephobic surfaces that closely mimic real-world outdoor environment.

The ultimate goal of this research is to develop efficient icephobic surfaces that effectively mitigate surface icing. By exploring the interconnected parameters and using cutting-edge machine learning techniques, significant advancement can be made in the field of icephobic surface design.

Objective

The main goal of this research is to study the process of ice formation and ice adhesion on various structured surfaces (both non-ordered and ordered structures) to gain deeper insights into how surface structure influences droplet impingement dynamics, freezing delay time, and ice adhesion strength. Additionally, the research aims to identify optimal surface structures that enhance droplet bouncing, maximize ice nucleation time, and reduce ice adhesion strength. In order to pursue this main goal, the specific objectives are as follows:

- Studying the impact dynamics of water droplets on non-ordered surfaces—ranging from hydrophobic to superhydrophobic to evaluate the influence of impacting velocity, droplet diameter, surface characteristics and temperature on droplet behavior.
- Investigating the effect of surface wettability, surface roughness parameters, surface temperature and droplet volume on ice nucleation time.
- Exploring the effect of ordered surface structure with different geometric parameters on icephobic performance in terms of ice nucleation time.

- Exploring the effect of ordered surface structure with different geometric parameters on icephobic performance in terms of the ice adhesion strength.
- Comparing the ice nucleation time generated by experiments with theoretical nucleation time that extracted from Classical Nucleation Theory.
- Comparison of three models based on machine-learning for prediction droplets impact dynamic.
- Proposing equations based on machine-learning for prediction of probability of impact dynamic.
- Developing of a predicting tool for ice nucleation time using Machine Learning approaches.

Originality

Ice formation is a ubiquitous phenomenon in many important aspects of industries and our lives. Various methods have been applied to tackle this problem by preventing or delaying ice to be formed. The initial step in design of an efficient icephobic surfaces would be the substantial understanding of water droplet behavior, ice nucleation, ice adhesion and the effect of different parameters on them. In this research, water droplet impact, the ice nucleation and ice adhesion will be studied to investigate the effect of surface structure somehow to enhance droplet rebounding, the freezing delay time, reduce the ice adhesion strength and the originality is:

1. **In-depth Examination of Droplet Dynamics on Microstructured Surfaces:**

Originality: This research provides one of the most comprehensive experimental analyses of droplet behavior on a range of non-ordered, microstructured silicone rubber surfaces with

varying wettability. While there have been studies on droplet dynamics, the breadth of parameters and surface types studied here is novel.

2. **Novel Use of Machine Learning for Droplet Behavior Analysis:**

Originality: The application of three distinct machine learning techniques to assess and predict droplet dynamics is pioneering in the field. The proposed equations, which predict droplet impact dynamics, further enhance the novelty by providing a practical tool that aligns closely with experimental data.

3. **Comprehensive Study of Ice Nucleation on Microstructured Surfaces:**

Originality: While previous studies on ice nucleation have focused broadly on surface characteristics such as arithmetic average and root mean squared, our work investigates more thoroughly by highlighting specific roughness parameters like surface skewness, ten-point height, maximum height of the profile, and a range of wettability properties. This specialized focus, along with a systematic evaluation of surface temperature and droplet volume, sets our research apart and facilitates the development of more effective icephobic material designs.

4. **Innovative Use of Machine Learning for Predicting Ice Nucleation Time:**

Originality: The use of machine learning as a predictive tool in the context of ice nucleation tome is unique. By looking at many factors together and offering a predictive model for ice nucleation time, this research introduces a fresh perspective and a useful tool to the study of ice formation.

5. **Understanding Ice Nucleation Through Surface Geometry and Wetting Dynamics:**

Originality: While much has been explored about surface geometry's role in delaying ice formation, our study takes a distinctive approach. Using a combination of experimental and theoretical approaches, we investigate ice nucleation on silicon wafers with specific pillar

configurations. Notably, we explore the often-overlooked aspect of partial wetting within these structures, especially at sub-freezing temperatures. Our insights not only offer a deeper understanding of ice nucleation processes but also guide the design of optimized surfaces for improved ice resistance.

Methodology

The main objective of this research is offering the optimum surface structure to enhance surface icephobicity in terms of droplet bouncing, icing delay time and the ice adhesion strength. For the first step, different surfaces are prepared and characterized using SEM and profilometry to study the surface morphology. Non-ordered silicone rubber surfaces are fabricated via a microcompression molding technique. In the stage of fabricating of ordered structured surfaces, photolithography is used to generate these surfaces. The detailed steps to obtain the objectives of this project can be categorized in two separate categories as follows, involving non-ordered and ordered surfaces (Figure 2):

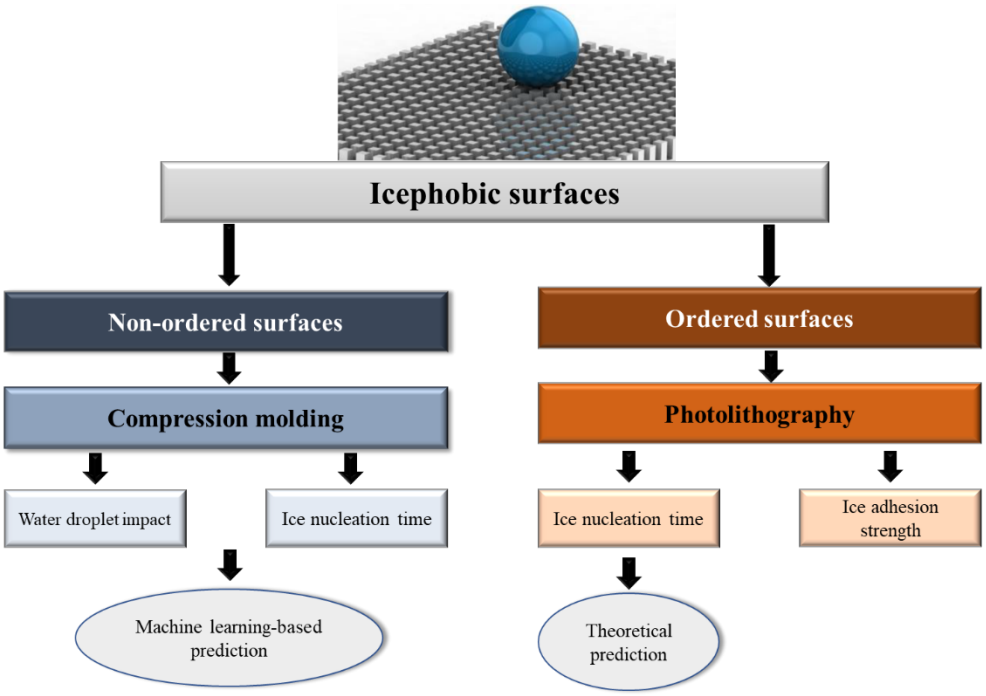

Figure 2: Schematic of methodology.

The values of water contact angle and contact angle hysteresis are used to study the wettability of the surfaces and measured using the Optical Goniometry. Then, in the next step, the prepared surfaces will be used to study droplet impact, ice nucleation time and ice adhesion strength. The experimental setup consists of thermally insulated and optically transparent chamber, temperature sensor, humidity sensor**,** drop injection systems, high speed camera, data acquisition systems, cold base, micro push-off test (Figure 3).

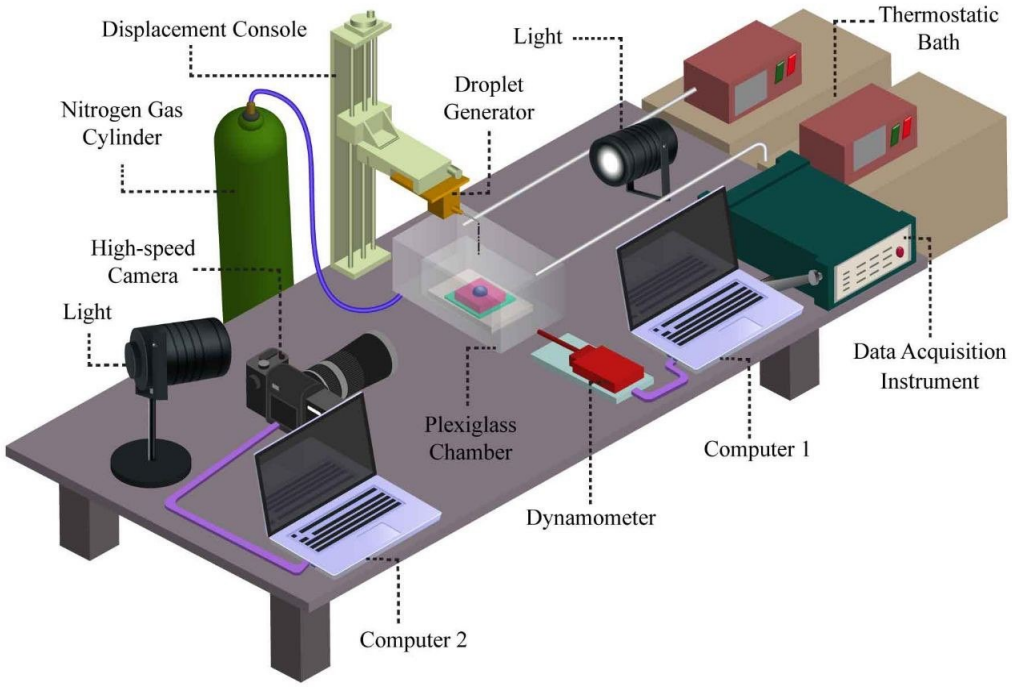

Figure 3: Schematic representation of experimental tests: Droplet impact, Ice nucleation, and Ice adhesion.

Step 1. Icephobicity of non-ordered surfaces:

***Water droplet impact*:** The investigation involves studying water droplet impact on silicone rubber surfaces. Hydrophobic and superhydrophobic surfaces are fabricated through compression molding, using high-temperature vulcanized (HTV) silicone rubber. Experimental tests are conducted using these different non-ordered, microstructure surfaces with varying wettability properties (hydrophobic to superhydrophobic). The aim is to assess the morphology of impacting drops on these surfaces, considering drop diameter, velocity, and surface features like contact angle, contact angle hysteresis, roughness values, and temperatures. Three machine-learning techniques (decision tree, random forest, and logistic regression) are employed as a novel approach to investigate droplet behavior at different temperatures. The analysis evaluates the outcome regime of impact droplet behavior based on the contact angle, contact angle hysteresis, temperature, surface roughness values,

Webber, and Reynolds numbers. The study also proposes equations to predict the probability of impact dynamics as a function of the analyzed parameters.

***Ice nucleation time*:** The study focuses on investigating the optimal surface characteristics to enhance the ice nucleation time of water droplets on silicone rubber surfaces. To achieve this, experimental tests are conducted using the same set of non-ordered, microstructure surfaces with varying wettability properties (ranging from hydrophobic to superhydrophobic) and roughness parameters (including arithmetic average, root mean squared, ten-point height, maximum height of the profile, and skewness). The evaluation aims to understand how surface features such as wettability, roughness parameters, surface temperature, and droplet volume influence the ice nucleation process. Furthermore, the research proposes the successful application of a machine learning approach (Artificial Neural Network) as a predictive tool for estimating ice nucleation time on both superhydrophobic and hydrophobic surfaces, considering all relevant variables together. It is worth noting that the surfaces used in this study for investigating ice nucleation time were the same as those used in the study focusing on droplet impact dynamics.

Step 2. Icephobicity of ordered surfaces:

***Ice nucleation time*:** The methodology of this part involves a combination of experimental investigations and theoretical predictions to examine the impact of partial wetting in geometrically ordered micro pillar structures on the delay of ice nucleation. The experimental approach involves combining photolithography processing and chemical modification to fabricate various hydrophobic and superhydrophobic surfaces using silicon wafer as the substrate. The surfaces are designed with different topographies, including well-

textured micro-cylindrical pillars of varying spacing and height, to analyze the freezing delay time of water droplets on these surfaces. Specifically, to modify the cylindrical posts on the silicon substrate and enhance their hydrophobicity, TPFS (Trichloro (1H, 1H, 2H, 2H-perfluorooctyl) silane 97%) was utilized as the modification agent. To assess the surface wettability and morphology, contact angle measurements, scanning electron microscopy, and 3D profilometry are utilized. To support and validate the experimental findings, theoretical predictions based on the heterogeneous ice nucleation theory are made. The relationship between wetting fraction, micropillar spacings, and experimental temperatures is thoroughly analyzed to understand the crucial effect of wetting fraction on the retardation of ice formation.

***Ice adhesion strength*:** In this part of the study, we investigate the ice adhesion strength on the ordered silicon wafer surfaces mentioned in the previous section. These surfaces, with varying micro-cylindrical pillar structures and wetting fractions, serve as the foundation for examining the effect of surface parameters on ice adhesion. To measure the force required to remove ice from these surfaces, we employ a micro droplet push-off test. This test allows us to quantify the adhesion strength between the ice and the microstructured surfaces. By conducting the push-off test on different surfaces with varying micropillar spacings, heights, and wetting fractions, we can discern how these surface parameters influence ice adhesion strength.

It is worth mentioning that our research investigates the impact of water droplets on non-ordered surfaces and the adhesion of ice on ordered surfaces. Due to constraints such as the COVID-19 pandemic (laboratory closures during lockdowns led to delays in

experimental activities) and time limitations, we were unable to conduct identical experiments for both non-ordered and ordered surfaces.

Thesis outline

In this context, a summary of the subsequent seven body chapters comprising this Ph.D. thesis is outlined briefly.

In Chapter 1, the emphasis is on providing an overview of superhydrophobic surfaces to establish a foundational understanding of their characteristics. The thesis primarily investigates the effects of ordered and non-ordered surfaces on icephobicity, making it necessary to provide a brief description of both surface types. This chapter also explores the concept of icephobic surfaces, which are defined based on criteria such as enhanced droplet bouncing, delayed freezing time, and reduced ice adhesion. Additionally, the chapter covers research efforts aimed at understanding these phenomena and the associated factors. Towards the end of the chapter, a definition of machine learning is presented, followed by a brief literature review of its applications in the field of icephobicity. In the following chapters, each written article related to the above-mentioned project is discussed.

In Chapter 2, the temperature dependency of water droplet impact on hydrophobic and superhydrophobic non-ordered silicone rubber surfaces is investigated. The chapter focuses on exploring how the behavior of droplets changes with temperature and utilizes machine learning-based methods to predict the dynamic behavior of droplets at different temperatures. To carry out the experiments, a range of non-ordered, microstructured silicone rubber surfaces with varying wettability properties, from hydrophobic to superhydrophobic, were fabricated through compression molding. A comprehensive series of experiments was

then conducted to analyze the impact of drop properties (such as drop diameter), kinematic parameter (velocity), and surface features (contact angle, contact angle hysteresis, roughness value, and temperature) on water droplet behavior. To complement the experimental approach, three machine learning techniques (logistic regression, decision tree, and random forest) were employed to develop predictive models. These models were trained using experimental results to forecast the behavior of droplets under different temperature conditions. The findings were published in an article titled *"Temperature-dependent droplet impact dynamics of a water droplet on hydrophobic and superhydrophobic surfaces: an experimental and predictive machine learning–based study"* in the Journal of Heat and Mass Transfer. This research benefited from a collaborative effort with the University of Chicago, USA, which provided valuable insights and resources for the study. This collaboration allowed for expertise in machine learning techniques, enhancing the comprehensiveness of the investigation.

In Chapter 3, the primary focus of the research is to explore the optimal surface characteristics that can enhance the ice nucleation time of water droplets on hydrophobic and superhydrophobic silicone rubber surfaces (the non-ordered, microstructured surfaces studied in Chapter 2). The chapter aims to investigate this by combining experimental results with machine learning-based methods (artificial neural networks) to develop a prediction tool for ice nucleation time while considering various influencing parameters. Specifically, the influence of surface wettability and surface roughness parameters, including arithmetic average, root mean squared, ten-point height, maximum height of the profile, and skewness, as well as surface temperature and droplet volume, are thoroughly evaluated in relation to ice nucleation time. The results have been reported in an article titled *"Ice nucleation on silicone*

rubber surfaces differing in roughness parameters and wettability: experimental investigation and machine learning–based predictions" in the Journal of cold regions science and technology. Chapter 3 extended its scope with a collaborative partnership with the University of Hong Kong, further enriching the research's international perspective. This collaboration facilitated expertise in artificial neural networks, broadening the spectrum of analytical tools employed in the study.

In Chapter 4, the focus of the research shifts toward the impact of microstructural geometric features and temperature on ice nucleation time. The study encompasses both experimental and theoretical approaches. To conduct the experiments, ordered hydrophobic and superhydrophobic silicon wafer surfaces are fabricated using photolithography and subsequent chemical modification. The fabrication process involves designing a series of well-textured micro-cylindrical pillars on the surfaces. The focus is to analyze the influence of surface wettability, morphology, and temperature on droplet ice nucleation and determine the parameters that contribute to delaying the freezing time. The experimental results obtained for ice nucleation time are then compared and evaluated against the predictions derived from the heterogeneous ice nucleation theory. This allows for a comprehensive analysis and assessment of the experimental findings in the context of the theoretical framework. The findings and conclusions of this research have been submitted to the Journal of Colloid and Interface Science for publication, under the title " *Exploiting intermediate wetting on superhydrophobic surfaces for efficient icing prevention*." In Chapter 4, the research expanded its horizons through a joint effort with both the University of Drexel, USA, and Lucerne University, Europe. This collaboration not only diversified the geographical reach of the research but also provided a multidisciplinary approach, combining

expertise in simulation, theoretical modeling, and experimental validation. The partnership with these universities significantly contributed to the depth and rigor of the research findings.

In Chapter 5, the research builds upon the findings of Chapter 4 and extends to the analysis of ice adhesion strength on hydrophobic and superhydrophobic silicon wafer surfaces. With the understanding gained from the investigations into ice nucleation time, the focus now shifts towards examining the adhesion properties of ice formed on these surfaces. The ice adhesion strength of the silicon wafer surfaces is evaluated using a micro push-off test. This test allows for the measurement of ice adhesion strength and enables the assessment of how different surface structures with varying geometric parameters affect the adhesion of ice.

In Chapter 6, the significant findings and conclusions of the Ph.D. project are summarized.

In Chapter 7, helpful recommendations for future research are provided based on the obtained results.

CHAPITRE 1

LITERATURE REVIEW

1.1. Introduction

Advancements in developing high-performance anti-icing surfaces that offer extreme resistance to icing are essential for ensuring the safe operation and protection of outdoor systems. To address icing challenges, extensive research has focused on effectively incorporating superhydrophobic surfaces. These surfaces, inspired by natural phenomena such as lotus leaves, utilize low surface energy materials and surface roughness to enhance icephobic properties. By creating micro/nanostructures containing low surface energy chemicals and trapped air, these surfaces promote increased droplet roll-off, delay freezing times, and reduce ice adhesion. Several studies have reported a correlation between superhydrophobicity and repel impacting droplets before ice nucleation, a delay in ice accretion, and a reduction in ice adhesion (Figure 1-1) [14,32–36]. Contrary to these reports, some investigations, have raised questions concerning the use of superhydrophobic surfaces for icephobic applications [32,37].

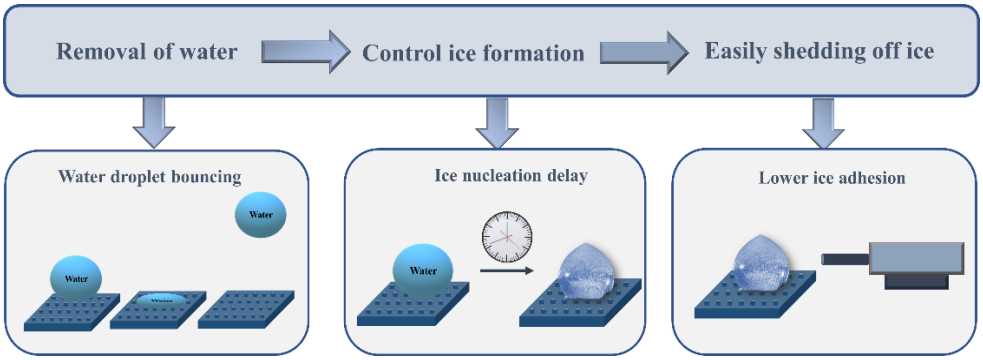

Figure 1-1: Expected behavior of an ideal icephobic surface.

In this chapter as a first step, an overview of superhydrophobic surfaces will be presented to provide a general understanding of these surfaces. Surface wettability can be altered by two approaches: (1) using low surface energy materials, and (2) changing surface roughness and topography through physical and chemical methods. Considering that this thesis focuses on the latter approach, investigating the effects of ordered and non-ordered surfaces on icephobicity, a brief description of both will be given. Given that a surface would be defined as icephobic when it satisfies one or more of these criteria including increasing droplet bouncing, increasing delay in freezing time and reducing ice adhesion, the concepts of droplet impact, ice nucleation and ice adhesion are presented. Research on understanding their theory and the related factors is then explained and elaborated on. The final section of this chapter provides a definition of machine learning and a brief literature review of its applications in the field of icephobicity.

1.1.1. Surface wettability and roughness

The contact angle of a droplet on the solid surface is used to measure the wettability of a surface. The Young equation describes the static contact angle (CA) by the surface/interface tension for an ideally flat surface (Figure 1-2 a) [38,39]:

$$cos\,\theta_Y = \frac{\gamma_{SV}-\gamma_{SL}}{\gamma_{LV}} \qquad \textit{Equation 1-1}$$

where γ_{SL}, γ_{LV} and γ_{SV} denotes the interface tensions of the solid/liquid, liquid/vapor and solid/vapor, respectively.

A solid surface is often rough and not perfectly smooth in the real world and the Young contact angle cannot describe the actual contact angle on a rough surface. Considering the surface roughness, there are two common models to describe the relation between surface roughness and contact angle: the Wenzel and the Cassie-Baxter models [40–42]. In the Wenzel model, it is assumed that a liquid can completely penetrate into rough surface structures (Figure 1-2 b) [43] and its equation is as follow:

$$cos\theta_w = r cos\theta_Y \qquad \textit{Equation 1-2}$$

where r is the surface roughness and θ_w and θ_Y are the Wenzel contact angle and the Young contact angle, respectively. According to this equation, increasing the surface roughness led to increasing the hydrophilicity or hydrophobicity of a hydrophilic or hydrophobic surface and vice versa.

The Cassie-Baxter model states that the liquid is suspended on top of the surface roughness and does not completely wet the surface (Figure 1-2 c) [44]. The air trapped between water droplet and substrate lead to easily rolling off the droplet. The apparent contact angle in the Cassie-Baxter model (θ_{CB}) can be expressed as:

$$cos\theta_{CB} = \Phi\,(1 + cos\theta_Y) - 1 \qquad \textit{Equation 1-3}$$

and Φ is the fraction of solid area.

Wenzel and Cassie-Baxter models represent two extreme wetting situations. However, in reality, there are numerous intermediate wetting states that can occur on actual

surfaces. According to the theory of intermediate wetting [45,46], the contact angle is described as follows:

$$\cos\theta_{PW} = (\Phi + (r_w - \Phi)f)\cos\theta_Y + (1-\Phi)(1-f)\cos 180 \qquad \textit{Equation 1-4}$$

where effective wetting ratio f is the ratio of solid–liquid contact area to the apparent area inside a structure.

While the Young, Wenzel, and Cassie-Baxter models provide valuable frameworks to understand contact angles on idealized surfaces, real-world surfaces have complexities that are not always captured by these models. In practical scenarios, when a liquid droplet moves on a substrate, we observe a "dynamic contact angle" rather than the static one predicted by the aforementioned models. The contact angle for a liquid droplet advancing on a surface is referred to as the advancing contact angle and the contact angle on the other side is the receding contact angle. The difference between the advancing and receding contact angles is the contact angle hysteresis (CAH) [47].

A superhydrophobic surface is defined as a surface with the contact angle higher than 150° and the contact angle hysteresis lower than 10° [48].

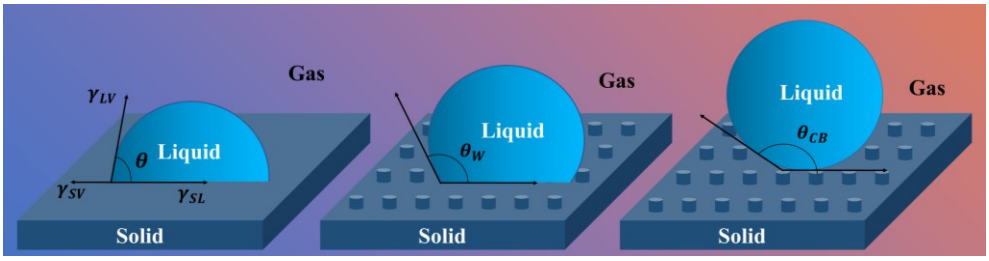

Figure 1-2: Typical wetting mechanisms. (a) Young contact mode on a flat surface. (b) Wenzel mode on a rough surface. (c) Cassie-Baxter mode on a rough surface with air trapping.

1.1.2. Common methods to create roughness/ Topographic modification

Topographic modification of surfaces refers to the process of altering the surface structure of a material in a controlled way, with the aim of achieving specific surface properties or functionalities. There are two main types of surface structures that can be created through topographic modification: ordered (patterned) and non-ordered (non-patterned) surface structures such as Figure 1-3.

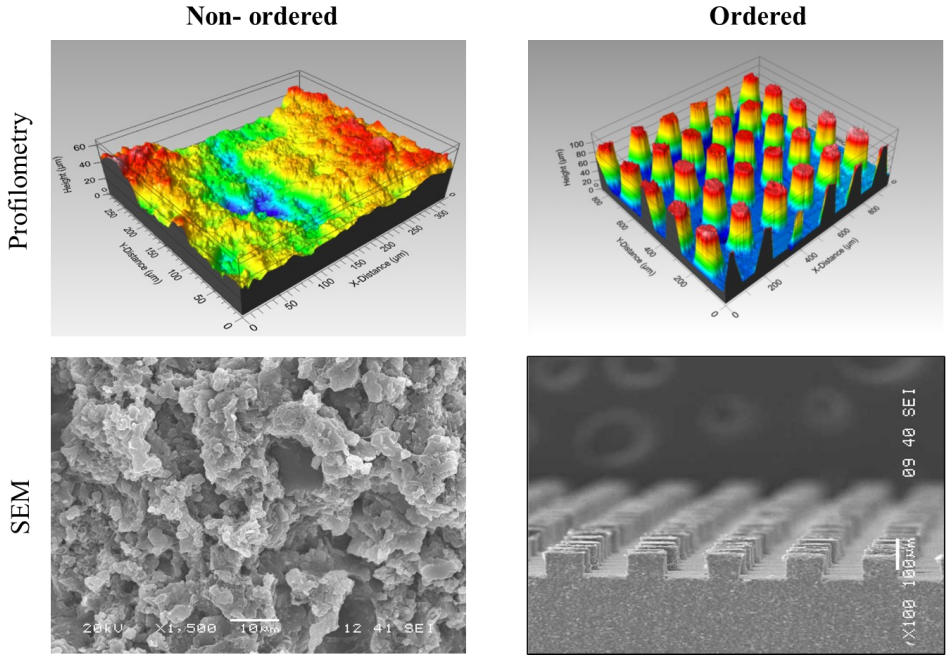

Figure 1-3: The profilometry and SEM images of non-ordered and ordered silicone rubber surfaces [49,50] *(Reprinted with permission and from open access).*

Patterned surface structures are characterized by the presence of well-defined, repeating patterns on the surface of the material. These patterns can be created using a variety of techniques, such as lithography, laser ablation or 3D printing [51]. Patterned surface structures have a wide range of applications, such as in the open microfluidic channels, self-assembly of microchips, or lithographic printing [20].

Non-patterned surface structures, on the other hand, refer to modifications of the surface that do not exhibit a clear, repeating pattern. Non-patterned surface structures can be created using techniques such as etching, chemical vapor deposition or spin-coating [48]. These techniques can be used to modify the surface morphology, chemistry, or roughness of a material, with the aim of achieving specific surface properties such as increased wettability, improved adhesion, or enhanced biocompatibility.

Overall, the choice between patterned and non-patterned surface structures depends on the specific application and the desired surface properties or functionalities. Patterned structures offer precise control over surface properties but may be more complex to fabricate. Non-patterned structures are simpler to fabricate and can modify a wider range of surface properties but may not offer the same level of precise control.

While both roughness and geometrical parameters are important for both types of surfaces, the geometrical parameters are more critical for patterned surfaces, while roughness is more critical for non-patterned surfaces. In the following section, a brief description of surface roughness parameters is given.

1.1.3. Surface roughness parameters

Surface roughness describes irregularities or deviations in a material's surface texture. Surface roughness can significantly affect the properties and performance of materials, including their mechanical, optical, and wetting properties. These roughness parameters are typically measured using a stylus-based instrument called a profilometer, which scans the surface and records the height profile data. There are several parameters commonly used to measure surface roughness, including [52]:

1. S_a (Arithmetical mean height): S_a is the arithmetic average of the deviations of the surface height profile from the mean line within the evaluation length. It is the most widely used surface roughness parameter and is expressed in micrometers (μm).
2. S_q (Root mean square height): S_q is the root mean square of the deviations of the surface height profile from the mean line within the evaluation length. It is also the most widely used measure of surface roughness and is expressed in micrometers (μm).
3. S_z (Ten point height): S_z is the average of the five highest peaks and the five deepest valleys within the evaluation length. It is a measure of the maximum height difference between the highest peaks and the deepest valleys on a surface and is expressed in micrometers (μm).
4. S_t (Maximum Height): S_t is the maximum height of the profile from the highest peak to the lowest valley within the evaluation length. It is a measure of the highest peak-to-valley distance on a surface and is expressed in micrometers (μm).
5. S_{sk} (Skewness): S_{sk} is a measure of the asymmetry of the surface height distribution around the mean line. It is expressed as a dimensionless number.
6. S_{ku} (Kurtosis): S_{ku} is a measure of the peakedness of the surface height distribution. Dimensionless numbers are used to express it.

Having defined the key parameters of surface roughness, it is pertinent to assess their impact. Following this, we will examine the correlation between these parameters and wettability, further elucidating their role in icephobic characteristics of surfaces.

1.2. **Droplet impact**

Droplet impact is a common occurrence in daily life, seen in events such as raindrops hitting the ground, ink droplets spreading, or coffee spills staining surfaces. In recent years, there has been a growing interest among scholars in the field of liquid droplet impingement on solid surfaces, a phenomenon first described by Worthington [53].

One of the most prominent uses of droplet impact is in spray cooling, which provides high rate heat transfer [54]. Another well-known application is in inkjet printing, where the physics of droplets is utilized for drop-on-demand pattern formation [55]. Additionally, droplet-based microfluidics is a rapidly growing technology that has a significant impact on the biomedical diagnostics, food, and chemical industries[56].

The anti-icing property of superhydrophobic coatings makes it a desirable material for use in aerospace and power industries, including aviation, power lines, insulators, and helicopter blades. This is because water droplets easily leave the surface when it is slightly tilted or blown by wind. Spray painting and coating, liquid atomization, trickled bed reactors, erosion of turbine blades and aircrafts, fire suppression, refrigerated cycles, and the retarding of ice formation on the surface of heat exchangers are some of the other notable applications of droplet impinging in engineering fields [57–59].

The impact of droplets on solid surfaces has also been extensively studied in connection with several natural phenomena, such as self-cleaning, which has captured the attention of scientists since the discovery of the water repellent properties of lotus leaves. Other areas of interest include soil erosion, atmospheric and oceanographic science, the formation of central peaks in craters, and the impact of acid rain on leaves [60].

Droplet impact on static solid surfaces exhibits different regimes, including spreading, receding, rebounding, and splashing (Figure 1-4), which are influenced by various factors such as droplet size, impact velocity, surface roughness, and liquid properties like surface tension and viscosity.

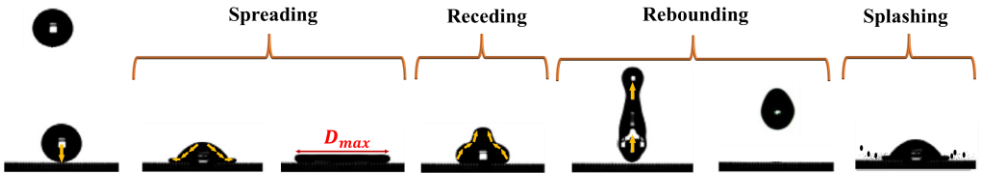

Figure 1-4: Different regimes of droplet impact on static solid surfaces.

The spreading regime occurs when a droplet impacts a solid surface and rapidly spreads out, forming a thin liquid film that wets the surface. The droplet initially flattens upon impact, and the liquid film continues to spread until it reaches a maximum size. The initial velocity of the droplet upon impact plays a significant role in its spreading behavior. Upon impact, the kinetic energy in the vertical direction is transferred to the radial direction, promoting droplet spreading. The spreading regime is typically observed for droplets at low Weber numbers and low surface temperatures, as well as smooth solid surfaces [61–63].

The maximum spreading diameter of the droplet is a critical parameter for characterizing the spreading regime (Figure 1-5), as it determines the amount of surface area available for heat transfer, particularly in heat transfer-related applications [63]. Several factors, including droplet impact velocity and surface wettability, can affect the maximum spreading diameter of the droplet [64]. Various models have been developed to predict the maximum spreading ratio, denoted as $\beta = \frac{D_{max}}{D_0}$, as a function of impact parameters. Some commonly used formulas in the literature include (Table 1-1):

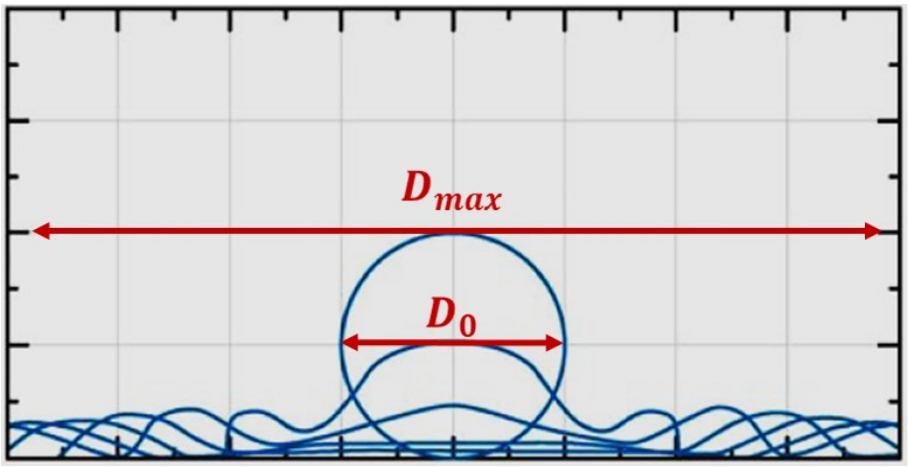

Figure 1-5 : Impact spreading of a droplet.

Table 1-1: Maximum spreading diameter dependence on physical non-dimensional variables explained by physical models.

Formula	Ref.
$\frac{1}{Re}(\frac{\beta}{1.2941})^5 + \frac{3\beta^2}{We} = 1$	[65]
$\frac{1}{Re}(\frac{\beta}{1.2941})^5 + \frac{3[(1-\cos\theta)\,\beta^2 - 4]}{We} = 1$	[66]
$\beta = 0.61(ReWe^{.5})^{0.166}$	[67]
$\beta = \sqrt{\frac{We+12}{3(1-\cos\theta)+4(\frac{We}{\sqrt{Re}})}}$	[64]
$\beta = We^{1/4}$	[68]
$\beta = \frac{1}{20}(\frac{We}{\frac{1}{2}(1-\cos\theta)})^{\frac{1}{2}}$	[69]
$(We+12)\beta = 8 + \beta^3[3(1-\cos\theta)+4(\frac{We}{\sqrt{Re}})]$	[70]
$\beta = 0.72(ReWe^{.5})^{0.14}$	[71]
$\beta = 0.87\,Re^{1/5} - 0.4\,Re^{2/5}\,We^{-1/2}$	[72]
$\frac{We}{12} + 1 = \left(\frac{2}{3}\right)\frac{1}{\beta} + \left\{\frac{1}{4}[1-\cos\theta]\right\}\beta^2 + (\frac{R_a\sqrt{Re}}{6}\,\frac{We}{D_0})\beta^2$	[73]

The receding regime is a phase that occurs during the impact of droplets on solid surfaces, where the droplet starts to contract after reaching its maximum spreading diameter [61]. This phenomenon is driven by the liquid surface tension, which acts like a cohesive force, pulling the droplet back together. The receding regime is influenced by several factors, including surface temperature and liquid surface tension. It is important to note that the receding regime can be suppressed under certain conditions. For example, when the droplet impacts a surface with low surface tension liquids, such as some liquid fuels, the contraction phase may be significantly reduced or even eliminated, resulting in minimal or no receding behavior. Likewise, at sufficiently low surface temperatures, the receding phase can be hindered or even completely absent. A droplet impacting an ice film may, for example, cause its contact interface to freeze after it reaches maximum spreading, preventing the formation of receding regimes [62,74,75].

In the rebounding regime, a droplet impacts a solid surface and fully rebounds without spreading or wetting the surface. Whether a droplet exhibits rebounding behavior depends on several parameters, including the surface wettability, temperature, and kinetic energy of the droplet [76]. In the rebound regime, if a droplet has a high contact angle and sufficient kinetic energy, it may bounce off the surface upon impact. This can occur when the droplet possesses enough energy to overcome the adhesive forces between the droplet and the surface, causing it to recoil and detach from the surface. However, the rebounding regime can also be absent under certain conditions. For example, on a super-cooled superhydrophobic surface, a water droplet may freeze upon impact and adhere to the surface as it spreads, resulting in no rebounding behavior. This is due to the high surface energy required to overcome the adhesive forces and detach the droplet from the surface.

In the splashing regime, a droplet impacts a solid surface with high kinetic energy or high impact velocity, and it breaks up into smaller droplets, resulting in the ejection of satellite droplets from the main droplet. The breakup of the droplet can occur either immediately upon impact (prompt splashing) or after a short spreading phase (corona splashing), and satellite droplets can be ejected in various directions. The occurrence of splashing is influenced by several factors, including droplet size, impact velocity, surface roughness, and liquid properties such as viscosity and surface tension. Generally, higher impact velocities, larger droplet sizes, rougher surfaces, and lower liquid viscosity and surface tension increase the likelihood of splashing [77–79].

Therefore, when a liquid droplet impacts a solid surface, it can result in various behaviors, including deposition, prompt splash, corona splash, receding break-up, partial bouncing, and full bouncing, shown in Figure 1-6 [80]. These phenomena have been well documented in the literature [61,81]. A number of factors play a significant role in the dynamics of a droplet impact on a surface, including the properties of the droplet (density, viscosity, and surface tension), its kinematic parameters (impact velocity), and the characteristics of the surface (roughness, geometry, and wettability) [60,82–84]. To evaluate the effect of these factors, several dimensionless numbers are used that reflect the relative strength of driving and resistive forces during the spreading and retraction of the droplet. The most common of these are given in Table 1-2 where ρ is the liquid density, u_o is the impact velocity, D_o, σ, and μ are the drop diameter, surface tension, and liquid viscosity, respectively.

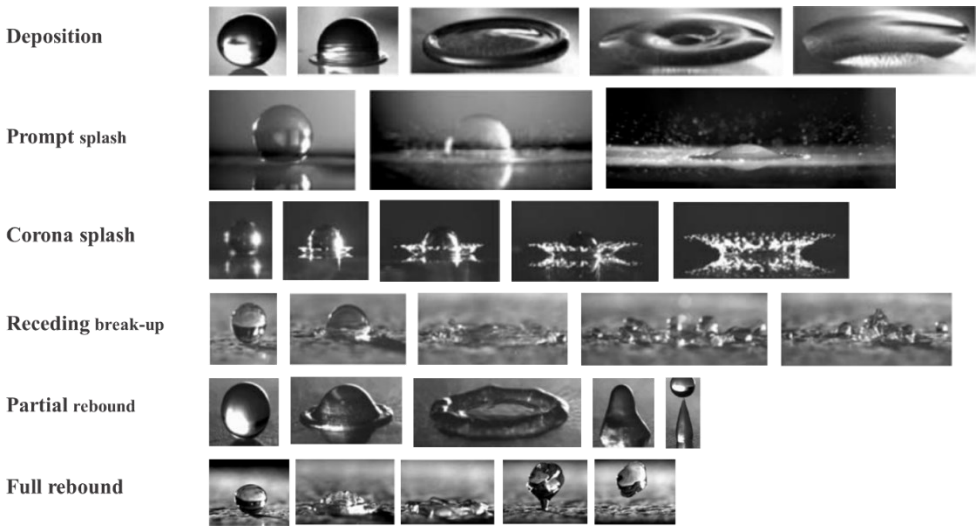

Figure 1-6: Morphology of drop impact on a dry surface [80] *(Reprinted with permission).*

Table 1-2: Key dimensionless numbers to study droplet impact dynamics.

Dimensionless Number	Formulation
Weber number (ratio of inertial to surface tension forces)	$We = \frac{\rho {u_0}^2 d_0}{\sigma}$
Reynolds number (ratio of inertial to viscous forces)	$Re = \frac{\rho u_0 d_0}{\mu}$
Ohnesorge number	$Oh = \frac{\sqrt{We}}{Re} = \frac{\mu}{\sqrt{\rho \sigma d_0}}$
Capillary number (ratio of the viscous force to interfacial tension)	$Ca = \frac{\mu u_0}{\sigma}$

The impact of a droplet on a surface results in the conversion of inertial energy to surface energy and causes the droplet to spread and deform. The wetting properties of the surface and the amount of energy dissipated during the impact determine the pattern formed on the surface. With superhydrophobic surfaces, the impact energy is largely converted into surface energy because the high contact angle minimizes energy loss, allowing for bouncing due to the energy stored in the droplet deformation during the impact. However, surfaces with high energy dissipation result in reduced kinetic energy and prevent bouncing [80,85,86].

Droplet impact phenomena and regimes are highly influenced by a variety of factors (including droplet properties, operational parameters, and surface characteristics), which are mentioned earlier. Described here are the key surface conditions that influence the dynamics of droplet impact on solid substrates. There are four sections describing the effect of surface parameters including wettability, roughness, geometry, and temperature on droplet impacts (Figure 1-7).

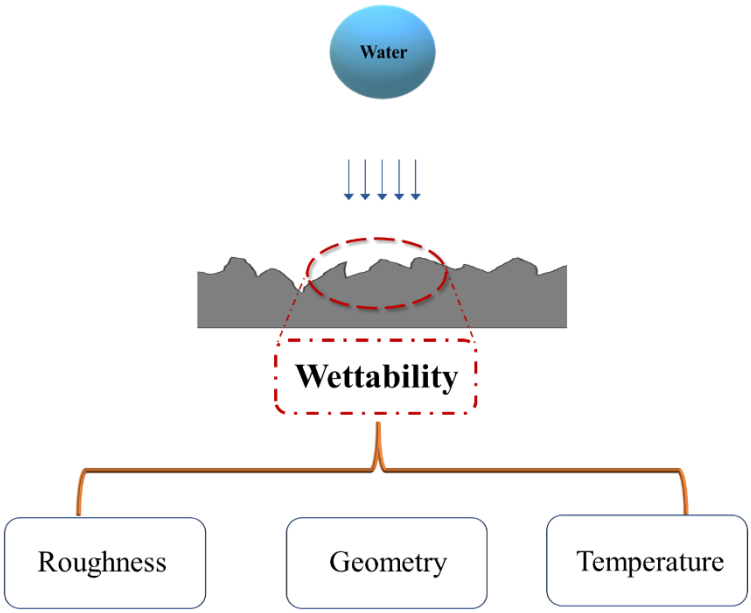

Figure 1-7: Schematic of four characteristics of the surface affecting droplet impact.

1.2.1. The effect of surface wettability

Wetting behavior has been extensively studied in relation to surface geometry as well as the impact of surface roughness on droplet impact. Droplet dynamics after impact are greatly affected by the wettability of a surface. Mao et al. [74] were one of the first to investigate the effect of surface wettability on the spread and rebound of droplets upon impact on flat surfaces at room temperature. They concluded that liquid viscosity and impact velocity strongly influence the maximum spread of a droplet. Liquid viscosity and static

contact angle determine the tendency of a droplet to deposit or rebound, and it follows that low viscosity, high impact velocity, and large contact angle increase rebound.

Later, Rioboo et al. [87] carried out research to investigate the influence of surface wettability on droplet spreading. They found that non-wettable surfaces exhibit differences in the final stages of spreading. In support of this, Moita and Moreira [88] find that a decreasing contact angle results in a faster spreading rate. The experiments in this study were conducted at very low impact velocities, where the wettability effect may be more apparent. As Pasandideh-Fard et al. [64] report, wettability is negligible for high Weber numbers, but significant for low impact velocities. Although wettability may be negligible in some cases, contact angles seem crucial in spreading and receding mechanisms, which cannot be ignored [89,90].

Bange and Bhardwaj [91] conducted a numerical analysis to examine how droplets behave when they come into contact with superhydrophobic surfaces. They discovered that a droplet would rebound off the surface if its overall energy at the moment of maximum recoil is greater than the sum of its initial surface energy and gravitational energy. Khojasteh et al.[92] studied water droplet impact on flat and curved hydrophobic and superhydrophobic surfaces. Their findings indicate that droplets on curved surfaces have a greater maximum spreading diameter compared to those on flat surfaces, while the contact time remains nearly identical for both surfaces. Furthermore, as the Weber number increases, both the maximum spreading diameter and contact time of the droplet increase.

1.2.2. The effect of surface roughness

The impact behavior of droplets on solid surfaces is affected by multiple factors, and one important parameter is the roughness of the target surface. Surface roughness refers to the irregularities or variations in height on the surface of a material, and it can significantly influence how droplets behave upon impact. The interaction between droplets and rough surfaces can affect droplet spreading, bouncing, splashing, wetting behavior, and energy dissipation during impact. Understanding how surface roughness impacts droplet impact behavior is of practical significance in various technological and environmental contexts.

Tsai et al. [82] experimentally investigated the drop impact dynamics on various superhydrophobic surfaces, including regular polymeric micropatterns and rough carbon nanofibers, that displayed similar static contact angles. Their findings suggested that the impact events are minimally affected by the multiscale surface roughness at the nanoscale level for small Weber numbers below 120. However, this surface roughness plays a significant role for larger Weber numbers exceeding 120. Tang et al. [77] reported the detailed dynamic motions of droplets onto a flat stainless steel surface to study how impact dynamics are influenced by surface roughness. They showed that as the Weber number and surface roughness increase, splashing occurs during impact, leading to the ejection of secondary droplets. The droplet spreading is accelerated by higher *We* values but slowed down by increased surface roughness and Ohnesorge number (*Oh*). The maximum spreading diameter primarily depends on the (*We/Oh*) ratio, and slightly decreases with greater surface roughness. Higher values of Weber number or roughness promote the transition from spreading to splashing.

Quetzeri-Santiago et al. [93] focused on the contact line and splashing dynamics of droplets on rough substrates, demonstrating the influence of the Weber number and contact angle on the maximum spreading diameter. They showed that parameters like the splashing ratio, peak to peak roughness, and maximum dynamic contact angle successfully differentiate splashing behavior on various surfaces and liquids. Their study demonstrates that enhancing surface roughness at the micrometer level leads to a higher maximum dynamic contact angle. Conversely, they have noted that micrometer-scale roughness does not impact the spreading dynamics on superhydrophobic surfaces induced by nanometer-scale features.

Goede et al. [94] examined how surface roughness influences droplet splashing by altering the root mean square roughness of the surface upon impact. Their study revealed that the splashing velocity is impacted solely when the roughness of the droplet is sufficiently large to disturb the spreading droplet and change the splashing mechanism from corona to prompt splashing.

Zhang et al. [95] found that the increase in surface roughness could provide wide channels for air to escape and suppress the corona splash, while the larger surface roughness could also disrupt the expanding lamella and promote the prompt splash.

Bao et al. [96] conducted experimental research on water droplet rebound behavior upon contact with rough surfaces. In this work, the effects of surface properties on bouncing–wetting transition of water droplet impacting rough surfaces in the Weber number (We) range from 18 to 221 are experimentally investigated. They noted that as surface roughness increased, the droplets exhibited stronger wetting properties and significantly reduced rebound tendency. Similarly, Cruz et al. [97] also empirically studied droplet dynamics on

rough surfaces and arrived at conclusions consistent with Bao et al. [96], finding that increased surface roughness led to enhanced droplet spreading and splashing, and reduced rebound.

1.2.3. The effect of surface geometry

In addition to the influence of surface roughness on droplet impact, studies have demonstrated that surface geometry also influences droplet impact. Patil et al.[84] examined impact dynamics of a microliter droplet on a micropillared hydrophobic surface under the influence of pitch of the pillars and impact velocity. They have suggested a map of different regimes (non-bouncing, complete bouncing and partial bouncing) based on experimental data, which exhibits the transition of droplet wetting concerning the pitch of pillars and impact velocity. The results indicate that droplets do not bounce on surfaces with smaller or larger pitches, whereas bouncing occurs in pitches of intermediate range. The transition from Cassie to Wenzel, which involves liquid penetration into gaps between pillars, primarily occurs at high pitches and impact velocities.

Wang et al. [98] examined how droplets behave when they hit pillar-arrayed polydimethylsiloxane (PDMS) surfaces with different solid fractions. Their study found that as the solid fraction decreases, the range of Weber numbers that cause droplets to fully rebound also decreases. Xia et al. [99] conducted the experiment involved observing the water droplets impacting on the pillar-patterned superhydrophobic surface. Their study introduced a theoretical model for estimating the maximum spreading factor of droplets on superhydrophobic surfaces, which took into account the geometrical parameters of the pillars and viscous energy dissipation.

Singh et al. [100] investigated the hydrodynamics of droplet impact on doubly re-entrant pillars. Through numerical simulations and experimental studies, they explored how adjusting the structural parameters of these pillars affects their ability to repel droplets. They focused on parameters such as height, diameter, overhang length, and thickness to understand their impact on droplet repellency. The study identified the pitch of the pillars as the most influential parameter in governing droplet repellency. Xia et al. [101] explored the impact dynamics of droplets on pillared hydrophobic surfaces with varying solid fractions. Employing numerical simulations, they observed three pressure peaks during droplet impact, shedding light on the complex interplay between droplet behavior and surface characteristics. The researchers determined that the solid fraction dictated critical impact velocities and influenced cavity formation and bubble entrapment mechanisms. Additionally, they noted that higher solid fractions resulted in reduced wetting spread and impacting depth.

Hua Tan [102] conducted a thorough numerical and experimental investigation on the splashing behavior of μm-sized droplets impacting textured surfaces featuring square-arrayed pillars. The results revealed that during high-speed droplet impact on microstructured surfaces, the spreading lamella predominantly traversed the gaps between pillars rather than wetting the entire surface. Additionally, the maximum spreading diameter on textured surfaces was smaller than that on smooth surfaces due to increased viscous resistance from the pillars. The study highlighted the influence of impact velocity and surface morphology, demonstrating that higher impact velocities and closer pillar spacing increased splashing propensity. Conversely, densely packed or taller pillars mitigated splashing due to increased viscous drag from the pillars. In a study by Matheu Broom and Geoff R. Willmott [103], the focus was on understanding the asymmetrical spreading behavior of water drops impacting

regular micropillar arrays on horizontal surfaces. They explored various parameters such as impact velocity and surface microstructure design to observe transitions from symmetric to highly asymmetrical droplet spreading using high-speed imaging and experimentation. The study focused on examining the influence of surface microstructure parameters, including the shape and dimensions of the micropillars. Specifically, they varied the cross-sectional shape (circular or square), pillar width (20 μm), pillar height (15, 22, or 30 μm), and pitch (40, 60, or 80 μm) of the micropillar arrays. The findings revealed intriguing correlations between spreading outcomes and microstructure parameters. For instance, they observed that the extent of asymmetry in droplet spreading increased with parameters such as impact velocity, pitch, and the use of square pillars rather than circular ones. Additionally, the study identified how changes in microstructure parameters influenced the formation and evolution of protrusions and fingers at the droplet rim.

1.2.4. The effect of surface temperature

Substrate temperature plays a significant role in droplet impact dynamics. When a droplet impacts a substrate, the temperature difference between the droplet and substrate can cause a significant change in the behavior of the droplet. Recently, research has been conducted to understand the impact of the subcooling temperature on droplet impact dynamics, which is a common occurrence in nature and has numerous applications in industries.

When considering the dynamics of water droplets impacting in icing conditions, it is important to note that the behavior of the droplets, the wetting properties, and frost formation

on the surface are all influenced by temperature, which can lead to reduced droplet movement [104].

Maitra et al. [105] aimed to investigate how the morphology of superhydrophobic surfaces, both on the micro and nanoscale levels, affects their ability to resist droplet impalement under severely undercooled conditions. The researchers achieved this by testing the impact of room temperature droplets on undercooled substrates that had been precisely engineered with various textures. They successfully predicted the morphology-dependent Weber number required for the transition from droplet rebound to impalement. An interesting finding was that the critical Weber number (a Webber number beyond which a droplet will stick to the surface due to complete penetration and impalement) for the droplet impalement was independent of the substrate temperature ranging from room temperature to −30°C. This is because the meniscus penetration occurred rapidly at the onset of impact, which was significantly faster than the timescale of heat transfer. However, Maitra et al. [106] also examined the issue of supercooled water droplets impacting superhydrophobic textures under conditions of drop supercooling as low as −17°C. The study revealed that increased viscous effects had a significant impact on all stages of impact dynamics, particularly with a reduction of maximum spreading and an increase of the contact time.

In a study conducted by Khedir et al. [107], water drop impact tests were carried out on a superhydrophobic surface at low temperatures of up to −10°C and low impact speed of 0.54 m/s. The study found that the contact time remained unchanged at such a low impact speed. However, the drop restitution coefficient, which measures the ratio of the drop velocity after and before impact, was found to decrease as the temperature was lowered, due to increased viscous effects. While according to a study conducted by Alizadeh et al. [108],

the impact dynamics of water droplets on surfaces ranging from hydrophilic to superhydrophobic with a Weber number of 138 showed a significant temperature dependency. The study found that lower substrate temperatures resulted in reduced droplet retraction.

Shang et al. [109] also conducted experiments to investigate the spreading characteristics of water droplets upon impact on a smooth hydrophilic silicon surface. They determined the maximum spreading parameter for various degrees of subcooling of the silicon surface. The study focused on two ranges of the Weber number: the low Weber number region and the high Weber number region. Shang et al. [109] found that in the low Weber number region, the maximum spreading parameter decreases as the degree of solid surface subcooling increases. This decrease is attributed to stronger viscous dissipation and a larger capillary effect. Conversely, in the high Weber number region, the maximum spreading parameter initially decreases and then rises with an increase in the degree of solid surface subcooling. In another study, Xin Zhou et al. [110] analyzed the bounce behaviors of double droplets simultaneously impacting a cold superhydrophobic surface, which is a common scenario in multi-droplet impingement during ice formation processes. Through a combination of experimental investigations and numerical simulations, the researchers identified five distinct impacting-freezing modes: no-coalescence rebound, partial-coalescence rebound, complete-coalescence rebound, no-coalescence adhesion, and coalescence adhesion. The study analyzed the effects of horizontal spacing, impact velocity, and surface temperature on various parameters. The study found that the behavior of coalescing droplets transitioned from partial-coalescence rebound to complete-coalescence rebound and coalescence adhesion modes as the surface temperature decreased, attributed to

the increase in ice nucleation rate. Additionally, increasing the Weber number was found to increase the likelihood of droplet adhesion and influence the transition between rebound modes.

Zhang et al. [111] conducted a numerical investigation on the dynamics of droplet impact and freezing on ultra-cold surfaces, focusing on the formation of distinct freezing morphologies and their dependence on surface temperature and Weber number. They extended the study of surface temperatures to −100°C through simulations using the Volume of Fluid (VOF) method coupled with dynamic contact angle and Solidification/Melting models. They established a morphology map based on surface temperature and Weber number and found that the spreading behavior of the contact line was more sensitive to surface temperature. Yu et al. [112] investigated the dynamic behavior of water droplets impacting superhydrophobic surfaces in a supercooled environment, with a focus on understanding the influence of temperature differences between the droplet and the cold surface. The study revealed that changes in droplet properties, particularly viscosity, significantly impact dynamic behavior. At low Weber numbers, the change in viscosity minimally affects contact diameter and contact time but notably affects droplet height during retraction. Surprisingly, decreasing surface temperature led to slower droplet retraction and increased contact time, contrary to intuition. Conversely, increasing droplet temperature under constant surface temperature exhibited similar behavior, suggesting a complex interplay influenced by possible liquid-phase condensation processes within the microstructure. The study emphasized the significant role of droplet temperature in influencing retraction dynamics and contact time on superhydrophobic surfaces, highlighting

the importance of considering solid-liquid temperature differences and potential droplet condensation within microstructures.

Yao et al. [113] conducted a comprehensive investigation (experimental observations and numerical simulations) into the dynamic and freezing behavior of water droplets impacting superhydrophobic ultra-cold surfaces, spanning a temperature range from −10°C to −60°C. The experiments revealed three distinct droplet behaviors as surface temperature decreased: full rebound, partial rebound, and full adhesion. Notably, as surface temperature decreased, the growth rate of contact time increased with lower Weber numbers, particularly evident in the case of full rebound. Conversely, the variation in surface temperature minimally affected dynamic behavior on ultra-cold surfaces below −40°C, especially in scenarios of full adhesion. Furthermore, the study investigated the impact of surface temperature on the maximum spread factor of droplets, revealing a reduction in spread factor from 2.55 to 2.44 as surface temperature decreased from 20°C to −60°C, with a more pronounced effect observed at higher Weber numbers. Guo et al. [114] investigated the bouncing regimes of supercooled water droplets impacting superhydrophobic surfaces with controlled temperature and humidity. They fabricated post-array and flat superhydrophobic surfaces to study droplet impact dynamics. On flat superhydrophobic surfaces, two regimes were observed: conventional rebound and full adhesion, with adhesion occurring at low surface temperature and high Weber number. On post-array superhydrophobic surfaces, four regimes were observed, including pancake rebound, conventional rebound, partial rebound, and full adhesion. Frost formation between posts reduced capillary energy, transitioning pancake bouncing to conventional rebound at lower temperatures.

Summary

Droplet impact on solid surfaces is a fundamental phenomenon with extensive applications, involving various regimes such as spreading, receding, rebounding, and splashing. These behaviors are influenced by several key factors. Surface wettability plays a significant role in determining droplet wetting and rebounding behaviors. Superhydrophobic surfaces, which minimize energy loss, promote bouncing by utilizing stored energy during impact. Surface roughness is another crucial parameter that affects droplet impact behavior. Surface roughness may have minimal impact at low Weber numbers but becomes significant at higher Weber numbers, potentially inducing splashing and altering droplet spreading. Surface geometry, particularly the dimensions of pillar arrays, can dictate whether a droplet bounces, partially bounces, or does not bounce at all upon impact. Surface temperature is a critical variable, especially in icing conditions. Subcooling temperature influences droplet impact behavior, impacting frost formation, droplet movement, and rebound. In summary, droplet impact behavior is a complex interplay of various factors, including surface parameters like wettability, roughness, geometry, and temperature. Understanding how these factors affect droplet impact is crucial for optimizing processes in multiple industries and designing materials with tailored properties. Figure 1-8 provides a concise representation of the key factors influencing droplet impact behavior.

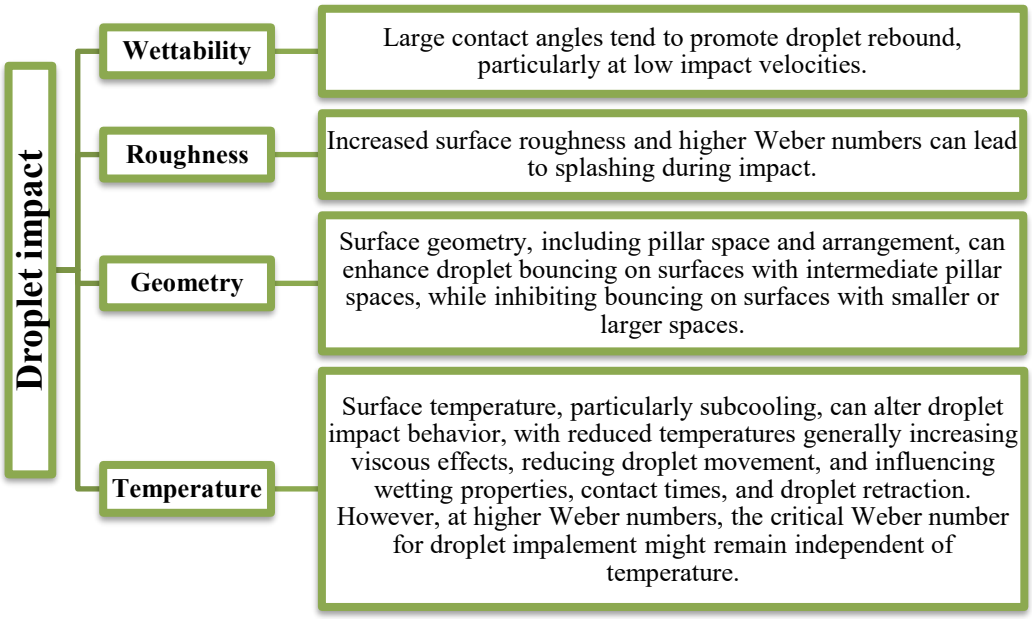

Figure 1-8: Summery of factors influencing droplet impact behavior.

1.3. Ice nucleation

Water droplets do not freeze immediately after contacting a cold surface. It remains in a metastable supercooled state for some time due to a freezing delay. The ice nucleation phenomenon and surface characteristics have a profound effect on freezing delay time [115,116]. Freezing delay time is defined as the time interval between the impact of the droplet on the pre-cooled substrate and the onset of freezing and can be measured by a microscope or CCD (Charged Coupled Device) camera.

In this section, we investigate the intricate mechanisms behind ice formation. Ice nucleation, the process by which ice crystals form from water vapor or liquid water, is a complex phenomenon that occurs through two main pathways: homogeneous and heterogeneous nucleation that will be discussed. Furthermore, the effect of surface features on ice nucleation is a critical aspect of this research. The characteristics of a surface, such as its wettability, roughness, geometry, and temperature, can significantly influence the rate and

extent of ice nucleation (Figure 1-9). Understanding how surface features impact ice nucleation is crucial for various applications, ranging from atmospheric science to icephobic materials. Through a comprehensive review of the literature and experimental data, we aim to elucidate the underlying principles governing ice formation, contributing to our understanding of this complex process and its practical applications.

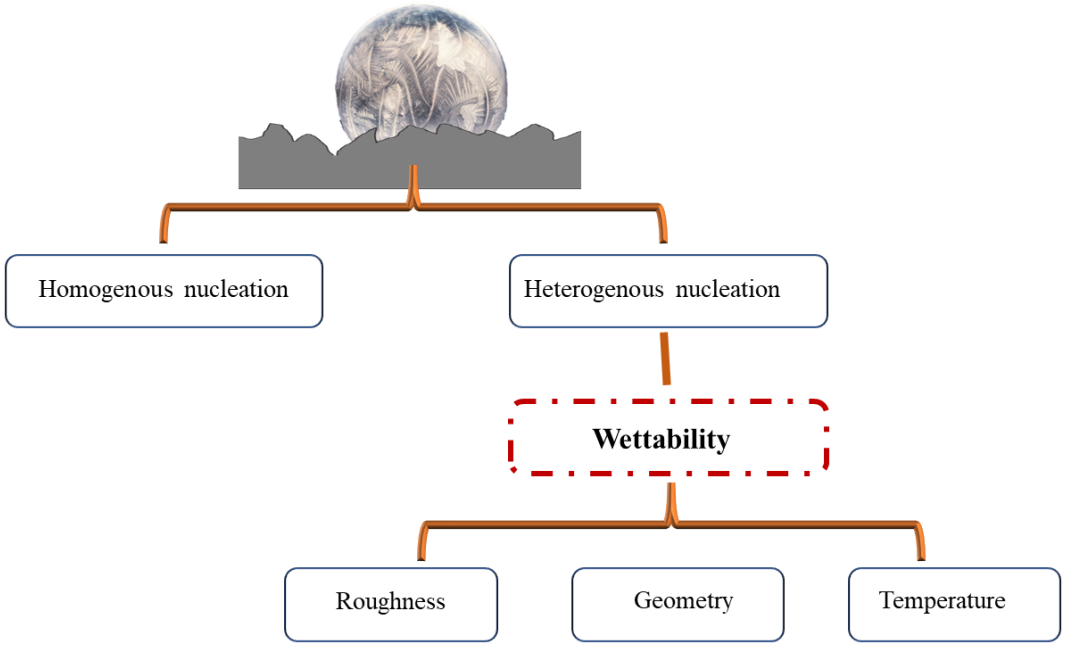

Figure 1-9: Schematic of four characteristics of the surface affecting ice nucleation time.

1.3.1. Ice formation mechanism

A phase change process from liquid water or water vapor into solid form is referred to ice formation process, beginning with nucleation and growing to complete freezing through different routes [12]. Thermodynamically, ice formation could occur through three different pathways including (1) vapor- solid (desublimation), (2) vapor- liquid- solid (condensation- freezing), and (3) liquid- solid (freezing). Each of these favorable pathways is governed by different mechanism of ice nucleation and growth [9]. In order to rationally

develop an icephobic surface, satisfying all or some of the following conditions for each phase would be an asset [117]:

(1) Vapor phase: inhibit ice nucleation or condensate formation.

(2) Liquid phase: delay ice nucleation and improve water repellency.

(3) Solid phase: reduce ice adhesion.

Nucleation is a physical process that can be considered as the crucial and fundamental step in the ice formation process. It includes the formation of the initial embryos of tiny stable solids from a supercooled or supersaturated mother phase (vapor or liquid phase). For freezing and ice growth to occur, an ice nucleus must reach a certain size called the critical size (r^*) to be thermodynamically stable (Figure 1-10). Below this critical size, an ice nucleus is unstable and will be destroyed, reverting to the mother phase [118]. Ice nucleation and its growth will happen under a thermodynamic driving force. Following are the basic steps of crystallization of the entire freezing systems:

1. Achieving of driving force by change in equilibrium condition
2. Nucleation
3. Ice crystals resulted from the growth of the nuclei

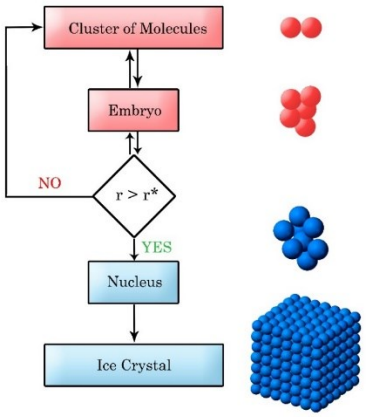

Figure 1-10: Ice formation (r and r are radius and critical radius of an embryo, respectively)* [21] *(Reprinted with permission).*

1.3.2. Crystallization (phase equilibrium)

In general, ice formation process is referred to the process of phase change of a mother phase (liquid water or water vapor) at higher entropy to a solid crystal phase (ice) with lower entropy. In order to form a new phase (ice), there must be a decrease in entropy that is reflected in the existence of an energy barrier. The thermodynamic driving force is needed to overcome the energy barrier, which is the chemical potential difference between chemical potential of mother phase (μ_M) and solid phase (ice (μ_I)) [118–121]:

$$\Delta\mu = \mu_M - \mu_I \qquad \textit{Equation 1-5}$$

In order to favor the condition for ice embryo to grow, this chemical potential difference (Equation 1-5) is related to variation in pressure or temperature. In case of ice formation from water vapor phase, change in chemical potential is contributed to variation of pressure, called supersaturation [122,123]:

$$\Delta\mu = k_B T ln\frac{P}{P_0} \qquad \textit{Equation 1-6}$$

where k_B, T, P and P_0 denote Boltzmann's constant, the actual temperature, the given pressure, and the equilibrium pressure.

Temperature dependency of chemical potentials for crystallization from the liquid phase has also been defined as supercooling and expressed as [27,124]:

$$\Delta\mu = \frac{\Delta h_{WI}}{T_m}(T_m - T) \qquad \textit{Equation 1-7}$$

which Δh_{WI}, $T_m$and T are enthalpy of freezing, melting point temperature and the actual temperature.

In case of supercooling, for $T > 0$ ($\Delta\mu > 0$) and $\Delta T = T_m - T$, ice crystal would be initiated and grow thermodynamically. On the other hand, if temperature increase (($\Delta T < 0$, $\Delta\mu < 0$), melting of the solid ice will happen. At equilibrium state, chemical potential of mother phase and ice are the same ($\Delta T = 0$, $\Delta\mu = 0$) and no phase change occurs [3].

1.3.3. Concepts of ice formation and nucleation on a surface

The fundamental and crucial step in the ice formation process is nucleation. To develop an effective and sustainable icephobic surface that inhibits ice formation, a precise and substantial understanding of ice nucleation is necessary.

The most common theory of nucleation is known as Classical Nucleation Theory (CNT), which was developed in 1928 and states that ice formation process includes the formation of ice nuclei having some specific size (the critical size) with the same macroscopic properties like their bulk phases and the growth of these nuclei into ice crystal [125–128]. According to CNT, identical properties for small nuclei and their corresponding

bulk phase is one of the initial assumptions that can be mainly valid at small or moderate supersaturation.

Based on CNT, some parameters including Gibbs free energy barrier of freezing which is a thermodynamic quantity and the ice nucleation rate, related to kinetics of ice nucleation describe the ice nucleation process.

Nucleation process mainly occurs in two different modes: homogeneous and heterogeneous nucleation that are characterized using absence and present of any external agents, respectively that are discussed in the following sections.

1.3.4. Homogeneous nucleation

In a supercooled or supersaturated system, homogeneous nucleation of ice from either vapor or liquid phase takes place in lack of any external substrate (outdoor surfaces, solid particles, etc.) [129]. Experimental assessing homogenous nucleation (homo-N) is quite restricted due to presence of impurities which induce heterogenous nucleation (hetero-N) [130]. In the framework of second law of thermodynamics, a process including conversion of disordered water molecules (either in vapor or in liquid state) at higher entropy into highly ordered molecules (ice) at lower entropy is occurring. Therefore, a certain amount of energy barrier exists that has to be overcome using a supersaturation and/or supercooling (driving force) [20,123]. Overcoming energy barrier of nucleation gives chance to the unstable embryos to get larger than a critical size and commence their spontaneous growth until the formation of ice crystals [131].

In the context of classical nucleation theory (CNT) applied to homo-N kinetics, researchers commonly focus on the formation of liquid nuclei in the vapor phase, known as the 'mother phase.' This choice is driven by the isotropic surface tension of the liquid, which leads to spherical equilibrium shape of the small liquid embryos and simplifies mathematical models, as elaborated in reference [21]. In the scope of CNT, properties of small cluster of molecules are assumed the same as the properties of the constituent atoms in the infinitely large phase along with a surface energy term to compensate the difference between corresponding values in small and infinitely large phases [120,132,133]. Therefore, change in Gibbs free energy of system (ΔG_{MI}) is as below (Equation 1-8):

$$\Delta G_{MI} = -V_I(\mu_I - \mu_M) + \sigma_{MI}S \qquad \textit{Equation 1-8}$$

where V_I is the volume of solid phase (ice), and σ_{MI} is the surface energy of aggregated molecules in newly formed solid phase. μ_I and μ_M are chemical potential of solid (ice) and mother phases (which can be either liquid or vapor), respectively.

Considering a supercooled and supersaturated water vapor as the mother phase, there are two possible pathways to form ice; **1)** direct ice nucleation that is known as desublimation, **2)** condensation and subsequent ice nucleation form liquid water. Homo-N of ice directly from the vapor phase is not possible in atmosphere and can just be realized under laboratory condition, firstly, because of the high supersaturation that is required. Secondly, liquid drops would nucleate from the vapor phase before this supersaturation was reached and lastly the atmosphere can contain condensation nuclei [123,134]. Therefore, the only pathway would be water condensation and then ice formation from liquid water. CNT predicts the change in free energy of system (ΔG_{WI}) for ice nucleation inside a liquid water

by Equation 1-9 (Utilizing Equation 1-8 as a generalized form of ΔG with assuming spherical equilibrium shape of small embryos, $S = 4\pi r^2 \; and \; V_I = \frac{-4\pi r^3}{3}$) [133].

$$\Delta G_{WI} = -\frac{4\pi r^3}{3}(\mu_I - \mu_W) + 4\pi r^2 \sigma_{WI} \qquad \textit{Equation 1-9}$$

Figure 1-11 schematically shows the change in free energy of system with the radius of ice embryo. Until the critical size (extremum of diagram), change in free energy of system increases with increasing the radius of newly born ice embryo. Beyond the critical size, with increasing the size of ice nucleus, system free energy decreases down to spontaneous ice formation state. Using $\partial \Delta G_{WI}/\partial r = 0$ at extremum, following relations for the critical radius of embryo (r^*) and critical energy barrier (ΔG^*) will be obtained (Equation 1-10 and Equation 1-11):

$$r^*_{WI} = \frac{2\vartheta_I \sigma_{WI}}{\Delta h_{WI}(^{\Delta T_m}/_{T_m})} \qquad \textit{Equation 1-10}$$

$$\Delta G^*_{WI} = \frac{16\pi {\sigma_{WI}}^3 \vartheta_I^2}{3[\Delta h_{WI}(^{\Delta T_m}/_{T_m})]^2} \qquad \textit{Equation 1-11}$$

where Δh_{WI} is the molar enthalpy of freezing, and ΔT_m is the degree of supercooling. The equations from the Classical Nucleation Theory provide a quantitative framework to understand and predict the nucleation behavior of ice embryos in supercooled systems, which can be invaluable in both research and practical applications. The equations highlight the dependence of nucleation on key parameters like degree of supercooling, offering a way to understand how changing conditions affect nucleation behavior.

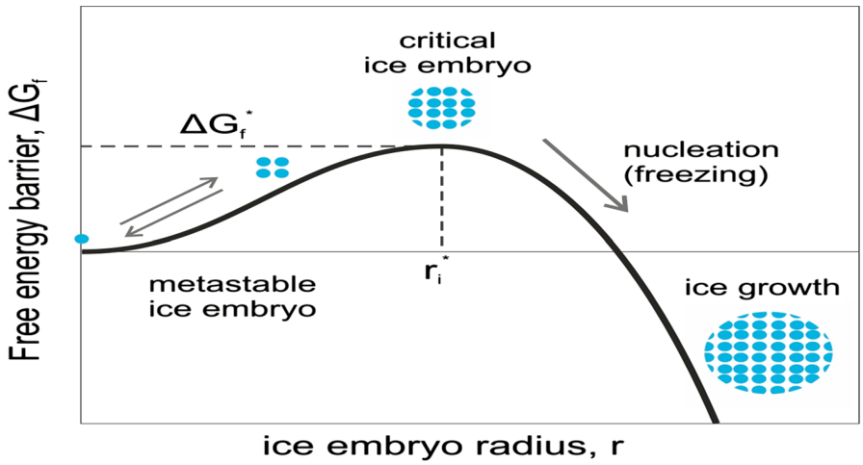

Figure 1-11: Variation of ΔG with the radius of embryo. The extremum of function ΔG determines the value of critical radius (r), geometrical boundary between ice embryo and ice nucleus and the maximum work required to form a nucleus (ΔG*)* [19,20].

1.3.5. Heterogenous nucleation

In practice, eliminating the role of foreign solid particles (e.g. dust particles, interfaces of nucleating systems) is almost impossible and promote ice nucleation [131]. Solid particles and surfaces have long been known as an agent with convoluted effect on liquid/vapor-to-solid phase transformations [135]. Therefore, identifying their interactions with ice nucleation and growth is essential towards designing icephobic surfaces [136]. In contrast with homo-N where the nucleation probability is homogenous throughout the system, hetero-N process refers to the situation in which the probability of nucleation is much higher around some foreign bodies than other parts of the system and undercooled liquid water containing solid particles will generally freeze at temperatures higher than the homo-N point [20,131,137].

In hetero-N, the presence of foreign particles significantly reduces the interfacial or surface free energy and the required nucleation barrier. An interfacial correlation factor

$f(m,x)$ can be used to quantify the effect of external particles and can be expressed by following equation:

$$f(m,x) = \Delta G^*_{Hetero}/\Delta G^*_{Homo} \qquad \textit{Equation 1-12}$$

where ΔG^*_{Hetero} presents the critical energy barrier of heterogeneous nucleation and ΔG^*_{Homo} is the critical homogenous nucleation barrier as defined analytically by Equation 1-11.

The surface parameter $f(m,x)$ is a function of both contact angle and surface curvature. $x = R/r^*$, R is radius of curvature of solid particle or surface textures (index of surface unevenness) and m is parameter represents the contact angle between ice nucleus and nucleating surface ($m = cos\theta_{MI} = (\sigma_{SM} - \sigma_{SI})/\sigma_{MI}$), $f(m,x)$ can be defined as follow (Figure 1-12) [138]:

- considering concave radii of curvature

$$f_{\cup}(m,x) = \frac{1}{2}\left\{1 - \left[\frac{1+mx}{g}\right]^3 - x^3\left[2 - 3\left(\frac{x+m}{g}\right) + \left(\frac{x+m}{g}\right)^3\right] + 3mx^2\left[\frac{x+m}{g} - 1\right]\right\} \qquad \textit{Equation 1-13}$$
$$g = (1 + 2mx + x^2)^{0.5}$$

- considering convex radii of curvature

$$f_{\cap}(m,x) = \frac{1}{2}\left\{1 + \left[\frac{1-mx}{g}\right]^3 + x^3\left[2 - 3\left(\frac{x-m}{g}\right) + \left(\frac{x-m}{g}\right)^3\right] + 3mx^2\left[\frac{x-m}{g} - 1\right]\right\} \qquad \textit{Equation 1-14}$$
$$g = (1 - 2mx + x^2)^{0.5}$$

For both cases (concave and convex curvature), the value of geometrical parameter *f* ranges from 0 to 1. It reveals that the hetero-N has a lower energy barrier in comparison with

homo-N with the same radius of critical nucleation and consequently required lower degrees of supersaturation or undercooling to occur. A concave curvature is generally more favorable for ice nucleation compared to a convex curvature due to the reduced the geometrical factor.

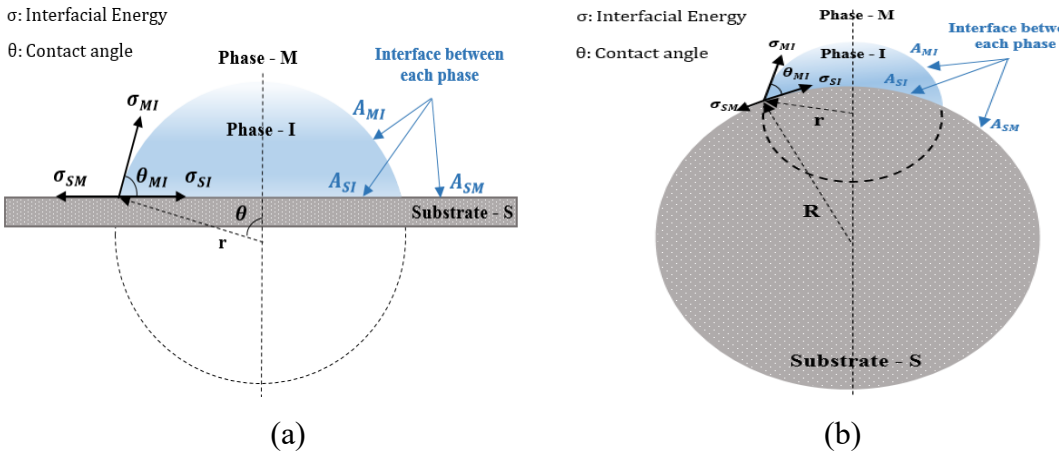

Figure 1-12: Schematic of formed embryo (a) on a smooth substrate (b) on a convex foreign body as nucleating substrate.

1.3.6. Nucleation rate

The possibility of freezing could be estimated through the nucleation rate of a single embryo, which is inversely proportional to the delay time of ice nucleation and is based on kinetic theory. The nucleation rate of ice embryos (J) can be estimated as Becker and Doring proposed the following equation to estimate the rate of ice nucleation per unit time and surface area that is related to the free energy barrier of nucleation of critical embryo [122,133,139]:

$$J(T) = K(T)A \exp\left(\frac{-\Delta G(T)}{K_B T}\right) \qquad \textit{Equation 1-15}$$

where $K(T)$, A, $\Delta G(T)$, k_B, T respectively represent the diffusive flux of water molecules across the ice surface, the droplet-substrate contact area, the free energy barrier, the

Boltzmann constant, and the temperature. In Equation 1-15, $K(T)$, can be expressed as follows:

$$K(T) = \frac{K_B T}{h} \exp\left(\frac{-\frac{K_B T^2 E}{(T - T_R)^2}}{K_B T} \right) n \qquad \textit{Equation 1-16}$$

where k_B, h, and n are the Boltzmann constant ($1.38 \times 10^{-23}\, J/K$), Planck constant ($6.62 \times 10^{-34}\, J/S$), and the number density of water molecules at the ice nucleus/water interface ($n \approx 10^{19}\, m^{-2}$). In the temperature range of $150K$ to $273K$, $T_R = 118\, K$ and $E = 892\, K$ have been determined experimentally for liquid water [140]. They are fitting parameters used for the calculation of diffusivity of water, expressed by the empirical Vogel-Fulcher-Tammann Equation [140].

1.3.7. Approaches to increase heterogeneous nucleation energy barrier

There are two main parameters that affect the critical energy barrier for heterogeneous nucleation: Δμ related to degree of supercooling and f that is the interfacial correlation factor and this factor is a function of the roughness radius of curvature (R) and the contact angle between ice nucleus and the surface structure. Figure 1-13 shows plots of f as a function of x ($= R/r^*$, R is radius of curvature of solid particle or surface textures and r^* critical radius of an embryo) for different values of θ on surfaces with concave pits and convex bump. It reveals that when ($x \leq 10$), f depends on both m (is a parameter representing the contact angle between ice nucleus and nucleating surface) and x that means that surface structure should be favorable to nucleation. However, for relatively large value of x ($x \geq 10$), the effect of surface structure in not important [20].

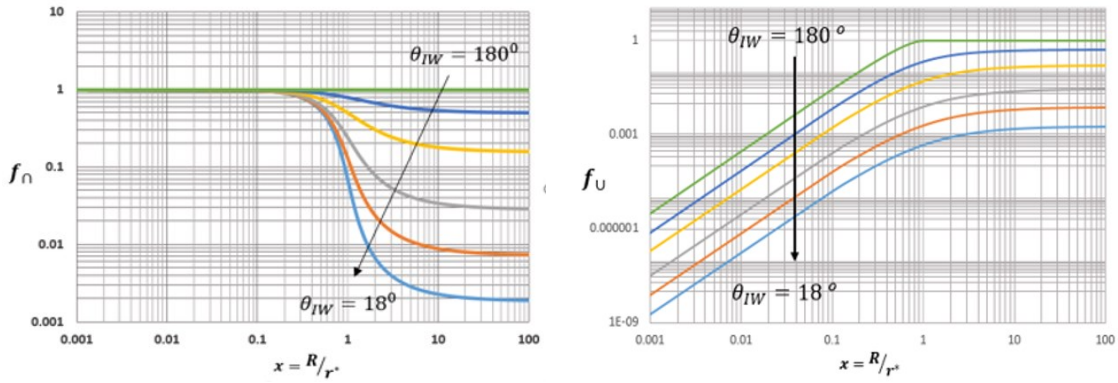

(a) (b)

Figure 1-13: Evolution of the geometrical factor f as a function of x and m for (a) convex pit and (b) for concave bump, Diagrams were plotted at five different values of contact angle 18º, 25.8º, 36.9º, 60º, 90º and 180º [141] *(Reprinted with permission). In the given figure, the contact angle values are associated m = cos (θ_{IW}) ranging from 1 to −1, which corresponds to contact angle values between 0 and 180 degrees. Different curves are plotted for cos (θ_{IW}) values of 1, 0, 0.5, 0.8, 0.9, and 0.95, starting from the top, thereby spanning the θ_{IW} range from 180 to 18.2.*

1.3.8. The effect of surface wettability

When dealing with freezing delays on superhydrophobic surfaces, the contact area between the droplet and the solid has been shown to play an important role in the freezing process. From nucleation theory, a reduced contact area reduces the nucleation rate proportionally. However, some studies have reported the opposite effect of surface wettability on freezing delay time. In the context of Classical Nucleation Theory (CNT), it is important to consider the surface wettability, specifically with regard to its interaction with ice, as indicated by the ice-water contact angle. Linking surface wettability with respect to water (sessile droplet contact angle θ_W) and contact angle of formed ice inside water droplet (θ_{IW}) could be helpful in analyzing nucleation behavior of surfaces due to exact information and data of surface wettability.

This relationship can be theoretically expressed, assuming the formation of a spherical segment of an ice nucleus immersed in a supercooled water droplet sitting on an ideally smooth (no surface roughness) solid surface (Figure 1-14 a), as below [19,141]:

$$cos\theta_{IW} = (\sigma_I - \sigma_W)cos\theta_W/\sigma_{IW} \qquad \textit{Equation 1-17}$$

where σ_I and σ_w and represent the ice-air and water-air interfacial energy, respectively.

The ice nucleation on nanostructured surfaces must account for the existence of a quasi-liquid layer between the ice nucleus and the solid substrate which leads to a change in ice-water contact angle (Figure 1-14 b). So, a clear correlation between the ice−water contact angle variation and quasi-liquid layer formation due to surface curvature is shown as:

$$\cos(\theta_{IW})\frac{\sigma_{IW}}{\beta} = \sigma_{SW} - \sigma_{SLL} - \frac{\sigma_{ILL}}{\beta} = \left(\sigma_{SW} + \frac{\sigma_{IW}}{\beta} - \sigma_{SI}\right)e^{\frac{-d}{\xi}} - \frac{\sigma_{IW}}{\beta} \qquad \textit{Equation 1-18}$$

where σ_{ILL}, σ_{SLL}, σ_{SI} and σ_{IW} denote the surface energies of the interface between ice and the quasi-liquid layer, the substrate and the quasi-liquid layer, the substrate and ice, and the ice and liquid, respectively. $\beta = (\frac{R}{R-d})^2$ and R is the radius of curvature of surface, and the symbols d and ξ represent the thickness of the quasi-liquid layer and a characteristic decay length, respectively [21,141].

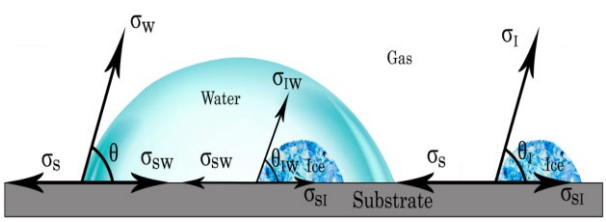

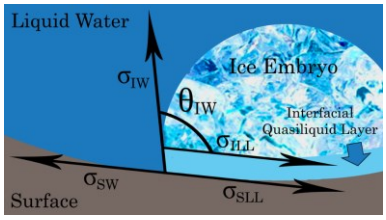

(a) (b)

Figure 1-14: Interfacial forces in the case of formed ice embryo inside both liquid water and air. subscripts S, I, W stand for substrate, ice and water, respectively (b) Quasi-liquid layer underneath ice embryo on a nanoscale cavity [141] *(Reprinted with permission).*

We will now proceed to examine specific instances and research findings that elucidate the role of surface wettability in ice nucleation and freezing phenomena. Eberle et al. [141] used nanostructuring surfaces to suppress the formation of ice nuclei. They prepared 11 different nanostructured surfaces with controlled roughness radii of curvature and wettability by photolithography and chemical modification. The nanostructuring surfaces with three orders of magnitude change in root mean square roughness (RMS) size (~ 0.01 to 100 nm) lead to reduce ice nucleation temperature to ~ −24°C, low ice adhesion and 25 hours freezing delay of a sessile supercooled water droplet at −21°C. They tried to develop surfaces with extraordinary anti-freezing properties using the intertwined effects of nucleation thermodynamics and superhydrophobicity.

Sessile droplet freezing on polished (hydrophilic) silicon wafer and cylindrical micro-micro hierarchical (hydrophobic) silicon surface at −6.3 °C, the contact angles of water (at 25.7 °C) on which were 78.77° and 143.82°, respectively showed that hierarchical micro-micro structure has higher ice nucleation time in comparison with hydrophilic surfaces [142]. The hierarchical structure has higher surface roughness than the critical radius of homogenous nucleation. According to the classical nucleation theory, in this case, wetting characteristic of the surface controls the free energy barrier means that the larger contact angle, greater free energy barrier for nucleation.

The combination of micro-nano structures and chemical modification is also studied in the work of Qi et al. [36] to investigate the freezing delay of the prepared surfaces at the temperature of −10°C and humidity of 40% and obtained 97 min delay in icing that present a desirable anti-icing property of the superhydrophobic surfaces. They observed that the contact angle strongly influenced the freezing time of water droplets on hydrophilic, hydrophobic, and superhydrophobic surfaces, i.e., a longer freezing time as contact angle increased. The freezing time of droplets with different wettability has also been studied by Bodaghkhani et al. [143]. Using experimental and numerical simulations, it was determined that the smaller the static contact angle, and the lower surface temperature of droplets, the faster they freeze.

1.3.9. The effect of surface roughness

Regarding the effect of surface features on the ice nucleation, roughness is one of the unclear issues. In general, it may be expected that as ice crystals form on rough surfaces, the nucleation time can be shorter than on smooth surfaces, as rough surfaces provide more nucleation sites [144]. It should be noted, however, that surface roughness is also dependent on the size and shape of roughness features, as well as the chemical properties of the surface. A certain type of roughness feature may promote ice formation more effectively than another, depending on its size and spacing. For example, Cao et al. [145] discovered that the effectiveness of a superhydrophobic coating ability to prevent ice formation is determined by both its superhydrophobicity and different sizes of surface roughness. This suggests that the ability of a surface to resist icing is not solely based on its degree of superhydrophobicity. They found that there was almost no ice formation when superhydrophobic coatings had roughness particles smaller than 50 nm. A significant increase in icing probability was

observed when coarse particles exceeded 50 nm in size. Therefore, the importance of having an appropriate size of surface roughness structure in superhydrophobic coatings for their anti-icing performance can be observed. As Jung et al. [146] also reported, water contact angle and surface roughness were factors influencing ice formation. In Figure 1-15, they found that roughness values have an inverse relationship with freezing delay for surfaces with low roughness values (i.e., 1.4–6 nm, technically smooth surfaces). When rough surfaces are involved, however, contact angle is a dominant factor in delaying ice formation, resulting in an increase in freezing delay as contact angle increases.

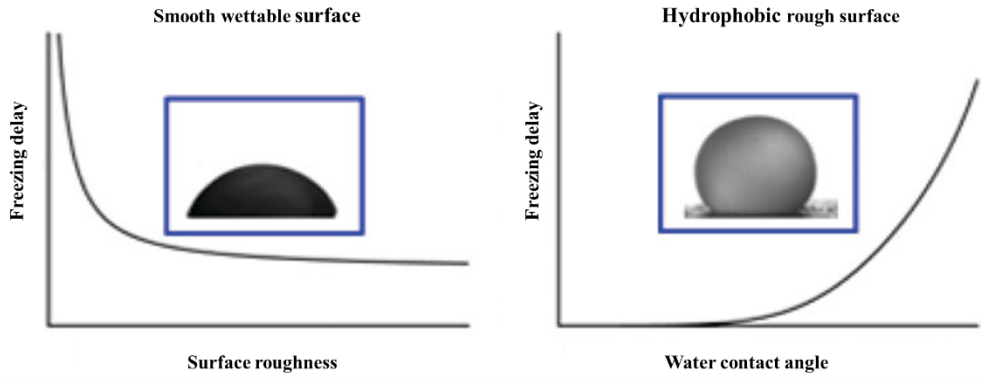

Figure 1-15: The relationship between freezing delay and (a) roughness for smooth surfaces, (b) water contact angles for rough surfaces [146] *(Reprinted from Open Access).*

Hao et al. [115], prepared five kinds of substrate with different topology and wettability to study the freezing delay time and the freezing time of sessile droplet on smooth, micro-structured and micro/nano-structured surfaces. Based on experimental data and theoretical analysis, they suggested that the surface roughness significantly influences the ice nucleation time. In this study, smooth surfaces with roughness less than a critical ice nucleus experience a longer freezing delay than superhydrophobic surfaces with hierarchical

structures. However, Heydari et al. [147] conducted an experiment to measure the freezing temperature and freezing delay time of surfaces with similar chemistry but varying topography and roughness. These surfaces included both smooth and rough surfaces with an RMS of about 1 nm to 250 nm. The results of the experiment showed that the freezing delay time of water was not noticeably influenced by the surface topography and roughness, despite the differences in surface texture.

Overall, there is a great deal to learn about the specific mechanisms involved in the effect of surface roughness on ice nucleation time, and there is a lot to learn about the effect of surface roughness on ice nucleation time.

1.3.10. The effect of surface geometry

For studying potential anti-icing applications, such as ice nucleation time, the patterned and ordered substrates are ideal as a model system, which can be precisely controlled and analyzed to determine which parameters are most effective for designing icephobic surfaces. Although there has been significant progress over the last years in understanding how surface geometrical parameters affect ice nucleation time, it remains an interesting topic for discussion. There is still uncertainty about parameter selection, and the exact influence these surface geometrical parameters on ice nucleation time has not yet been fully understood.

Nguyen et al. [148] studied how different parameters of surface texture, such as the diameter and height of pillars, affect the performance of a passive anti-icing approach. They investigated the adhesion strength and freezing delay time of water droplets on surfaces with uniform textures, where the pillar top diameters varied from 30 to 145 nm and the heights

ranged from 300 to 575 nm. They concluded that surfaces that are well-textured with nanopillars, particularly those with small top diameters, regardless of their height, may exhibit reduced adhesion force and prolonged freezing delay time during subsequent de-icing processes.

In the study conducted by Milles et al. [149], hierarchical textures were created on pure aluminum surfaces using laser ablation, resulting in the formation of superhydrophobic surfaces after 13-16 days of exposure to air. The experimental results demonstrated that these patterned superhydrophobic surfaces exhibited excellent ice-repellent properties, with the freezing time of droplets being nearly three times longer compared to untreated samples.

Meyta et al. [150] focused on investigating the nucleation behavior of a supercooled water droplet on surfaces with nanoscale textures using molecular dynamics simulations. The findings obtained from the molecular dynamics simulations reveal that the nucleation rate is influenced by the surface fraction and the wetting states. Specifically, an increase in surface fraction promotes nucleation rate for water droplets in the Cassie-Baxter state, whereas the opposite behavior is observed for droplets in the Wenzel state. Additionally, their research also investigated the impact of nanopillar height on ice nucleation. The results reveal that the nucleation rate is augmented as the nanopillar height increases. This phenomenon is attributed to the larger contact area between the water droplet and the surface as the nanopillar height increases, thereby promoting ice nucleation.

Hou et al. [14] fabricated micro-cubic arrays on silicon wafer surfaces with the same value of height as 20 μm and various micro-spacing distances from 30 μm to 130 μm. The research investigated the impact of surface microstructure size on anti-icing and icephobic

performance, as assessed by icing delay time and ice adhesion strength. The results showed that the presence of air pockets entrapped in the microstructures led to a significant delay in ice formation, with the delay time being two orders of magnitude greater than that observed on the pristine surface. Furthermore, the ice adhesion strength was reduced on the microstructured surface, indicating improved icephobic properties.

Overall, understanding how well-textured surfaces influence ice nucleation can aid in the design of materials with tailored ice nucleation properties for various applications.

1.3.11. The effect of surface temperature

Critical Energy barrier of nucleation is inversely proportional with the square of supercooling ($\Delta {T_m}^2$) and therefore decreases with increase in the degree of supercooling (decrease in governing temperature, T) (Equation 1-11). It reveals that at earlier stages of temperature reduction (higher temperatures), reduction in critical energy barrier is more than low temperatures. In other words, the rate of decrease in critical energy barrier decreases with decrease in temperature (Figure 1-16). Moreover, the greater the degree of undercooling, the smaller the critical radius of the formed nuclei.

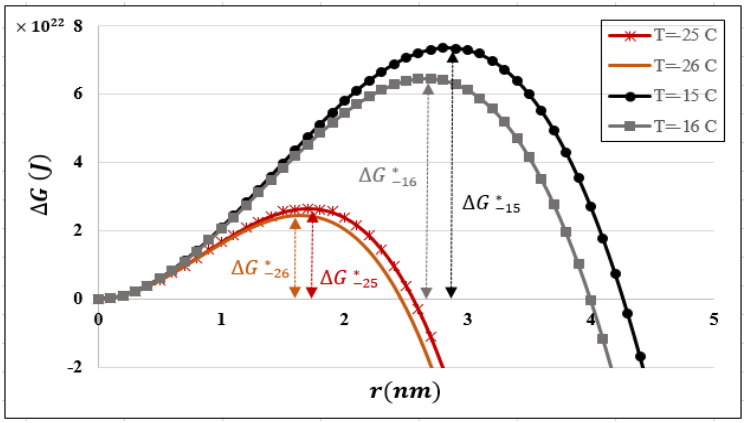

Figure 1-16: Variation of ΔG with radius of embryo at different temperatures. Diagrams were plotted using constant properties $\Delta h_{WI} = 278\ MJ/m^3$ *,*$\sigma_{WI} = 2.17\ mJ/m^2$ *and* $T_m = 273.15\ k$ [132].

Rahimi et al. [151] measured the freezing delay of 6μL water droplet on precooled aluminum substrate modified chemically to obtain different hydrophobic and hydrophilic surfaces without modification of surface topography at different temperature from −5 to −25 °C. In their experiment, a slightly hydrophilic substrate modified by (3-aminopropyle) triethoxyilance showed longer freezing delays than both more hydrophilic and hydrophobic surfaces because of the surface chemistry and suggested that the ice nucleation kinetics depends on surface wettability and chemistry. For all samples, it is observed that the freezing delay decreases with decreasing substrate temperature.

Summary

As discussed in this section on freezing delay time, ice nucleation is a common stage in all ice formation processes, influenced by various factors such as surface characteristics and the degree of supercooling. It is essential to recognize that the relationship between these factors and ice nucleation is intricate and often lacks specific trends. The connection between surface properties, including wettability, roughness, geometry, and temperature, and ice nucleation is multifaceted. Although superhydrophobic surfaces have demonstrated the potential to delay ice formation, it is important to emphasize that this effect is not universally consistent and can vary. The impact of surface roughness on ice nucleation is intricate, with both rough and smooth surfaces potentially affecting nucleation rates under different scenarios. Surface geometry has been observed to influence ice nucleation, but the precise nature of these relationships can vary. Lower temperatures are typically associated with shorter ice nucleation delays. In summary, the relationship between surface characteristics

and ice nucleation is not straightforward, necessitating a comprehensive understanding of these interactions for the design of materials with tailored ice nucleation characteristics for icephobic applications. Figure 1-17 present an informative summery of these key factors influencing ice nucleation time.

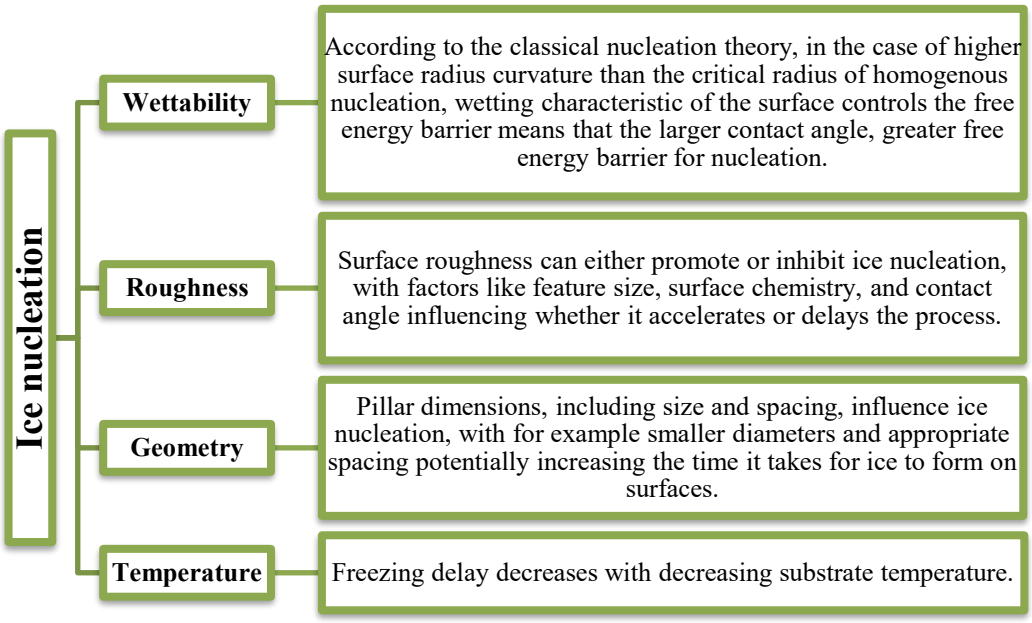

Figure 1-17:Summery o f the key factors influencing ice nucleation time.

1.4. Ice adhesion

One of the main criteria for evaluating the anti-icing properties of surfaces is the ice adhesion strength, indicated how simple the ice could be removed from the surface (how much energy is needed to remove the formed ice). Ice formation is an inevitable phenomenon under sufficient and extreme supercooling conditions. So, low ice adhesion strength means easy removal of the formed ice can be considered as a critical requirement and a promising strategy for anti-icing surfaces [152–154].

Fundamentally, the ice adhesion strength can be expressed as:

$$\tau = \frac{F}{A}$$ *Equation 1-19*

where τ , F and A are the ice adhesion strength, removal force and interface area of ice, respectively [155].

The theory behind ice adhesion strength involves multiple mechanisms. One of the main mechanisms is mechanical interlocking, where ice crystals penetrate into surface irregularities or roughness, creating strong adhesive bonds. Other mechanisms are electrostatic forces, hydrogen bonding, and van der Waals forces [26].

The ice adhesion can be measured through different techniques and the lack of a standard method for measuring the ice adhesion strength leads to many ice adhesion testing facilities and discrepancy in evaluating the surface icephobicity based on the ice adhesion strength [156,157]. One common method is the shear test, where a sample of ice adhered to a surface is subjected to a shearing force until detachment occurs. The force required to detach the ice is measured, and the adhesion strength is calculated as the ratio of the force to the contact area. Other techniques such as tensile test and centrifugal test can also be used depending on the specific requirements of the research or application.

Several factors can influence the measurement of ice adhesion strength, including the properties of the ice, surface characteristics, and environmental conditions. The temperature, humidity, and freezing rate during ice formation can affect the structure and strength of ice crystals, and consequently, the adhesion strength. Surface roughness, geometry, chemistry, and temperature can also impact ice adhesion, as they can affect the mechanisms of mechanical interlocking, molecular bonding, etc.

Understanding the mechanisms of ice adhesion strength and the factors that influence is crucial for developing effective strategies to mitigate or control ice adhesion. For example, modifying surface properties, such as applying anti-icing coatings or using surface treatments, can reduce ice adhesion strength by inhibiting mechanical interlocking or molecular bonding. Additionally, understanding the relationship between environmental conditions and ice adhesion strength can help in designing more efficient de-icing techniques and infrastructure maintenance strategies.

The following sections summarize just the impact of surface features on ice adhesion the same as other parts (droplet impact and ice nucleation), elucidate how surface characteristics can influence the strength of ice adhesion. Surface properties, such as wettability, roughness, geometry, and temperature, play a crucial role in determining the mechanisms of ice adhesion. Understanding the role of surface features in ice adhesion can contribute to the development of innovative strategies for mitigating ice adhesion and improving de-icing techniques in various applications.

1.4.1. The effect of surface wettability

The work of adhesion that is the free energy for ice detachment from the solid surface is calculated to estimate the ice adhesion characteristics. Consider the water droplet freezes to ice; the work of adhesion ($W_{a)}$ to remove the ice is introduced by Dupre as:

$$W_a = \gamma_{SV} + \gamma_{LV} - \gamma_{SL} \qquad \textit{Equation 1-20}$$

where γ_{SL}, γ_{LV} and γ_{SV} denotes the interface tensions of the solid/liquid, liquid/vapor and solid/vapor, respectively.

Young-Dupre equation is defined by combing of Equation 1-1 and Equation 1-20 [157,158]:

$$W_a = \gamma_{LV}(1 + cos\,\theta_c) \qquad \textit{Equation 1-21}$$

According to this equation, the calculation of the thermodynamic work of adhesion is performed by the surface tension of liquid and the contact angle of liquid on the solid surface.

However, Gao and McCarthy [159,160] suggested that substitution of the contact angle in Equation 1-21 with the receding contact angle (θ_{rec}) leads to practical work of adhesion (W_p) as:

$$W_P = \gamma_{LV}(1 + cos\,\theta_{rec}) \qquad \textit{Equation 1-22}$$

According to these equations, the ice adhesion strength may correlate strongly with the contact angle and the receding contact angle. In addition, the effect of surface structure on ice adhesion strength is also investigated but its correlation is not yet clear [30,161–165].

Meuler et al. [166] studied the relationship between ice adhesion and surface wettability for smooth surfaces. It was found that there is a linear correlation between the ice adhesion strength as the practical work of adhesion and $(1 + \cos\theta_{rec})$ defined in Equation 1-21.

It is commonly believed that there is a relationship between superhydrophobicity and decreased ice adhesion strength. Several groups have observed the correlation that superhydrophobic surfaces have lower ice adhesion strength [167,168]; however, others have reported that the superhydrophobicity cannot reduce ice adhesion [169,170]. Some groups

have emphasized on relation between ice adhesion and receding contact angle or contact angle hysteresis [171].

For example, Zou et al. [164] investigated the strength of ice adhesion on various surfaces with different roughness and energy levels. The results revealed that the ice adhesion strength is only correlated with the water contact angle when the surfaces have similar roughness. Furthermore, surfaces with higher roughness exhibit significantly higher ice adhesion strengths compared to smoother surfaces. This finding suggests that simply aiming for a higher water contact angle may not necessarily lead to effective reduction of ice adhesion if the surface has high roughness, and proper consideration of surface roughness is important in designing icephobic surfaces. The increased ice adhesion on superhydrophobic surfaces due to frost formation on superhydrophobic textures has also reported by [172]. However, A. Doton et al [173] observed the relation between wettability and ice adhesion that the higher contact angle leads to lower ice adhesion.

1.4.2. The effect of surface roughness

Surface roughness can have a significant effect on ice adhesion strength. The roughness of a surface can affect the formation, structure, and adhesion of ice by influencing the physical and chemical interactions between the surface and the ice. One of the key mechanisms by which surface roughness impacts ice adhesion is through mechanical interlocking. Rough surfaces provide more surface area and irregularities, such as peaks and valleys, that can physically interlock with ice crystals. As ice forms, it can penetrate into the crevices and asperities of the rough surface, creating a stronger physical bond. This mechanical interlocking can significantly increase the ice adhesion strength of a surface. As

an example, T.Baharathidason et al. [162] studied the icephobicity of hydrophilic, hydrophobic and superhydrophobic surfaces in terms of the ice adhesion strength to investigate the effect of wettability and surface roughness. They concluded that smooth hydrophobic surfaces with low surface energy showed lower ice adhesion strength compared with the superhydrophobic coatings with micro-bumps and nano protrusions because both surface energy and surface roughness affect the ice adhesion strength. Memon et al. [174] also demonstrated that the ice adhesion strength can be systematically reduced by decreasing the surface roughness, regardless of the wettability of the surface.

However, it is important to note that the relationship between surface roughness and ice adhesion strength is not always straightforward. At extremely high roughness levels, air entrapment can occur, creating a layer of air between the rough surface and the ice, which can reduce the effective contact area and weaken the ice adhesion strength. In the study conducted by Ling et al. [175], it was demonstrated that the decrease in ice adhesion strength was attributed to the occurrence of microcracks resulting from surface roughness, which led to concentrated stress at the interface, as well as the limited contact area between the formed ice and the surface due to reduced solid-liquid contact. However, they also noted that surface roughness could have a negative impact on icephobicity, as it may cause interlocking of ice within the surface structures.

Additionally, other factors such as size of roughness features, temperature, humidity, and ice formation conditions can also influence the relationship between surface roughness and ice adhesion strength. Varanasi et al. [172] revealed that in cold and humid conditions, frost formation between surface asperities caused a transition from Cassie-to-Wenzel wetting, leading to a significant elevation in ice adhesion strength.

Momen et al. [165] also demonstrated the dominant effect of roughness on ice adhesion strength. Their findings also indicated that the size or length scale of surface roughness or structures plays a crucial role in determining ice repellency.

1.4.3. The effect of surface geometry

Patterned surfaces, which exhibit specific geometrical features or arrangements, can have a significant effect on ice adhesion strength. Surface geometry can also affect the mechanical interlocking between the surface and the ice, like surface roughness. For instance, surfaces with sharp edges or asperities can penetrate the ice and anchor it more effectively, leading to higher ice adhesion strength [176].

The relationship between surface geometry and ice adhesion strength is intricate, influenced by factors like temperature, humidity, and ice formation conditions, as well as interactions with other surface properties such as roughness or chemistry. Patterned surfaces aim to reduce ice adhesion, and by fine-tuning their geometrical parameters, they can be optimized for various applications and environmental conditions to facilitate easier ice removal.

He et al. [161] studied the role of microstructure geometry on wettability and ice adhesion. They measured the ice adhesion for surfaces with micro-nano-pillars 3-5 times smaller than microstructure and smooth surfaces because the total contact area of micro-nano-pillars was far less than that of micro-pillars and smooth surface. The relationship between contact angle and receding contact angle with ice adhesion on micro-nano structure and microstructure surfaces were also investigated. Their experiment validated the linear

relationship between the work of adhesion with the receding contact angle for both micro-nano structure and microstructure surfaces.

Hou et al. [14] developed micro-cubic arrays on silicon surfaces and studied the icing process to investigate the impact of the geometrical parameters (micro-spacing distances ranging from 30 μm to 130 μm, with a uniform edge length and height of 20 μm) of these designed microstructures on ice adhesion strength, using experimental and simulated data. The ice adhesion strength was measured to be as low as 16 kPa when using micro-cubic arrays with a center-to-center spacing distance of 30 μm. This was due to the entrapped air pockets acting as microcracks under shear force, resulting in a lower fracture critical stress. They emphasized that understanding the size effect of microstructures on ice adhesion strength can be useful in designing effective anti-icing/icephobic materials.

In the study conducted by McDonald et al. [177], ice adhesion strength of water droplet was evaluated on micro-patterned hydrophobic surfaces. This patterned surface consists of a hexagonal array of PDMS pillars. Each pattern area has pillars with diameters of 30 and 45 μm height, whereas the lower density pattern has a pillar-to-pillar spacing of 67.5 μm, as opposed to 45 μm for the higher density pattern. According to the results, incorporating a pattern onto the PDMS surface decreases the strength of adhesion between ice and the surface, and surfaces with a higher density of patterns performed better than the lower density patterned and flat PDMS surfaces due to the interfacial area of contact.

1.4.4. The effect of surface temperature

The surface temperature can play a significant role in ice adhesion strength. It affects both the rate of ice formation and the strength of the bond between the ice and the surface.

At sub-zero temperatures, the freezing process involves formation of ice crystals that interlock with surface irregularities, creating a mechanical bond between the ice and the surface. As the temperature decreases further, frost or ice protrusions on the surface provide additional points for mechanical interlocking, further strengthening the bond between the ice and the surface.

These changes in ice adhesion strength due to temperature variations can pose challenges in various applications, such as transportation, infrastructure, and energy systems, particularly during cold weather conditions. For instance, JunFei et al. [178] investigated the impact of surface temperature and wettability (hydrophilic, hydrophobic, and superhydrophobic surfaces) on freezing and ice adhesion strength. They found that superhydrophobic surfaces can delay freezing and reduce ice adhesion, possibly due to the presence of interfacial air pockets. However, at lower temperatures, the effectiveness of superhydrophobic surfaces diminishes as interfacial air pockets are squeezed out. Similarly, Boinovich et al. [179] compared ice adhesion strength on different types of aluminum samples, including hydrophilic, hydrophobic, superhydrophobic, and slippery surfaces. They observed that the ice adhesion strength on superhydrophobic and slippery surfaces was highly dependent on temperature.

Summary

Cold weather conditions can lead to the formation of ice on surfaces, which can increase the risk of accidents and disrupt industrial processes. Therefore, the strength of ice adhesion to surfaces is a key criterion for assessing anti-icing properties, as it indicates how easily ice can be removed. Ice adhesion strength is influenced by multiple mechanisms,

including mechanical interlocking, electrostatic forces, hydrogen bonding, and van der Waals forces. Various techniques exist for measuring ice adhesion strength, but a lack of standardized methods leads to discrepancies in evaluation. Surface characteristics such as temperature, roughness, geometry, and wettability, along with environmental conditions, can significantly affect ice adhesion. Superhydrophobic surfaces often exhibit lower ice adhesion, but the relationship is not universally consistent. Surface roughness can impact ice adhesion through mechanical interlocking, but the relationship is complex. Surface geometry, particularly patterned surfaces, can also influence ice adhesion and should be optimized for reducing ice adhesion in various applications. Finally, surface temperature plays a role, with lower temperatures generally leading to stronger ice adhesion. Understanding these factors is crucial for developing effective strategies to reduce ice adhesion and improve de-icing techniques. In Figure 1-18, you will find a concise depiction of these factors that impact ice adhesion.

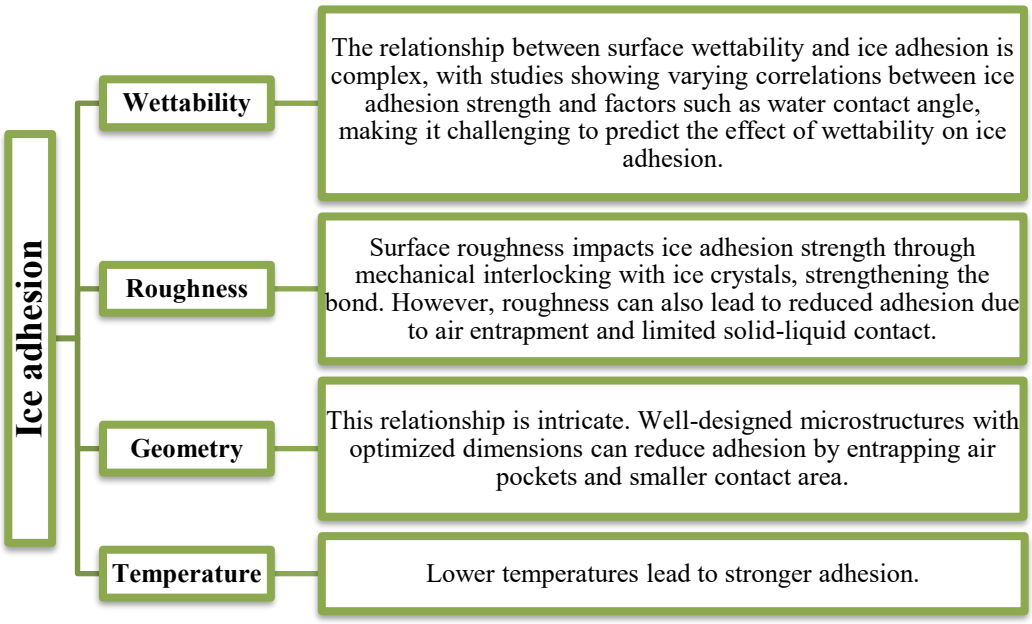

Figure 1-18: Summery of factors influencing ice adhesion.

1.5. Machine learning

Machine learning is a subfield of artificial intelligence, encompassing the development of algorithms and computational models. These enable computers to learn from and make predictions or decisions based on data. Through iterative processing and analysis of data, machine learning algorithms extract patterns to improve performance over time. This improvement is achieved by adjusting internal parameters iteratively, enhancing the algorithm's ability to understand and respond to complex tasks in a manner similar to intelligent human behavior [180]. Machine learning can support engineering tasks to effectively manage data to get good insights from it. By giving some training data, various systems can be developed to help machine to learn by self [181].

Experiments in conventional multi-factor systems will be conducted by varying one factor at a time. Not only is it time consuming, but the interactions among variables may also be ignored and lead to low efficiency of the systems. Another major shortcoming of the traditional approaches is the fact that highly complex and nonlinear systems may govern the parameters. Consequently, it is hard and sometimes even impossible to present them with traditional models. Even if such a model has been developed, it might be impractical for prediction [182].

Today machine learning techniques have demonstrated their superb ability and have received much attention. These techniques may overcome the drawbacks of the conventional approach when dealing with complex and nonlinear systems. Machine learning would help a lot in saving operating costs and improving the speed of data analysis. As the name implies,

machine learning can learn complex relationships between independent and dependent variables through nonlinear data processing as well.

The concept of machine learning comes from artificial intelligence that can be broadly defined as one of the most fostered research areas in recent years and has prompted researchers to apply techniques from this field in many tasks like classification, person identification, object recognition, etc. in order to making identifying and patterning of data easier [183–185]. It is common to observe machine learning as data mining or predictive analytics consists of designing efficient and accurate prediction algorithms that increase automating tasks as well as development of minimal human interaction algorithms [186]. Machine learning research uses these algorithms to make data-driven predictions or decisions relying on patterns and models from training data inputs that do not need explicit instructions (Figure 1-19). Machine learning can be used as an analyzing tool for many real life data such as data retrieval intelligent gadgets, self-driving cars, etc. [187].

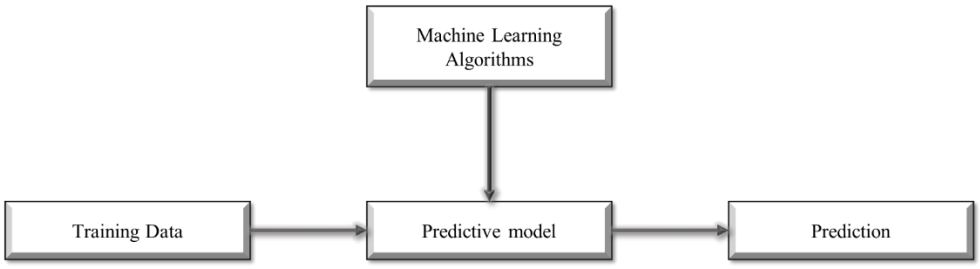

Figure 1-19: Concepts of machine learning.

Machine learning algorithms can be classified into two broad types of learning: supervised learning and unsupervised learning (Table 1-3). The algorithms in the supervised learning such as classification and regression tasks are used to build mathematical models from labeled data including the input features and the possible outputs and to predict unseen

data [188]. Considering unsupervised learning, clusters that can be defined as sets of data with common characteristics in identified according to mathematical models made from algorithms. In unsupervised learning, it is possible to recognize patterns in data and categorize them without any information about the actual labels (Figure 1-20) [187,189,190].

Table 1-3: A comparison of supervised learning and unsupervised learning [191].

Parameters	Supervised learning	Unsupervised learning
Definition	In supervised learning, there are input and output variables, and an algorithm helps to understand how information is mapped from input to output.	A type of machine learning that involves only input and no output is unsupervised learning.
Type of data	supervised learning predicts the outcome from the input data by labeling it.	Unsupervised learning relies on inherited structure from unlabeled input data to make predictions.
Accuracy	The results of supervised learning are more reliable and accurate.	As compared to supervised learning, unsupervised learning produces average results.
Complexity	supervised learning has a high computational complexity.	Unsupervised learning has a lower computational complexity.

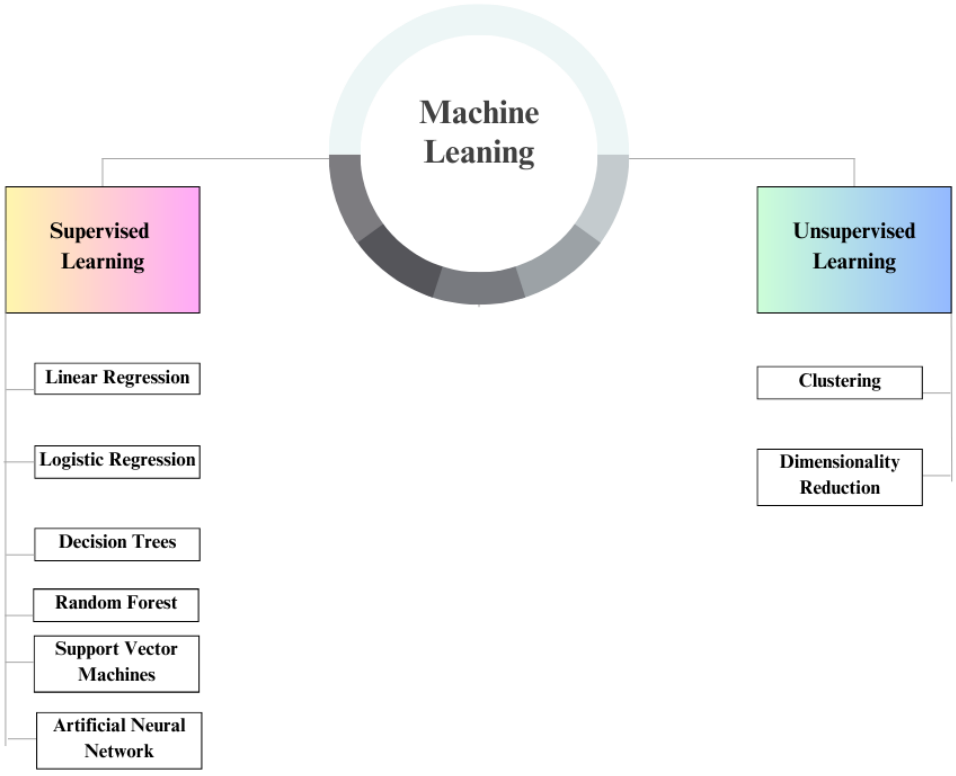

Figure 1-20: Machine learning algorithms.

1.5.1. Supervised learning

Supervised machine learning requires labelled data, and the data is divided into two parts, a testing data set and a training data set. Some outputs from the training data set need to be predicted. The goal is to teach the machine to recognize patterns that are similar to those found in the training data set and to apply those patterns to the test data set in order to predict the output with real values. Here is a list of some of the common algorithms used in supervised learning [192,193] and Table 1-4 presents the Pros-Cons comparison of these supervised machine learning algorithms:

- ***Linear Regression:***

Linear regression is the simplest type of regression. It involves trying to fit a straight line (a straight hyperplane) to the data, which is possible when the relationship between the factors in the data is linear [193]. The mathematical form of the linear equation is as follows:

$$y = \beta_0 + \beta_1 x_1 + \beta_2 x_2 + \cdots + \beta_n x_n \qquad \textit{Equation 1-23}$$

where y shows the predicted value, x represents the independent variable, β_0 is the y-intercept, and $\beta_1, \beta_2, \ldots, \beta_n$ are the coefficients associated with each independent variable.

- ***Logistic Regression****:*

Logistic regression is used for binary classification problems. It models the probability of a binary outcome based on the input features [194].

$$Ln(\frac{P}{1-P}) = \beta_0 + \beta_1 x_1 + \beta_2 x_2 + \cdots + \beta_n x_n \qquad \textit{Equation 1-24}$$

where P is the probability of the binary output variable.

- ***Decision Trees (DT):***

Decision Tree is a supervised Machine Learning strategy for solving classification and regression issues that involves continually separating data depending on a certain parameter. The leaves are where decisions are made, and the nodes are where the data is split [194].

- ***Random Forest (RF):***

Random forest is an ensemble learning method that combines multiple decision trees to make predictions. As the name implies, it generates a forest that is rather random. As a result, the strategy should be designed in such a way that more trees are present in the forest, making it more accurate.

- ***Support Vector Machines (SVM):***

SVMs are employed in both classification and regression. Each data item is displayed as a point in n-dimensional space in this approach (where n is the number of features in our dataset). Each feature's value is equal to the coordinate's value. It divides the training datasets into classes by identifying a line (hyperplane) that separates them. It works by maximizing the minimum distances between the closest data point and the hyperplane.

- ***Artificial Neural Network (ANN):***

A neural network is a set of methods that try to find hidden connections in a set of data in a way that is similar to how the human brain works. Neural networks can change based on what information is fed into them. This means that the network can produce the best result possible without having to change the output criteria. There are three parts to neural networks: the input layer, the hidden layer, and the output layer. The information comes from the input layer, and then the hidden layer processes it. The output is figured out, and the results are sent to the output layer.

Table 1-4: Pros-Cons of supervised machine learning algorithms [193,195].

Algorithm	Advantages	Disadvantages
Linear Regression	easy to understand, easy to avoid overfitting,	unsuitable for dealing with non-linear relationships, difficulty in handling complex patterns, oversimplification of real-world problems.
Logistic Regression	output interpreted as probability with broad applications, ability to handle nonlinearity, computational efficiency,	requires a large sample size for stable results, prone to over fitting
Decision Trees	non-parametric, handles features interactions, handle variety of data, missing values, ease in interpretation, robust to noise	hard to deal with high-dimensional data, challenging to control the size of the tree, prone to overfitting, significant time required to build the tree, limited ability to handle complex interactions
Random Forest	scalable, less prone to overfitting, robust to noise	as more trees are added, the process gets slower.
Support Vector Machines	less probability of over fitting, high accuracy, can handle complex functions with suitable kernel functions, can scale up with high-dimensional data	complex, difficulty in finding suitable kernel functions, slower training speed, Poor performance of SVM with noisy datasets
Artificial Neural Network	capable of handling non-linear or dynamic relationships, robustness to handle noisy data	lengthy training time, efficient training requires large sample sets, black box

1.5.2. Unsupervised learning

Unsupervised learning involves training a model on unlabeled data with the goal of identifying patterns, structures, or relationships in the data. Finding hidden patterns or groups without a clear target label is the key objective [192,196]. In unsupervised learning, some common methods are:

- ***Clustering:***

Clustering algorithms group similar data points together based on their features. Clustering systems put together groups of data points that are similar based on what they have in common. k-means clustering and hierarchical clustering are two examples of this [193].

- ***Dimensionality Reduction:***

These algorithms reduce the dimensionality of the data while preserving important information. Principal Component Analysis (PCA) and t-SNE (t-Distributed Stochastic Neighbor Embedding) are commonly used techniques. The complexity and processing time of the suggested technique are both reduced with the aid of dimensionality reduction [193,196].

1.5.3. Machine learning application in wettability and icephobicity

Machine learning is a widely used technique for various purposes in computer science and mathematics, but it can be considered relatively new to be applied in wettability and icing, with some focusing on superhydrophobicity and others on icing that would an exciting field of research [197–199]. As an example, a machine learning model has been developed by Yancheshme et al. [200], which takes into account drop properties, surface characteristics, and process parameters in order to predict maximum spreading factors. Similarly, Tembely et al. [201] presented supervised machine learning algorithms, including linear regression, decision trees, random forests, and gradient boosting, for determining the maximum spreading factor. A correlation was achieved between the maximum spreading factor and relevant features such as flow controlling dimensionless numbers and substrate wettability using machine learning techniques. Yee et al. [202] conducted a study in which they attempted to predict the dynamic morphology of splashing drops during impact. To address the difficulty of predicting splashing drop morphology, they focused on the application of image data in order to explore the possibility of using computer vision— the ability of machine learning to generate and process images —as a strategy for resolving the problem.

Zhang et al. [203] employed artificial neural networks and evolutionary computation techniques to advance our comprehension of superhydrophobic surfaces. They investigated the correlation between water droplet volume, nanoparticle weight, falling distance between the surface and droplet, and several surface properties (contact angle, sliding angle, and adhesive force). Similarly, Li et al. [187] utilized machine learning to forecast the severity of aircraft icing under different conditions such as liquid water content, droplet diameter, and exposure time.

Considering the application of machine learning in icephobicy, Ringdahl et al. [198] utilized molecular dynamics simulations and machine learning techniques to investigate ice adhesion strength on rough surfaces. This pioneering study marked the first instance of employing machine learning for anti-icing surface design and demonstrated promising predictive capabilities. Ramachandran [204] also developed machine learning models to optimize the icephobicity of concrete, utilizing artificial neural networks to predict surface ice adhesion strength and the coefficient of restitution of water droplets rebounding from the surface under freezing conditions. Fitzner et al. [205] devised a data-driven machine learning-based approach to identify descriptors for heterogeneous ice nucleation, aimed at enhancing the quantitative understanding of this process.

Summary

The droplet impact behavior, ice nucleation and adhesion processes are affected by some factors such as environmental conditions (humidity and temperature), surface features (contact angle, contact angle hysteresis, roughness parameters, and geometrical features) and the droplet size. These process parameters need to be carefully optimized to increase droplet

bouncing, freezing delay time and decrease the ice adhesion strength. Therefore, in this research, taking advantages of machine learning would help us to investigate the number of variables affecting the icephobic behavior of structured surfaces in terms of water droplet impact, ice nucleation time and ice adhesion strength, see the interaction between parameters, identify the most important factors, optimize them to increase droplet bouncing, freezing delay time and develop a prediction tools for prediction water droplet behavior and measuring the ice nucleation time as a function of affecting parameters.

CHAPITRE 2

ARTICLE 1: Temperature-dependent droplet impact dynamics of a water droplet on hydrophobic and superhydrophobic surfaces: an experimental and predictive machine learning–based study

S. Keshavarzi[1*], J. Sourati[2], G. Momen[1], R. Jafari[1]
[1]Department of Applied Sciences, University of Québec in Chicoutimi, Chicoutimi, Québec, Canada
[2] University of Chicago, Illinois, IL, USA
Email address: samaneh.keshavarzi1@uqac.ca

This article has been accepted in:

Journal of Heat and Mass Transfer

2.1. Abstract

Heightening the water repellency of surfaces can serve anti-icing purposes by removing water drops before they freeze and adhere to a surface. Here we study the impact dynamics of water droplets on silicone rubber surfaces—ranging from hydrophobic to superhydrophobic—at −20, −10, and 25 °C. We evaluate the influence of static contact angle, contact angle hysteresis, surface roughness, temperature, impacting velocity, and droplet diameter on droplet behavior (e.g., deposition, bouncing, splash). Minor effect of temperature on droplet dynamics on microstructured surfaces for a wide range of Weber and Reynolds numbers is observed. Experimental observations show that full bouncing only occurs on superhydrophobic surfaces with a CA > 160° and a CAH < 2° at temperatures above 0 °C for *We* <110 and *Re* <5000. Increasing the impact velocity of the droplet on rough surfaces

heightens the probability of splashing. This experimental data is then coupled with machine-learning techniques (logistic regression, decision tree, and random forest) to comprehensively investigate droplet impact behavior on hydrophobic and superhydrophobic surfaces at various temperatures. We predict the behavior probability of impacting droplets on surfaces as a function of Weber number, Reynolds number and surface features (static contact angle, contact angle hysteresis, temperature, and surface roughness). Our experimental results and machine learning–based predictions are highly consistent, demonstrating that machine learning can effectively predict droplet motion on hydrophobic and superhydrophobic silicone rubber surfaces at different temperatures.

Keywords: superhydrophobic, surface features, temperature, droplet impact, freezing, machine learning

2.2. Introduction

Ice formation on structures poses a major hazard for exposed infrastructure and equipment and can lead to serious incidents, including aircraft crashes, the collapse of transmission lines, and damage to industrial facilities [1,3,206,207]. Ice removal techniques from solid surfaces can be classified into active de-icing and passive anti-icing methods. The latter means offers numerous advantages over active de-icing [9,13,24]. Passive anti-icing includes icephobic surfaces, which prevent ice formation on the surface without requiring external energy. These icephobic surfaces usually operate by exhibiting an improved water repellency (droplet mobility) to remove water droplets before their freezing, hinder ice nucleation on the surface, reduce the ice adhesion force, or a combination of these properties [19,21–23].

Improving our knowledge about ice nucleation, ice formation, and ice adhesion processes can help overcome issues related to surface icing and enhance the design of icephobic surfaces. Superhydrophobic surfaces can be very effective in preventing ice formation compared with hydrophilic or hydrophobic surfaces because of their ability to repel impacting droplets before ice nucleation [32,33]. Nonetheless, some studies have reported the opposite effect of superhydrophobicity on ice mitigation [32,37].

Much focus has been placed on ice accretion and the related impact and freezing processes of water droplets on cold surfaces [208–211]. The impinging of a droplet on a surface leads to a conversion from inertial energy to surface energy, droplet spreading, and droplet deformation. The wetting properties of surfaces and the extent of energy dissipation when a droplet lands on a surface produce various impact droplet patterns [81]. For superhydrophobic surfaces, the pure conversion of kinetic energy into surface energy is expected because the air pockets trapped at the interface minimize the dissipation of the kinetic energy of the droplet. Thus, bouncing is possible because of the sufficient energy stored in deformation during droplet impact. However, high-energy dissipation for other surfaces, such as hydrophilic surfaces, reduces the kinetic energy available for bouncing [60,85].

Different phenomena arise during droplet impaction onto a solid surface, such as deposition, receding, splashing, and bouncing [61]. The outcome of an impacting droplet is determined by multiple factors, including droplet properties (e.g., viscosity, density, surface tension), operational parameters (e.g., velocity), and surface characteristics (e.g., wettability) that are altered by surface roughness or texturing [33,212,213]. Dimensionless parameters are used to account for these factors affecting droplet impact dynamics. These critical

parameters include the Reynolds number, $Re = \rho u_0 d_0/\mu$, the Weber number, $We = \rho {u_0}^2 d_0/\sigma$, the capillary number, Ca=μ/σ, and the Ohnesorge number, $Oh = \mu/\sqrt{\rho\sigma d_0}$, where u_0 is the impact velocity, d_0 is the initial droplet diameter, and ρ , μ, and σ are the liquid density, viscosity, and surface tension, respectively [214]. Surface wettability is commonly stated in terms of the contact angle (CA) of a water droplet and contact angle hysteresis (CAH), which is the difference between the advancing and receding CAs. The latter is often used as a measure of droplet mobility across a surface.

A critical characteristic affecting liquid droplets on cold solid substrates is surface temperature. Under icing conditions, water droplet properties, wetting properties, and frost formation depend greatly on surface temperature and cause the impacted water droplet to move less rapidly across the cold surface [104]. The effect of substrate roughness and temperature on droplet impact dynamics on cooled superhydrophobic surfaces has been discussed by Maitra et al. [215]. They found that the critical Weber number for the droplet impalement was independent of the substrate temperature. However, Alizadeh et al. [29] reported a strong temperature dependency for the impact dynamics of water droplets on hydrophilic to superhydrophobic surfaces at a Weber number of 138. Lower substrate temperatures lead to less droplet retraction. Zheyan et al. [75] reported the detailed dynamic motions of a water droplet impacting an ice surface and concluded that the lowering of the ice surface temperature decreases the maximum spreading factor.

Much effort has been placed on investigating the impact behavior of water droplets on cold superhydrophobic surfaces; however, most of these studies have been confined to narrow parameter ranges. Mishchenko et al. [216] focused on the design of ice-free

nanostructured surfaces and evaluated droplet behavior on supercooled nano- and microstructured surfaces able to repel impacting water before ice nucleation. They performed impact tests using 15 μL water droplets falling from 10 cm onto cold surfaces (−25 to −30 °C) and found that the rebounding process was suppressed on surfaces colder than −25 °C. Ding et al. [217] investigated the effect of superhydrophobic surface inclinations and the degree of supercooling on water droplet dynamics. In their study, a 14 μL water droplet was projected at 0.99 $m \cdot s^{-1}$ onto a superhydrophobic surface having a static CA of 160 ± 1°. They observed that the droplet successively underwent full rebound, partial rebound, and no rebound as surface temperatures decreased. Zheng et al. [218] demonstrated that supercooled droplets impacting inclined and dry superhydrophobic surfaces can bounce off without freezing because of a reduced surface contact time and contact area of the impinging water droplets on properly designed surfaces. Finally, Li et al. [219] investigated the influence of a supercooled water droplet on cold hydrophilic and superhydrophobic surfaces. They observed that solidification of a 1.6 mm diameter supercooled droplet impacting a cold superhydrophobic substrate at 3.4 $m \cdot s^{-1}$ reduced droplet bouncing.

Most research in this area has focused on the outcome of droplet regimes relying on a few select parameters. Critically, these studies lack an analysis incorporating all possible parameters, especially as the droplet impact process is a complex interaction of multiple variables, as discussed above. However, the development of machine learning–based methods that can consider all influential parameters affecting impacting droplet behavior can offer some design criteria for water-repellent superhydrophobic surfaces subjected to various temperatures. Machine learning can support engineering tasks to manage and extract insights

from the resulting data [181,220]. Furthermore, these approaches can reduce the high costs and time required for carrying out multiple complex experiments.

Artificial intelligence and statistical-learning methods are increasingly used in various fields, such as computer science, material science, and aircraft icing research [197–199]. For example, Zhang et al. [203] used artificial neural networks and evolutionary computation to enhance our understanding of superhydrophobic surfaces by determining the relationship between water droplet volume, nanoparticle weight, the falling distance between the superhydrophobic surface and the water droplet, and multiple properties (droplet CA, sliding angle, and adhesive force). Li et al. [187] also applied machine learning to predict the severity of aircraft icing in relation to various conditions, including liquid water content, droplet diameter, and exposure time. Although it is possible to examine the effect of various parameters in conventional experimental investigations, machine-learning models improve our ability to find patterns within large data sets.

There is currently no comprehensive study that has examined the influence of surface characteristics on the dynamic behavior of water droplets at different temperatures while incorporating machine learning approach. In our previous work [221], we investigated the drop dynamic behavior on hydrophobic and superhydrophobic surfaces at room temperature in line with finding some design criteria (in terms of surface CA, CAH, and roughness values) based on machine learning approach to improve the feasibility of achieving the bouncing of drops when they impact on hydrophobic and superhydrophobic surfaces. The goal of the presented research is to investigate temperature dependency of water droplet impact on hydrophobic and superhydrophobic surfaces and coupling the experimental results with machine learning-based methods for prediction of the drop dynamic behavior at different

temperatures. It is worth mentioning that this new article complements the previous article by examining the temperature dependency of the droplet dynamic, using linear and nonlinear methods of machine learning to predict the droplet dynamic, providing different equations for prediction the droplet behavior and studying the relative importance of affecting parameters on water droplet impact.

In this paper, we study the temperature dependency of impact dynamics. We quantify the influence of drop properties, kinematic parameters, and surface characteristics on impacting droplet behavior (e.g., deposition, bouncing, and splashing) on silicone rubber surfaces (hydrophobic to superhydrophobic). A machine-learning technique is applied to evaluate the outcome regime of impact droplet behavior based on CA, CAH, temperature (T), and the root mean square surface roughness value (S_q), *We* and *Re* numbers. We demonstrate that machine learning can effectively predict droplet impact behavior. We formulate three different methods using a decision tree, random forest, and logistic regression to develop a data-driven approach for predicting droplet impact behavior by exploring the complex interactions between CA, CAH, S_q, T, and the *We* and *Re* numbers. Our experimentation and machine-learning approach is a novel means of investigating droplet behavior on hydrophobic to superhydrophobic surfaces at different temperatures. Moreover, we develop correlations through logistic regression for predicting the behavior probability of impacting droplets as a function of the analyzed parameters. We selected these three machine-learning methods for predicting impact droplet behavior, as they are state-of-the-art techniques having a strong predictive capability.

2.3. Material and Methods

2.3.1. Sample preparation

High-temperature vulcanized (HTV) silicone rubber was used as the process material. A chemical-etching method was used to produce microstructured aluminum templates (A6061) using a 4.8, 9.8, 14.8, 19.8 wt% hydrochloric acid solution and immersion of aluminum templates in this solution for 2 h. A micro-compression molding machine with two temperature-adjustable platens (Carver Inc. USA) was used to mold the rubber samples. The hydraulic press system can precisely control an applied force of 3 to 194 kN [207]. The rubber material is cast in three pieces of flat molds, each with a right rectangular prism cavity of 25 x 15 x 6 mm^3. After the template was placed in the cavity, the rubber material was placed over it. Next, the top of the mold was closed. The mold was set in the press machine to begin the process. In the press machine, the following mold parameters were set: a molding pressure of 35 MPa, a curing time of 4.7 minutes, and a mold temperature of 149 °C. After the process was complete, the mold was opened, and the silicone rubber with the size of 25 x 15 x 6 mm^3 was removed from the aluminum template (Figure 2-1).

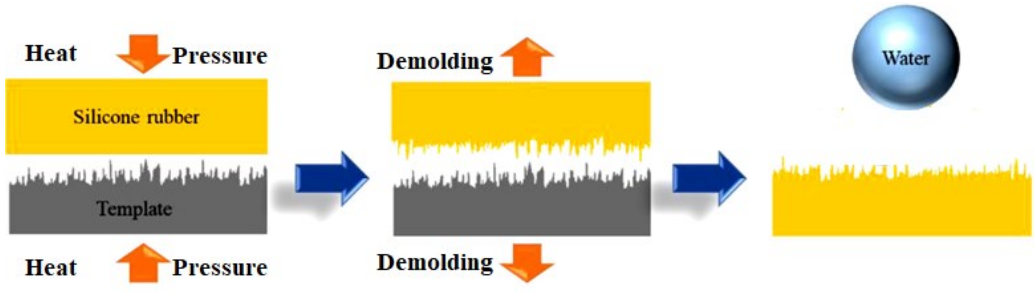

Figure 2-1: Schematic of the fabrication of micro-nanostructured silicone rubber surfaces via a microcompression molding technique [207].

2.3.2. Surface Characterization

Using a Kruss™ DSA100 goniometer at 25 °C, we measured the water CA using a water droplet of 4μL deionized water based on the method of Young-Laplace. A CAH is equal to the difference between the advancing and receding contact angles when a droplet moves on the surface. All wettability measurements were taken at five different points on each sample to ensure accuracy and reproducibility. For each sample the average and standard deviation were reported. The surfaces were characterized using a confocal laser microscopy profiler (Profil3D, Filmetrics, USA) and a scanning electron microscope (JSM-6480 LV, JEOL Japan). In Figure 2-2, the surface structures of different samples are presented as SEM images and 3D profiles.

In the case of Sample1, which was replicated on a smooth aluminium template, it exhibited hydrophobic surface characteristics (due to its low surface energy), while the other samples exhibited superhydrophilicity (because they were replicated on aluminium templates with varying acid concentrations). Therefore, to fabricate superhydrophobic surfaces, we used a low-surface-energy material with intrinsic hydrophobicity, combined with a sufficient level of surface roughness. In the Sample 2, 3, 4, and 5 samples, S_q increased by 1.87, 3.77, 4.49, and 4.28 respectively compared to sample1. Table 2-1 shows CA, CAH, and S_q of these five microstructured surfaces.

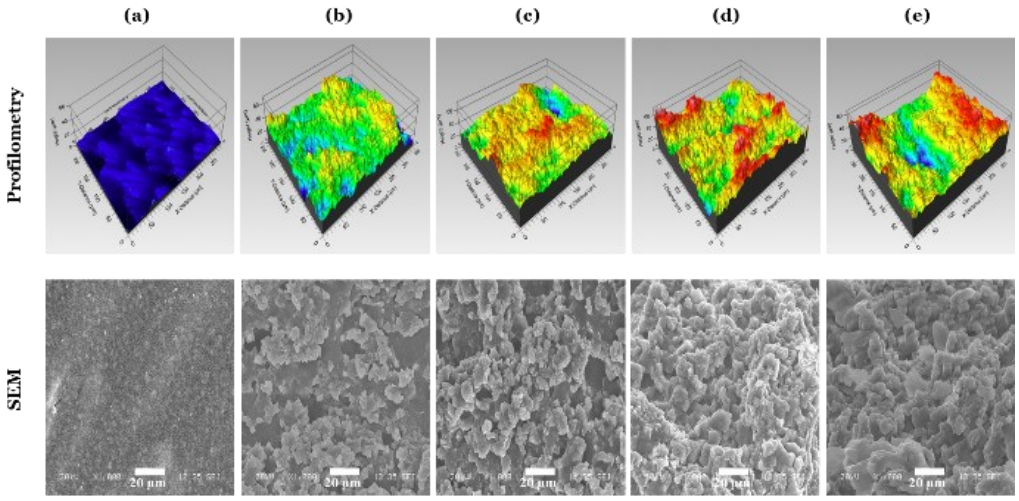

Figure 2-2: The 3D surface profiles and SEM images of samples (a) 1, (b) 2, (c) 3, (d) 4, and (e) 5 [221].

Table 2-1: Surface characteristics of hydrophobic and superhydrophobic surfaces and kinematic parameters used in the experiments. For all samples, falling velocity (u_0) varied between 0.4 and 2.7 m/s, droplet size (d_o) was either 2.67 or 3.02 mm, and the surface temperatures (T) were −20, −10, and 25 °C.

Sample No.	CA (°)	CAH (°)	S_q (µm)
1	116.0 ± 2	46.5 ± 2.4	1.76 ± 0.17
2	154.5 ± 1.4	28.0 ± 1.6	3.29 ± 0.4
3	165.3 ± 1.1	1.5 ± 0.2	6.64 ± 0.32
4	166.6 ± 0.9	0.6 ± 0.3	7.90 ± 0.24
5	162.8 ± 0.9	1.3 ± 0.8	7.54 ± 0.33

2.3.3. Experimental Setup

The experimental freezing setup included a thermally insulating and optically transparent chamber, high-speed camera, thermostatic bath, cold base, droplet injection system, test samples, data acquisition system, temperature sensor, humidity sensor, and a vibration-free table (Figure 2-3). The double layer chamber that is thermally insulating and optically transparent will be used to control the temperature and humidity of experiment and affecting parameters on ice nucleation to be uniform during the experiment and increase the accuracy and reproducibility of the experiments. Its transparency would facilitate imaging of

the freezing droplet. By having a small interior chamber (150 mm length ×150 mm width ×110 mm height) inside a large chamber (420 mm length ×420 mm width × 400 mm height), the droplet could be subjected to a uniform environment. During the cooling process, the relative humidity of the chamber can be controlled with a constant flow of dry nitrogen gas (N_2). We adjusted the temperature of the cold base using a thermostatic bath. The chamber's temperature and relative humidity were around 25 °C and 30% ± 3%, respectively. A high-speed camera and LED illuminator monitored the droplet impact process and visually recorded the droplet movement on the surfaces.

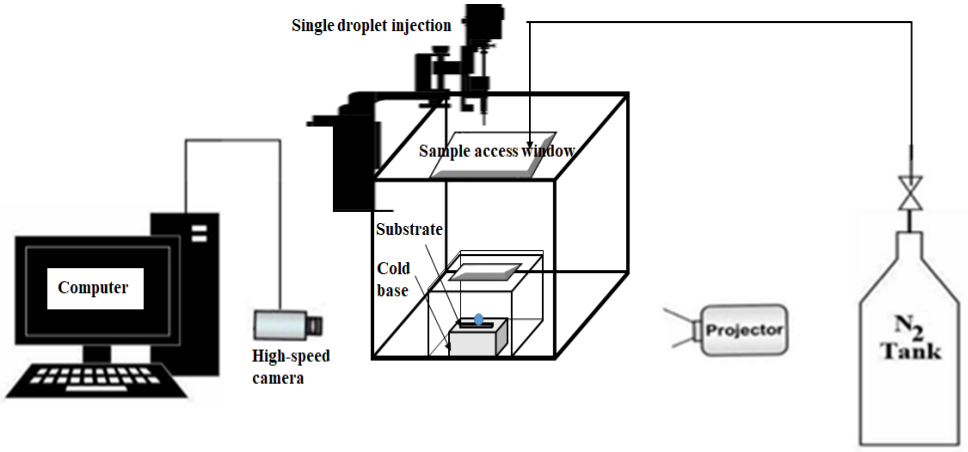

Figure 2-3: Schematic of the experimental setup.

We used two different syringe nozzles to vary drop diameters, all the spherical water droplets had a fixed volume of 10 µL (2.67 mm in diameter) and 20 µL (3.02 mm in diameter). We released 2.67 and 3.02 mm diameter droplets at room temperature from a droplet injection system at various heights, corresponding to initial droplet impact velocities ranging between 0.4 and 2.74 $m \cdot s^{-1}$. We placed a high-speed camera (MotionBLITZ, MIKROTRON, EoSens Cube 7, Germany) to record the droplet impact behavior at 3000 fps. Before each test, we adjusted the plate's temperature to either 25, −10, or −20 °C and placed the sample on the plate. We repeated each test (a specific combination of parameters) at least

three times. We computed the impact velocity of the droplets from the elapsed distance and time recorded by the camera and the ImageJ software [221]. All experimental parameters, including the droplet properties, surface characteristics, surface temperature, and impact velocity, are summarized in Table 2-1.

2.3.4. Machine-Learning Methods

Among the various machine-learning methods, regression and classification are the most commonly used methods. To predict the impacting droplet behavior on the silicone rubber surfaces, we applied three machine-learning models: logistic regression (LR), decision tree (DT), and random forest (RF). DT machine-learning models partition the feature space into several decision regions by successively dividing the space through simple decision rules, where each rule can be as simple as thresholding a single feature [222]. Each decision region is then assigned a single class label based on the class of its training samples. When the tree is fully constructed, the class of any given test sample is predicted by identifying the decision region into which the sample falls. These models are applicable to multiclass and nonlinear classification problems.

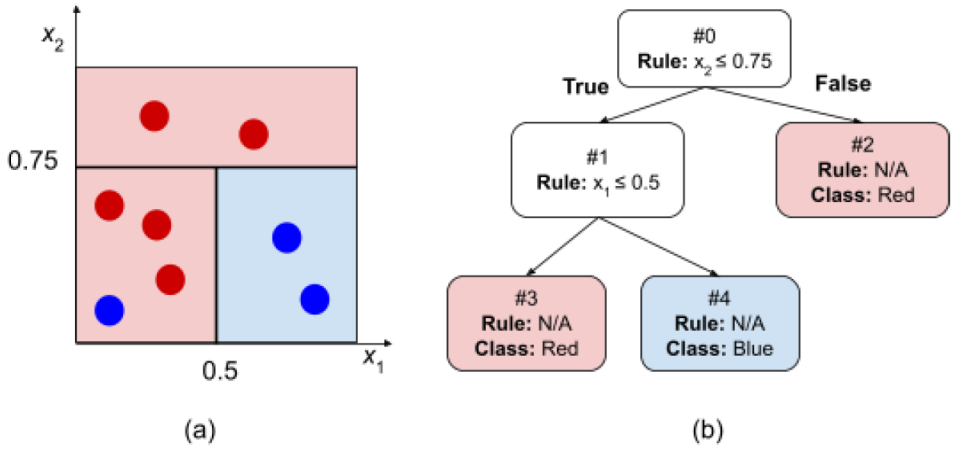

Figure 2-4: An example illustrating DT classifier. (a) A 2D feature space corresponding to a data set with 2D feature vectors. The training samples are shown with red and blue circles with their color representing the class. The space is partitioned by a DT classifier trained over the training examples. (b) DT classifier that is trained over the training samples.

Figure 2-4 shows an example of how a DT partitions 2-dimensional feature space of a 2D data with red (five labeled samples) and blue classes (three labeled samples). The left figure (Figure 2-4 (a)) indicates the partitioning of the space, where the color of each region represents the class label assigned to it (red shadow for class red and blue shadow for class blue). The right figure (Figure 2-4 (b)) shows the corresponding DT as a tree structure where each node contains a rule in the form of a feature thresholding. If the rule is satisfied for any test sample (True), we choose the left node in our next step, otherwise (False) we go to the right node. Starting from the root node (#0), we keep choosing nodes based on the nodes' rules until we get to a node without any children. Such nodes are usually called "leaves". Each leaf is associated with a partition in the feature space and is assigned a class label based on the class majority of the training samples belonging to that partition. In our example in Figure 2-4, node #2 is a leaf that corresponds to the horizontal rectangle at the top of Figure 2-4 (a) which has two red training samples, hence is assigned the red class. Any test that falls in this partition (i.e., $x_2 \geq 0.75$) will be predicted as a "red" sample.

Training a decision tree starts from the root node corresponding to the entire feature space, where a feature and a cut-off threshold are selected so that the selected feature partitions the data into two groups having the highest possible sample homogeneity. Each partition forms a new node in the tree, where the same procedure is repeated to further divide the data set into two additional leaves. The divisions continue until either all the paths have reached the maximum number of divisions from the root, i.e., maximum depth (denoted by

d_{max}), or all the leaves are assigned partitions with a sample homogeneity higher than a pre-specified threshold. Nodes at which splitting is stopped are referred to as leaves. When classifying the groups of data, the homogeneity of samples is inversely defined on the basis of the impurity of their class labels. Lower impurity implies higher homogeneity, and the smallest impurity is achieved when the class labels of all samples are identical. In our experiments, we used the Ginni index to measure class impurity, defined as:

$$Ginni = 1 - \sum_{i=1}^{c} P_i^2 \qquad \textit{Equation 2-1}$$

where P_i denotes the empirical distribution of the i^{th} class. We also ensured that all leaves contained at least one sample.

Training the DT can easily lead to an over-partitioning of the feature space, which, in turn, implies overfitting and instability. A common approach to alleviate this issue is to build an ensemble of trees via bootstrapping, a method commonly referred to as random forest (RF). This method consists of constructing multiple DTs, each separately trained with a distinct randomized data set that is obtained by sampling with replacement from the original data set [223]. Each tree in the forest will make an individual prediction of the class label of a test sample, and the final prediction will be reported through majority voting. In contrast to individual trees, RFs can assign a probability to their inferences, enabling an uncertainty analysis of the results. In our experiments, we trained 50 DTs to build our RF.

For an alternative approach, we also tried logistic regression (LR) in our experiments as a linear classifier that is widely used because of its simplicity [224]. This model is a single-layer neural network where the output undergoes a softmax function (a function in form of

$e^{z_i} / \sum_{j=1}^{n} e^{z_j}$ for normalizing a set of real-valued scores z_1, ..., z_n) to generate a probability distribution, which is to be interpreted as the probability of belonging to different classes. Compactly representing this model, given the input vector $x = [x_1,...,x_6]$ = [T, *Re*, *We*, CA, CAH, S_q], LR produces the output as the probability that x belongs to class i ():

$$P(y = i \mid x) = e^{\beta_{i1}x_1+\cdots+\beta_{id}x_d} / \sum_{j=1}^{6} e^{\beta_{j1}x_1+\cdots+\beta_{jd}x_d} \qquad \textit{Equation 2-2}$$

where β_i= $[\beta_{i0}, \beta_{i1},.., \beta_{i6}]$ denotes the parameters corresponding to the i^{th} class. The exponents of these class probabilities are also known as the log-likelihood of the data sample x given the parameter values β_i, $1 \leq i \leq 6$. In the training step, parameters are tuned by maximizing (through the gradient ascent) the summation of the log-likelihood terms of the training data given their observed class labels plus a regularization penalty term that is usually in the form of the L1 [225] or L2 [226] norm of the parameter vectors. We used the latter in our experiments with a regularization coefficient of 1. Note that log-likelihoods are linear with respect to the data features; hence, logistic regression is known to have a lower class separability power than DT and RF, which experience greater nonlinearity.

2.3.4.1. Prediction Rules

2.3.4.1.1 Decision Tree

Class prediction in DT models includes following a set of simple decision rules over individual features. To keep our discussion concise, here we visualize only our shallowest DT model (d_{max} = 4) and demonstrate how class is inferred through its branches and leaves. The tree structure and trained parameters of this model are shown in Figure 2-5, in which each tree node (*rectangle*) is labeled by its parameters and training data statistics. The first

line of each node specifies the node ID. The second line shows the node's decision rule as an inequality for an individual feature. These inequalities divide the feature space into two halves producing one "child" node per partition. Moreover, a set of multiple inequalities collectively defines a partition (subregion) of the feature space. Each node in our tree is assigned a feature space partition that is determined by the set of its ancestors' inequalities. For instance, the root is assigned the whole feature space because it has no ancestors (hence, no partitioning), and the partition for Node #3 is defined by the inequalities $\{S_q \leq 3.281, We \leq 87.925\}$. The leaves do not have decision rules as they lack descendants. The third line in each node indicates the Ginni index value of the class labels for all the training samples falling inside the node's partition. Two more properties are present inside the leaves (i.e., nodes without descendants): "class sizes," explicitly listing the class distribution of the training samples inside the corresponding partitions, and "class," representing the predicted class inferred by the leaf. The inferred class is determined by the class having the largest number of training samples in the leaf's partition. Furthermore, class probabilities are obtained by estimating the empirical distribution from the class sizes.

Decision-tree predictions (class assignment) for any given test sample begin from the root node (#0), shown at the top of the tree, and move forward sequentially by choosing the next node based on the current node's decision rule. This sequential decision-making task ends once it reaches a leaf. Using Figure 2-5, we can follow, as an example, the test sample with the feature values x = [T, *Re*, *We*, CA, CAH, S_q] = [−10, 3303.94, 52.22, 166.6, 0.6, 7.9]. Starting from the root node, the first decision rule we consider is $S_q \leq 3.281$. Given that our test's S_q is 7.9, the rule's inequality does not hold, and therefore, we choose Node #2 (the child node on the right in the figure) as our next node. The decision rule for Node #2 is *We*

≤ 87.925, which is held in the case of our test sample ($We = 52.22$). Therefore, we choose Node #3 (the left child of Node #2 in Figure 2-5) as our third step. Repeating this procedure, we encounter the decision rule $T \leq 24.843$ in Node #3, which holds; thus, we move to Node #4, followed by decision rule $Re \leq 3526.178$, which also holds; hence we move to Node #5. At Node #5, our prediction procedure ends because there are no further descendants. The predicted class in this leaf is PB (Figure 2-5). To measure the uncertainty of this prediction, we can compute the empirical class distributions by normalizing the class sizes such that they sum to one. From Figure 2-5, the class sizes are [0, 55, 0, 297, 8, 0] (the total number of training samples in Node #5's partition is 55 + 297 + 8 = 360). Normalizing, this yields the empirical distribution [0, 55/360, 0, 297/360, 8/360, 0] = [0, 0.153, 0, 0.825, 0.022, 0] corresponding to classes BS, D, FB, PB, PS, and S, respectively. Hence, our final prediction for this test sample will be class PB with a probability of 0.825.

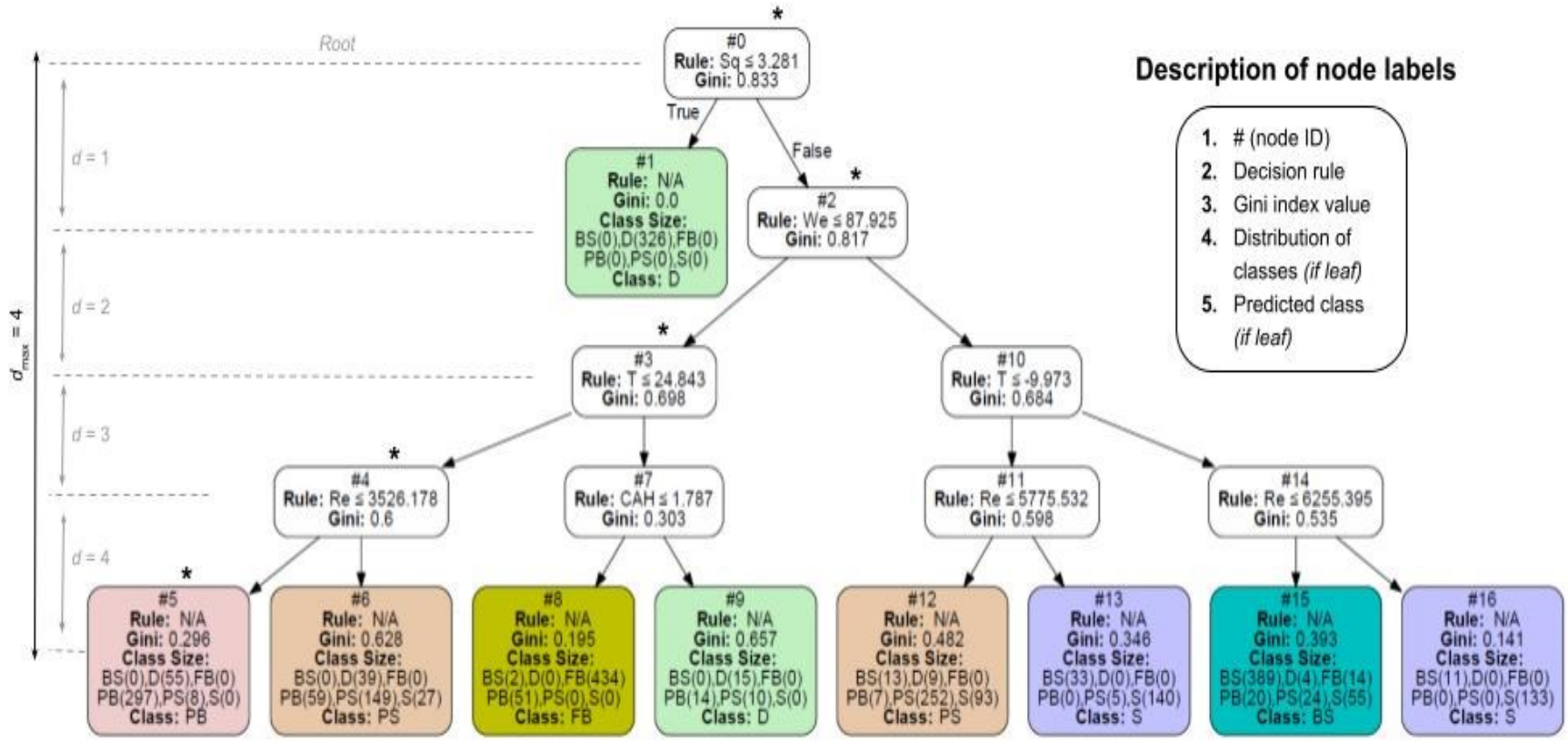

Figure 2-5: Tree structure and parameter values of our trained decision tree (DT) (d_{max} = 4). The asterisks (over selected nodes) indicate the decision path of the class inference of the exemplary test sample discussed in Section 2.4.1.1

2.2.4.1.2 Logistic Regression

The class probabilities in this model are described through softmax functions. From the trained parameters and the equation above (Equation 2-2), the class probabilities can be described as:

$$P(y=D \mid x) \ \ exp(0.004-0.097\ T-0.003\ Re\ +0.064\ We+0.004\ CA+0.454\ CAH-0.021\ S_q) \quad \textit{Equation 2-3}$$

$$P(y=PB \mid x)exp(0.317\ T-0.002\ Re-0.049\ We+0.044\ CA-0.23\ CAH+0.044\ Sq) \quad \textit{Equation 2-4}$$

$$P(y=FB \mid x)exp(-0.002-0.079\ T+0.005\ Re-0.046\ We-0.103\ CA-0.09\ CAH-0.024\ Sq) \quad \textit{Equation 2-5}$$

$$P(y=PS \mid x)exp(-0.023\ T-0.003\ Re+0.04\ We+0.089\ CA-0.066\ CAH) \quad \textit{Equation 2-6}$$

$$(y=BS \mid x)exp(-0.119\ T-0.001\ Re+0.032\ We+0.029\ CA+0.073\ CAH-0.022\ Sq) \quad \textit{Equation 2-7}$$

$$P(y=S \mid x) \ \ exp(-0.001+0.002T+0.004Re-0.041\ We-0.064\ CA-0.141\ CAH+0.218\ Sq) \quad \textit{Equation 2-8}$$

Note that these equations do not indicate equalities. The right-hand side of each equation is proportional to the corresponding class probability. The exact class probabilities can be obtained by normalizing these values by their summation. To predict the class label of a test sample, we can simply compute all the right-hand sides of the equations and then select the class having the highest score among all the classes.

These LR-based equations are a powerful means of modeling multilabel outcomes, such as the various phenomena (deposition, full bouncing, partial bouncing, and splashing, etc.) that occur during a droplet impact on a solid surface to measure the statistical significance of each independent variable with respect to probability. To better understand how to make class predictions with LR, let us consider a test sample with the feature x = [T, *Re*, *We*, CA, CAH, S_q] = [25, 4237.42, 85.9, 162.8, 1.3, 7.54]. Inserting these values into the class probability equations produces the non-normalized class scores: [91.65, 0.00, 11.44,

94.84, 0.00, 0.16], implying that the fourth class (i.e., PS) is assigned the largest score and is therefore the predicted class. The second and fifth classes (D and BS, respectively) obtained near-zero scores. Normalizing these values by division to their summation will give us a probability distribution that can be interpreted as the certainty of our trained LR model regarding the predicted class. For this test example, the probability distribution is [0.46, 0.00, 0.06, 0.48, 0.00, 0.00], implying that our model probabilistically infers that this sample belongs to Class 1 (S) with a probability of 46%, Class 3 (PB) with a probability of 48%, and Class 4 (PS) with a probability of only 6%.

2.4. Results and Discussion

2.4.1. Outcome of Droplet Impact Dynamics

We first investigated the influence of surface temperature on impact dynamics by varying the substrate temperature (−20, −10, and 25 °C) while maintaining the initial droplet temperature at room temperature. For the 25 °C experimental results, we relied on some previously published data from our lab [221]. As illustrated in Figure 2-6, the water droplets vary in their impact behaviors on the surfaces, including full bouncing (FB), partial bouncing (PB), deposition (D), prompt splashing (PS), bouncing-splashing (BS), and splashing (S) [61].

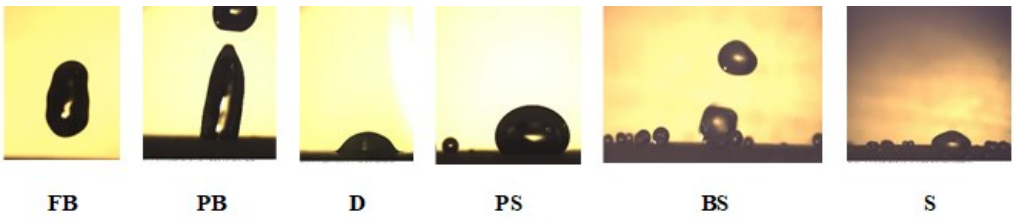

Figure 2-6: Droplet impact regimes on silicone rubber surfaces. Regimes include full bouncing (FB, T = 25 °C, S_q = 7.54 µm, We = 15.81), partial bouncing (PB, T = −10 °C, S_q = 6.64 µm, We = 45.25), deposition (D, T = −10 °C, S_q = 1.76

μm, We = 16.81), prompt splashing (PS, T = −10 °C, S_q = 7.9 μm, We = 62.37), bouncing-splashing (BS, T = −10 °C, S_q = 7.9 μm, We = 142.62), and splashing (S, T = −10 °C, S_q = 7.54 μm, We = 208.74).

Impacting a droplet on hydrophilic, hydrophobic, and superhydrophobic surfaces alters the resulting regime in terms of deposition, bouncing, splashing, etc. Spreading or sticking of droplets can be observed when the test surfaces are hydrophilic or hydrophobic. In contrast, droplet mobility increases on superhydrophobic surfaces having a low CAH. The kinetic energy of the impacting droplet on the hydrophobic and superhydrophobic surfaces is converted into surface energy, and a small amount of energy is lost through viscous dissipation energy. Balances between inertia, viscosity, and capillary forces control the dynamic of droplets [81]. Surface properties, such as wettability, roughness, and temperature, markedly affect the bouncing and deposition of droplets; at lower temperatures, for example, the losses from viscous dissipation increase and lead to less available energy for bouncing. Therefore, the probability of bouncing decreases at lower temperatures [108].

Impacting water droplets at cold temperatures (−10 and −20 °C) operated in five regimes, i.e., deposition, partial bouncing, splashing, prompt splashing, and a transition regime between bouncing and splashing (Figure 2-7). Figure 2-7 a1, a2 shows the dimensionless parameters for droplets hitting a hydrophobic surface (CA = 116°, CAH = 46.5°). For all *Re* and *We* numbers between 1380 and 7480 and 9 and 267, respectively, deposition occurs, and the liquid droplet cannot rebound. At lower *Re* and *We* numbers (*Re* <5293 and *We* <134 at –10 °C, *Re* <4646 and *We* <103 at –20 °C) for a non-water-repelling superhydrophobic surface of roughness 3.29 μm, the deposition of droplets and a prompt splashing occurs (Figure 2-7 b1,b2)), whereas at higher *Re* and *We* numbers, the impinging droplets splash.

Droplet impingement on water-repellent superhydrophobic surfaces having a lower CAH and varying roughness values (6.64, 7.54, and 7.9 µm) is shown in Figure 2-7 c–e, respectively. Depending on the surface roughness value, partial bouncing, deposition, splashing, prompt splashing, and bouncing-splashing can occur. At lower *Re* and *We* numbers, the droplets experience partial bouncing on these water-repellent surfaces. At intermediate *Re* and *We* numbers, prompt splashing occurs, and eventually, the droplets show a splashing behavior at higher *Re* and *We* numbers. Droplets were not deposited during the impact process for the superhydrophobic surface with the highest CA, highest roughness, and lowest CAH, although the probability of bouncing-splashing increases as surface roughness is greater for these surfaces at –10 °C.

(a1)

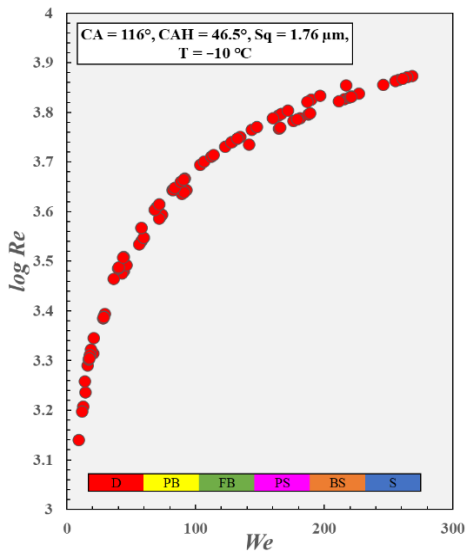

(a2)

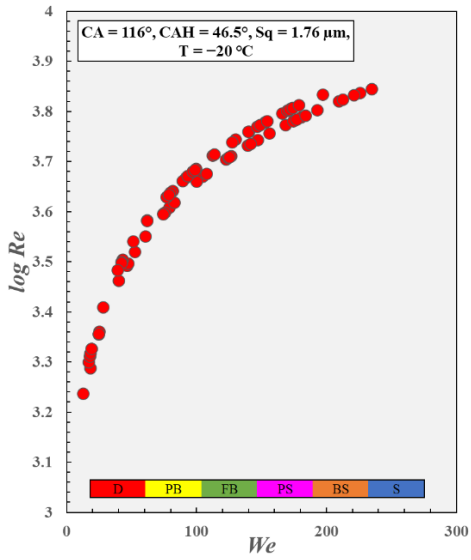

(b1)

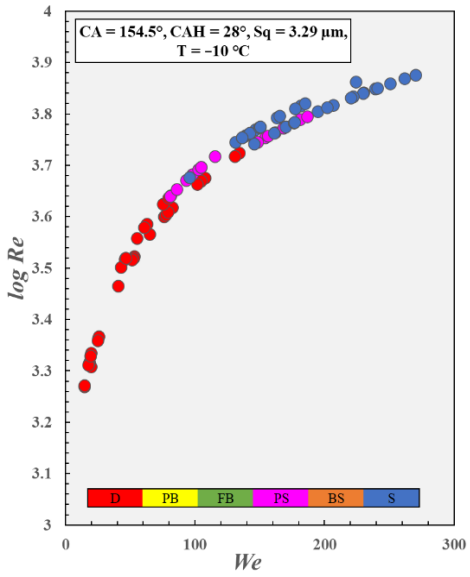

(b2)

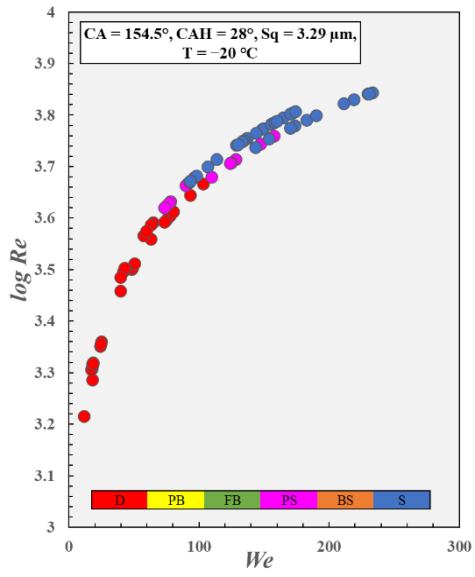

(c1)

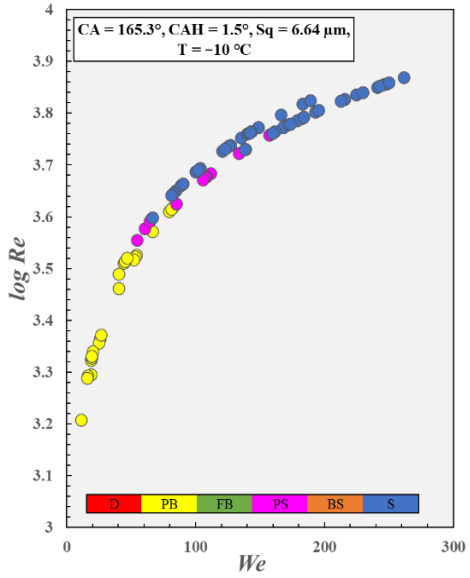

(c2)

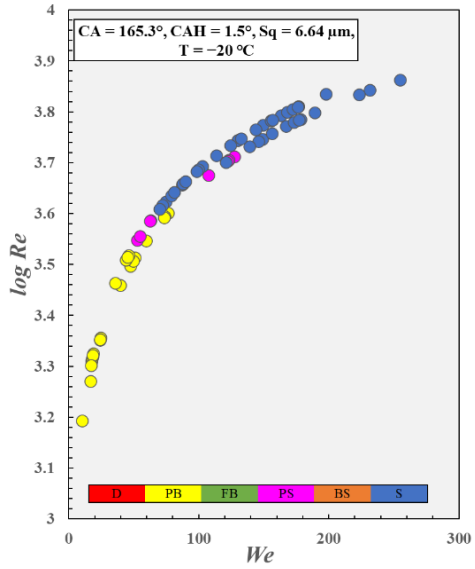

(d1)

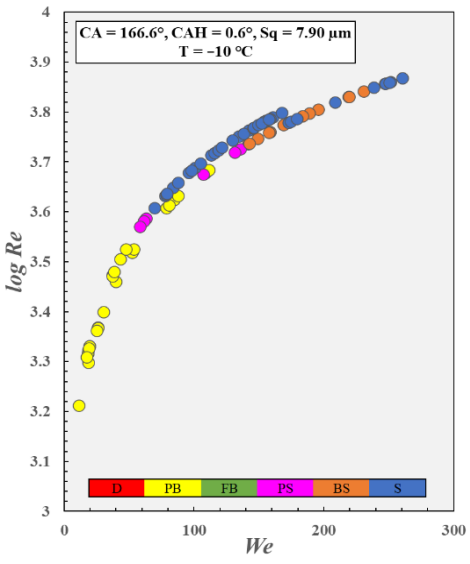

(d2)

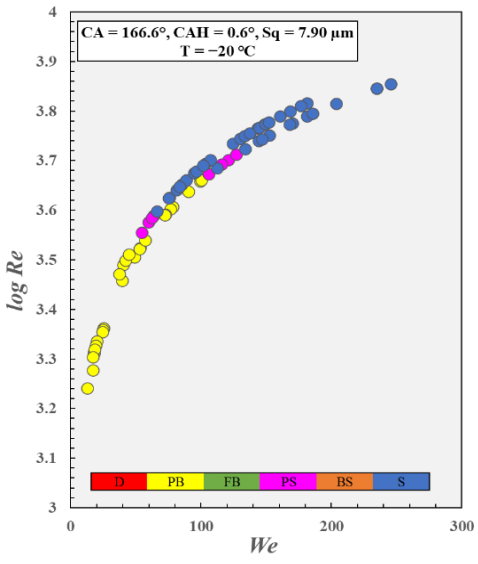

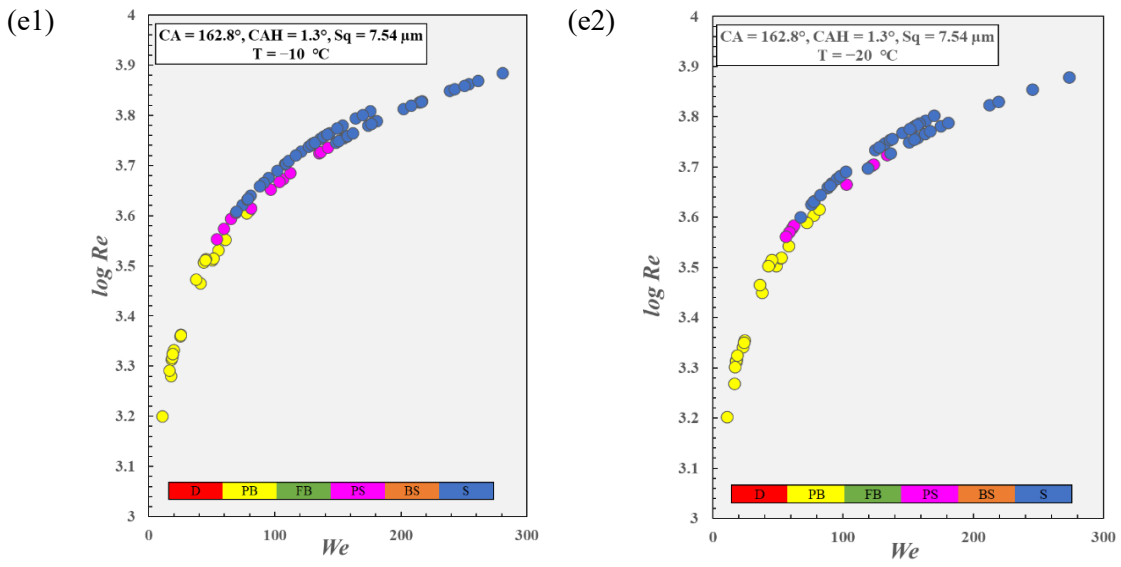

Figure 2-7: Impact dynamics on silicone rubber surfaces: ***a1*** *S_q = 1.76 µm, T = –10 °C;* ***a2*** *S_q = 1.76 µm, T = –20 °C;* ***b1*** *S_q = 3.29 µm, T = –10 °C;* ***b2*** *S_q = 3.29 µm, T = –20 °C;* ***c1*** *S_q = 6.64 µm, T = –10 °C;* ***c2*** *S_q = 6.64 µm, T = –20 °C;* ***d1*** *S_q = 7.90 µm, T = –10 °C;* ***d2*** *S_q = 7.90 µm, T = –20 °C;* ***e1*** *S_q = 7.54 µm, T = –10 °C;* ***e2*** *S_q = 7.54 µm, T = –20 °C.*

Figure 2-8 a–e shows the impacting droplet behaviors at three surface temperatures for five different hydrophobic and superhydrophobic substrates. We observe that the effect of temperature is negligible for hydrophobic substrates and for non-water-repelling superhydrophobic surfaces having a roughness of 3.29 µm (Figure 2-8 a, b). Impacting droplets are not affected by low temperatures on substrates 1 and 2. For the droplet impact on hydrophobic substrate 1, all operating conditions promote the spreading of the droplet; however, for non-water-repelling superhydrophobic substrate 2, having a lower Weber number (<130), deposition occurs.

When observing impacting droplets on water-repellent superhydrophobic substrates (Figure 2-8 c–e), we note that at low droplet velocity, the superhydrophobic surfaces of varying roughness (6.64, 7.54, and 7.9 µm) had better water repellency at sub-zero temperatures. These water-repellent superhydrophobic substrates reduce the probability of rebounding at lower temperatures. Droplets can partially or completely bounce off all water-

repellent superhydrophobic surfaces at temperatures above 0 °C for *We* <110 and *Re* <5000; however, as the temperature of the surfaces is reduced, droplets show partial bouncing on the same substrates (having the same *We* values of <110), which related to the viscous dissipation.

Increasing the impact velocity of the droplet on rough surfaces heightens the probability of splashing (Figure 2-8), as has been reported in other studies [80,227]. However, increased droplet velocity reduces the probability of bouncing, particularly at low temperatures; for example, we did not find conditions in which full bouncing could be observed at low temperatures. In contrast, at room temperature, we observe the complete retraction of water on water-repellent superhydrophobic surfaces (green symbol in Figure 2-8). The most commonly observed behaviors of droplet dynamics on superhydrophobic surfaces at room temperature are complete bouncing, partial bouncing, and splashing [60].

Temperature, therefore, has a minor effect on droplet dynamics on cold hydrophobic and superhydrophobic silicone rubber surfaces for a wide range of *We* numbers and substrate temperatures. A possible reason for this temperature-independent nature of droplet impacting is the delay of solidification. A spreading velocity greater than that for solidification, even in the case of solidification at the early stages of drop impact, leads to this limited influence of sub-zero temperatures on droplet impact [219].

Another reason relates to heat transfer [108]. A rougher superhydrophobic surface characterized by a low CAH can entrap more air pockets in the interface between the surface and the water droplet. This entrapment reduces the contact area with the droplet and acts as an insulator to heighten the heat transfer barrier. The reduced contact area and heat transfer

ability of superhydrophobic surfaces efficaciously limit increases in viscosity by decreasing the temperature. The reduced heat transfer from a cold hydrophobic or superhydrophobic surface to a droplet at high *We* numbers can limit water droplet dynamics on these surfaces. Therefore, substrate temperature has a similar but weaker effect on the superhydrophobic substrates at higher droplet velocities.

Moreover, the effect of surface temperature on droplet bouncing at lower *We* numbers for water-repellent superhydrophobic silicone rubber surfaces can be explained by the extent of energy dissipation and the wetting transition within the surface structures. Lower temperatures increase the viscosity of droplets, thereby increasing contact time and viscous dissipation while reducing the probability of bouncing. Moreover, surface wettability is significantly influenced by temperature. The wetting transition of a Cassie-Baxter to a Wenzel state by decreasing the temperature can reduce droplet bouncing [60,228].

Therefore, unlike many previous studies that examined the impact behavior of water droplets on cold superhydrophobic surfaces with a limited set of parameters, we investigated the effects of a wider range of influencing factors [216–219]. In general, for a wide range of *We* and *Re* numbers, our experimental results showed that the temperature has a minor impact on droplet dynamics on cold hydrophobic or superhydrophobic silicone rubber surfaces while previous studies reported a strong temperature dependency for the impact dynamics of water droplets [75,108,216]. Increasing *We* number and surface roughness, heightens the probability of splashing, as has been reported in other studies [77,80,227].

We then examine all possible variables simultaneously using machine-learning methods in the next section to analyze droplet regime; however, many works do not include

an analysis that incorporates multiple factors simultaneously [76,108,229]. Many studies have reported the use of machine learning techniques in material science, superhydrophobicity and icephobicity [187,203,229,230]. In this work we describe to the best of our knowledge the first application of machine learning to the detailed dynamic of water droplets impacting hydrophobic and superhydrophobic surfaces at different temperatures. Although the number of publications focused on droplet impact dynamics has increased recently, various aspects need to be studied for the design of high-performance technical devices. The complexities of the impact process and the interaction of various influencing parameters could show the promise of the machine-learning approach. Therefore, if the dynamic behavior of droplets can be predicted before conducting experiments, assessing the performance of droplet-based devices and industrial applications can be done more accurately and effectively.

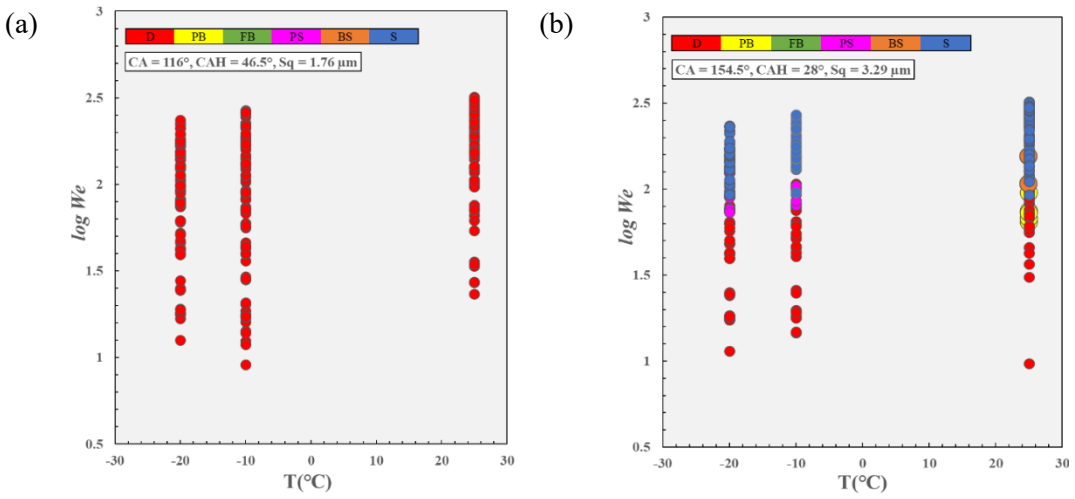

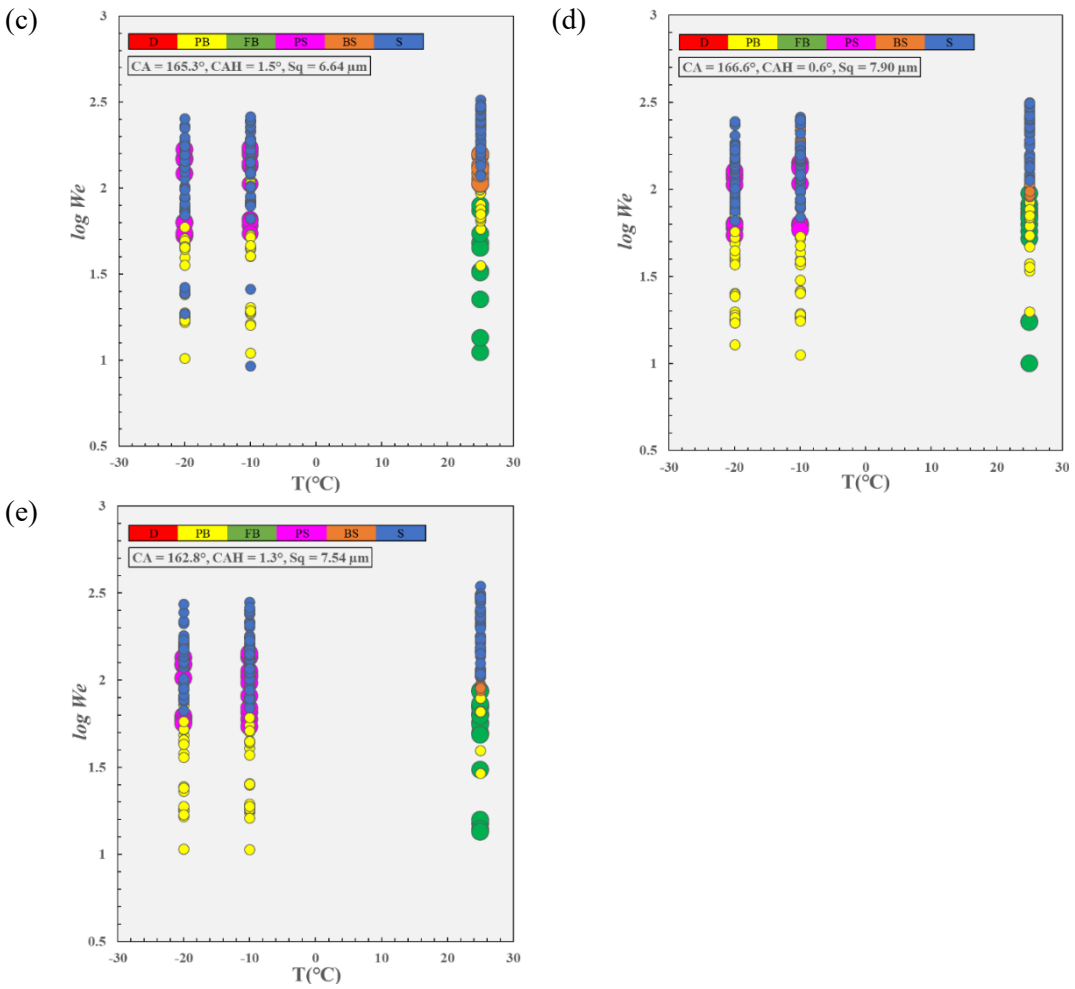

Figure 2-8: Droplet impact dynamics regime map for silicone rubber surfaces ***a*** *S_q = 1.76;* ***b*** *S_q = 3.29;* ***c*** *S_q = 6.64;* ***d*** *S_q = 7.90; and* ***e*** *S_q = 7.54 µm at different temperatures.*

2.4.2. Classification Results

We trained and evaluated the three classifiers on a data set that we obtained from our experiments of impacting droplet behavior on silicone rubber surfaces (hydrophobic to superhydrophobic surfaces). Our data set consisted of six-dimensional feature vectors (T, *Re*, *We*, CA, CAH, and S_q) and six classes (FB, PB, D, PS, BS, and S). We randomly split the data into training and test partitions; the training set served for fitting the models, and the test data was kept for evaluating the model. The impact drop regimes show a highly imbalanced distribution (Figure 2-9). To correct this imbalance between regimes, we augmented the

training data using the *synthetic minority oversampling technique* (SMOTE) [231]. Oversampling ensures an equal number of training samples for each class; however, the test data were untouched and hence remained with an uneven distribution between classes. We had 2,688 training samples and 257 test samples following this preprocessing step.

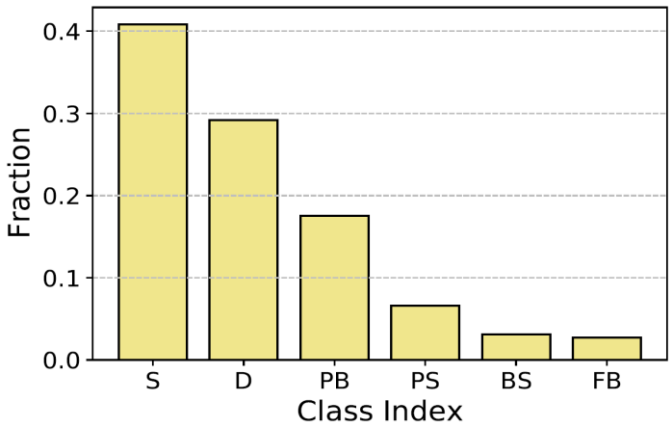

Figure 2-9: Histogram of classes within the initial data set before the use of SMOTE. Splashing (S) is the dominant class (class 1), whereas bouncing-splashing (BS, class 2) and full bouncing (FB, class 3) are the least represented classes. Other classes are partial bouncing (PB, class 4), deposition (D, class 5), and prompt splashing (PS, class 6).

We used precision and recall to evaluate the performance of the trained classifiers. These criteria are specifically designed to be used with imbalanced data sets. In a binary positive/negative classification scenario, precision indicates the portion of the model's positive predictions that truly belong to the positive class. Recall measures how well the predictions cover the entire positive class. A low precision implies a high rate of false positives, whereas a low recall indicates many false negatives within the predictions. To summarize these two criteria, we used the F_1 score, defined as the harmonic mean of the two. This score is also originally proposed for binary classification problems and is defined as $F_1 = \frac{2\ Pr.Rc}{(Pr+Rc)}$, where $Pr = \frac{TP}{TP+FP}$ and $Rc = \frac{TP}{TP+FN}$ are precision and recall, respectively, and TP, FP, and FN denote the number of true positives (test samples with positive class in reality

and in prediction), false positives (test samples with negative class in reality but positive in prediction), and false negatives (test samples with positive class in reality but negative in prediction), respectively. For multiclass problems like ours, F_1 is reported as the (weighted) average of F_1 scores individually evaluated for one-versus-rest of each class. In the case of weighted averaging, the score of each class is weighted according to its sample size, hence taking into account the existing class imbalance.

Table 2-2 summarizes the evaluation results of each classifier involved in our experiments. As is shown by our results, all the machine learning models were capable of predicting class labels though with different levels of accuracy; however, these results confirm the inferior classification ability of the linear LR model, showing that this model could not separate the training samples accurately and demonstrates the nonlinearity of the decision boundaries between the classes in our data sets. The model yielding the highest test accuracy had the highest complexity (non-linearity), which was expected as classifying real-world data usually demands highly non-linear models. Now as the complexity of learning models grows, interpretability of their outcomes become more challenging. More specifically, if one needs to translate the resulting prediction into a handful of simple algebraic rules, one would have to apply simpler (or even linear) techniques. Such interpretability power comes with a cost, i.e., a more modest generalization accuracy. Some relatively shallow DT (e.g., $d_{max} = 7$) are competitive against the deeper unconstrained DT (d_{max} = NA) or RF models in classifying the unseen test samples; however, they severely underperform when explaining the training data set. This observation indicates that the generalizability of classification models does not always linearly increase with their complexity.

Table 2-2: F_1 scores of the trained classifiers. Note that for the training data set, the weighted and unweighted average F_1 are the same because the class labels have been balanced through oversampling. Decision-tree (DT) models are trained using different d_{max} values and without any depth-dependent conditions (d_{max} = NA).

Metric (%)	**DT (evaluated for various d_{max})**								**RF**	**LR**
	4	**5**	**6**	**7**	**8**	**9**	**10**	**NA**		
Training										
F_1 (av.)	79.3	82.89	88.44	91.3	93.73	95.38	97.0	100	100	77.3
Test										
F_1 (av.)	63.15	63.41	67.91	74.18	71.08	69.66	71.88	73.54	75.19	60.21
F_1 (weighted av.)	74.6	72.99	80.99	86.05	85.47	85.3	86.11	87.44	89.04	77

In calculating the F_1 score, the predictions are obtained by selecting the class having the highest probabilities computed through the predictive model. For instance, computing F_1 in a binary classification is associated with placing a threshold for the positive class probabilities at 0.5. To obtain a more detailed portrait of the performance of a binary predictive model, we can change this threshold from 0 to 1 to obtain a range of F_1 scores or precision-recall pairs. Plotting the resulting precision versus the recalls yields what is usually called the precision-recall curve. An ideal classifier results in a recall and precision unit that is independent of the applied threshold; hence, the area under its precision-recall curve is 1. Figure 2-10 presents the precision-recall curves of the LR and RF classifiers operating in a one-versus-rest mode for each class. DT is not considered here because trees that are not too shallow (e.g., d_{max} = NA) typically assign degenerative class probabilities to samples (therefore, zero uncertainty); there are thus very few operating points on the precision-recall curve. We then compared our classifiers with random baselines, for which the precision remains constant and equal to the size ratio of the corresponding class (equivalent to the positive-to-negative class ratio of the corresponding one-versus-rest binary classification).

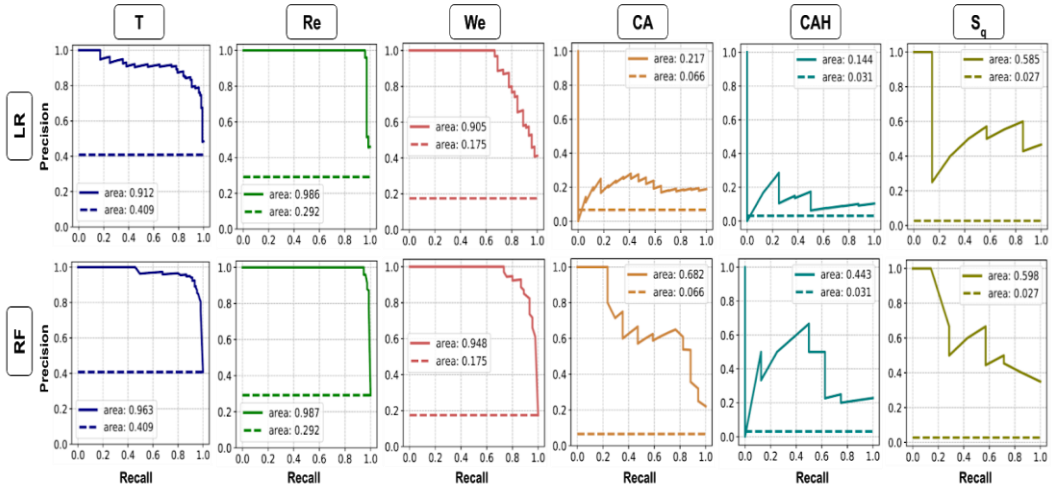

Figure 2-10: Precision-recall curves of the logistic-regression (LR) and random-forest (RF) classifiers. Each graph indicates the curves for binary classification of an individual class versus the rest (one-versus-rest). The dashed lines represent random classifiers that have constant precision-recall curves for any classification problem.

Figure 2-11 shows confusion matrices for the trained classifiers to better illustrate a binary comparison between the classes in the results. The (i,j)-th element of a confusion matrix shows the (normalized) count of samples that actually belong to class i but have been classified as class j. As can be observed in this figure, a common mistake among all the models is misclassifying samples of class BS as class S. In addition, a mistake that both our non-linear models (DT and RF) have committed is mistaking FB samples for class PB, whereas the linear model (LR) incorrectly labeled a significant number of PS samples as PB.

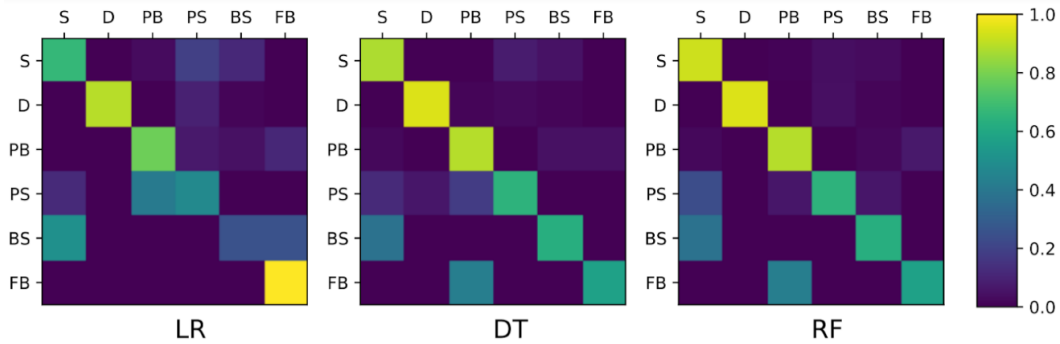

Figure 2-11: Confusion matrix for the trained classifiers. The elements are normalized over the rows to compensate for the imbalancedness of the test data set.

A completely different working condition of these three algorithms would lead to different results and prediction accuracy. For example, a particular formula for classifying and predicting is used for LR, whereas RF works by constructing nodes and trees. The classification model of impact droplets on hydrophobic and superhydrophobic silicone rubber surfaces obtains satisfying results on the basis of the algorithms tested on the experimental data. Linear-based algorithms (LR) are not as accurate as the more sophisticated and nonlinear algorithms (DT and RF) for classifying impact droplets in scenarios of more complex experimental conditions. This leads to inaccuracies; however, LR is slightly more effective than DT and RF at producing understandable and interpretable equations. Consequently, the strong performance of our models indicates their ability to determine the complex relationship between the various parameters affecting impact droplets.

2.4.2.1. Analyzing the Importance of Features

The main objectives of the classification techniques are (1) predicting the output for new input features as accurately as possible and (2) providing information about the relationship between the input variables and output. Some of these models are linear classification models (e.g., LR) that are understandable and interpretable; however, these models may not perform better than nonlinear models.

One of the critical inputs to these machine-learning algorithms is the feature importance measurement, which can have various applications, such as reducing the number of dimensions and selecting the most contributing factors in a given data set [232,233]. Depicting a one-to-one relationship between impact behavior and the experimental parameters (including *Re*, *We*, CA, CAH, S_q, and T) is possible; however, in this conventional

approach, quantifying variable importance is particularly challenging in the case of nonlinear relationships between parameters. Moreover, evaluating the simultaneous effect of each conditioning factor on impact behavior appears impossible through conventional methods.

We used multiclass supervised learning with a multitude of features to solve our classification task. We evaluated the performance of our models when all features are considered simultaneously. However, we can also isolate individual features and assess their respective importance in the classification. To perform the latter, we must apply distinct strategies for tree-based models (DT and RF) and logistic regression.

As explained above, decision trees comprise several nodes, each of which includes a decision rule as a function of a single feature. Here, we define the importance of each feature as the average reduction of the impurity criterion caused by that feature. Because we use the Ginni index to measure the impurity, the resulting score is also called the Ginni importance.

In the LR approach, we utilize the amount of change in the log-likelihood objective function of the LR model that is caused by a particular feature to measure its importance. More specifically, we repeat the training after removing a feature from the training data set and compute the log-likelihood objective function of the resulting model (excluding the regularization penalty term). The magnitude of the difference between the log-likelihood of the modified and original training models is the importance score of the considered feature.

In predicting the impact droplet process, the contribution of the different affecting parameters, their effectiveness, and their influence on the accuracy of the predictive models is critical. To demonstrate this, we present the relative importance of features (*Re*, *We*, CA, CAH, S_q, and T) for the three models (Figure 2-12). Here, we consider the DT model without

any depth-dependent conditions. We observe that all the models agree that T and *Re* are essential features to be retained. RF also assigns high importance to *We* number.

Interestingly, RF estimated that the *We* and *Re* numbers are the most important variables. T is the most important feature for surface properties, followed by CA, CAH, and S_q. Our experimental results (Figure 2-7, Figure 2-8) show that the *Re* and *We* numbers are the key factors affecting droplet behavior. For example, we observed a similar pattern for all water-repellent superhydrophobic silicone surfaces; however, depending on the selected *Re* and *We* numbers, it provoked either full bouncing, partial bouncing, deposition, splashing, prompt splashing, or bouncing-splashing. In this study, RF models perform better in analyzing feature importance given their agreement with the experimental results. Moreover, looking specifically at the dynamics of impacting droplets under icing conditions, as water droplet properties and wetting properties depend on temperature, it seems difficult to say that there is a linear relationship between these factors. This issue also highlights that using nonlinear algorithms such as RF to classify droplet behaviors under more complex experimental conditions is a valid and accurate approach for predicting droplet impact dynamics.

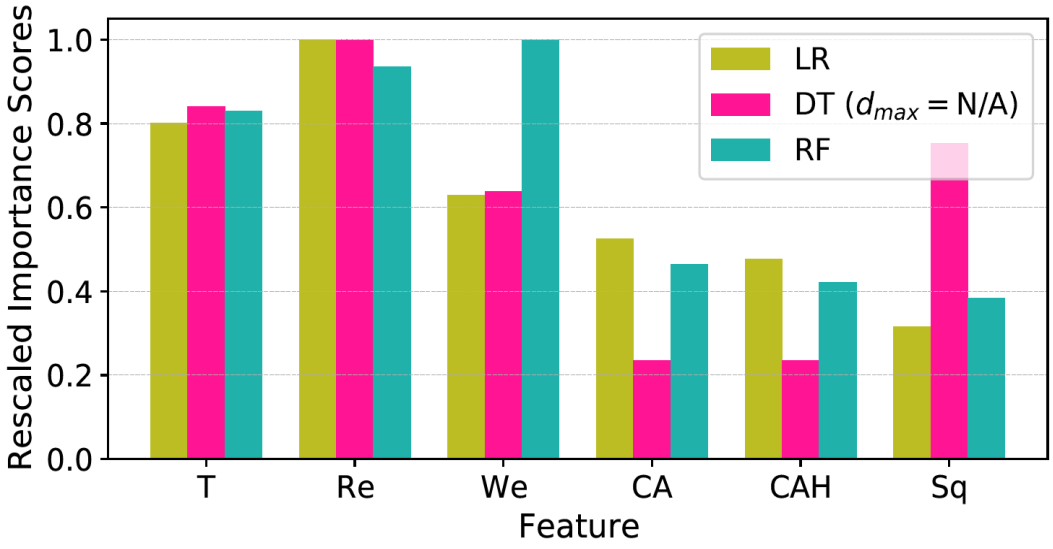

Figure 2-12: Importance analysis of the features; temperature (T), Reynolds number (Re), Weber number (We), contact angle (CA), contact angle hysteresis (CAH) and surface roughness (S_q)) for the three trained models of logistic regression (LR), decision tree (DT), and random forest (RF).

2.5. Conclusion

Here we studied droplet impacts on hydrophobic and superhydrophobic surfaces at different temperatures and proposed design guidelines for nonwetting surfaces under droplet impingement. We applied experimental and statistical approaches to analyze the impact dynamics of water droplets at −20, −10, and 25 °C and discussed the influence of the substrate roughness, temperature, and wetting properties. The experiments showed that full bouncing observed only on superhydrophobic having a CA>160° and a CAH < 2°; and temperature has a minor effect on droplet dynamics on cold hydrophobic and superhydrophobic silicone rubber surfaces for a wide range of *We* numbers and different substrate temperatures. Multiple machine-learning methods were used to predict the temperature-dependent droplet behavior on hydrophobic and superhydrophobic silicone rubber surfaces, taking into consideration the impact velocity, droplet diameter, and surface features (CA, CAH, Sq, and T). Our logistic regression–based models produced equations for probability, and we

combined experimental findings to model multilabel outcomes of different phenomena arising during droplet impact on a solid surface. We also used both linear (LR) and nonlinear (DT and RF) methods to assess the importance of surface characteristics and found that *We* and *Re* numbers were the most important factors followed by factors related to surface T, then CA, CAH, and S_q.

To the best of our knowledge, this work presents the first application of machine learning to experimental results obtained for the detailed dynamic motions of a water droplet impacting hydrophobic and superhydrophobic surfaces at different temperatures. Our results provide a means of predicting droplet impact behavior through the application of statistical LR modeling and the data-mining DT and RF modeling. All three machine-learning approaches agreed well with the experimental results for classifying droplet behaviors. Although all models exhibited a reasonable performance, the lower accuracy of the LR model indicated that the correlation was nonlinear. The dependency of water droplet properties and wetting properties on temperature makes finding a linear relationship between these parameters difficult. Thus, modeling water droplet behavior on the basis of these factors is not straightforward using conventional methods, illustrating the utility of the machine-learning approach.

CRediT authorship contribution statement

Samaneh Keshvarzi: Conceptualization, Investigation, Methodology, Validation, Writing – original draft, Writing - review & editing. **Jamshid Sourati**: Conceptualization, Methodology, Software, Validation, Investigation, Writing - original draft, Writing - review & editing. **Gelareh Momen**: Conceptualization, Project administration, Supervision,

Resources, Funding acquisition, Writing - review & editing. **Reza Jafari**: Conceptualization, Project administration, Supervision, Resources, Funding acquisition, Writing - review & editing.

Acknowledgments

The authors would like to acknowledge the financial support from Natural Sciences and Engineering Research Council of Canada (NSERC). Also, we would like to thank the help of Mr. Vahid Asghari for machine-learning programming and Mr. Khosrow Maghsoudi for sample preparation during the experiments.

CHAPITRE 3

ARTICLE 2: Ice nucleation on silicone rubber surfaces differing in roughness parameters and wettability: experimental investigation and machine learning–based predictions

S. Keshavarzi[1*], A. Entezari[2], K. Maghsoudi[1], G. Momen[1], R. Jafari[1]
[1]Department of Applied Sciences, University of Québec in Chicoutimi, Chicoutimi, Québec, Canada
[2] The Hong Kong Polytechnic University, Hong Kong
Email address: samaneh.keshavarzi1@uqac.ca

This article has been accepted in:

Journal of cold regions science and technology

3.1. Abstract

Superhydrophobic surfaces serving as icephobic surfaces are a passive means of limiting the icing of surfaces. Ice nucleation time depends on not only liquid properties and environmental conditions but also surface features; however, it is challenging to investigate ice nucleation time and the influencing parameters simultaneously. This manuscript presents two approaches, experimental testing and machine learning, to study ice nucleation time on exposed surfaces. Hydrophobic/superhydrophobic silicone rubber surfaces were fabricated,

and these surfaces varied in their wettability and roughness parameters. Superhydrophobic surfaces characterized by a higher arithmetic average, root mean squared, ten-point height, maximum height of the profile, and a Gaussian roughness distribution—skewness near 0—had longer ice nucleation times. We then used neural networks to model icephobicity in relation to ice nucleation time. The predicted ice nucleation time of the model, trained using some of the experimental results, demonstrated a good agreement with the experimental outcomes. Furthermore, this machine learning approach determined the relative importance of roughness parameters, surface wettability, temperature, and droplet volume in determining surface icephobicity. The proposed approach provides a starting point for studying heterogeneous ice nucleation prediction through an understanding of the key parameters required to optimize the icephobic behavior of superhydrophobic surfaces.

Keywords: heterogeneous nucleation, ice nucleation time, surface roughness parameters, machine learning, superhydrophobic surface, icephobicity

3.2. Introduction

Ice formation on exposed surfaces is common in cold climates and can represent a health and safety issue as well as affect the optimal performance of infrastructure, including irreversible damage to equipment and marked economic costs [9,234]. Therefore, effective measures are needed to remove accumulated ice or prevent its initial formation. These ice removal strategies can be divided into active and passive approaches. Active approaches involve applying external energy—involving chemical, mechanical, and thermal methods—and are thus often time-consuming, uneconomic, and often environmentally harmful. Passive

approaches delay ice formation or reduce ice adhesion without external energy being applied [25,26,235].

Much recent research has explored the use of superhydrophobic surfaces as icephobic surfaces for delaying freezing time and reducing ice adhesion; these surfaces comprise low surface energy materials and surface roughness. This passive anti-icing/deicing approach is inspired by lotus leaves, and these surfaces are fabricated by creating micro/nanostructures that contain low surface energy chemicals and trapped air within the micro/nanostructures. A correlation between superhydrophobicity and both a reduction in ice adhesion and a delay in ice accretion has been documented in several studies [14,34–36]. Superhydrophobic surfaces can prevent ice formation on a solid surface by decreasing both contact time and contact area and increasing droplet roll-off. Some investigations, however, have questioned the efficacy of superhydrophobic surfaces for icephobic applications [32,165].

The freezing of a water droplet on a cold surface does not occur immediately upon contact. For all ice formation mechanisms and scenarios, the ice nucleation process represents a fundamental and crucial step [21]. The ice nucleation process can be divided into homogeneous nucleation and heterogeneous nucleation, which correspond respectively to the absence or presence of external solid surfaces or particles during nucleation [130,131]. In reality, eliminating the role of foreign solid particles (e.g., dust particles, interfaces of nucleating systems) is almost impossible. Furthermore, there is a multitude of factors that can work either in concert or in competition to alter the nucleation process; e.g., environmental conditions, surface characteristics (in the case of heterogeneous icing), the amount of cooling, the degree of purity of the mother phase, droplet size, and the stochastic nature of ice nucleation [29,30,236]. Hence, understanding the ice nucleation process and its

interaction with both surface and environmental characteristics is vital. Although finding a relationship between these various affecting parameters and icephobicity is complex, it is critical for predicting ice nucleation time for application to icephobic surface design and optimization.

Rahimi et al. [151] compared the freezing delay of a water droplet on hydrophilic and hydrophobic substrates having similar surface topographies and found longer freezing delays for droplets on a slightly hydrophilic substrate; thus, ice formation kinetics depend on surface chemistry, as well as surface wettability and topography. In their study of water droplet freezing on hydrophilic, hydrophobic, and superhydrophobic surfaces, Qi et al. [36] observed that the contact angle strongly influenced water droplet freezing time, i.e., a longer freezing time as contact angle increased. Hao et al. [115] prepared five substrates differing in topology and wettability and assessed the ice nucleation and complete freezing time of sessile droplets on smooth, micro-structured, and micro/nanostructured surfaces. Surface roughness significantly influenced ice nucleation time, and they determined that a smooth surface having a roughness less than that of a critical ice nuclei experiences a longer freezing delay than a superhydrophobic surface with hierarchical structures. However, as reported in [142], sessile droplet freezing on polished (hydrophilic) silicon wafers and cylindrical micro-micro hierarchical (hydrophobic) silicon surfaces showed hierarchical micro-microstructures to produce longer ice nucleation times than hydrophilic surfaces; the hierarchical structure has a surface roughness greater than the critical radius of homogeneous nucleation—according to nucleation theory, ice nuclei must reach a critical radius for ice initiation and growth, a radius that varies with the degree of supercooling. When surface temperature is held constant, differences in ice nucleation onset between hierarchical and polished surfaces stem from

differences in surface topologies and determine the dominance of wetting characteristics on ice nucleation [142].

The effect of surface topography on ice nucleation is also unclear. Surface characteristics and possible methods of modifying them to prevent or delay ice formation are critical to understanding how surface conditions influence icing. Altering surface characteristics—by modifying surface properties, surface energy, and roughness—affects surface wettability and the energy barrier to nucleation and, hence, the nucleation rate [151]. Surface roughness, as a measurement of surface texture, cannot be adequately described using a single parameter such as root mean square roughness (S_q) or average surface roughness (S_a). Rather, a set of surface roughness parameters, including ten-point height (S_z), maximum height of the profile (S_t), skewness (S_{sk}), kurtosis (S_{ku}), and autocorrelation length (S_{al}), must be used to accurately evaluate the surface roughness [52,237,238]. Multiple studies have assessed the influence of roughness parameters on wettability and icing, with some focusing on superhydrophobicity [239–242] and others on icing [243–246]. Bosher et al. [239] used the nano- and microscale roughness characterization of surfaces to show that surface skewness is the major parameter influencing the water contact angle for identical nano-rough plasma-polymerized PDMS coatings. They concluded that a Gaussian distribution of the roughness height is best for achieving a superhydrophobic surface. Yuan et al. [240], using computer modeling, showed that decreasing skewness and holding kurtosis at around 3 were effective for ensuring droplet bouncing. Yeong et al. [243] investigated the effect of S_a, S_{sk}, S_{ku}, and S_{al} on ice adhesion strength and reported that low S_{al} values led to low ice adhesion, whereas Davis et al. [244] showed a correlation between reduced ice

adhesion and a combination of increased hydrophobicity, reduced roughness, increased skewness and kurtosis, and reduced autocorrelation length.

Although surface roughness plays a crucial role in affecting surface wettability and, consequently, the icing-related properties of a surface, there remains an absence of comprehensive studies focused on the relationships between surface wettability, roughness parameters, and ice nucleation time. Therefore, we chose to study five roughness parameters to determine the relationship between roughness parameters, wettability, and ice nucleation time. Nonetheless, analyzing these parameters together is challenging. To illustrate and understand these relationships, we propose and apply a novel machine learning–based model of ice nucleation time. We test five surfaces differing in roughness parameters and wettability to determine the combination of parameters favoring a maximum ice nucleation time.

Experiments in conventional multifactor systems can be conducted by varying one factor at a time. This approach is time-consuming, and interactions among variables may also be ignored, leading to a low efficiency of systems. Another major shortcoming of traditional approaches relates to highly complex and nonlinear systems that may govern the parameters; it is difficult and sometimes even impossible to present these types of systems using traditional models. Even when a traditional model capable of dealing with these complex systems is developed, it may be impractical for use in prediction [186]. As a possible solution, machine learning techniques have received much attention for their application to complex systems and their capacity to deal with issues of nonlinearity. Machine learning–based approaches can reduce operating costs and improve the speed of data analysis. Machine learning can also identify complex relationships between independent and dependent variables through nonlinear data processing [181,187,221]. Ringdahl et al. [198] applied

molecular dynamics simulations and machine learning to study ice adhesion strength on rough surfaces. It was the first time that machine learning was applied to anti-icing surface design and showed encouraging predictions. Ramachandran [204] developed machine learning models to optimize the icephobicity of concrete by using artificial neural networks to predict surface ice adhesion strength and the coefficient of restitution of water droplets bouncing off the surface under freezing conditions. Fitzner et al. [205] developed a data-driven machine learning–based approach to identify descriptors for heterogeneous ice nucleation as a means of increasing the quantitative understanding of heterogeneous ice nucleation. However, despite these advances, no existing research has reported using machine learning to predict ice nucleation time.

The main objective of our study is to determine the optimal surface characteristics to enhance anti-icing properties of surfaces through analysis of the ice nucleation of water droplets deposited onto solid hydrophobic to superhydrophobic surfaces. By analyzing the freezing of water droplets on the solid surface, we also investigate how surface characteristics, including surface wettability, surface roughness (S_a, S_q, S_z, S_t, and S_{sk}), droplet volume, and surface temperature, affect the ice nucleation process. Exploring these associated parameters represents a significant step for designing icephobic surfaces. We exploit the machine learning approach to investigate multiple variables affecting the icephobic behavior of surfaces, i.e., ice nucleation time, observe interactions between parameters, identify the most important factors (surface wettability, surface roughness (S_a, S_q, S_z, S_t, and S_{sk}), droplet volume, and surface temperature) affecting ice nucleation time, and develop a prediction tool for ice nucleation time as a function of the influencing parameters.

3.3. Material and Methods

3.3.1. Sample preparation

The required surface micro-nanostructures were created on high-temperature vulcanized (HTV) silicone surfaces via direct replication from a series of aluminum (A6061-T6) templates. The template patterns were fabricated using a chemical-etching method. The templates were immersed in a hydrochloric acid solution of varying concentrations: 4.8, 9.8, 14.8, 19.8 wt.% for 2 h to produce different surfaces [247]. A press machine (Carver, USA) having a maximum clamp force capacity of 194 kN was used to replicate the template patterns on the silicone rubber surfaces under the following molding parameters: a molding pressure of 35 MPa, a curing time of 4.7 min, and a mold temperature of 149 °C. Once the rubber was cured, the molds were opened, and the cured rubber was removed from the three-piece flat mold cavity (Figure 3-1). No subsequent processing was carried out on the silicone rubber surfaces prior to the freezing tests.

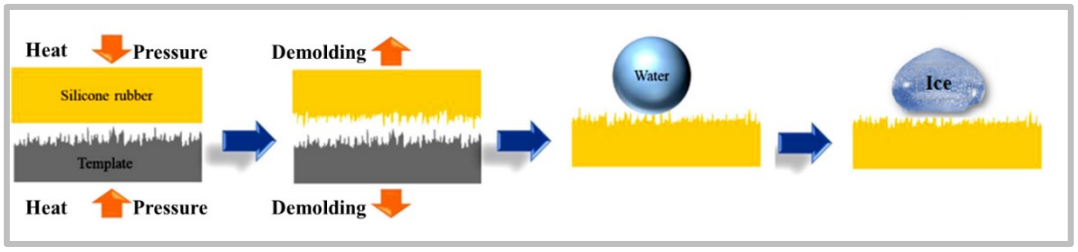

Figure 3-1: Schematic of the fabrication of micro-nanostructured silicone rubber surfaces via a microcompression molding technique [207].

3.3.2. Surface Characterization

A Kruss™ DSA100 goniometer at 25 °C ± 0.5 °C determined the contact angle (CA) of a 4 uL deionized water droplet on the produced surfaces. In addition, to avoid condensation affecting the measurements, anhydrous calcium sulfate desiccants (Indicating DRIERITE

impregnated with cobalt chloride) were used. Contact angle hysteresis (CAH) was calculated as the difference between the advancing and receding CAs of the moving water droplet on the surface. To ensure reproducibility and accuracy, we repeated each measurement at five points across each surface. The surface roughness parameters and the 3D profiles of the surfaces were obtained using a confocal laser microscopy profiler (Profil3D, Filmetrics, USA). Detailed measurement settings can be found in Table 3-1. To obtain the surface roughness, Fill In Invalids and Flatten filters used for data pre-processing. The morphology of fabricated surfaces was observed using a scanning electron microscope (SEM, JSM-6480 LV by JEOL Japan).

Table 3-1: Surface measurement parameters.

Parameter	**Unit**	**Value**
Magnification	-	50×
Area size	μm^2	386.3 × 339.3
Estimated vertical resolution	nm	56
Lateral sampling intervals	µm	0.176

3.3.3. Experimental Setup

We studied the ice nucleation of a single water droplet on hydrophobic/superhydrophobic silicone rubber surfaces using an experimental freezing setup that included a thermally insulating and optically transparent chamber, high-speed camera, thermostatic bath, cold base, drop injection system, test samples, data acquisition system, temperature sensor, humidity sensor, and a vibration-free table (Figure 3-2). A thermally insulating and optically transparent double-layer chamber was used to ensure that the parameters affecting ice nucleation were uniform during experiments to increase the

accuracy and reproducibility of the experiments. Its transparency facilitates imaging of the freezing droplet. The temperature of the cold base was adjusted using the thermostatic bath. Temperature and humidity sensors monitored the chamber temperature and humidity. A high-speed camera (MotionBLITZ, MIKROTRON, EoSens Cube 7, Germany) and LED illuminator were used to visually record the experimental outcome.

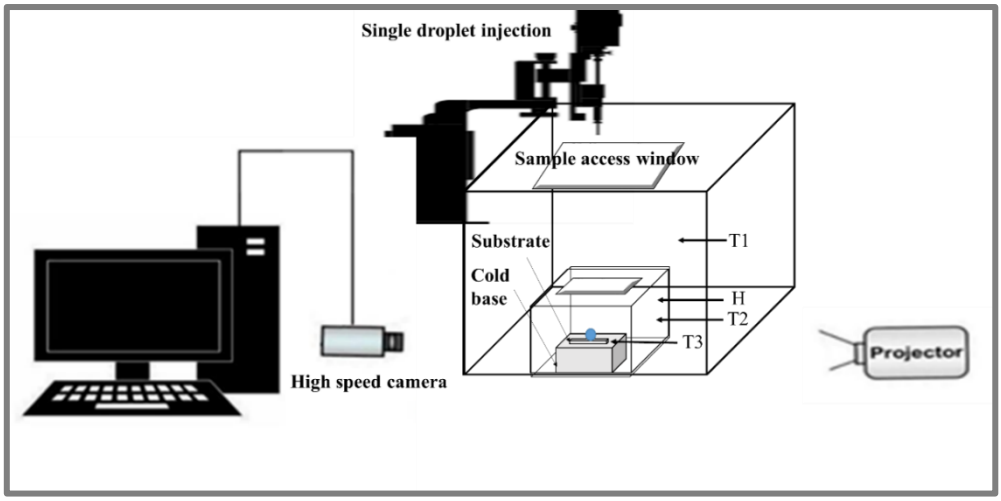

Figure 3-2: Schematic of the experimental setup for the ice nucleation study (H = humidity of small chamber (%), T1 = large chamber temperature (°C), T2 = small chamber temperature (°C), T3 = cold base temperature (°C)).

The temperature and humidity of the surrounding environment and chamber were recorded before the experimental tests. The temperature and the relative humidity of the chamber were set at 20 °C and 35% ± 3%, respectively. The cold base temperature was then decreased to temperatures of −10 and −20 °C, and the silicone rubber sample was placed on the cold plate. Once sample temperature was stable (prior to experimentation, the temperature of the surface was measured with an IR camera and a thermocouple (K-type) which was removed during the experiments), a droplet (either 10 or 20 µL) was placed onto the cold surface with no frost formation, and its freezing process was recorded using the high-speed camera. For each test, two steps in the freezing of droplets were identified. The first step,

defined as nucleation time, represented the moment from when the droplet was placed onto the surface until the rapid recalescent stage. This stage can be easily monitored using a high-speed camera at 1000 frames per second. This step was followed by the complete freezing step. The reported nucleation times are an average of 10 experimental runs.

3.4. Results and Discussion

3.4.1. Surface Characterization

Table 3-2 shows the wettability properties of each sample along with the surface roughness parameters, and Figure 3-3 illustrates various surface structures using SEM images and 3D profiles. Standard surface roughness parameters including S_a (the average surface roughness) and S_q (the root mean square roughness) are generally used to evaluate surface roughness; however, these two values are unable to adequately describe the surface roughness, as they relate only to vertical height and provide no description of horizontal surface features. Relying on only these two parameters can produce very similar roughness values despite very different surface morphologies, and the reverse is also true [248]. To determine those parameters best describing the icephobicity of silicone rubber surfaces, we relied on a combination of commonly used roughness parameters (S_a and S_q) and some less common parameters (S_z (ten-point height), S_t (maximum height of the profile), and S_{sk} (skewness)). Understanding more topographical characterization parameters can help in design of icephobic surfaces to offer the optimum surface characteristics to enhance anti-icing properties of surfaces can be considered as one of the highly important issues. In our current study, the main shortcoming is the limited number of roughness parameters that we used.

Sample 1 was a hydrophobic surface (CA ~116° and CAH ~46.5°) replicated from a smooth aluminum template. Therefore, the hydrophobic property of Sample 1 stemmed solely from the intrinsic hydrophobicity of the silicone rubber. The surface roughness of the other prepared samples differed markedly from that of Sample 1 (Table 3-2); for example, the root mean squared (S_q) of Samples 2, 3, 4, and 5 increased about 1.87, 3.77, 4.49, and 4.28× that of Sample 1. This combination of elevated surface roughness and surface hydrophobicity of the silicone rubber produced the superhydrophobic properties observed for samples 2–5. In addition to S_q, both S_z and S_t testify to the created surface profiles being characterized by relatively high peaks and deep valleys. It is also noteworthy that the skewness value (as an indicator of the asymmetry of the profile about the mean plane) varied between −0.37 and 0.43.

Table 3-2: Water contact angle (CA), contact angle hysteresis (CAH), and 3D roughness values of the produced surfaces at 25 °C ± 0.5 °C and a relative humidity of about 25%.

Sample No.	**CA (°)**	**CAH (°)**	**S_a (µm)**	**S_q (µm)**	**S_z (µm)**	**S_t (µm)**	**S_{sk}**
1	116.0 ± 2	46.5 ± 2.4	1.46	1.76	3.74	3.6	0.28
2	154.5 ± 1.4	28 ± 1.6	2.13	3.29	14.21	18.4	0.31
3	165.3 ± 1.1	1.5 ± 0.2	5.21	6.64	21.65	24.86	0.43
4	166.6 ± 0.9	0.6 ± 0.3	6.49	7.9	33.67	39.97	0.18
5	162.8 ± 0.8	1.3 ± 0.8	6.03	7.54	28.54	33.99	−0.37

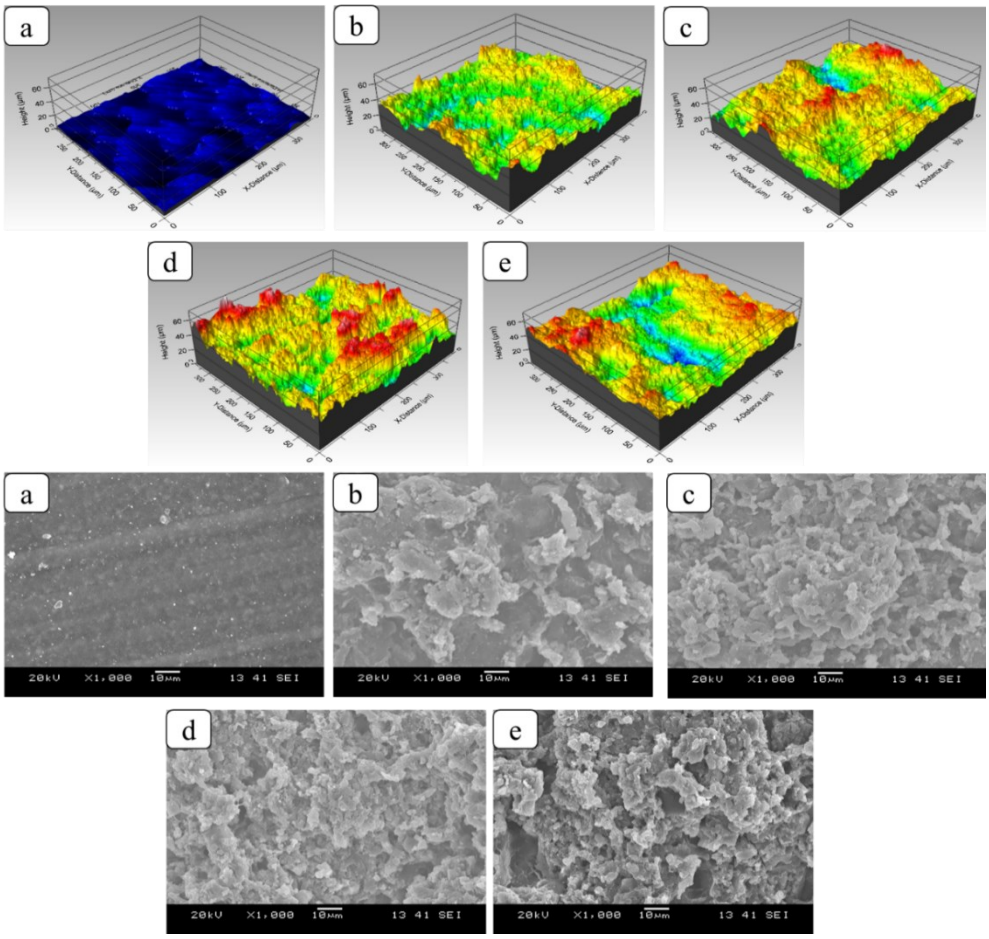

Figure 3-3: The 3D surface profiles and SEM images of samples (a) 1, (b) 2, (c) 3, (d) 4, and (e) 5.

3.4.2. The Effect of Surface Wettability and Roughness

Ice nucleation, formation, and freezing delay can be affected markedly by surface characteristics such as surface wettability, roughness, and surface chemistry [147,249–251]. Establishing the relationships between surface roughness and wettability and the ice nucleation process represents a problem in the design of icephobic surfaces. To determine these complex correlations among surfaces features and ice nucleation time, we investigated the ice nucleation process of sessile droplets on cold surfaces of differing wettability and roughness (Table 3-2). Figure 3-4 shows the shape of water droplets at various times during freezing on the five surfaces. It is also worth mentioning that the contact angle measurement

in Table 3-2 was at 25 °C ± 0.5 °C and RH = 25% while Figure 3-4 was at −10 °C and RH = 35 %. Therefore, the contact angles of the droplets shown in Figure 3-4 do not match the contact angle information in Table 3-2.

Surfaces	Deposing onto surface	Ice nucleation step	Complete freezing
Sample 1	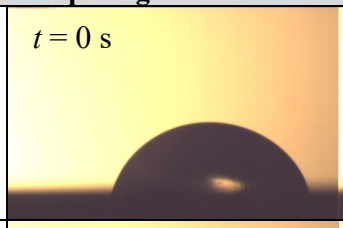	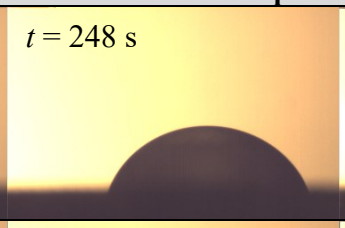	
Sample 2	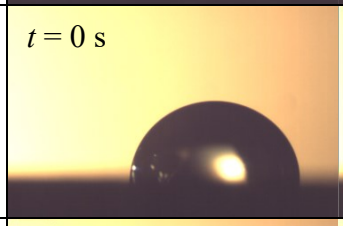	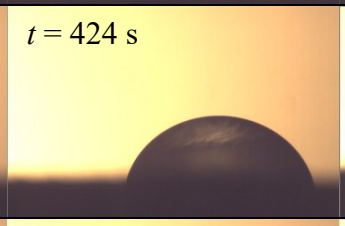	
Sample 3	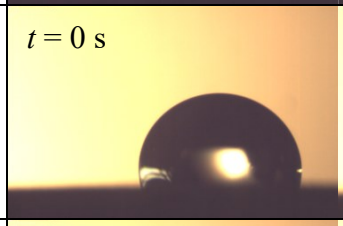		
Sample4	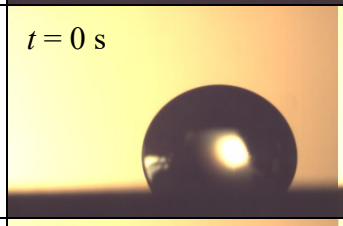	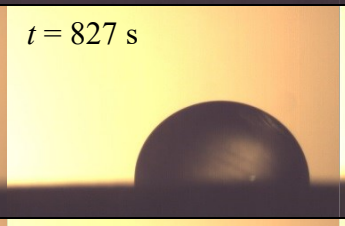	
Sample 5	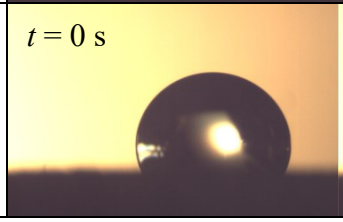	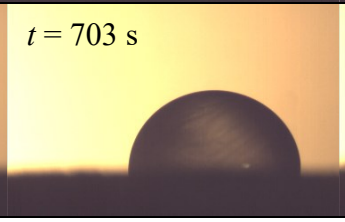	

Figure 3-4: Images of the freezing of a 10 µL droplet on different solid surfaces at −10 °C.

Ice nucleation times for 10 µL droplets placed onto these five substrates at −10 °C varied markedly (Figure 3-5). Sample 1, the unaltered silicone rubber, had an ice nucleation time of 248 s, whereas this increased to 424 s for Sample 2 (CA ~154.5° and CAH ~28°) and to 827 s for Sample 4 when the CA and surface roughness were 166.6° and 7.9 µm,

respectively, and CAH decreased to 0.6°. The slight decrease in CA and roughness and an increase in CAH of Sample 5, relative to Sample 4, produced a decrease in ice nucleation time to 703 s. Similar trends were observed at different temperatures and droplet volumes (Figure 3-5). The roughest surface (Sample 4) offered the longest nucleation time, as more air was trapped in the interface between the rough surface and the water droplet. The trapped air acts as a thermal insulator and reduces heat transfer between the droplet and the solid substrate.

Classical nucleation theory [19,125] holds that two main parameters affect the critical energy barrier of heterogeneous nucleation: ΔT_m, which relates to the degree of supercooling, and *f*, the interfacial correlation factor (Equation 3-1). The latter parameter is a function of the roughness radius of curvature (R) and the CA between the ice nucleus and the surface structure (θ_{iw}).

$$\Delta G^*_{WI} = \frac{16\pi {\sigma_{WI}}^3 \vartheta_I^2}{3\left[\Delta h_{WI}\left(\Delta T_m / T_m\right)\right]^2} f(R, \theta_{iw}) \qquad \textit{Equation 3-1}$$

where Δh_{WI}, T_m, σ_{WI}, and ϑ_I are the enthalpy of melting, melting point temperature, the interfacial ice-water tension, and the molar volume of the solid phase, respectively.

When the radius of the curvature of a solid particle or surface texture is much greater than the critical radius of homogeneous nucleation, *f* depends only on the ice-water contact angle [20]. In this study the surface curvature effect of heterogeneous nucleation theory was not considered. The experiments do not investigate the curvature effect and the results can be interpreted without this effect.

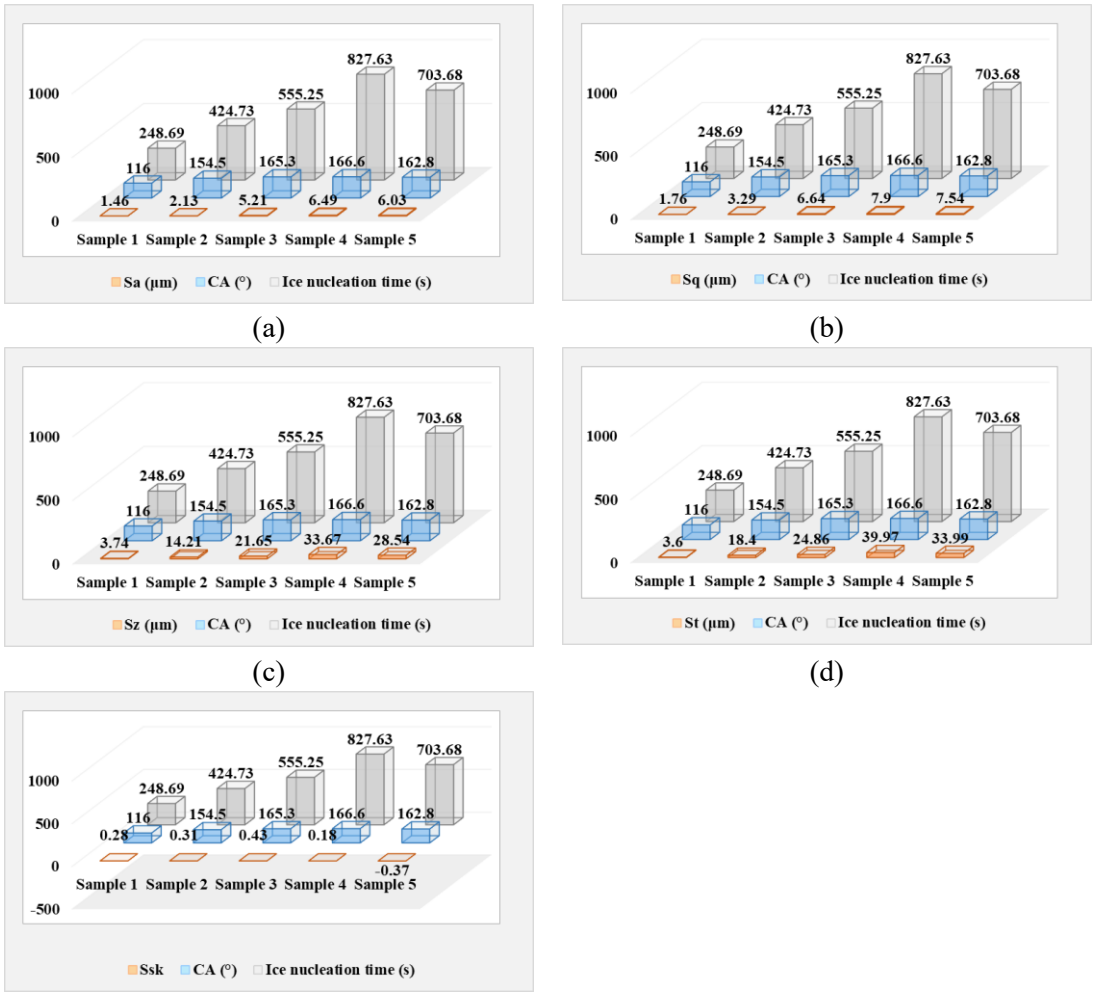

Figure 3-5: Ice nucleation times for a 10 µL droplet on different surfaces as a function of CA and (a) S_a, (b) S_q, (c) S_z, (d) S_t, and (e) S_{sk} at −10 °C.

We observed a significant increase in ice nucleation time as CA increased and CAH decreased because of the reduced contact area and presence of air pockets within the surface microstructures. It means that wetting characteristics of our samples has a strong effect on the ice nucleation time as the greater the CA, the longer freezing delay time. The superhydrophobic surfaces had a smaller contact area between the water droplet and substrate. A smaller contact area, therefore, can lead to a relatively low heterogeneous nucleation rate from classical nucleation theory.

To illustrate how surface roughness affects ice nucleation time, we can plot ice nucleation time and CA against five common surface roughness parameters (S_a, S_q, S_z, S_t, and Ssk) (Figure 3-5). The clear relationship between the ice nucleation time and CA and both S_a and S_q demonstrates that a marked microstructure height prevented the droplet from touching the base of the microstructures. The same conclusion can also be drawn when evaluating the relationship between ice nucleation time, CA and both S_z and S_t.

On the pristine silicone rubber surface, roughness parameters were $S_a = 1.46$ μm, $S_q = 1.76$ μm, $S_z = 3.74$ μm, and $S_t = 3.6$ μm. The parameters describing microstructure height demonstrated a significant influence on surface wettability and ice nucleation time. The increase in CA and ice nucleation time for the superhydrophobic surfaces (Samples 2–5) can be explained by increased S_a, S_q, S_z, and S_t. Furthermore, the three superhydrophobic surfaces having a CAH <10° (samples 3–5) showed considerably higher S_a, S_q, S_z, and S_t than those of the superhydrophobic silicone rubber having a CAH >10° (Sample 2). Greater roughness increased the CA, in accordance with Cassie-Baxter wetting models, where surface roughness directly influences the wetting state (samples 3–5). As S_a, S_q, S_z, and S_t of these silicone rubber surfaces increased, a greater number of grooves were apparent underneath the droplet. A droplet on a rough surface having larger S_a, S_q, S_z, and S_t values would have a smaller liquid–solid contact area and, therefore, a longer ice nucleation time. If S_a, S_q, S_z, and S_t are not large enough, liquid can penetrate the grooves, and the droplet remains in a Wenzel state where the ice–solid contact area is greater.

Surface skewness values were between −0.5 and 0.5 (Figure 3-5); therefore, the height distribution of all surfaces was highly symmetrical and minimally skewed. The optimal performance in terms of a long ice nucleation time and high CA were obtained for a

surface with S_{sk} close to zero. Regardless of whether there was a lower S_{sk}, corresponding to more valleys or a greater S_{sk}, corresponding to more peaks, CA decreased. Therefore, surfaces having a Gaussian distribution of roughness were more likely to be superhydrophobic and icephobic with longer freezing delay times. Sample 4 had the longest freezing delay time (827.63 s) and a near-zero S_{sk} (0.18).

Therefore, the ice nucleation times correlated well with the roughness parameters. Very rough surfaces dominated by peaks should show better water repellency (higher CA and lower CAH) and greater icephobicity in terms of a longer ice nucleation time. Nonetheless, it remained uncertain which specific roughness parameters were best correlated with surface hydrophobicity/superhydrophobicity and icephobicity. We therefore used machine learning to identify these parameters (Section 3.4.5).

3.4.3. The Effect of Surface Temperature

The measured ice nucleation times were plotted (Figure 3-5) to investigate the relationship between the ice nucleation time and surface temperature. According to average values of ice nucleation time (Figure 3-6), as surface temperature decreased from −10 to −20 °C, the shortest ice nucleation time dropped from 248.69 to 80.38 s for a 10 μL water droplet (observed on Sample 1) and the longest nucleation time dropped from 827.63 to 345.60 s (observed on Sample 4). Classical nucleation theory best explains this tendency of shorter ice nucleation times at lower temperatures. This theory posits that the critical energy barrier of nucleation is inversely proportional with the square of supercooling ($\Delta {T_m}^2$) and therefore decreases with an increase in the degree of supercooling (decrease in governing temperature, T) (Equation 3-1) [151].

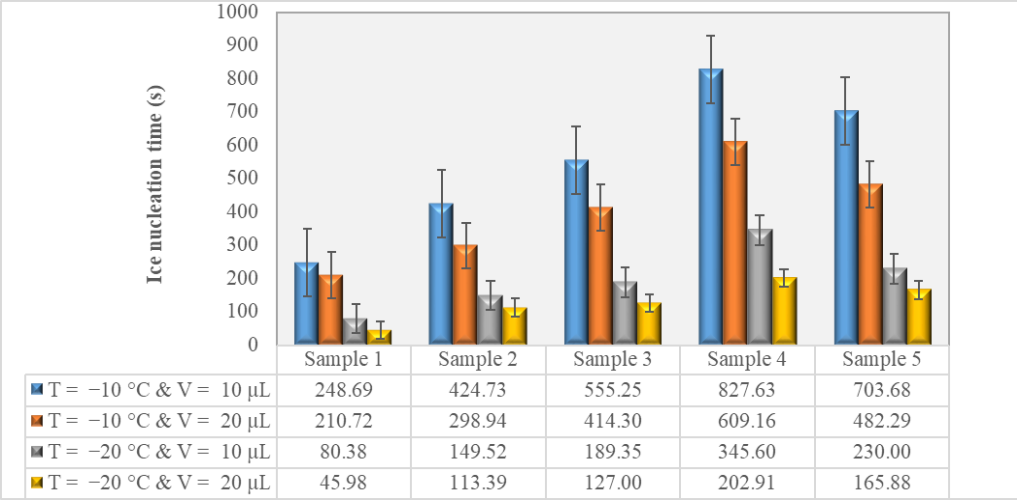

	Sample 1	Sample 2	Sample 3	Sample 4	Sample 5
T = −10 °C & V = 10 µL	248.69	424.73	555.25	827.63	703.68
T = −10 °C & V = 20 µL	210.72	298.94	414.30	609.16	482.29
T = −20 °C & V = 10 µL	80.38	149.52	189.35	345.60	230.00
T = −20 °C & V = 20 µL	45.98	113.39	127.00	202.91	165.88

Figure 3-6: Comparison of ice nucleation times of 10 µL and 20 µL water droplets on the various silicone rubber surfaces at −10 °C and −20 °C.

3.4.4. The Effect of Droplet Size

The icing on surfaces characterized by different surface structures (from hydrophobic to superhydrophobic) was then tested, focusing on the effect of droplet volume at two temperatures. As droplet volume increased, ice nucleation time markedly decreased (Figure 3-6). According to classical nucleation theory, ice nucleation is dominated by the most active nucleation site above the critical radius. The probability of nucleation appears less likely for smaller drops because of their smaller volume [20]. Zhang et al. [252] experimentally and statistically analyzed the effect of droplet size and nucleation time on the nucleation temperatures of water droplets (1, 5, and 10 µL) placed on a cold horizontal aluminum plate. They observed that nucleation temperature decreased (and the standard deviation increased) as droplet volume decreased. Moreover, larger droplets had a higher nucleation rate with lower nucleation temperatures. Smaller droplets have a lower nucleation temperature because there are fewer critical nuclei inside the droplet and at the solid–liquid or gas–liquid interface than within a larger droplet.

Furthermore, the possibility of freezing can be estimated using the nucleation rate of a single embryo, a rate which is inversely proportional to the delay time of ice nucleation and is based on kinetic theory. The nucleation rate of ice embryos (*J*) can be estimated using the equation of Becker and Doring that estimates the rate of ice nucleation per unit time and surface area in relation to the free energy barrier of nucleation of critical embryo [122,133,139]:

$$J \approx K \exp\left(\frac{-\Delta G^*}{k_B T}\right) \qquad \textit{Equation 3-2}$$

where *J* is the embryo formation rate, *K* is the kinetic constant, k_B is the Boltzmann constant, and ΔG^* is the critical energy barrier according to Equation 3-1 [210].

$$J = 1/(t_{nucleation} A) \qquad \textit{Equation 3-3}$$

where *A* is the contact area which is in relation to the volume *V* via the water contact angle to air [146] :

$$A = \frac{(9\pi V^2)^{\frac{1}{3}} sin^2\theta}{((2+\cos\theta)(-1+\cos\theta)^2)^{\frac{2}{3}}} \qquad \textit{Equation 3-4}$$

This equation indicates that larger droplets produce shorter freezing delay times at a constant nucleation rate, and our results validate this explanation. For example, at −10 °C for Sample 1, the ice nucleation time was 248.69 s for a 10 µL water droplet, whereas ice nucleation occurred at 210.72 s for a 20 µL droplet (Figure 3-6). In contrast, the ice nucleation times at −10 °C for 10 µL and 20 µL water droplets on the rougher surfaces (Samples 2–5) were longer, and ice nucleation times for a 10 µL droplet was always greater than for a 20 µL droplet on the same surface (Figure 3-6). A similar pattern was observed for droplets on the −20 °C surfaces. It should be noted that the magnitude of differences in ice nucleation

times at the different temperatures was much greater for the roughened samples than for Sample 1.

3.4.5. Machine Learning

3.4.5.1. Model Development

The above investigations showed that a longer ice nucleation time on these silicone rubber surfaces can be achieved by decreasing droplet volume and increasing the surface roughness parameters to also obtain a Gaussian height distribution. However, to measure the correlation between these parameters, we tested the performance of machine learning models. Machine learning can construct a nonlinear mapping of ice nucleation time and the operating conditions (e.g., surface wettability, roughness, temperature, and droplet volume), using limited experimental data (200 data points), to then predict ice nucleation times and the corresponding operating conditions.

Machine learning models are often based on supervised learning, where models are trained to predict true labels of a training data set and are then evaluated against a test set. There are several traditional machine learning methods, including linear regression, artificial neural networks (ANN), nearest neighbors, support vector machines, and random forest (RF) models. Models of linear regression are intuitive, easy to understand, and can be performed using linear algebra; this results in clear and concise mathematical formulas. Nonetheless, linear regression may not be applicable to data sets having a high degree of nonlinearity. Overfitting issues in linear regression models are generally not detected or resolved by commercially available software. ANNs, on the other hand, do not produce simple correlation formulas, although they do outperform linear regression models when dealing

with nonlinearity within data sets. Unfortunately, overfitting problems can also occur in ANN models. In addition, ANN performance decreases as the nonlinearity of the model increases.

As a branch of deep learning, deep neural network (DNN) models are powerful tools used primarily in computer vision, voice recognition, pattern recognition, and language processing. As with other neural network approaches, DNN includes three primary components in its core: input layer(s), hidden layer(s), and the output layer(s). ANNs and DNNs differ primarily in their number and type of hidden layers, where each layer's output becomes the input for the next layer [253]. Figure 3-7 shows a DNN having three hidden layers. In each hidden layer, there are several nodes and an activation function. Although different activation functions can be used, one activation function is generally used for all neurons within a layer (see Section 1 of the APPENDIX I, Supplementary material for more technical details). The input layer consists of T (temperature), V (volume), CA, CAH, S_a, S_q, S_z, S_t, and S_{sk}, with ice nucleation time as the output.

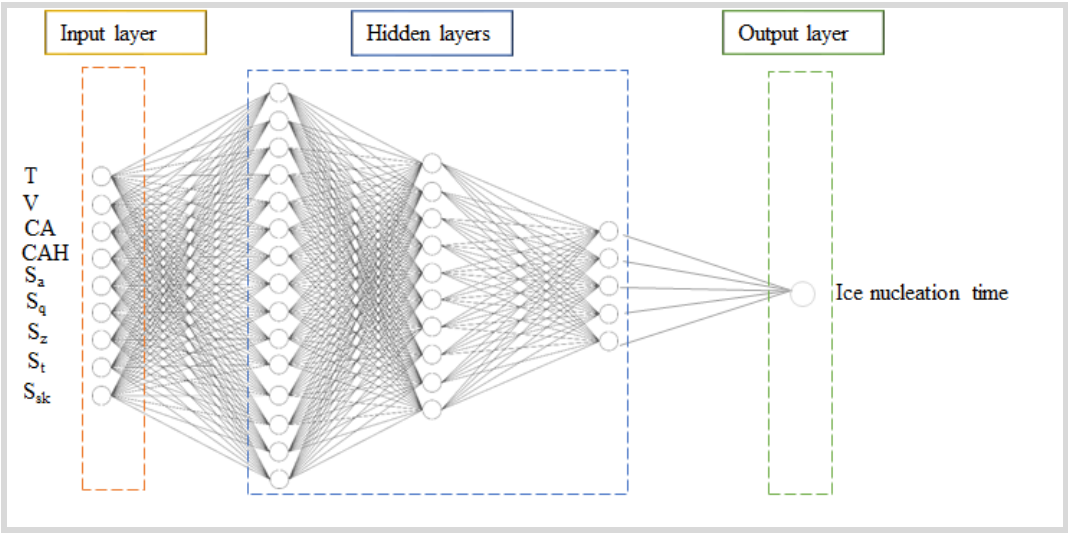

Figure 3-7: An example of a deep neural network (DNN) with three hidden layers; temperature (T = 10 and 20 °C), droplet volume (V = 10 and 20 µL), contact angle (CA), contact angle hysteresis (CAH), the root mean square roughness (S_q), the average surface roughness (S_a), ten-point height (S_z), maximum height of the profile (S_t), skewness (S_{sk}) (Table 3-2 data).

For creating and assessing the DNN models, the online Python code of Asghari et al. [220] was used. The mean squared error (MSE) of the prediction for the output variable was determined using Equation 3-5,

$$MSE = \frac{1}{m}\sum_{i}^{m}(\hat{y}_i - y_i)^2 \qquad \textit{Equation 3-5}$$

MSE must be smaller than the variance of the output variable for a valid prediction model. Making predictions can be difficult when (1) the variance problem occurs, where a model performs slightly better than the base model, and (2) the overfitting problem, which occurs when a model performs well for the training set but poorly for other data sets (e.g., test or cross-validation data sets). When there are sufficient hidden layers and nodes, it is possible to create a model having no errors for a training data set, although the model will perform poorly when applied to any other data set. A successful DNN model commonly has the data set divided into three pieces at a 70:15:15 distribution. The middle set (called the cross-validation set) compares the performance between the various candidate models. In the end, the performance of the chosen optimal model is reported with respect to the final data set (test set). The error and variance error must be small in a properly constructed model.

In this study, the data set was sliced into three parts, with 70:15:15 portions for the training, cross-validation, and test data sets, respectively. The bias error and variance error of a model should be low. There are several hyperparameters that DNN requires to be implemented, such as types of layers, number of layers, number of nodes in each layer, activation functions for each layer, cost function, an optimization algorithm, and a learning rate. Selecting the values for some of these hyperparameters of DNN is not an exact science; they are mainly determined by the modeler's experience. The hyperparameters of DNN used

in this study and their corresponding values are summarized in Table 3-3. A linear activation function is considered for the final layer, as the aim of this study is to predict ice nucleation time as a regression problem. For the first and hidden layers, Tanh and Relu activation functions were utilized, respectively. For the cost functions, the MSE of the predictions was used. The Adam optimizer was also applied for optimization, and optimization stopped when the cost's variation (reduction) fell to less than 1% of the variance of the output variables of the previous 50 steps.

Table 3-3: Hyperparameters of a DNN structure.

Hyperparameters	**Status**
Type of layers	Fully connected layers
Input layer activation function	tanh
Hidden layers activation function	relu
Output layer activation function	linear
Optimizer	Adam
Cost function	MSE (mean squared error)
Minimum delta and patience	0.01 , 50
Epoch	500
Batch size	16
Slicing proportions	70:15:15
Number of hidden layers and nodes	To be decided in the following steps
Weight regularization parameter and type	To be decided in the following steps
Learning rate	0.0001 (the default value of KERAS)

Input variables in data sets vary in order of magnitude and range. As this can lower the efficiency of the optimization, features were scaled to an interval of [0, 1] through Equation 3-6:

$$y(x_i) = \frac{x_i - min_x}{max_x - min_x} \qquad \textit{Equation 3-6}$$

3.4.5.2. Model Results

The training of machine models requires a massive amount of data. However, by carefully designing the network architecture, training can function using small- to medium-sized data sets. High-performance models can be generated by an efficient search of these developed architectures. Moreover, by reducing the number of neurons in the network and pruning connections within the network, this grow-and-prune can boost model performance and reduce computational costs of the inference process [254]. The produced correlation coefficients were strong (Table 3-4) and confirmed the use of DNN to assess and predict ice nucleation time from various roughness parameters and wettability.

In the model development process, no overfitting was observed, as the error of the cross-validation set, and training set were quite similar. Because the model prediction error was less than the output variables' variance, there was no variance problem. Moreover, there was a good correlation between the predicted and actual values of the output variables (Figure 3-8). In addition, the error percentage of prediction did not show any trends (Figure 3-9).

Table 3-4: The developed model performance and the cost functions on training, cross-validation, and test data sets, MSE (Mean of squared error), MAE (Mean of absolute error), and MAPE (Mean of absolute percent error).

	CorrCoef	R^2	MSE	MAE	MAPE
DNN-Ensemble-OnTrain	0.996628	0.993267	375.4751	14.42525	6.887508
DNN-Ensemble-OnCV	0.996795	0.9936	333.9455	13.51721	5.933723
DNN-Ensemble-OnTest	0.995501	0.991022	407.1518	16.49789	8.012416
DNN-Ensemble-OnCVTest	0.994723	0.989474	518.7683	18.77193	8.352949

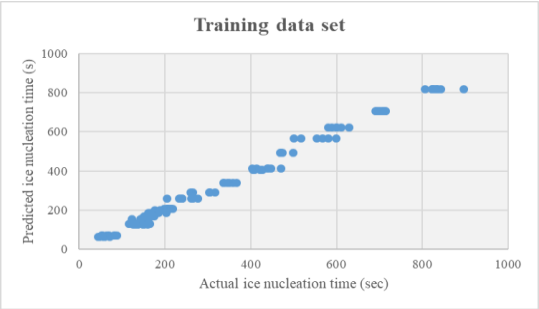

(a)

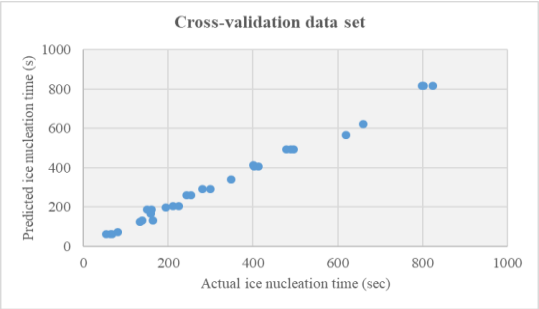

(b)

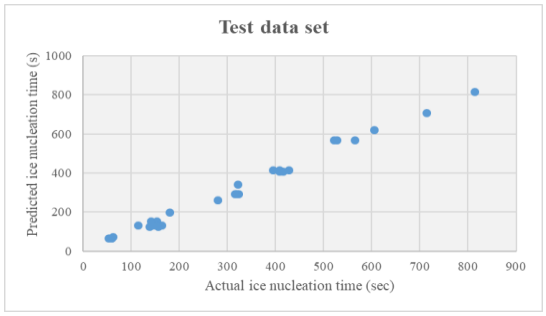

(c)

Figure 3-8: Predicted and actual values of the a) training, b) cross-validation, and c) test data set.

(a)

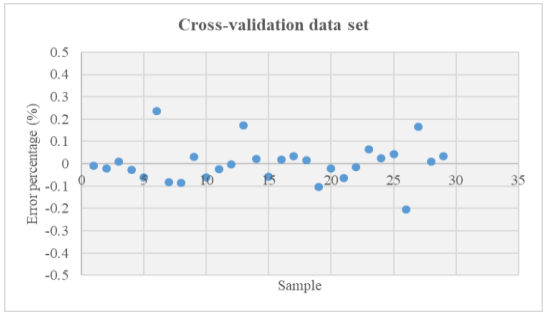

(b)

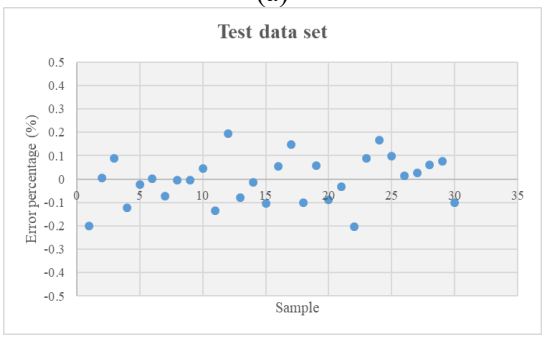

(c)

Figure 3-9: Error of prediction (%) for the (a) training, (b) cross-validation, and c) test data sets.

As presented in Section 3.4.2, changes in surface roughness parameters increase the ice nucleation time. To investigate correlation coefficients between variables, a cross correlation matrix was used (see Section 2 of APPENDIX I, the Supplementary material for more technical details). It remained uncertain from our experimental stage which roughness parameters were most closely correlated with surface hydrophobicity and icephobicity. A machine learning approach can address this issue, however, by analyzing the relative importance of features. Although DNN models have been called black boxes, methods do

exist to better understand machine learning models, including DNN models. Game theory was applied to machine learning models by Lunderberg and Lee [255], who proposed SHapley Additive exPlanations (SHAP). Considering each input variable to be a player and the prediction to be a game, they showed how each input variable played a part in every prediction. Therefore, SHAP values reflect the relative importance of each input variable to a DNN regression model.

When the average absolute SHAP value for all input variables was plotted, we observed that T, S_z, V, S_t, CA, CAH, S_{sk}, S_a, and S_q were the most important parameters affecting ice nucleation time (Figure 3-10). From classical nucleation theory (Equation 3-1, Equation 3-2, and Equation 3-3), the nucleation rate relates to the degree of supercooling, droplet volume, roughness radius of curvature (R), and the CA between the ice nucleus and the surface structure (θ_{iw}). Looking specifically at the inverse relationship of the critical energy barrier of nucleation to the square of supercooling, temperature dependence of droplet properties, and wetting properties, we observed that the effect of temperature on ice nucleation rate dominated, as confirmed by our machine learning approach. In terms of the effect of surface roughness and wetting state on ice nucleation, S_z was predicted as the most important of the various surface roughness parameters, whereas S_a and S_q have generally been the only surface roughness parameters considered to have an effect on ice nucleation [36,115,151]. Our findings are promising, as for the first time, the impact of the physical parameters of a water droplet (e.g., volume), environmental conditions (e.g., temperature), surface wettability (i.e., CA and CAH), and several surface roughness parameters (i.e., S_a, S_q, S_t, S_z, and S_{sk}) on the icephobicity of hydrophobic/superhydrophobic surfaces were compared and illustrated simultaneously.

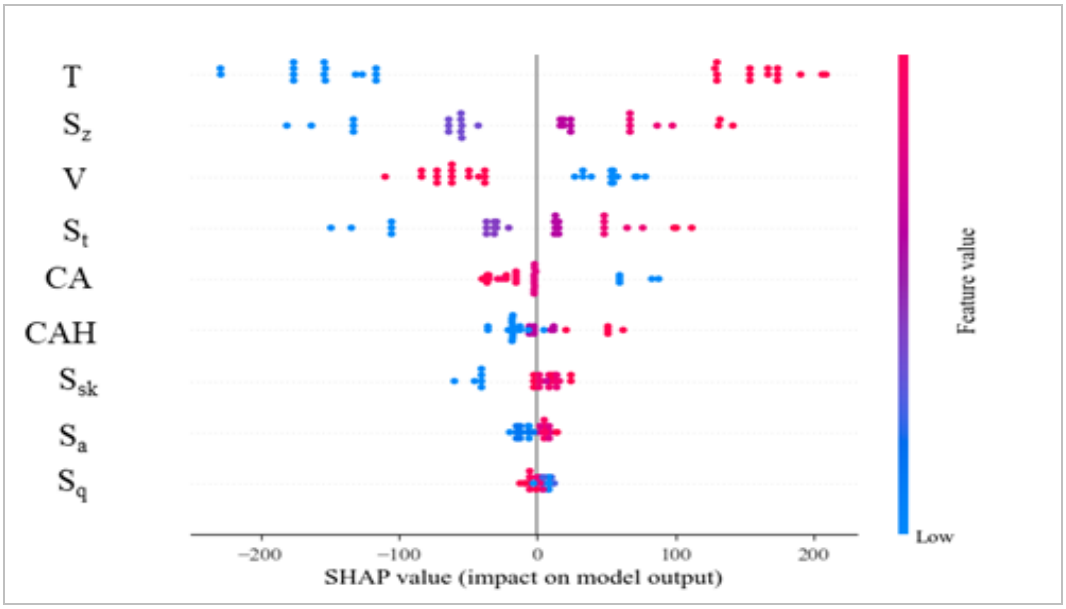

Figure 3-10: Importance analysis of the studied features; temperature (T), droplet volume (V), contact angle (CA), contact angle hysteresis (CAH), the root mean square roughness (S_q), the average surface roughness (S_a), ten-point height (S_z), maximum height of the profile (S_t), and skewness (S_{sk}).

3.5. Conclusion

In this study, we successfully accomplished our two main objectives. First, we determined the ability of hydrophobic/superhydrophobic silicone rubber surfaces to increase the ice nucleation time. Five substrates having various roughness parameters and wettability were fabricated. We detailed the relationships between surface wettability, roughness parameters, surface temperature, water droplet size, and ice nucleation time. As substrate temperature decreased and droplet volume increased, the freezing delay was reduced for all five surfaces. Thus, S_a, S_q, S_z, S_t, and S_{sk} parameters can be used to determine surface texturing, where higher S_a, S_q, S_z, and S_t values and a S_{sk} value close to 0 (i.e., a Gaussian distribution for roughness height) lead to superhydrophobic surfaces having a CAH <10º and longer ice nucleation time.

The second objective was to accurately predict ice nucleation time. A new machine learning–based approach was proposed and used to model ice nucleation time on the prepared hydrophobic/superhydrophobic silicone rubber surfaces. Using a neural network approach, we developed a model to reliably predict ice nucleation time. Moreover, to understand the roughness parameter that best determines surface icephobicity, we investigated the relative importance of a range of features (T, V, CA, CAH, S_a, S_q, S_z, S_t, and S_{sk}). T, S_z, and V were the most important factors determining ice nucleation time. This study demonstrated an increased ice nucleation time on superhydrophobic surfaces and produced a promising machine learning–based approach for predicting ice nucleation time on surfaces.

CRediT authorship contribution statement

S. Keshavarzi: Conceptualization, Investigation, Methodology, Validation, Writing – original draft, Writing - review & editing. **A. Entezari**: Conceptualization, Methodology, Software, Validation, Investigation, Writing - original draft, Writing - review & editing. **K. Maghsoudi**: Conceptualization, Methodology, Software, Validation, Investigation, Writing - original draft, Writing - review & editing. **G. Momen**: Conceptualization, Project administration, Supervision, Resources, Funding acquisition, Writing - review & editing. **R. Jafari**: Conceptualization, Project administration, Supervision, Resources, Funding acquisition, Writing - review & editing.

Acknowledgments

The authors would like to acknowledge the financial support from Natural Sciences and Engineering Research Council of Canada (NSERC). We also thank Carol Mercier at the

Anti-icing Materials International Laboratory (LIMA), UQAC, for helping develop the experimental setup.

CHAPITRE 4

ARTICLE 3: Exploiting intermediate wetting on superhydrophobic surfaces for efficient icing prevention

Samaneh Keshavarzi[1]*, Gelareh Momen[1], Patric Eberle[2], Amir Azimi Yancheshme[3], Nicolas J. Alvarez[3], Reza Jafari[1]

[1]Department of Applied Sciences, University of Québec in Chicoutimi, Chicoutimi, Québec, Canada

[2] Institute of Electrical Engineering, Lucerne University of Applied Sciences and Arts, Lucerne, Switzerland

[3]Chemical and Biological Engineering Department, Drexel University, Philadelphia, USA
Email address: samaneh.keshavarzi1@uqac.ca

This article has been submitted to:

Journal of Colloid and Interface Science

4.1. Abstract

Freezing of supercooled droplets in technological systems can lead to major safety, energy, and economic consequences. Superhydrophobic surfaces with their high water repellency and little droplet solid-to-liquid contact are promising candidates for preventing ice formation. However, droplets on superhydrophobic surfaces commonly not only wet the top asperities (Cassie State), but also partially wet the microstructure, leading to intermediate wetting states. Little research has been conducted into the resulting implications for ice

nucleation retardation on superhydrophobic surfaces. Here, we investigate ice nucleation of supercooled droplets in the intermediate wetting regime using precisely fabricated micropillar structures with varying pillar spacings and heights for modulating the wetting fraction in the microstructure. We find at −10/−20 °C that at a critical pillar spacing, a maximum in ice nucleation delays is observed, with the microstructure partially wetted. The effective contact area solid-to-liquid of the droplet along the partially wetted microstructure reaches a minimum at the critical pillar spacing, consistent with nucleation theory. Our results show that with increasing supercooling from −10 to −20 °C, the wetting fraction in the microstructure increases due to lower de-wetting capillary forces. Higher micropillar heights were found to increase ice nucleation delays, as wetting fraction in the microstructure was reduced. Our results and framework demonstrate the role of microstructure geometry and provide rational guidance for the design of ice resistant superhydrophobic surfaces in the widely occurring intermediate wetting regime.

Keywords: Heterogeneous nucleation, Nucleation rate, Ice nucleation time, Surface topography, Surface wettability, Partial wetting

4.2. Introduction

In a variety of technological systems critical for society, such as aerospace, outdoor infrastructure, transportation, power, refrigeration and energy systems icing can lead to lower efficiency, lower safety and economic damage [1–3]. Therefore, effective measures must be taken to remove ice or prevent its formation. Such measures can be classified into two categories: active or passive de/anti icing methods. The potential environmentally harmful and energy-intensive drawbacks of the active de-icing methods lead to pay more attention to

passive approaches that exploit thermodynamic micro-/nano effects of surface morphology, (bio)chemical surface properties and light harvesting. Passive approaches focus on high surface water repellency for easy droplet shedding and ice removal, and preventing and delaying ice formation to avert the serious consequences of icing on safety, environment and economy [14–16,49,141,256–259].

To prevent ice formation (anti-icing) or facilitate ice removal (de-icing), hydrophobic and superhydrophobic surfaces have been extensively studied due to their low water adhesion properties and expected benefits from reduced droplet contact area in ice nucleation retardation [9,105,175,260,261]. In addition to the water repellency, their low heat-transfer rate can be advantageous, rendering them overall promising candidates for designing anti-icing or icephobic surfaces. To understand the icing of these surfaces and to design such surfaces passively icephobic by the properties of the surface, clear relations between icing behaviour and surface properties are needed taking into account the intertwined dependencies on environmental conditions [9,26,32,37,146,147,262–264]. Superhydrophobic surfaces are characterized by a high water-air contact angle (CA) of greater than 150° and a low contact angle hysteresis (CAH less than 10°). Such surfaces exhibit a micro/ nano roughness and a surface chemistry with hydrophobic (> 90°) intrinsic contact angle, which is the contact angle of a flat surface of the same chemistry. The two fundamental wetting regimes are: (1) the Cassie-Baxter state (CB) [44], where the droplet is suspended on the top asperities of the microstructure and air cushions in the microstructure, and (2) the Wenzel state [43], where the droplet penetrates into the microstructure and completely wets the structure. However, wetting of superhydrophobic surfaces is commonly in an intermediate state between CB and

Wenzel with a varying degree of partial wetting (PW) within the micro/nanostructure of the surface [45,46,265].

Surface roughness, - morphology and surface chemistry are factors that influence surface wettability and wetting states. Environmental conditions and icing under specific atmospheric conditions can change the wetting of the droplet on the surface [266–269]. While the effect of various surface morphologies on ice nucleation have been studied (as shown in Table 4-1), a fundamental understanding of partial wetting in the microstructures at temperatures below the freezing point and the effects on ice nucleation are missing. Particularly for surfaces engineered for a low solid-to-liquid contact area aimed at wetting in CB state for high water repellency, partial wetting may commonly occur in the microstructure, counteracting the expected benefits in icing [162]. To this end, we study the wetting fraction in the micropillar structures at different micropillar spacings at −10 °C and −20 °C experimental temperature and explore the crucial effect of the wetting fraction on the retardation of ice formation. We show that the degree of partial wetting in geometrically ordered micro pillar structures depends not only on pillar parameters but also changes with temperature. We show with experiments, supported and consistent with theoretical predictions, the effect of intermediate wetting on the delay of ice nucleation and how micropillar structures should be designed to maximize nucleation retardation.

Table 4-1: Effect of surface geometrical parameters on ice nucleation time (D: Pillar diameter/ length, H: Height, S: Space).

Ref.	Surface type	Chemical agent	Geometrical parameters	Temperature (°C)	Water droplet volume (µL)	Relative humidity (%)	Maximum nucleation time (sec)
[270]	Titanium alloy	Hexane solution of trichloro (1H,1H,2H,2H-perfluorooctyl)silane	Pits S = 50 µm H = 22.3 µm	−10	5	45	1049.8
			Pits S = 50 µm H = 22.3 µm	−20	5	45	4.5
			Grooves S = 50 µm H = 28.7 µm	−10	5	45	995.7
			Grooves S = 50 µm H = 28.7 µm	−20	5	45	3.5
[271]	5052 Aluminum alloy	-	Micro-grating P = 40 µm H = 43 µm	−23	50	-	4212
[272]	7075 Aluminum alloy	Copper chloride solution	Micro cylindrical D = 50 µm S = 50 µm	−13	50	53	494
[273]	T2 Copper	-	Closed-pore structure P = 100 µm H = 20-30 µm	−10	3	45	3459
				−15	3	45	1615
[148]	Quartz glass	Polystyrene (PS) beads	Truncated cone shape D = 30 nm, H = 300 nm, S = 150 nm	−20	5	<5	49.2
[14]	Silicon wafer	Heptadecafluoro-1,1,2,2-tetradecyl (FAS-17)	Micro-cubic array D = 20 µm, H = 20 µm, S = 30-130 µm	−15	4	<5	1285

4.3. Material and Methods

4.3.1. Sample preparation

A SU-8 layer on a silicon wafer surface was photolithographically structured and then chemically modified to produce patterned hydrophobic and superhydrophobic surfaces with different geometric features. The target product is an array of cylindrical posts formed in SU-8, each post being 10 μm in diameter (D) and 10 and 20 μm in height (H). We fabricated 14 different samples, each 15 x 15 mm, with the space (S) between posts being 5, 10, 20, 30, 40, 70, or 100 μm, in various combinations.

In brief for the fabrication process, a 100 mm diameter silicon wafer (500 μm thick, single-side polished <100> crystal orientation, n-type, P-doped) was solvent cleaned, plasma cleaned, and dehydrated. SU-8 2010 and 2025 were spin coated on the wafer, which was patterned using 365 nm light with an Intelligent MicroPatterning SF-100 Xpress maskless photolithography system using an exposure time established experimentally. After developing, the resist was hard baked at 150°C. The designs were manually cleaved into 22 x 19 mm dies with the pattern having borders of 2 mm on three sides and 5 mm on one side. To chemically modify the cylindrical posts on the silicon substrate and change their hydrophobicity, TPFS (Trichloro (1H, 1H, 2H, 2H-perfluorooctyl) silane 97%) was utilized as a modification agent.

4.3.2. Surface characterization

A KrussTM DSA100 goniometer was used to measure the CA of sessile droplets of deionized water on the produced surface. In this study, scanning electron microscopy (SEM) was used to characterize the morphologies of photolithography-processed surfaces (SEM,

JSM-6480 LV by JEOL Japan). Moreover, an optical profiler (Profil3D, Filmetrics, USA) was used to capture the 3D profiles of the surface structures. At temperature (T) of 22 ℃, −10 ℃, and −20 ℃ and relative humidity of 30 ± 5 %, measurements were conducted. For each surface, we measured the CAs five times to obtain the average CA.

4.3.3. Experimental Setup

Figure 4-1shows a schematic of the experimental setup used for the freezing experiments. A thermally insulated and optically transparent chamber, a high-speed camera, a thermostatic bath, a cold base, a system for injecting droplets, test samples, a data acquisition system, temperature and humidity sensors, and a vibration-free table were used in the experimental freezing setup. This thermally insulated and optically transparent double layer chamber ensured stable and uniform temperature and humidity conditions in the chamber, minimizing the effects of atmospheric variations on wetting and ice nucleation. Its transparency enables imaging of the freezing droplet. Small interior chambers (150 mm long by 150 mm wide by 110 mm high) within a large exterior chamber (420 mm long by 420 mm wide by 400 mm high) provides a uniform environment for the droplet. The thermostatic bath was used to adjust the temperature of the cold base. In the chamber, temperature and humidity sensors were used to monitor these parameters. The experiment was visually recorded using a high-speed camera (MotionBLITZ, MIKROTRON, EoSens Cube 7, Germany) and LED illuminator.

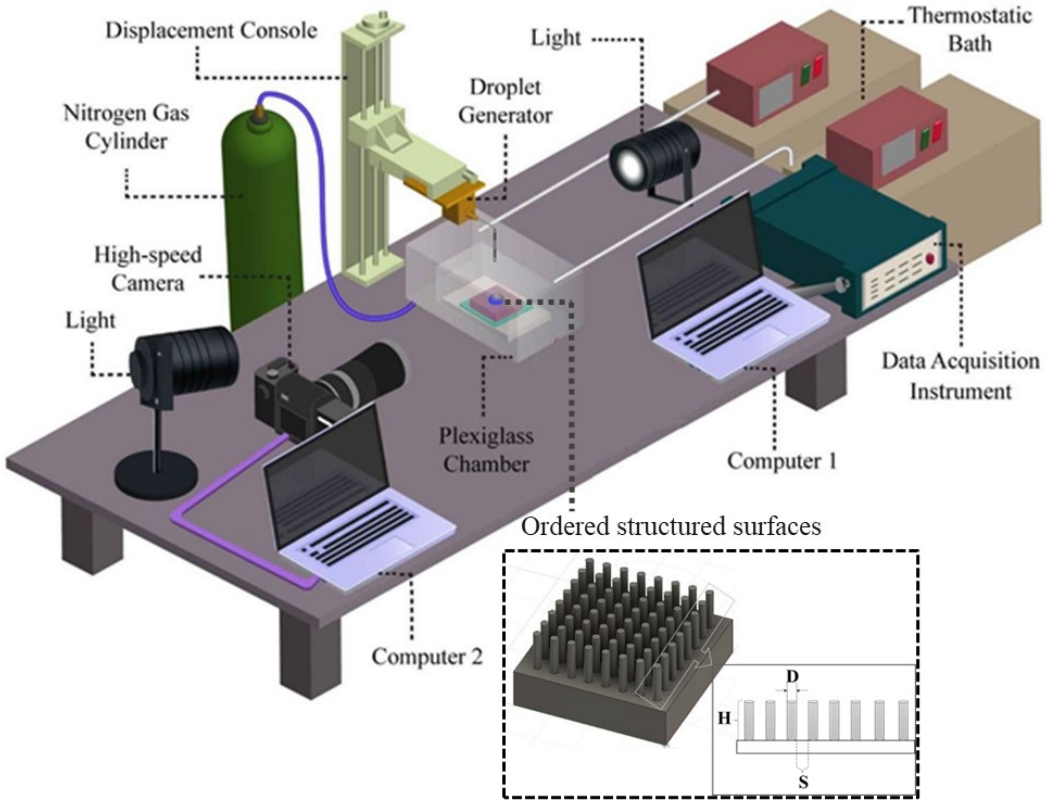

Figure 4-1: Schematic of the experimental setup. A sessile water droplet is placed using a droplet generator on the surface investigated in a double-insulated chamber. Freezing process is monitored using a high-speed camera. The experimental temperature in the chamber is stabilized using a thermostatic bath.

Freezing of sessile water droplets on the micropillar surfaces was studied at the temperatures −10 °C and −20 °C. To ensure that the temperature of the surface resting on a cooling plate was stable, a thermocouple (K-type) and an IR camera were used to measure the surface temperature before the experiments. A room temperature 10 µL droplet was gently placed on the cold surface using the droplet injection system, and the freezing process was captured using a high-speed camera. Throughout the experiments, the ice front was initially formed at the solid-to-liquid interface with subsequent propagation to the top of the droplet, suggesting heterogeneous nucleation at the solid-to-liquid interface (see images in APPENDIX II, Supporting Information, Figure A-II. 1 and Figure A-II. 2). Based on almost 10 droplet freezing processes per micropillar surface, the average ice nucleation delay time

was determined. Delay times were measured experimentally by the time elapsed between when the water droplet with a volume of 10 μL is placed onto the surface at −10°C or −20°C and when the ice nucleation happens, as shown in APPENDIX II, Figure A-II. 1 and Figure A-II. 2. The cooling times of water droplets from 22 °C to −10 °C and −20 °C were determined using numerical simulation as described in the next section, primarily because our thermal camera is not suitable for measuring water droplet temperature profiles, and supercooled water droplets were not utilized in our experiments. We included this contribution to the observed ice nucleation delay by subtracting the cooling time from the measured delay time, even though other studies for ice nucleation delay times normally do not take into account the water-cooling period, since it may be short. Ice nucleation probability strongly increases with decreasing temperature and, therefore, we considered the cooling time in the determination of the ice nucleation delay time [141,274].

4.3.4. Modeling and Numerical Simulation for cooling time measurements

To determine the cooling time of the droplets in our experiments, we utilized a numerical approach to simulate the cooling of water droplets deposited on micro-structured surfaces. As the droplets were gently deposited on the surfaces, we ignored the fluid flow movement and just considered the conduction heat transfer in fluid and solid substrate (Equation 4-1).

A transient 3D Finite element method was used to simulate the temperature distribution inside the droplet, substrates and its micropillars with the aid of commercial COMSOL v.5.6 solving the following heat conduction equation:

$$\rho_i C_{p,i} \frac{\partial T_i}{\partial t} + \nabla.(-k_i \nabla T_i) = 0 \qquad \textit{Equation 4-1}$$

where ρ, C_p, and k are density, specific heat, and thermal conductivity of domain, respectively. Subscript i represent the droplet phase, solid substrate, and the surrounding air.

Figure 4-2 a shows the computational domain. Owing to the symmetries, we could reduce the computational domain to one quarter of the simulated situation droplet with substrate. Note the effect of surrounding air in between the droplet and substrate was also taken into account in our computations.

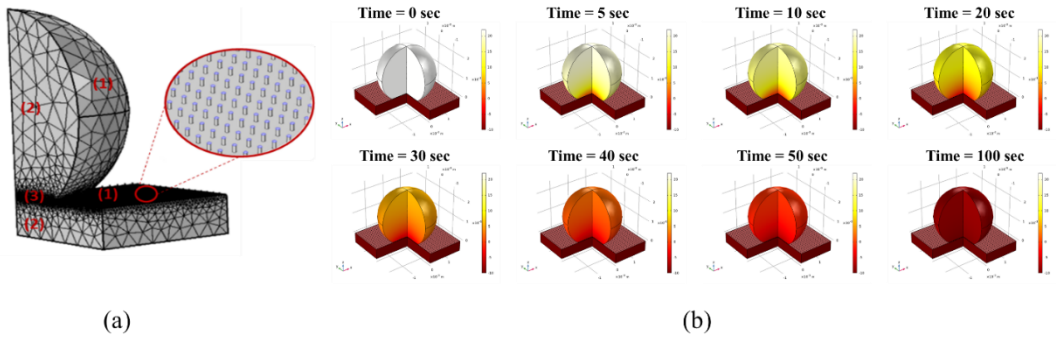

(a) (b)

Figure 4-2: (a) Computational domain, grids and surface boundaries used to simulate the cooling process of water droplet deposited on micro-structured surfaces. (b) Temperature distribution profiles at different time instances for a micro-structured surface with S=100 μm, H=20 μm, at bottom temperature of −20 ℃.

The temperature at the bottom of the substrate was fixed in the simulation by setting boundary condition to −10 °C or −20 °C. At both fluid and substrate free surfaces, denoted by (1) in Figure 4-2 a, convection (heat flux) with heat transfer coefficient (h) of 0.1 was considered, $q = h(T_{amb} - T)$. At symmetrical faces (2), the gradient of T is zero, i.e. $n.q = 0$, and at fluid-substrate interface, temperature continuity was considered ($T_i = T_j$). This boundary condition accounts directly for heat loss from the solid through conduction.

Cooling-induced temporal changes in the temperature distribution inside the droplet (Figure 4-2 b) were simulated for the different substrates investigated (pillar height and spacing) at two experimental temperatures (−10/−20 °C). From this, the approximate cooling time in each configuration was determined, with the cooling time relevant for nucleation at the substrate-droplet interface. It should be noted that the different contact angles of the droplet at the different conditions were considered in the model.

4.4. Results and discussion

4.4.1. Surface morphology

Scanning Electron Microscopy (SEM) and optical microscopy images of the obtained surface morphologies, as shown in Figure 4-3, show evenly distributed micropillars with only minor defects. Figure 4-3 also shows the three-dimensional (3D) optical microscope images of the structures. Figure 4-4 shows measured height profiles and nanoscale roughness of the pristine silicon wafer with a measured root-mean-square surface roughness of 2.62 nm obtained from 3D microscopy.

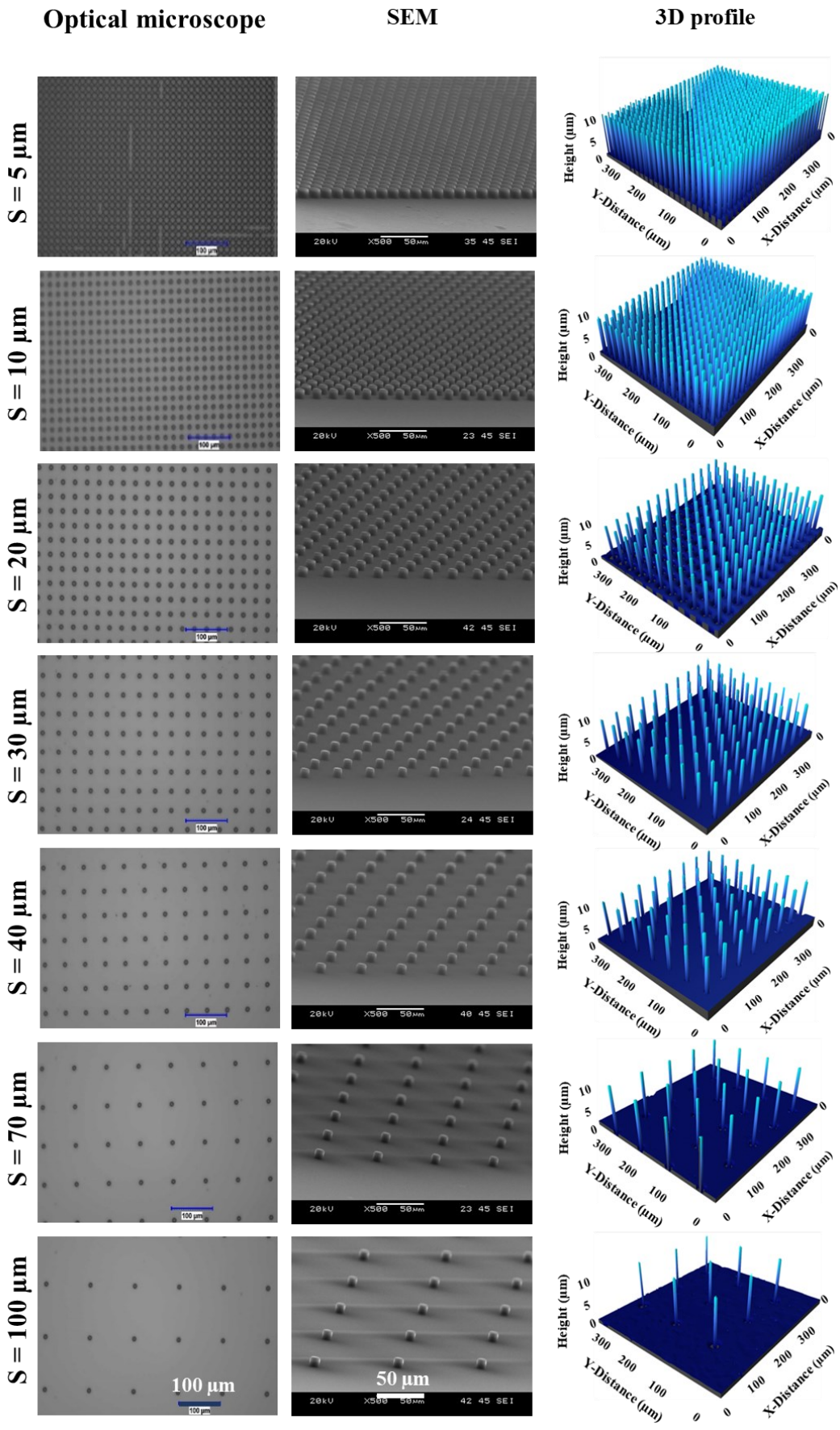
Optical microscope
SEM
3D profile
S = 5 µm
S = 10 µm
S = 20 µm
S = 30 µm
S = 40 µm
S = 70 µm
S = 100 µm
100 µm
50 µm
Height (µm)
Y-Distance (µm)
X-Distance (µm)

Figure 4-3: Optical microscope, SEM, and 3D profile images of the SU-8 micropillars on Si surface with different spacings S and H = 10 µm.

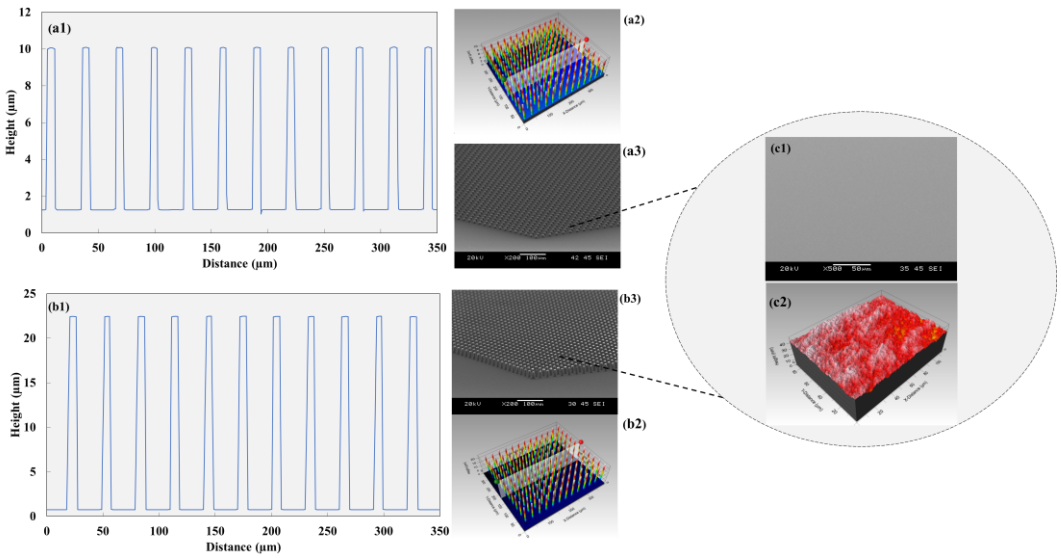

Figure 4-4: (a1) Surface height map, (a2) 3D profile, (a3) SEM image of the patterned surface with D = 10 µm, H = 10 µm, S = 20 µm, (b1) Surface height map, (b2) 3D profile, (b3) SEM image of the patterned surface with D = 10 µm, H = 20 µm, S = 20 µm, (c1) SEM image, and (c2) 3D profile of the pristine silicon surface.

4.4.2. Surface wettability

For the fabricated micropillar surfaces, we observed hydrophobicity and superhydrophobicity, and the measured CAs were between the predictions of the Wenzel and CB states as shown by Figure 4-5 a and b (see also APPENDIX II, Supporting Information, Section 2). This suggests intermediate wetting state with partial wetting in the micropillar structures [45].

When pillar-to-pillar spacing distance *S* is increased from 5 to 20 µm, the CA at first increases gradually from 141° to 152.7° and then falls to 118.3° when the pillar-pillar spacing distance reaches 100 µm for H = 10 µm, as shown in Figure 4-5. For H = 20 µm, a similar trend is observed, the CA increases significantly from 143.8° to 160.2° for S 5 to 20 µm and then decreases sharply to 116.6° when S reaches 100 µm. Since all samples in this study had

the same intrinsic chemical properties, macroscopic wettability is mainly a function of geometrical properties of the surface microstructures, namely the pillar-to-pillar spacing distances, diameter, and height of micro-cylindrical pillar array structures.

To investigate the effect of temperature on the CA of the droplet, measurements were taken at both –10 ℃ and –20 ℃. The results showed (1) that the CA decreases with lowering the temperature and (2) that at both temperatures the contact angle shows the same trend with varying the pillar-to-pillar spacing as at room temperature. For example, the measured contact angle with H = 10 μm and S = 20 μm has decreased from 152.7° at room temperature to 129.1° and 124.9° at –10 ℃ and –20 ℃, respectively. Or, for surfaces with H = 20 μm and S = 20 μm, the contact angle decreased from 143° at –10 ℃ to 139.4° at –20 ℃. Or. For both surfaces series and temperatures (–10/–20 °C) a maximum in CA was observed at S = 20 μm.

Using the theory for intermediate wetting [45,46], the contact angle can be described by:

$$\cos\theta_{PW} = (\Phi + (r_w - \Phi)f)\cos\theta_Y + (1-\Phi)(1-f)\cos 180° \qquad \textit{Equation 4-2}$$

Therefore, the wetting ratio (f) becomes

$$f = \frac{\cos\theta_{PW} + 1 - \Phi(\cos\theta_i + 1)}{(r_W - \Phi)\cos\theta_i + (1-\Phi)} \qquad \textit{Equation 4-3}$$

where θ_i, r_W, Φ are the CA of the flat surface, the area ratio of micropillar structure to flat surface, and the area ratio of top-surface of micropillars to flat surface, respectively. The wetting fraction f is the area ratio of the wetted area in the micropillars to the total droplet contact area, both areas are projected onto the flat surface to form the ratio.

Figure 4-5 c and 5d show the determined wetting fractions using Equation 4-3 for the substrates investigated at room temperature and at the two experimental temperatures. The trend shows that the wetting fraction increases with increasing *S* for all temperatures. In other words, the droplet increasingly wets the space between the micropillars with increasing *S*. This can be explained, on the one hand, by the deeper penetration of the droplet meniscus into the space between the micropillars with increasing *S* and, on the other hand, by the reduction of the de-wetting Laplacian pressure induced by the droplet meniscus between the micro pillars. Due to the nearly vertical sidewalls of the micropillars (see Figure 4-3) and the hydrophobic CA at the sidewalls, which can be approximated by the intrinsic CA, the Laplacian pressure is de-wetting and counteracts the gravitational force of the droplet. Intrinsic CA was determined from smooth substrates with same surface chemistry as 110.6° at T = 22 °C, 95.9° at T = –10 °C and 93.3° at T = –20 °C.

Interestingly, our results show a clear increase in the wetting fraction *f* for S = 5 µm to 100 µm when the temperature is lowered, and the droplet is supercooled. This is particularly evident for samples with the lower pillar height of 10 µm. The temperature effect of *f* can be attributed to the temperature dependence of the intrinsic CA, which decreases with decreasing temperatures. As a result, the Laplacian pressure (de-wetting) decreases and the meniscus of the droplet wets more in the micropillar structure, thus increasing wetting fraction *f*.

For clarity, we also show in Figure 4-6 the effective solid-to-liquid contact area *A* of the droplet, which attains a minimum at *S* = 20 µm. *A* in partial wetting can be estimated using *f* as [265]

$$A = A'\left(\Phi + f(r_W - \Phi)\right) \qquad \textit{Equation 4-4}$$

where A' is the area under the droplet projected on the flat surface. A' can be determined from the droplet volume (V) and the CA using Equation 4-5 [146]:

$$A' = \frac{(9\pi V^2)^{1/3} sin^2\theta}{((2+\cos\theta)(\cos\theta - 1)^2)^{2/3}} \qquad \textit{Equation 4-5}$$

If the droplet were in CB state, a continuous decrease in A would be expected with increasing spacing S (decreasing Φ). In the present partial wetting, the effect of Φ-decrease in A is effectively counteracted with the increase in wetting fraction f for $S > 20$ µm. This leads to A decreasing up to $S = 20$ µm and then increasing with increasing S, explaining the observed behavior in CA with variation of S.

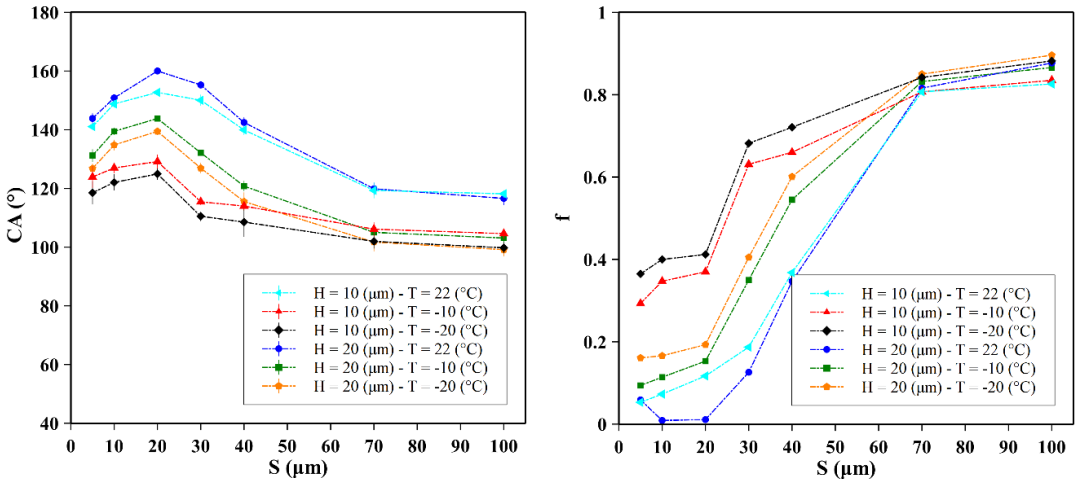

(a) (b)

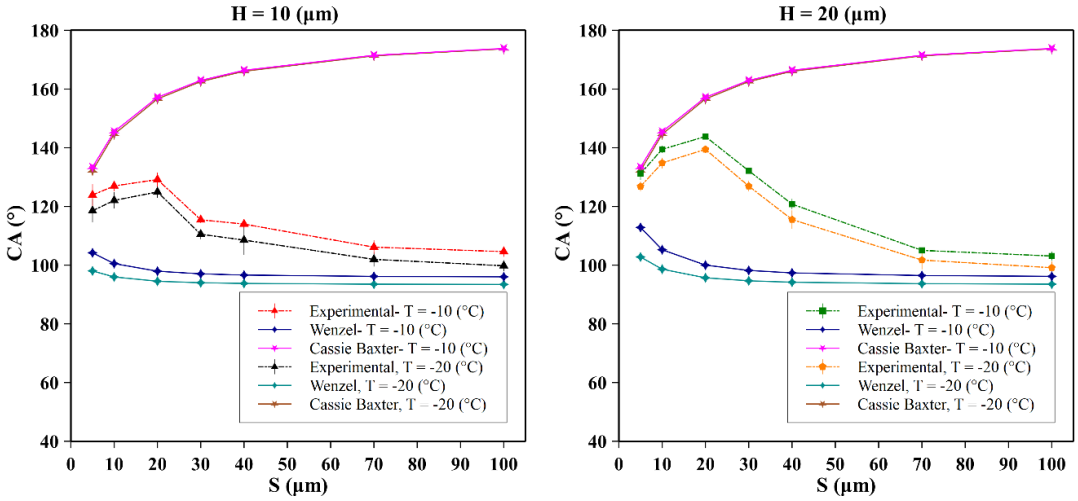

Figure 4-5: (a) Measured water-air contact angles (CA) of sessile droplets and (b) wetting fractions f of the micropillar surfaces at room and supercooled temperatures (−10/−20 °C). (c) and (d) show measured CAs in relation to predictions of Cassie-Baxter and Wenzel model for H = 10 µm and H = 20 µm, respectively.

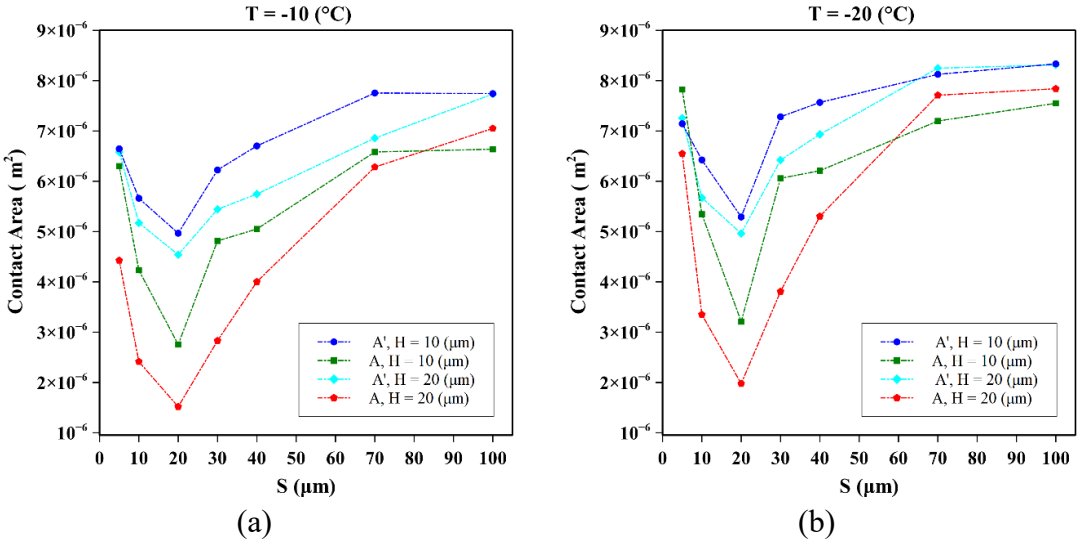

Figure 4-6: Effective solid-to-liquid droplet contact area A and A′ area under the droplet projected on a flat surface for H = 10 µm and H = 20 µm at supercooled temperatures (a) −10 and (b) −20 °C.

4.4.3. Ice nucleation delay time

For the ice nucleation delay study, we carefully deposited at room temperature a droplet of 10 µl using the droplet injection system on the cold surface, which was in the cooled chamber at −10/−20 °C experimental temperature. The nucleation delay and the

freezing process were measured with (high speed) camera recordings. Nucleation delays were determined from the time of droplet deposition until the freezing process started with the recalescence stage of the solidification. Since ice nucleation delay is strongly temperature dependent, we used FEM simulations to determine the time required for the droplet to cool from room temperature to the experimental study temperature.

Temperature distribution profiles at different time instances were obtained for the micro-structured surfaces at bottom temperatures of −10 ℃ and −20 ℃, which are shown in Figure A-II. 3-7 (APPENDIX II, Supporting Information, Section 3) at different points in the water droplet, including the bottom, middle, and top points using FEM simulations. It should be mentioned that due to the lengthy computational time required for the simulation of surfaces with pillar spaces of 5 μm, we were unable to include it in our study. Considering the exponential dependence of the cooling process on temperature, a threshold of +0.5 °C above the temperature (−10/−20 °C) was applied to measure the cooling times. For all micropillar surfaces cooling times at both experimental temperatures −10°C and −20° are shown in Figure 4-7.

Our findings indicate that the time it takes for the droplets to cool down accounts for less than 10% of the total time it takes for them to freeze. Only at a pillar spacing distance (S) of 100 μm and a substrate temperature (T) of −20 °C the cooling time is about 20 % of the total freezing time. We accounted for the cooling phase in our experiments by subtracting the cooling time at the bottom of the droplet from the experimentally measured ice nucleation delay time to obtain the corrected ice nucleation delay time.

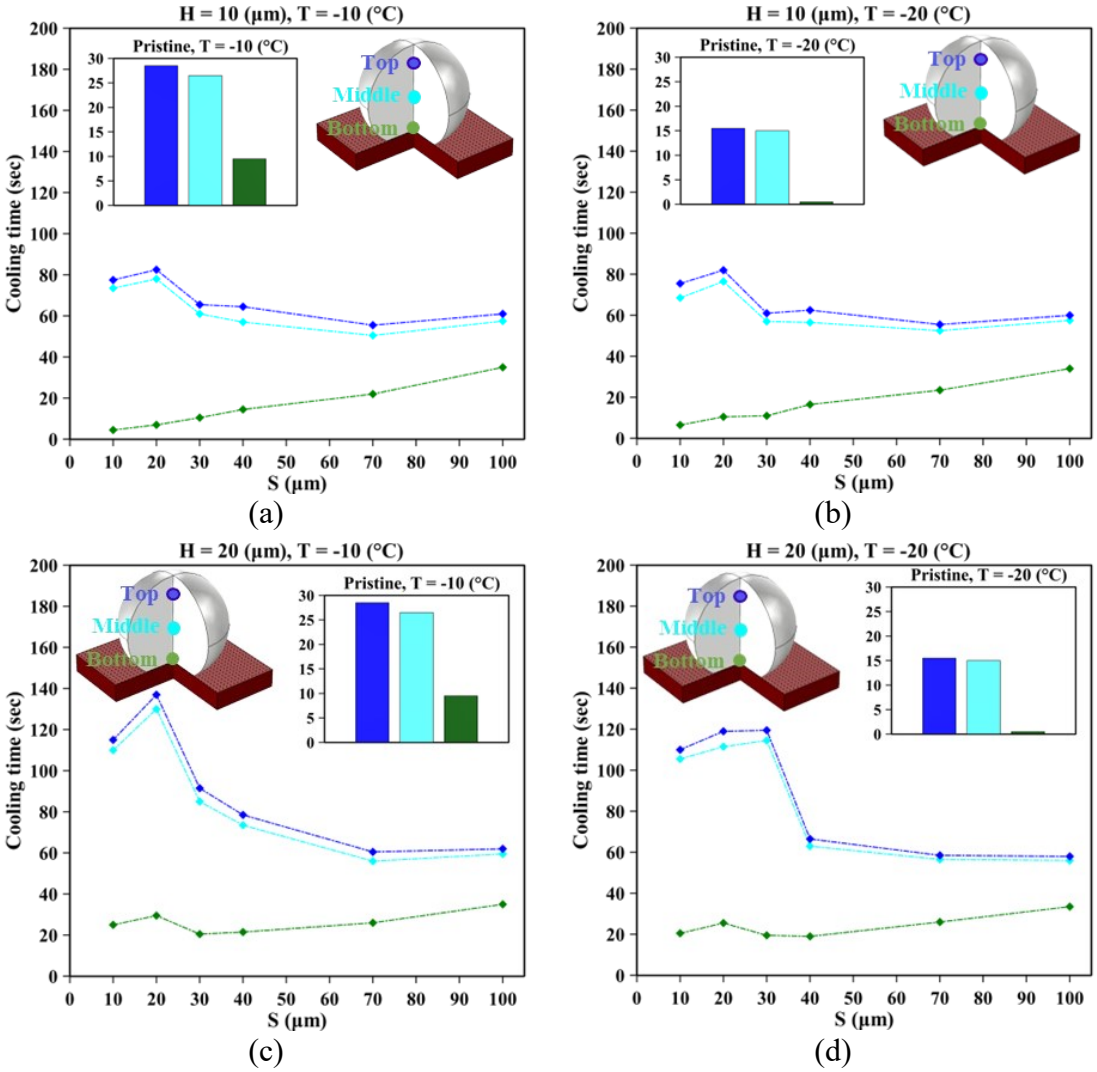

Figure 4-7: Cooling time of room temperature water droplet (a) H = 10 μm & T = −10 °C, (b) H = 10 μm & T = −20 °C, (c) H = 20 μm & T = −10 °C, (d) H = 20 μm & T = −20 °C.

Figure 4-8 shows the obtained ice nucleation delay times of supercooled 10 µL sessile droplets on the micropillar substrates in relation to micropillar spacings for H = 10/20 µm studied at the experimental temperatures of T = –10 and T = –20 °C. Figure 4-8 shows also the predictions using classical nucleation theory (CNT).

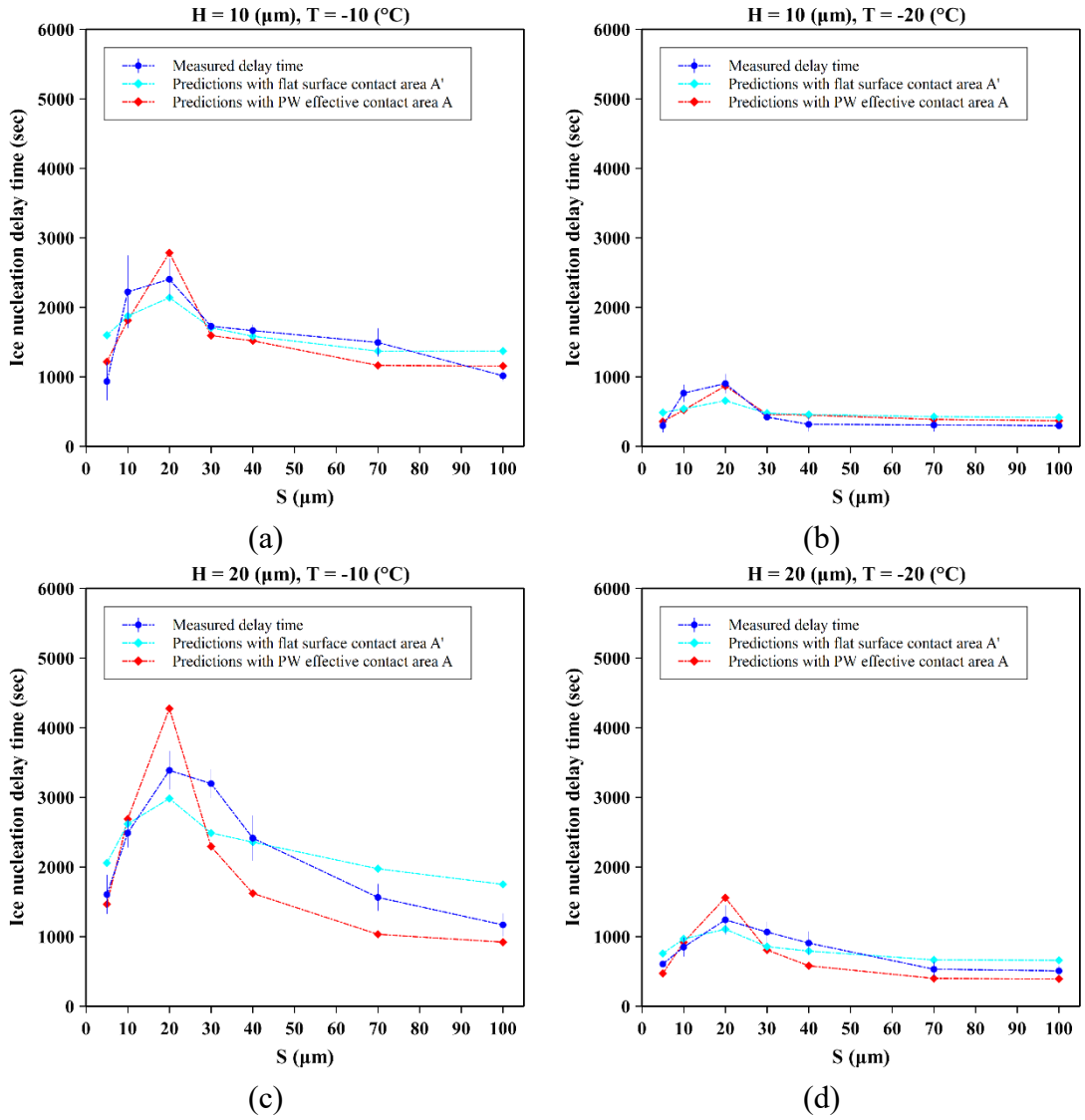

Figure 4-8: Experimental and theoretical ice nucleation delay time on the silicon wafer surfaces with H = 10 μm at (a) −10 °C and (b) −20 °C, and H = 20 μm at (c) −10 °C and (d) −20 °C.

Ice nucleation delays in Figure 4-8 show a similar trend with increasing micropillar spacing S as the CAs shown in Figure 4-5. For both micropillar heights and both experimental temperatures delay times increase up to $S = 20$ μm, where the maximum delay was measured, and for larger S the delay times decrease. Using the CNT, this can be attributed to the variation of the solid-to-liquid contact area A with the pillar spacing S (see also variation of A with S in Figure 4-6). The maximum delay in ice nucleation is obtained at the minimum

solid-to-liquid contact area A of the droplet. At the critical distance S_c, A is minimal and can be obtained by solving $dA/dS = 0$. When analyzing the effect of pillar height, it was found that icing delays are in general larger for samples with H = 20 μm than for those with H = 10 μm. For example, at a surface temperature of −20 °C, the averaged nucleation delay time on H = 20 μm samples is almost 606, 847, 1241, 1066, 907, 181, and 124 s longer than that on H = 10 μm where the nucleation delay time is 297, 766, 904, 420, 316, 113, and 76 s (Figure 4-8). Surfaces featuring higher pillar structures reduce the likelihood of penetration of the droplet into the pillars and wetting the microstructure, indicated by a smaller f and A values and larger CA, and thus exhibit a larger liquid-air interface. Consequently, such surfaces experience longer ice nucleation delay times.

Hou et al. [14] found a similar trend in the ice nucleation delay times for microcubic pillar surfaces with variation of the pillar-to-pillar spacing. Ice nucleation delay times increased up to a threshold in spacing and then decreased for larger spacing. However, in departure to Hou et al. [14] and other studies on ice nucleation on superhydrophobic surfaces [148,150,261], we studied the wetting fraction in the microstructure of the micropillar surfaces at supercooled temperatures and, thus, were able to establish the physical relation to the obtained ice nucleation delays using CNT.

In the present study, ice formation was observed to be initiated by heterogeneous nucleation at the solid-to-liquid interface. To initiate the freezing process, an ice nucleus of critical size must be formed, which involves overcoming an energy barrier associated with a thermodynamic probability. For heterogeneous nucleation, it can be estimated using [122]

$$J(T) = K(T)A \exp\left(\frac{-\Delta G^*_{Hetero}(T)}{K_B T}\right) \qquad \textit{Equation 4-6}$$

where $K(T)$, A, $\Delta G(T)$, k_B, T respectively represent a kinetic constant considering the diffusive flux of water molecules across the ice surface, the droplet-substrate contact area, the free energy barrier, the Boltzmann constant, and the temperature. The averaged nucleation delay is given by the rate with t = 1/J.

The critical energy barrier for heterogeneous nucleation of an ice embryo is given as

$$\Delta G^*_{Hetero} = \frac{16\pi\gamma_{IW}^3}{3(\Delta G_V)^2}\,\phi(\theta) \qquad \textit{Equation 4-7}$$

Here $\gamma_{IW}(mJm^{-2})$ and ΔG_V (MJm^{-3}) are the ice-water interfacial tension and the free energy difference (per unit of volume) between ice and water (see APPENDIX II, Supplementary, section 3 Materials for detailed equations and parameter values).

$\phi(\theta)$ is a geometric parameter that can be given by [36]:

$$\phi(\theta) = \frac{(1 - cos\theta_{IW})^2(2 + cos\theta_{IW})}{4} \qquad \textit{Equation 4-8}$$

where θ_{IW} is the contact angle of the ice embryo (ice-water). Using the liquid-to-solid contact area *A* of the droplet and Equation 4-6 to Equation 4-8, ice nucleation delays can be estimated. For this, the contact angle ice-water θ_{IW} in Equation 4-8, describing the contact angle of the heterogeneously forming ice embryo at the liquid-solid interface, is an unknown parameter and is determined by fitting the predictions of the CNT to the experimentally measured delays. We obtained $\theta_{IW} = 49.6°$ at $T = -10℃$ and $\theta_{IW} = 83.3°$ at $T = -20$ ℃ for sample of $H = 10\ \mu m$ and $\theta_{IW} = 49.3°$ and $\theta_{IW} = 83.6°$ for sample of $H = 20\ \mu m$ at $-10℃$ and $-20℃$, respectively. Our results show a temperature dependence for θ_{IW}, with lower value at –10 °C than at –20 °C. This observation is consistent with other studies using surfaces modified with long-chain alkyl silanes. It is assumed that alkyl silanes have due their

flexibility the ability to better adapt to the molecular ice structure with increasing temperature [141,275].

Figure 4-8 shows the predictions of the CNT with the fitted θ_{IW} and the experimentally measured nucleation delays. The good agreement of the predictions with the experimental data using the solid-to-liquid contact area A as nucleation sites in our calculations, suggests that nucleation primarily took place at the solid-to-liquid interface. This is found for both surface series and experimental temperatures. For surfaces with H = 20 μm, the predictions using the flat contact area A' as nucleation sites appear also to agree with the measured nucleation delay times. However, the predicted variation in ice nucleation delay times with variation of S is markedly less than the experimentally observed variation. In this case, nucleation would take place at the top surface of the micropillars and at the bottom of the microstructure, but not at the sidewalls of the micropillars, which seems less likely since the sidewalls and top of the micropillars are both made of SU-8. Other heterogeneous nucleation processes such as condensation or de-sublimation at the vapor-to-solid interface of the vapor/air cushions in the micropillar structure are associated with a larger critical free energy for embryo formation and, thus, less likely [274]. This can be explained by the larger interfacial energies to the vapor phase compared to the interfacial energy ice-water.

4.5. Conclusion

In this study, we investigated for the first time at supercooled temperatures the role of geometrical features of microstructures on ice nucleation prevention in the commonly occurring intermediate wetting on superhydrophobic surfaces. We observed that the degree

of partial wetting depends not only on the spacing of pillars but also on temperature and wetting fraction in the microstructure increases with increasing supercooling. This can be attributed to the decline in intrinsic water-air CA with supercooling, resulting in a reduction in the de-wetting capillary pressure in the micropillar structure. At a critical micropillar spacing, the ice retardation is maximized, correlating with a minimum solid-to-liquid contact area of the droplet. The design of the microstructure requires careful selection of morphological parameters such as height, top surface and spacing of the pillars in order to minimize the effective solid-to-liquid contact area, which does not correlate with minimizing the wetting fraction in the microstructure. The presented experiments and framework accounting for the intermediate wetting and intertwined thermodynamic interactions on superhydrophobic surfaces provides guidelines for the design of such surfaces for ice prevention and important insights into the mechanisms of icing phenomena on microstructured surfaces.

CRediT authorship contribution statement

Samaneh Keshavarzi: Conceptualization, Investigation, Methodology, Validation, Writing – original draft, Writing - review & editing. **Gelareh Momen**: Conceptualization, Project administration, Supervision, Resources, Funding acquisition, Writing - review & editing. **Patric Eberle:** Conceptualization, Investigation, Validation, Writing – original draft, Writing - review & editing. **Amir Azimi Yancheshme:** Conceptualization, Methodology, Software, Validation, Investigation, Writing - original draft, Writing - review & editing. **Nicolas J. Alvarez:** Conceptualization, Software, Validation, Investigation, Writing - review & editing. **Reza Jafari**: Conceptualization, Project administration, Supervision, Resources, Funding acquisition, Writing - review & editing.

Acknowledgments

The authors would like to acknowledge the financial support from Natural Sciences and Engineering Research Council of Canada (NSERC) and Development of Collaborative Academic and Research Program to Study Ice Accretion on Structures in Cold Regions (CoARIce project). We also thank Carol Mercier at the Anti-icing Materials International Laboratory (LIMA), UQAC, for helping develop the experimental setup.

CHAPITRE 5

Ice Adhesion on Structured Surfaces: Exploring Geometric Parameters and Wetting States

5.1. Abstract

Ice adhesion on structured surfaces is a critical challenge with implications for various industries, from transportation to energy. In this study, we systematically investigate the influence of geometric parameters, specifically pillar spacing and height, on ice adhesion. Moreover, we explore wetting states, including partial wetting, across all sample configurations, providing a comprehensive perspective on ice adhesion on structured surfaces. Through the fabrication of hydrophobic and superhydrophobic silicon wafer surfaces with well-textured micro-cylindrical pillars, the ice adhesion strength was quantitatively evaluated by subjecting the frozen droplets to shearing forces using a micro push-off test. The results indicate that patterning the surfaces reduce the measured ice-adhesion strength, primarily due to a reduction in the interfacial contact area. We observe that increasing the spacing between micropillars initially leads to a decrease in the contact area, followed by a subsequent increase beyond a threshold value. Similarly, the ice adhesion strength exhibits a similar trend, decreasing with greater spacing until the threshold, after which ice adhesion strength increase. These results provide valuable insights into the influence of microstructural features on ice adhesion and contribute to the development of surfaces engineered for controlled ice adhesion properties.

Keywords: Ice adhesion strength, Surface topography, Micro-patterned surfaces, Surface wettability, Partial wetting, Contact area

5.2. Introduction

The need to combat ice accumulation on vital surfaces, including infrastructure maintenance and transportation safety, has prompted the exploration of icephobicity—a multifaceted concept with several distinct definitions [15]. These definitions include surfaces' ability to repel incoming water droplets in cold environments, their capability to delay or impede ice nucleation and frost accumulation, and their effectiveness in reducing the adhesion strength between surfaces and ice [9,24]. Given the inevitability of ice formation in frigid environments over time, achieving surfaces with ultra-low ice adhesion (<10 kPa) emerges as one of the most practical approach for dealing with ice-related challenges [152,156].

Among the innovative strategies to mitigate ice adhesion, hydrophobic and superhydrophobic surfaces have gained significant attention [37,243]. Superhydrophobicity is achieved through low surface energy materials and surface roughness or texture [276]. When water contacts such surfaces, it can exhibit two main states: the Cassie-Baxter state, where water droplets rest on the surface with trapped air underneath, and the Wenzel state, where water infiltrates the surface's textures [43,44]. Interestingly, the behavior of hydrophobic surfaces often manifests in an intermediate (partial) wetting state between Cassie-Baxter and Wenzel, characterized by varying degrees of wetting within the micro/nanostructure of the surface [45,46,265].

The influence of superhydrophobic surfaces on reducing ice adhesion strength has been a subject of significant debate over the past decades. Some researchers have reported a notable decrease in ice adhesion [167,168]; however, contrasting findings have indicated that superhydrophobic surfaces can actually increase ice adhesion [169,170].

While the influence of various surface structures on ice adhesion has been extensively examined (as demonstrated in Table 5-1), a comprehensive understanding of partial wetting within these structures at temperatures below the freezing point and its implications on ice adhesion remains a gap in current knowledge. This paper thoroughly explores the ice adhesion strength, with a specific emphasis on the relationship between surface geometry and ice adhesion strength, including the phenomenon of intermediate (partial) wetting. Photolithography processing and chemical modification were combined to fabricate different hydrophobic and superhydrophobic surfaces based on silicon wafer. Several surfaces with similar chemistry but different topography, including a series of well-textured micro-cylindrical pillars with different space and height, were fabricated to determine the ice adhesion strength of frozen water droplets. By exploring this complex relationship, our aim is to better understand how surface structure impacts ice adhesion and provide guidance for designing surfaces that resist ice more effectively.

Table 5-1: Ice adhesion strength of structured surfaces (D: Pillar diameter/ length, H: Height, S: Space)

Ref.	Surface type	CA (º)	Temperature (°C)	Water droplet volume (µL)	Relative humidity (%)	Ice adhesion strength (KPa)
[277]	Pristine Silicon wafer	-	-15	5	40	600 to 1200
	SHP Silicon wafer	155	-15	5	40	≤ 100
[177]	Pristine PDMS	117	-15	15	40	561.4
	Pattern PDMS (D = 30 µm, H = 45 µm, S = 45 µm)	144	-15	15	40	320.4

	Pattern PDMS (D = 30 µm, H = 45 µm, S = 67.5 µm)	147	-15	15	40	263.8
[164]	As received (AR) aluminum (Al)	83	-10	4	45	330
	Silicon-doped hydrocarbon and then fluorinated-carbon coated AR Al	119	-10	4	45	160
	Sandblasted (SB) Al	37	-10	4	45	610
	Silicon-doped hydrocarbon and then fluorinated-carbon coated SB Al	134	-10	4	45	300
[178]	Hydrophilic Aluminum	45.1	-9	5	70	150
			-14	5	70	160
			-19	5	70	170
	Hydrophobic Aluminum	126.2	-9	5	70	50
			-14	5	70	60
			-19	5	70	70
	Superhydrophobic Aluminum	158.5	-9	5	70	20
			-14	5	70	55
			-19	5	70	110
[278]	Pristine glass surface	30	-15	15	50	172.4
	superhydrophobic carbon nano-film	155	-15	15	50	474
[161]	Pristine Silicon wafer	64.1	-15	10	30	2000
	Micro cubic pillars Silicon wafer (D = 20 µm, H = 10 µm, S = 20 µm)	111.9	-15	10	30	1300
	Micro- nano cubic pillars Silicon wafer (D = 20 µm, H = 10 µm, S = 20 µm) (D_{nano} = 0.2 µm, H_{nano} = 3 µm, S_{nano} = 0.2 µm)	147.3	-15	10	30	420
[148]	Pristine glass surface	117	-20	5	-	1500
	Cone shape nano pillars (D_Top = 30 nm, H = 300 nm, D_Botttom = 150 nm)	169	-20	5	-	~10

5.3. Material and Methods

5.3.1. Sample preparation

In this chapter, the same samples and sample preparation procedures as detailed in the previous chapter (Chapter 4) were used. A silicon wafer surface was structured via photolithography, resulting in hydrophobic and superhydrophobic patterns with varying geometric features, including cylindrical posts with different heights and spacings (Figure 5-1). The silicon substrates were also modified with TPFS (Trichloro (1H, 1H, 2H, 2H-perfluorooctyl) silane 97%) to alter their hydrophobicity.

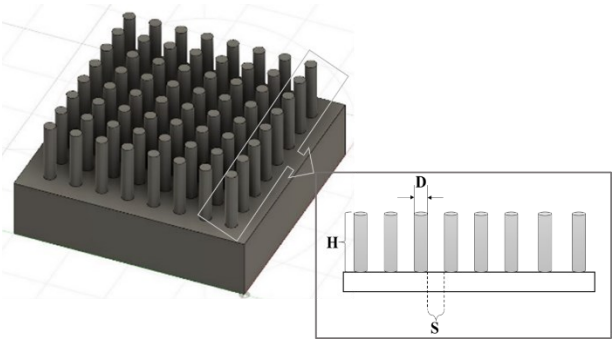

Figure 5-1: Schematic of ordered structured surfaces; D: diameter, H: height, S: Space.

5.3.2. Surface Characterization

The surface characterization methods employed in this chapter were consistent with those utilized in the Chapter 4. These methods included measuring contact angles of deionized water droplets, characterizing surface morphologies using SEM, and capturing 3D profiles of surface structures using an optical profiler.

5.3.3. Experimental Setup

The experimental setup for this chapter closely resembled the setup detailed in the previous chapter (Figure 3). Key components included a thermally insulated chamber, a high-speed camera, a thermostatic bath, a cold base, a droplet injection system, test samples, a data acquisition system, temperature and humidity sensors, a micro push-off test apparatus, and a vibration-free table.

Experimental procedures involved recording temperature and humidity, lowering the cold base temperature to −20°C, introducing 10 μL deionized water droplets, monitoring freezing processes with the high-speed camera, and quantifying forces using a custom-made ice push-off test called micro-push off set-up. Notably, for the measurement of ice adhesion

strength, a specific procedure was followed. As depicted inFigure 5-2, the water droplet froze on the silicon wafer's surface, securely fixed to the objective table. A probe equipped with a mechanical sensor was meticulously positioned under controller guidance. Following precise positioning, the probe was set into horizontal motion, exerting pressure on the frozen water droplet. Real-time data of the shear force was continuously captured by the mechanical sensor. To determine the contact area between the silicon wafer's surface and the frozen droplet, a theoretical calculation was performed (chapter 4, section 4.4.2). Subsequently, we calculated the ice adhesion strength as the ratio of the recorded shear force to the computed contact area.

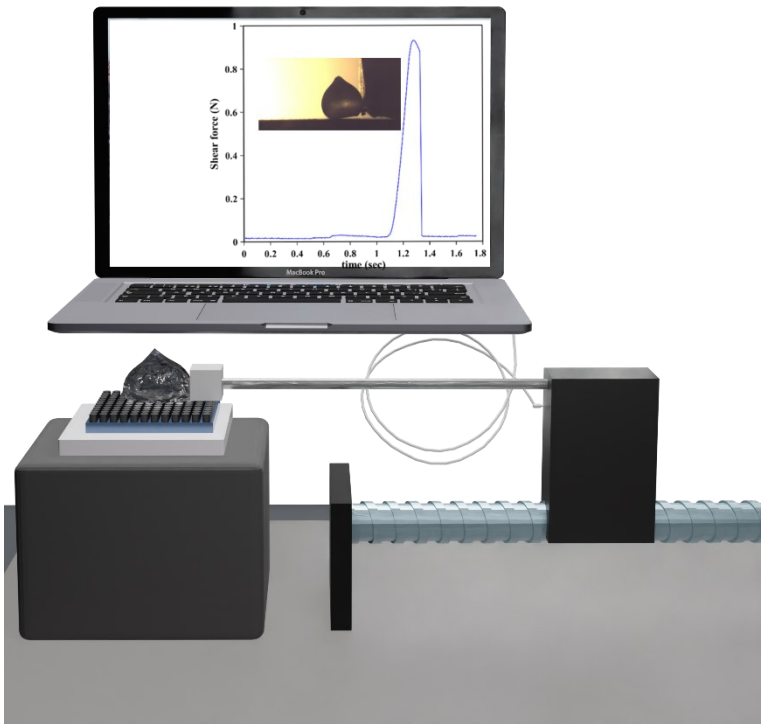

Figure 5-2: Schematic of micro push-off test

5.4. Results and Discussion

5.4.1. Surface Topography and Wettability

The following section provides a summarized overview of the surface topography and wettability of silicon wafer surfaces, as discussed in detail in our previous chapter (Chapter 4). This summary aims to provide a quick reference to key findings and observations without repeating the extensive details presented earlier.

In the previous chapter, we explored the surface topography and wettability of silicon wafer surfaces. SEM images and 3D profiles confirmed the successful fabrication of micropillar surface structures (Figure 5-3), with varying pillar-to-pillar spacings (S), including values of 5, 10, 20, 30, 40, 70, and 100 µm, and two different series based on pillar height: Series 1, with pillar heights of 10 µm, and Series 2, with pillar heights of 20 µm. These micropillars were characterized by cylindrical shapes with a 10 µm diameter and flat tops. Moreover, the nanoscale roughness of the original silicon wafer was quantified, revealing a root-mean-square surface roughness of 2.62 nm.

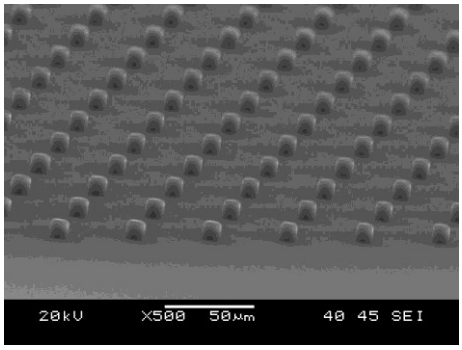

(a)

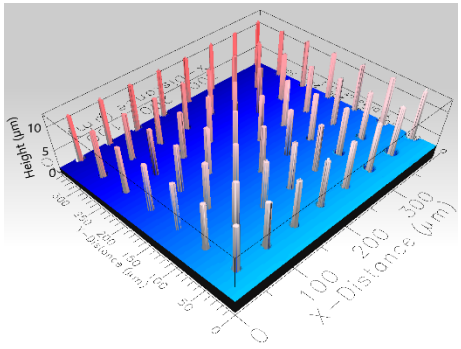

(b)

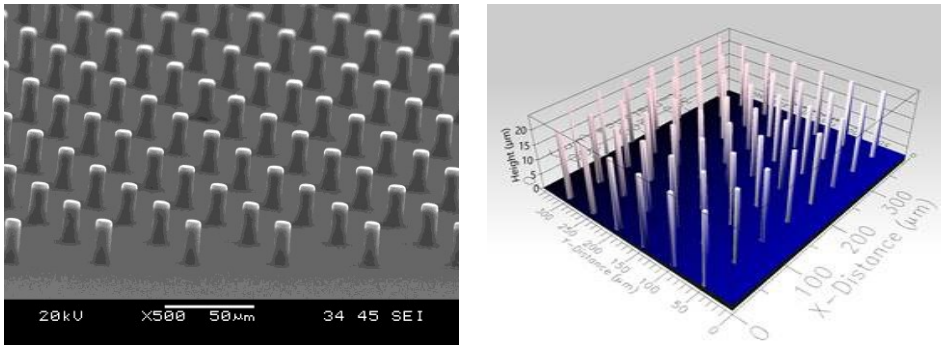

(c) (d)

Figure 5-3: (a) SEM and (b) 3D Profiler characterization of patterned Si structures with D = 10 µm, H = 10 µm, S = 40 µm, and (c) SEM and (d) 3D Profiler characterization of patterned Si structures with D = 10 µm, H = 20 µm, S = 40 µm.

Our study primarily focused on micropillar surfaces, which exhibited hydrophobic and superhydrophobic properties. The effect of S on contact angles was investigated in detail, as illustrated in Figure 5-4. It was observed that as S increased from 5 to 20 µm, the CA initially increased gradually and then decreased as S reached 100 µm. This trend was consistent across two series of samples with varying pillar heights. Despite similar intrinsic chemical properties, macroscopic wettability was primarily affected by the geometrical properties of the surface microstructures, including pillar spacing distances and pillar height. Contact angles (CAs) between the predictions of the Wenzel and Cassie-Baxter states were observed as shown in Figure 5-4 (c) and (d), indicating intermediate wetting with partial wetting characteristics.

Furthermore, the effect of temperature on CA was explored, with measurements conducted at both 22°C, −10°C and −20°C, as presented in Figure 5-4 (a) and (b). These results indicated that CAs decreased with decreasing temperature, following a trend observed at room temperature.

We used equations to describe wetting behavior, where wetting fraction (f) increased with increasing micropillar spacings for all temperatures (chapter 4, section 4.4.2). The

increase in f was more pronounced at lower temperatures, attributed to the temperature-dependent intrinsic CA. To quantify wetting behavior, we introduced the concept of wetting fraction (f). This parameter represented the area ratio of the wetted region between the micropillars to the total droplet contact area, projected onto the flat surface. Our analysis showed that f increased as S increased, indicating that the droplet progressively wetted the spaces between the micropillars. This effect was attributed to factors such as the deeper penetration of the droplet meniscus between pillars and the reduction in de-wetting Laplacian pressure.

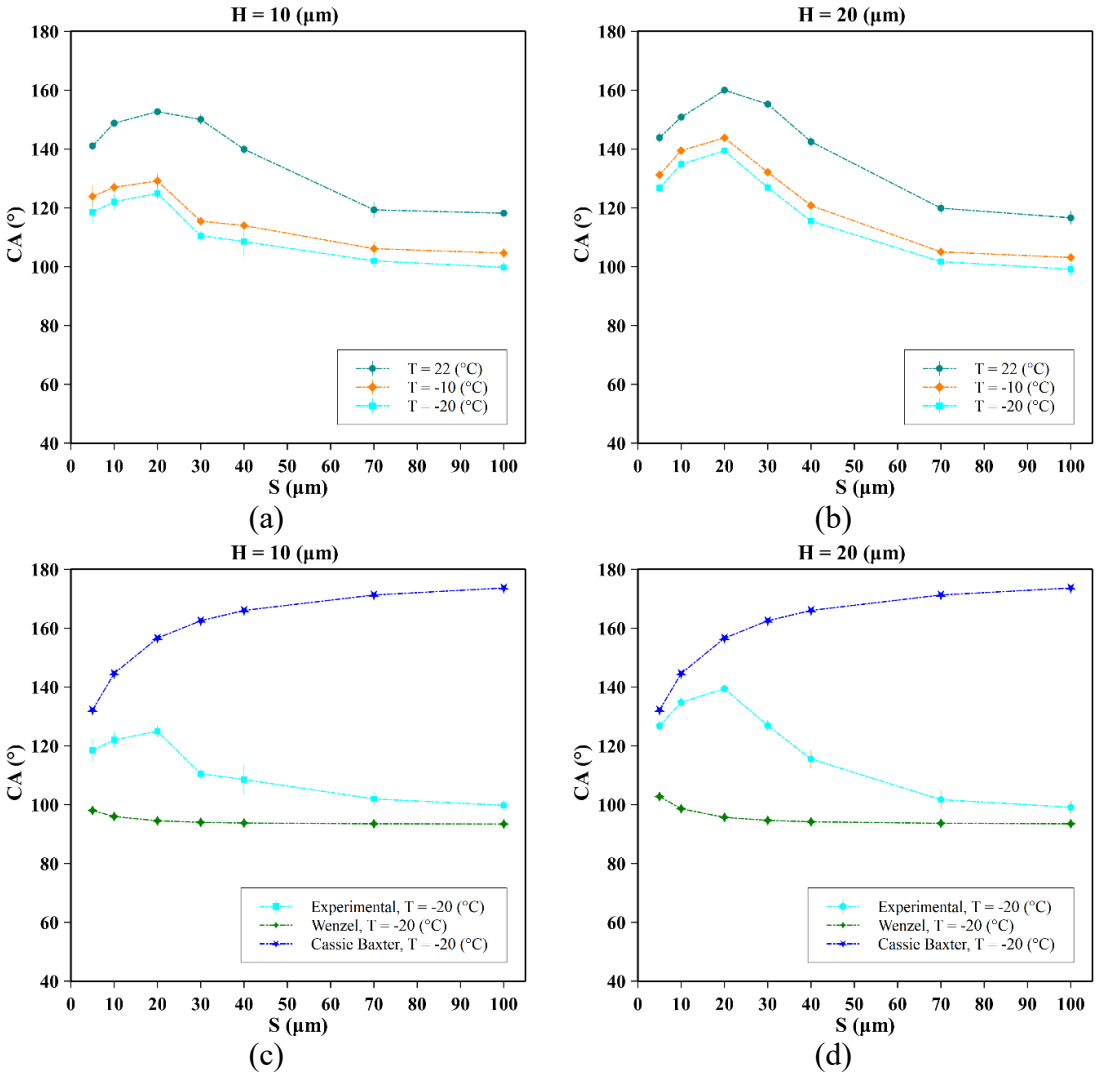

Figure 5-4: Water contact angle (CA) of the silicon wafer surfaces with (a) H = 10 µm and (b) H = 20 µm, and Wenzel and Cassie baxter model prediction of the silicon wafer surfaces with (c) H = 10 µm and (d) H = 20 µm.

5.4.2. Ice adhesion

To investigate how micro-patterning affects a material's icephobic properties, a micro push-off testing method was developed to quantitatively measure ice adhesion strength at the interface between ice and a silicon wafer. This method, shown in Figure 5-2, is similar in concept to a previous approach involving the removal of an ice cylinder from a surface using a probe (push-off test) [156]. However, our method eliminates the need to prepare an ice cylinder in advance.

After conducting multiple experiments, we refined several testing parameters. We decided to maintain a narrow gap of <0.5 mm between the sample surface and the probe, set the scanning speed to 0.5 mm/s, and consistently maintained the cooling plate temperature at −20°C.

During the probe's scan of the surface, we carefully recorded the force. Figure 5-5 visually represents typical force curves obtained from a push-off experiment. The key parameter for assessing relative ice adhesion strength on various surfaces is the maximum force observed, right at the moment when the droplet is detached from the solid interface (Figure 5-6). Consequently, we determine the shear stress, representing the ice adhesion strength, by dividing the knock-off force (Figure 5-7) by the projected contact area, as detailed in Figure 5-8. The ice-adhesion values are then presented in Figure 5-9, illustrating the average outcomes from almost 10 separate trial runs. Variability in the measured forces required to detach ice in push-off tests can result from several factors intrinsic to the experimental setup and external environmental conditions. These factors encompass surface

properties, ice formation conditions, experimental techniques, sample variability, environmental influences, and measurement errors. Moreover, it is essential to consider that the ice nucleation time of these samples vary, and the samples are in partial wetting modes. Consequently, ice formation on the surfaces and potential condensation between pillars could contribute to the observed differences in the forces needed to detach the ice. Understanding and controlling these sources of variability are crucial for ensuring the reliability and reproducibility of experimental results in ice adhesion studies.

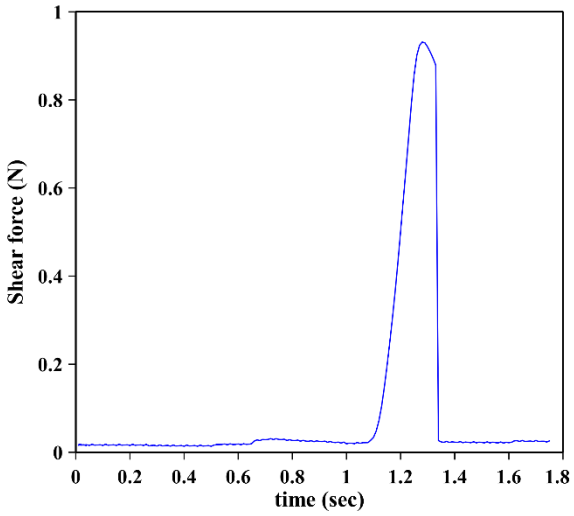

Figure 5-5: Force curve during ice adhesion test.

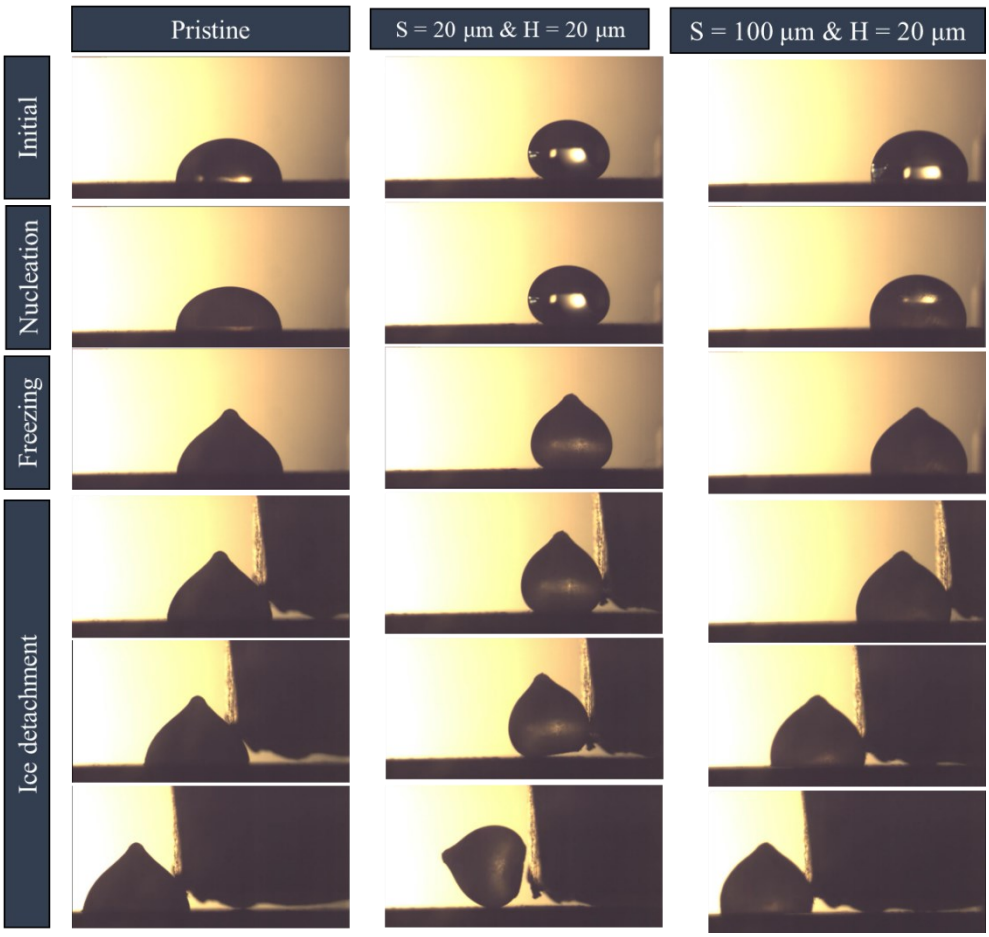

Figure 5-6: Images of freezing and push-off test on pristine and patterned silicon wafer surfaces.

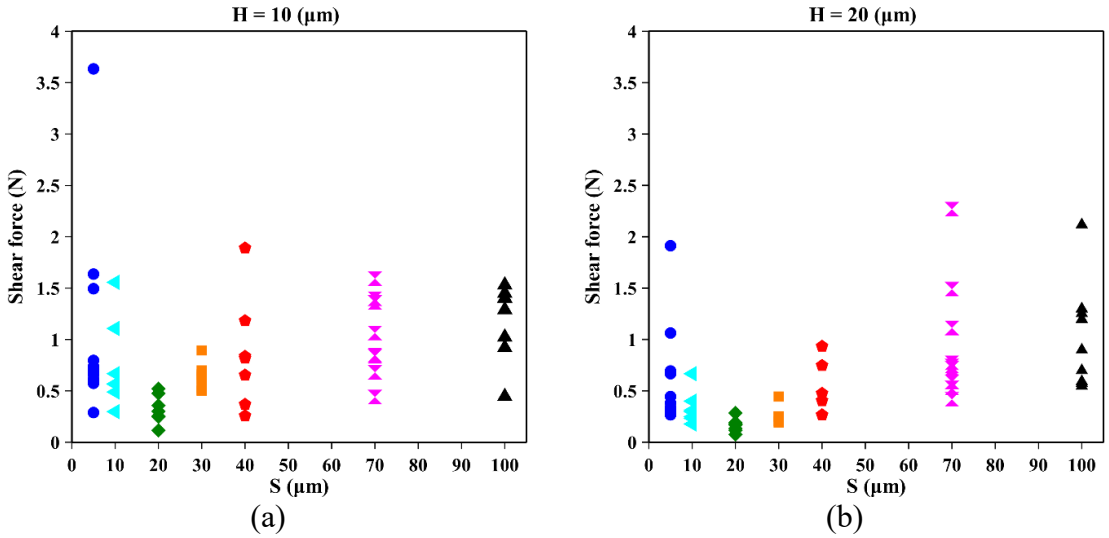

Figure 5-7: Measured maximum shear force of frozen water droplet on silicon wafer surfaces with (a) H = 10 µm and (b) H = 20 µm.

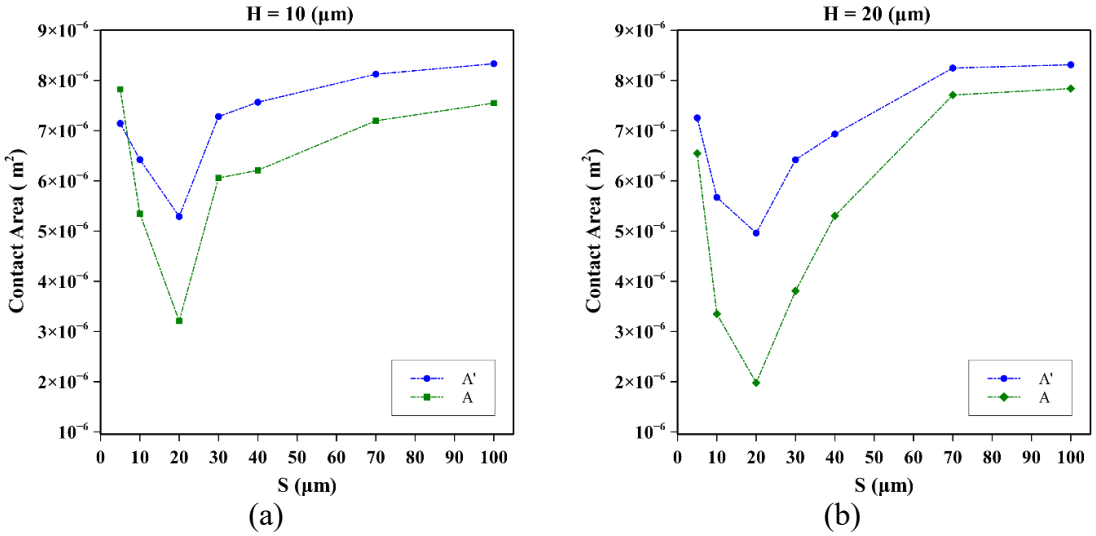

Figure 5-8: Flatt and effective contact area under frozen droplet on the silicon wafer surfaces with (a) H = 10 µm and (b) H = 20 µm.

Upon analyzing the data presented in Figure 5-9, which pertains to measurements taken on both micro-patterned and flat surfaces, a clear and significant difference becomes apparent in the force required to remove identical droplets from these two surface types. Since all the surfaces share the same chemical composition, it is plausible to suggest that the reduction in ice adhesion force on the micro-patterned surface is primarily due to differences in the contact area.

The observed decrease in ice adhesion strength as S increases from 5 to 20 µm can be attributed to reduced ice-solid contact area. This decrease aligns with previous studies on superhydrophobic surfaces, which often exhibit reduced ice adhesion due to their reduced contact area [76,161,177,278].

However, the increase in ice adhesion strength observed with an increasing S up to 100 µm can be attributed to the influence of capillary forces at larger pillar spacings. Capillary forces effectively draw water and ice into the spaces between the micro-pillars,

enhancing adhesion. This effect becomes more pronounced as S values increase because the capillary forces start to dominate over reduced contact area considerations.

This behavior can be further elucidated by two primary factors. Firstly, as S increases, the droplet meniscus exhibits deeper penetration into the spaces between the micropillars. Simultaneously, there is a corresponding reduction in the de-wetting Laplacian pressure induced by the droplet meniscus between the micro-pillars. Both factors significantly contribute to the enhanced ice adhesion.

Moreover, the larger spacing between the pillars facilitates fewer micro-pillars within a given area, thereby promoting a greater extent of direct contact between the ice and the surface. This reduction in pillar density corresponds to a decrease in the surface tension force acting on the droplet. Consequently, this reduction in surface tension leads to water droplets gravitating towards the surface asperities, further reinforcing the overall increase in ice adhesion strength.

Furthermore, the difference in ice adhesion strength between Series 1 and Series 2, with Series 2 consistently exhibiting lower adhesion, is noteworthy. This discrepancy suggests that the increased height of the pillars in Series 2 plays a pivotal role in controlling ice adhesion. One plausible explanation is that the taller pillars in Series 2 contribute to an enhancement in the surface's hydrophobicity. This heightened hydrophobicity, in turn, leads to reduced ice adhesion. Surfaces characterized by taller pillar structures also diminish the likelihood of droplet penetration into the pillars and wetting of the microstructure. This is indicated by smaller values for parameters such as 'f' and 'A' (chapter 4, section 4.4.2),

ultimately resulting in a larger liquid-air interface. Consequently, such surfaces experience lower ice adhesion.

Hence, if a sample surface were sufficiently textured to minimize droplet contact area, our results indicate that the more effective removal of accumulated ice would be achieved through the use of higher pillar heights and an optimized pillar spacing.

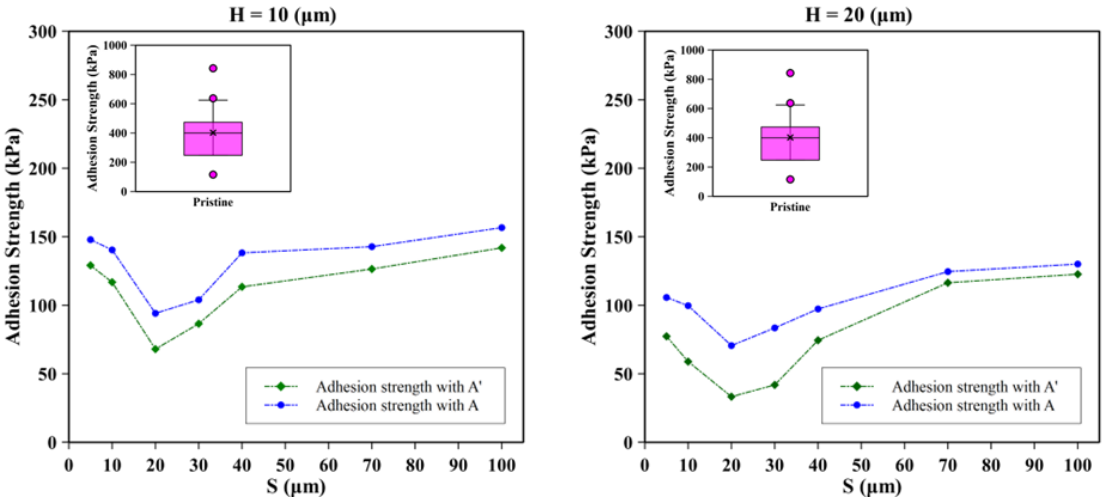

Figure 5-9: Averaged ice adhesion strength on the silicon wafer surfaces with (a) H = 10 μm and (b) H = 20 μm.

We now proceed to compare our study with the previous research, elucidating shared insights and distinctive facets that underscore the originality of our research. In the pursuit of understanding and mitigating the challenge of ice adhesion on structured surfaces, several key studies have illuminated this intricate field. Ge et al. [277] demonstrated the potential of superhydrophobic surfaces in reducing ice adhesion. Their findings revealed a notable reduction in ice adhesion strength compared to untreated surfaces. This exploration highlighted the significance of surface patterning as a promising approach. Then Hea et al. [161] explored the reduction of ice adhesion through hierarchical micro-nano pillars. While they emphasized the significance of contact angle and contact angle hysteresis in reducing

ice adhesion, their study also hinted at the possible relevance of partial wetting states, although it did not explicitly investigate these states.

Nguyen et al. [148], in their study on the effects of morphology parameters on ice adhesion, discussed the influence of parameters such as pillar diameter and height. However, their work primarily focused on the impact of these geometric features on ice adhesion, leaving the concept of wetting states, specifically Cassie-Baxter or Wenzel, unexplored. However, Huré et al. [279], in their examination of Cassie-Baxter versus Wenzel states' impact on ice adhesion, conducted shear adhesion strength measurements for both states. While they acknowledged the potential existence of partial wetting states, they did not provide detailed insights into these states' behavior in the context of ice adhesion. Hou et al. [14] also investigated superhydrophobic surfaces designed with micro-cubic array structures and varying micro-spacing distances (S). They observed that as S increased, ice adhesion initially rose and then decreased. Wetting state analysis revealed shifts from Cassie-Baxter to semi Cassie-Wenzel and eventually Wenzel states with increasing S. This study provides insights into how surface structure affects ice adhesion by investigating the Cassie-Baxter and Wenzel states.

McDonald et al. [177] took a comprehensive approach, considering ice adhesion strength on super-cooled hydrophobic surfaces. They evaluated local stress on individual micro-pillars, assuming a complete Cassie-Baxter wetting state. Their results revealed a fascinating inverse relationship between global adhesion force and local stress. Importantly, they suggested that the assumption of complete Cassie-Baxter wetting may not hold entirely true, hinting at the possibility of slight water or ice penetration into the patterned micro-pillar array during freezing.

Our study systematically investigates the influence of geometric parameters, specifically pillar spacing and height, on ice adhesion. Notably, we thoroughly explore wetting states, including partial wetting, across all sample configurations. In summary, our study not only builds upon the insights from prior research, expanding our understanding of ice adhesion phenomena, but it also introduces the crucial concept of partial wetting. This focused emphasis on understanding partial wetting states represents a substantial contribution, providing a more comprehensive perspective on ice adhesion on structured surfaces.

5.5. Conclusion

In this study, we examined the role of geometrical features of microstructures in ice adhesion, focusing on the influence of partial wetting within micro pillar structures. To quantify the ice-adhesion strength, an experimental micro push-off method was developed to provide a relative measure of the shear force required to remove frozen droplets from various surfaces.

By analyzing ice adhesion strength on hydrophobic and superhydrophobic silicon wafer surfaces with well-textured micro-cylindrical pillars, we determined that ice adhesion is dependent on pillar spacing, pillar height, and wetting state. The shear forces recorded for equivalent ice droplets indicated that the incorporation of surface patterns on silicon wafer reduced the ice-adhesion strength.

Increasing the spacing between micropillars initially decreased the contact area, which subsequently increased beyond a threshold value. Correspondingly, ice adhesion followed a similar trend, initially decreasing with greater spacing until the threshold S = 20

μm, after which ice adhesion increased. The sample with dimensions D = 10 μm, H = 20 μm, and S = 20 μm showed the lowest ice adhesion strength at a temperature of −20℃ for a 10 μL frozen water droplet. These findings provide important insights for the design of surfaces with controlled ice adhesion characteristics and contribute to our understanding of ice adhesion mechanisms on microstructured surfaces, offering valuable insights into optimizing ice adhesion properties in hydrophobic and superhydrophobic materials.

CHAPITRE 6

CONCLUSION

This Ph.D. thesis was dedicated to addressing the persistent challenges posed by ice formation and surface icing in various industries, emphasizing the development of passive anti-icing technologies through a comprehensive investigation of surface structure. This research journey, comprising interrelated chapters, was characterized by a comprehensive approach involving the fabrication and characterization of both non-ordered and ordered surfaces (microstructured silicone rubber and silicon wafer surfaces with varying wettability and geometric features). Through experimental setups and cutting-edge machine learning techniques, the impact of these surfaces on water droplet behavior, ice nucleation time, and ice adhesion strength was thoroughly investigated.

The first part of the research involved studying how water droplets behaved on different non-ordered silicone rubber surfaces, ranging from hydrophobic to superhydrophobic. Notably, superhydrophobic surfaces characterized by a contact angle exceeding 160° and minimal contact angle hysteresis demonstrated the remarkable ability to induce full droplet bouncing. Surface temperature had minimal influence on droplet behavior. Importantly, machine learning techniques, including decision trees, random forests, and logistic regression, emerged as invaluable tools, effectively predicting droplet dynamics

based on surface attributes, temperature, and droplet characteristics, with Weber and Reynolds numbers identified as pivotal factors.

The exploration continued with an in-depth analysis of ice nucleation time on those non-ordered silicone rubber surfaces. Surface properties such as wettability, roughness, droplet volume, and temperature were analyzed. Lower temperatures and larger droplet volumes were found to lead to reduced freezing delays. Furthermore, the significance of surface texturing became apparent, with surfaces featuring higher roughness values and a Gaussian roughness distribution exhibiting prolonged ice nucleation times. Employing a neural network model, the research successfully predicted ice nucleation times, highlighting the critical influence of surface temperature, roughness parameters, and droplet volume.

The subsequent part of the research explored ordered microstructural geometric surfaces on silicon wafers. Through meticulous experimentation and analysis, it was revealed that micro-cylindrical pillars with specific spacing and height parameters played a pivotal role in influencing ice nucleation time. As temperature decreased, partial wetting within micropillars increased, altering ice nucleation times. Balancing morphological parameters, specifically pillar spacing and height, proved to be critical in optimizing ice prevention on ordered superhydrophobic surfaces. This investigation into microstructure geometry represents a pioneering effort in understanding ice nucleation prevention on superhydrophobic surfaces in the intermediate wetting regime at supercooled temperatures. Additionally, a numerical method was utilized to simulate and analyze the cooling process of water droplets as they were deposited onto these microstructured surfaces. This approach further enhanced the understanding of the ice nucleation process. Notably, we observed that the degree of partial wetting is intricately influenced by both pillar spacing and temperature,

with heightened supercooling leading to a greater wetting fraction in the microstructure. At a critical micropillar spacing, we observed maximal delays in ice nucleation, aligning with a minimal solid-to-liquid contact area. Designing effective ice-preventing microstructures demands thoughtful consideration of morphological parameters, encompassing pillar height and spacing. Larger pillar heights were identified as beneficial, reducing wetting within the microstructure and extending ice nucleation delays. To optimize freezing delay, it is imperative to minimize the contact area between solid and liquid phases, requiring precise adjustments to morphology parameters.

In addition to the comprehensive exploration of ice nucleation, our final part of the study systematically investigated ice adhesion strength on hydrophobic and superhydrophobic silicon wafer surfaces featuring well-defined micro-cylindrical pillars. Through a custom micro push-off test method, we quantitatively measured the shear forces required to detach frozen water droplets from the surfaces. This approach allowed us to assess the impact of surface geometry on ice adhesion. Our results showed a strong dependence of ice adhesion strength on geometric parameters, particularly pillar spacing and height, as well as partial wetting states within the micro-pillar structures.

In conclusion, this comprehensive research effort significantly advanced our understanding of icephobic surfaces, encompassing water droplet behavior, ice nucleation time, and ice adhesion strength. The integration of experimental findings, theoretical frameworks, and machine learning applications provided a robust foundation for the development of effective anti-icing strategies. These insights hold tremendous potential for the development of passive anti-icing technologies, with implications for various industries facing the challenges of ice formation and surface icing.

CHAPITRE 7

RECOMMENDATION

In this Ph.D. thesis, we have identified optimal surface structures—non-ordered silicone rubber surfaces and ordered silicon wafer surfaces—that significantly enhance droplet bouncing, maximize ice nucleation time, and reduce ice adhesion strength. There are, however, several suggestions worth considering for future research. Following are these recommendations.

- In-Depth Exploration of Surface Roughness Parameters:

  An extension of the investigation could involve conducting a comprehensive study of various surface roughness parameters, such as variations in kurtosis, autocorrelation length, etc. The aim would be to analyze the impact of these parameters on icephobicity and to develop a comprehensive understanding of how surface roughness contributes to the prevention of ice formation.

- Varied Geometric Configurations:

  Conducting systematic experiments that explore a wide array of geometric configurations for microstructures or surface patterns to investigate how varying shapes, sizes, and arrangements of surface features affect icephobicity.

- Patterned Surface Fabrication:

  An area of investigation involves exploring cost-effective and scalable fabrication methods for patterned surfaces, encompassing micro- and

nanotexturing techniques like replication techniques by compression molding, and 3D printing. Furthermore, there is a need to optimize the fabrication process to ensure the uniformity and reproducibility of anti-icing surface features.

- Environmental Factors' Influence:

  An examination of the influence of environmental variables, including factors such as humidity, wind speed, and air temperature, on the effectiveness of anti-icing surfaces is recommended. Utilize systematic experimentation to gain insights into how these conditions may affect the performance of passive anti-icing technologies in real-world operational contexts.

- Simulation:

  Exploring numerical simulations to model droplet impact, ice nucleation, and adhesion processes on the tested surfaces is suggested. The utilization of computational fluid dynamics (CFD) and molecular dynamics (MD) simulations can provide valuable insights into the fundamental physics and can serve to validate the findings obtained through experiments.

- Coupled Experimental, Simulation, and Machine Learning Approaches:

  Exploring the integration of experimental, simulation, and machine learning approaches into a unified framework is recommended. This approach aims to enhance the accuracy and predictiveness of models used for evaluating anti-icing performance.

APPENDIX I

SUPPORTING INFORMATION FOR ARTICLE 2

Ice nucleation on silicone rubber surfaces differing in roughness parameters and wettability: experimental investigation and machine learning–based predictions

S. Keshavarzi[1*], A. Entezari[2], K. Maghsoudi[1], G. Momen[1], R. Jafari[1]
[1]Department of Applied Sciences, University of Québec in Chicoutimi, Chicoutimi, Québec, Canada
[2] The Hong Kong Polytechnic University, Hong Kong
Email address: samaneh.keshavarzi1@uqac.ca

This article has been accepted in:

Journal of cold regions science and technology

Section 1. DNN model:

In DNN model, there are a number of nodes as well as an activation function in each hidden layer. Although different activation functions can be used, it is common to use one activation function for all neurons within a layer.

Each layer's output becomes the input for the next layer, which is calculated by:

$$h^k = \sigma^k(b^k + W^k h^{k-1}) \qquad \textit{Equation A-I. 1}$$

where k is the layer number, h^k is the output array of the layer k (h^o is the network's input (named x here), $\sigma^k$is the activation function of the layer k, b^k is the array of bias values in layer k, W^k is the matrix of weights of the layer k. The output of the final layer is the prediction of the output variable.

To add nonlinearity to input-output relationships, activation functions are employed. When linear activation functions are applied to all layers, the prediction of DNN will be a linear combination of input variables no matter how many layers are presented. Hornnik et al. [280] demonstrated that any function with any degree of nonlinearity could be approximated by "squashing functions" and sufficient hidden layers. Squashing functions are nonlinear functions that transform input variables to a range, such as [-1, 1]. A rectifier like relu was also proposed and used during the past decade, especially in hidden layers [281]. Aside from being non-linear, this activation function also does not always activate all neurons at once. Some of the most common and well-known activation functions are shown in Table A-I. 1. There needs to be nonlinear and differentiable activation functions to allow optimization algorithms to better analyze them [282].

Table A-I. 1: Some of the most common activation functions

Activation Function	***Formula***
Sigmoid	$\mathrm{s(x)} = \frac{1}{1+\mathrm{e}^{-\mathrm{x}}}$
Tanh	$\tanh(\mathrm{x}) = \frac{\mathrm{e}^{\mathrm{x}}-\mathrm{e}^{-\mathrm{x}}}{\mathrm{e}^{\mathrm{x}}+\mathrm{e}^{-\mathrm{x}}}$
Relu	$\mathrm{y(x)} = \max(0, \mathrm{x})$
Leaky-relu	$\mathrm{y(x)} = \max(0, \mathrm{x}) : 0 < \alpha \ll 1$
Linear	$\mathrm{y(x)} = \mathrm{x}$

A DNN is trained by minimizing the difference between the actual output variables and the predictions. For this purpose, it is important to define a cost function that represents the dissimilarity referred to above. Table A-I. 2 shows examples of some of the most common cost functions used with a DNN trained on a dataset with m samples.

Table A-I.2: Common cost functions used in DNN

Cost function name	***Abbreviation***	***Formula***
Mean of squared error	*MSE*	$\mathrm{J}(\mathrm{y},\hat{y}) = \frac{1}{\mathrm{m}}\sum_{\mathrm{i}}^{\mathrm{m}}(\hat{y}_{\mathrm{i}} - \mathrm{y}_{\mathrm{i}})^2$
Mean of absolute error	*MAE*	$\mathrm{J}(\mathrm{y},\hat{y}) = \frac{1}{\mathrm{m}}\sum_{\mathrm{i}}^{\mathrm{m}}(\lvert\hat{y}_{\mathrm{i}} - \mathrm{y}_{\mathrm{i}}\rvert)$
Mean of absolute percent error	*MAPE*	$\mathrm{J}(\mathrm{y},\hat{y}) = \frac{1}{\mathrm{m}}\sum_{\mathrm{i}}^{\mathrm{m}}\left\lvert\frac{\hat{y}_{\mathrm{i}} - \mathrm{y}_{\mathrm{i}}}{\mathrm{y}_{\mathrm{i}}}\right\rvert$
Mean of squared logarithmic error	*MSLE*	$\mathrm{J}(\mathrm{y},\hat{y}) = \frac{1}{\mathrm{m}}\sum_{\mathrm{i}}^{\mathrm{m}}(\log(\hat{y}_{\mathrm{i}} + 1) - \log(\mathrm{y}_{\mathrm{i}} + 1))^2$

In the deep neural network, the weights are initialized at the start of training, with the bias vector at a constant value (1 typically). Using randomized weights, the DNN model will make an initial prediction. By optimization algorithms, the weights of DNN are updated in an iterative manner until the cost function is minimized. This optimization algorithm normally is called on the training data set in a DNN. Most optimization algorithms employed in the training of a DNN are variations of batch gradient descent (BGD). Gradient descent minimizes cost through an update of the model parameters in the opposite direction of the gradient of cost function(*J(θ)*) [282,283].This process involves calculating the learning rate (η) which determines the size of the steps needed for the (local) minimum to be reached. Equation A-I. 2 represents the BGD formulas as follows :

$$\theta_{updated} = \theta_{old} - \eta.\nabla_{\theta}J(\theta; x^m; y^m) \qquad \textit{Equation A-I. 2}$$

where θ is a neuron's weight (neuron is the connection between two nodes), m is the samples size, x^m is the set of input and and y^m is the output variables, and $\nabla_\theta J(\theta)$ is the average of the partial derivative of the cost function obtained by Equation A-I. 3:

$$\nabla_\theta J(\theta) = \frac{1}{m}\sum_{i=1}^{m}\frac{\partial}{\partial\theta}J(\theta; x^i; y^i) \qquad \textit{Equation A-I. 3}$$

where $x^i$and y^icorrespond to sample i's input and output variables. With BGD, all samples within a data set are used to update the parameters. Thus, finding an optimal point with a large dataset can be too slow. Stochastic gradient descent (SGD) [284,285], as shown in Equation A-I. 4, adjusts parameters one by one over the training samples.

$$\theta_{updated} = \theta_{old} - \eta.\frac{\partial}{\partial\theta}J(\theta; x^i; y^i) \qquad \textit{Equation A-I. 4}$$

Each of these iterations is called an epoch and it is repeated for each sample in the dataset. Online projects can benefit from SGD because it converges to the minimum more quickly than BGD. To reach the minimum, however, it fluctuates redundantly, and may result in it continuing to update after the minimum is reached since it must process all of the samples in the training dataset. The solution to this problem was the mini-batch gradient descent, where the parameters were updated with n training examples randomly selected from the entire dataset (Equation A-I. 5):

$$\theta_{updated} = \theta_{old} - \eta.\nabla_\theta J(\theta; x^{[i:i+n)}; y^{[i:i+n)}) \qquad \textit{Equation A-I. 5}$$

where [i:i+n]is a subset of input (x) and output (y) variables with the size of n. Mini-batch gradient descent is plagued with the problem that the same learning rate (η) is used for updating all parameters, making it difficult to select a learning rate [286]. Dauphin et al. [287] also reported limitations to SGD with saddle points, in which slopes of target function are trending in opposite directions in two dimensions. The problem has been addressed by a

number of algorithms, including Nesterov Accelerated Gradient [288], Adagrad [289], Adadelta [290], and Adam [291] algorithms. Among these algorithms, the Adadelta, RMSprop, and Adam methods are conceptually similar [220], as they update the initial learning rate for the different weights (W_{ij}) in the optimization process, but it is found that the Adam optimizer performed better than the other two [291]. As shown in Equation A-I. 6 and Equation A-I. 7, Adam algorithm modulates step t's learning rate by the first (m_t) and second moments (v_t) of past gradients.

$$m_t = \beta_1 m_{t-1} + (1-\beta_1)\nabla_\theta J(\theta) \qquad \textit{Equation A-I. 6}$$

$$v_t = \beta_2 v_{t-1} + (1-\beta_2)(\nabla_\theta J(\theta))^2 \qquad \textit{Equation A-I. 7}$$

The constants β_1 and β_2 are user-defined. Parameters m_t and v_t tend to remain close to zero in subsequent iterations since m_0 and v_0 are usually initialized as zero vectors. This issue can be addressed with bias-corrected formulae proposed by Kingma and Ba [291]:

$$\widehat{m_t} = \frac{m_t}{1-\beta_1^t} \qquad \textit{Equation A-I. 8}$$

$$\widehat{v_t} = \frac{v_t}{1-\beta_2^t} \qquad \textit{Equation A-I. 9}$$

According to the Adam algorithm, the parameters will be updated as follows (Equation A-I. 11):

$$\theta_{t+1} = \theta_t - \frac{\eta}{\sqrt{\widehat{v_t}}+\in}\widehat{m_t} \qquad \textit{Equation A-I. 10}$$

The proposed values for β_1, $\beta_2$and $\in$ are 0.9, and 0.999 and 10^{-8}, respectively. Data analysts do not usually change these parameters since they are inherent to the algorithm. In this study, we have adopted them in the optimizer algorithm, and it is to be noted that the pursuit of a global minimum is not always the right approach, as this may be associated with the issue of overfitting [292]. Fortunately, overfitting did not happen in our developed models.

Section 2. Cross correlation matrix:

To investigate correlation coefficients between variables, a cross correlation matrix was used. The results presented in Table A-I. 3 showed a strong correlation between the height parameters (S_a, S_q, S_z and S_t). Although the ice nucleation can be considered as a complex system with issues of nonlinearity, the correlation coefficients present the linear correlation between variables. So, in order to understand which parameters play more significant role in ice nucleation time, feature importance analyze performed using machine learning algorithms.

Table A-I. 3: Roughness parameter correlation matrix

	T (°C)	*V(µl)*	*CA (°)*	*CAH (°)*	*S_a (µm)*	*S_q (µm)*	*S_z (µm)*	*S_t (µm)*	*S_{sk}*	*Time (sec)*
T (°C)	1									
V(µl)	-0.091	1								
CA (°)	0.040	-0.021	1							
CAH (°)	-0.042	0.026	-0.931	1						
Sa (µm)	0.046	-0.035	0.871	-0.982	1					
Sq (µm)	0.046	-0.037	0.818	-0.961	0.995	1				
Sz (µm)	0.052	-0.044	0.885	-0.942	0.972	0.961	1			
St (µm)	0.052	-0.044	0.898	-0.931	0.957	0.941	0.998	1		
Ssk	-0.014	0.041	-0.219	0.341	-0.430	-0.440	-0.441	-0.445	1	
Time (sec)	0.740	-0.315	0.477	-0.511	0.542	0.542	0.575	0.573	-0.224	1

APPENDIX II

SUPPORTING INFORMATION FOR ARTICLE 3

ARTICLE 3: Exploiting intermediate wetting on superhydrophobic surfaces for efficient icing prevention

Samaneh Keshavarzi1*, Gelareh Momen1, Patric Eberle2, Amir Azimi Yancheshme3, Nicolas J. Alvarez3, Reza Jafari1
1Department of Applied Sciences, University of Québec in Chicoutimi, Chicoutimi, Québec, Canada
2 Institute of Electrical Engineering, Lucerne University of Applied Sciences and Arts, Lucerne, Switzerland
3Chemical and Biological Engineering Department, Drexel University, Philadelphia, USA
Email address: samaneh.keshavarzi1@uqac.ca

This article has been submitted to:

Journal of Colloid and Interface Science

Section 1. Heterogeneous nucleation from the solid-to-liquid interface to the top of the droplet of sessile water droplet on the micropillar surfaces with H = 20 μm at T = −10 °C and T = −20 °C.

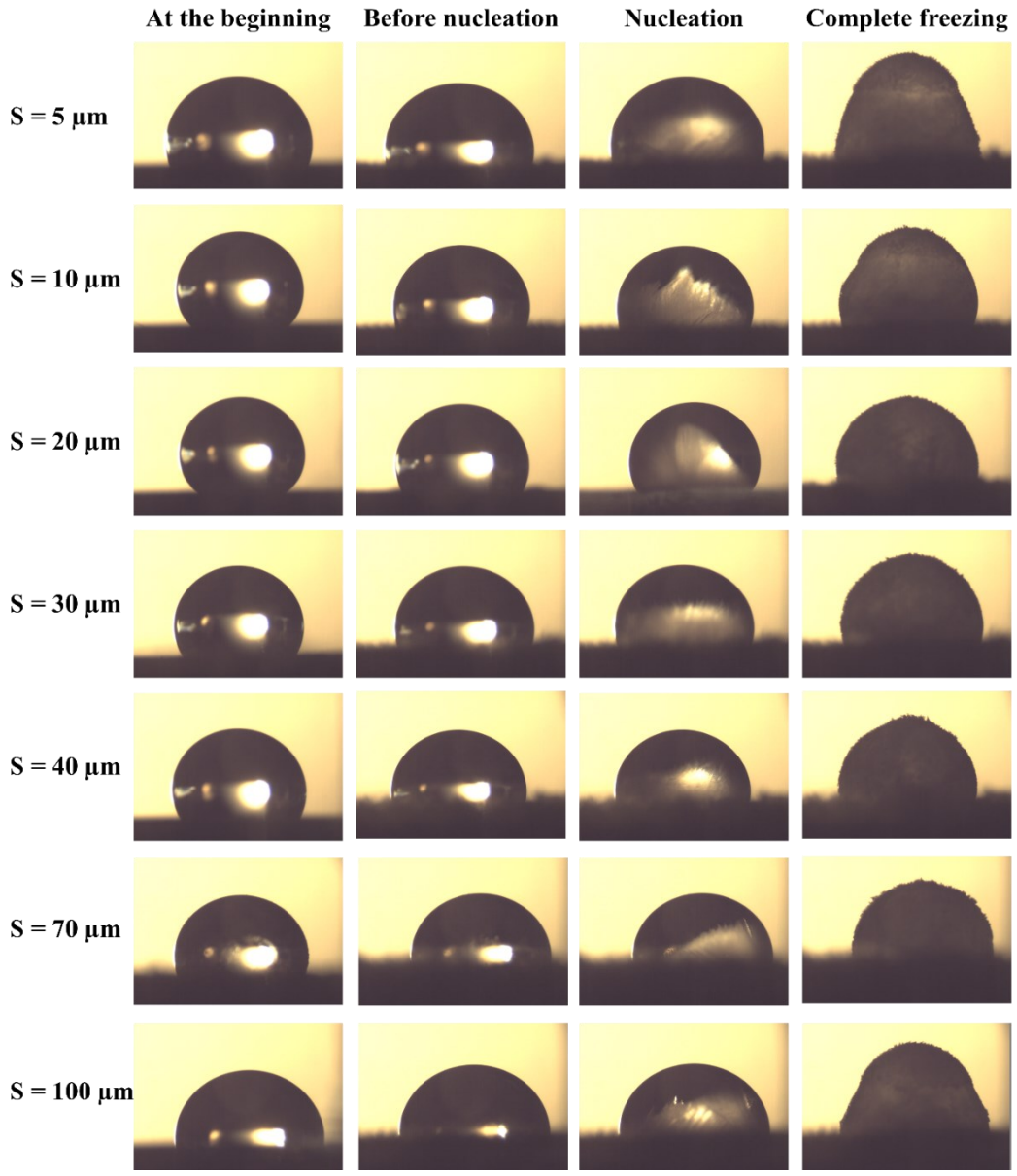

Figure A-II. 1: Freezing process of water droplet on the micropillar surfaces with H = 20 μm at T = −10 °C.

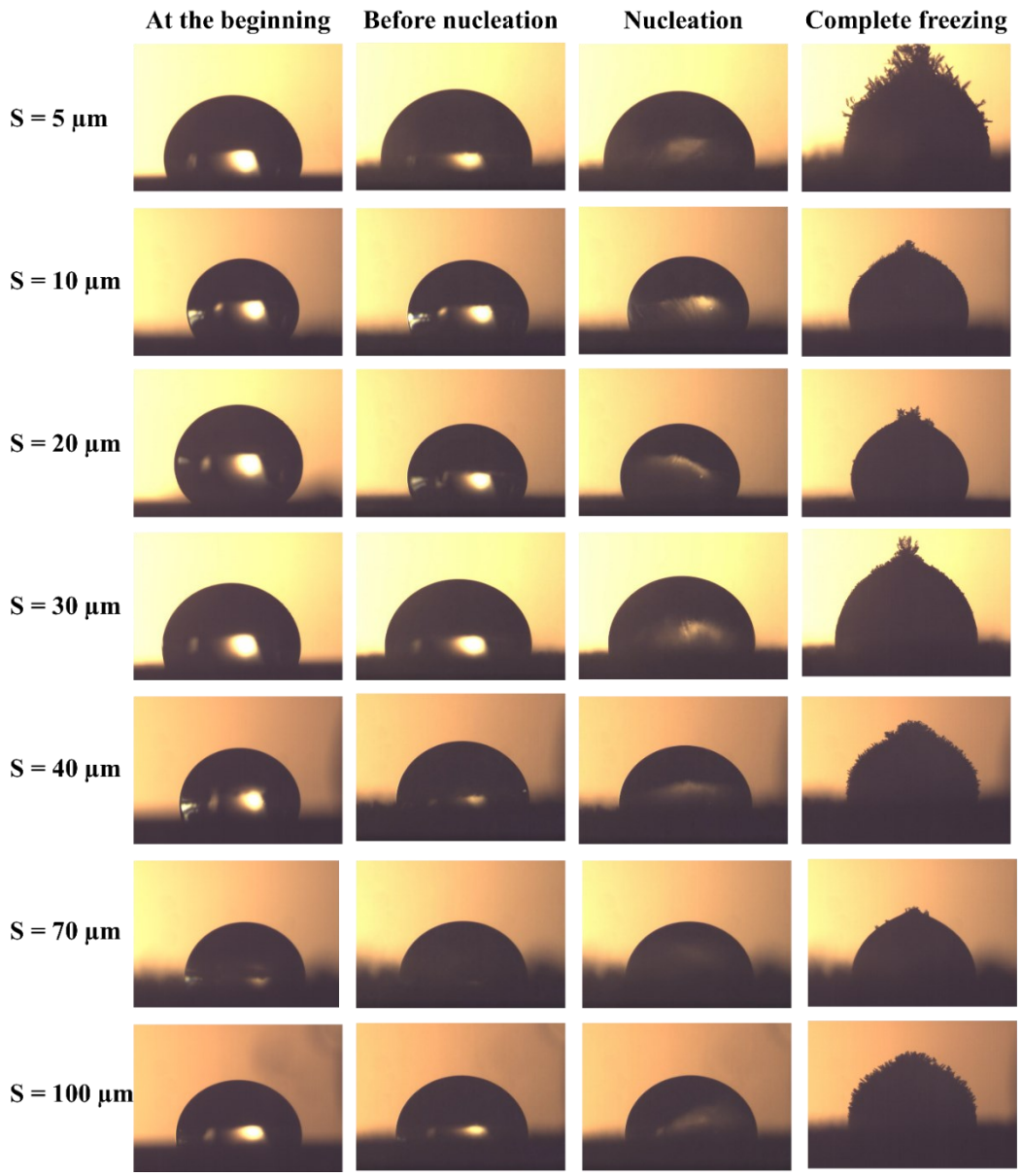

Figure A-II. 2: Freezing process of water droplet on the micropillar surfaces with H = 20 µm at T = −20 °C.

Section 2. Wetting theories

Young's equation can be used to calculate the equilibrium CA of a water droplet on an ideal smooth and chemically homogeneous solid surface:

$$\cos\theta_Y = \frac{\gamma_{SV} - \gamma_{SL}}{\gamma_{LV}} \qquad \textit{Equation A-II. 1}$$

where θ_Y is the intrinsic CA and γ_{SL}, γ_{LV} and γ_{SV} denotes the interface tensions of the solid/liquid, liquid/vapor, and solid/vapor, respectively [38].

According to the Wenzel model, the contact angle θ_W is:

$$\cos\theta_W = r\ \cos\theta_Y \qquad \textit{Equation A-II. 2}$$

where r is the surface roughness.

The apparent contact angle in the Cassie-Baxter model (θ_{CB}) can be expressed as:

$$\cos\theta_{CB} = \Phi(\cos\theta_Y + 1) - 1 \qquad \textit{Equation A-II. 3}$$

and Φ is the fraction of solid area.

Calculations of r and Φ are made according to surface structure geometry used in this paper [293]:

$$r = \frac{[(D + S)^2 + \pi DH]}{(D + S)^2} \qquad \textit{Equation A-II. 4}$$

$$\Phi = \frac{\pi D^2}{4(D + S)^2} \qquad \textit{Equation A-II. 5}$$

Section 3. Temperature distribution profiles of water droplet deposited on micro structured surfaces at bottom temperatures of −10 °C and −20 °C.

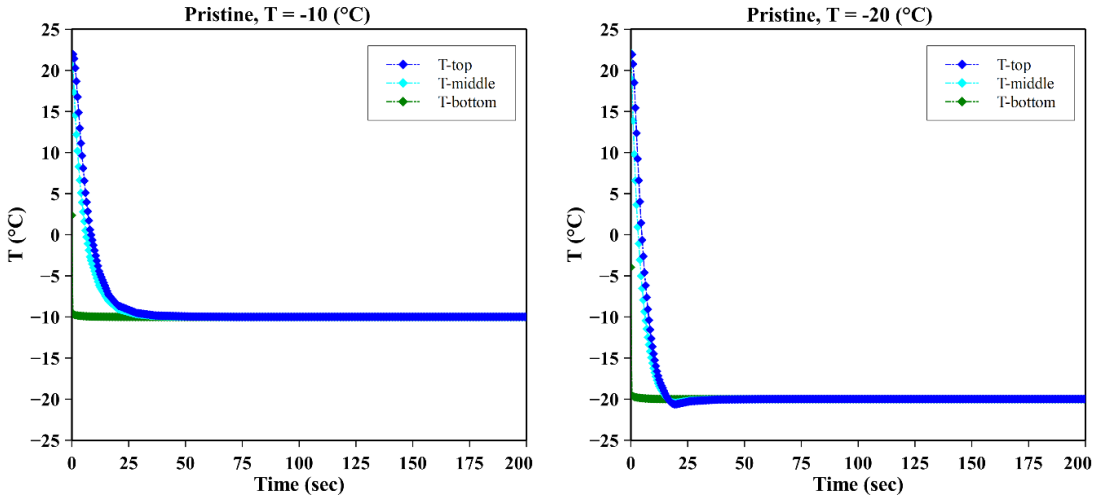

Figure A-II. 3: Temperature distribution profiles at different time instances for unstructured silicon wafer at (a) T = −10 °C and (a) T = −20 °C.

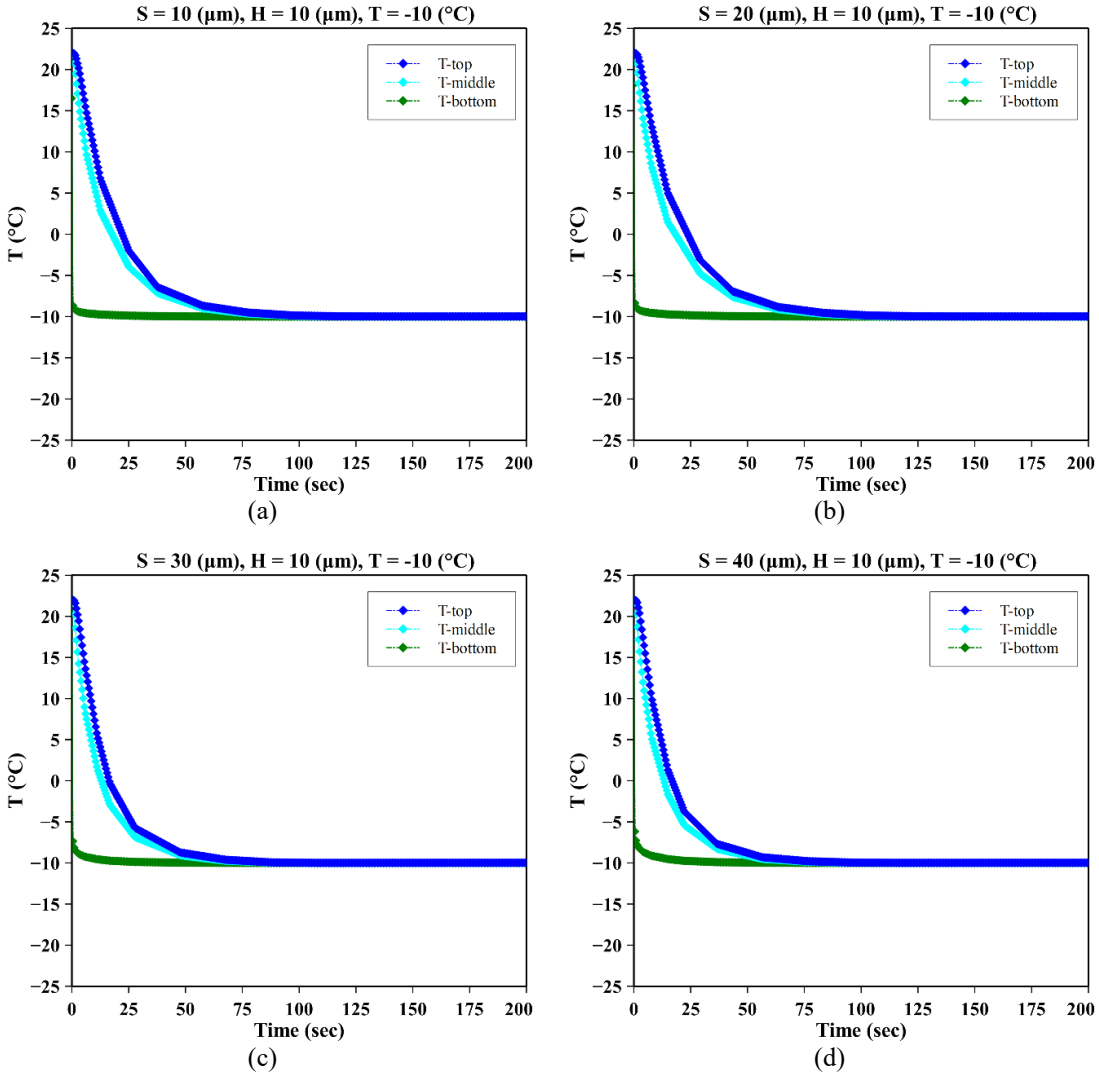

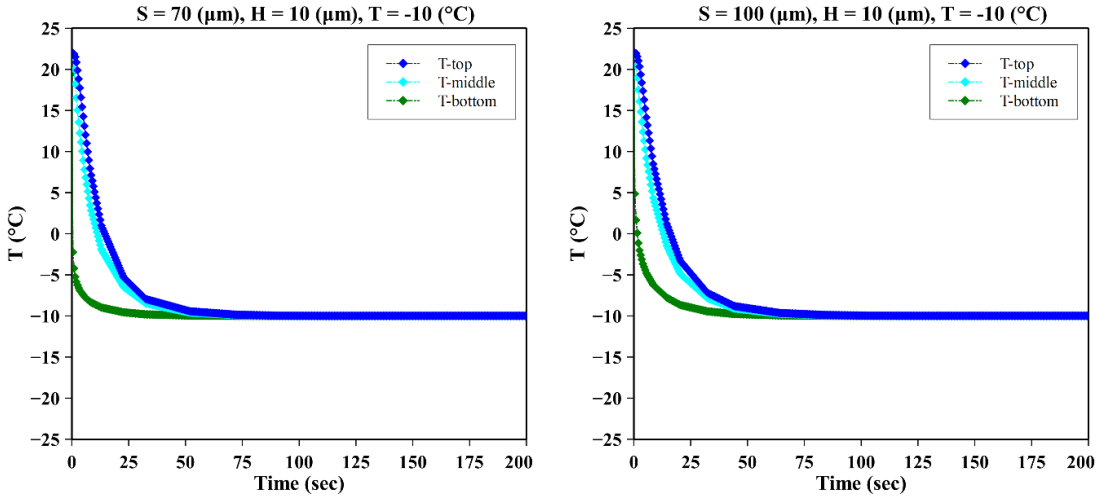

Figure A-II. 4: Temperature distribution profiles at different time instances for a micro-structured surface with H=10 µm at T = −10 °C; (a) S = 10 µm, (b) S = 20 µm, (c) S = 30 µm, (d) S = 40 µm, (e) S = 70 µm, (f) S = 100 µm.

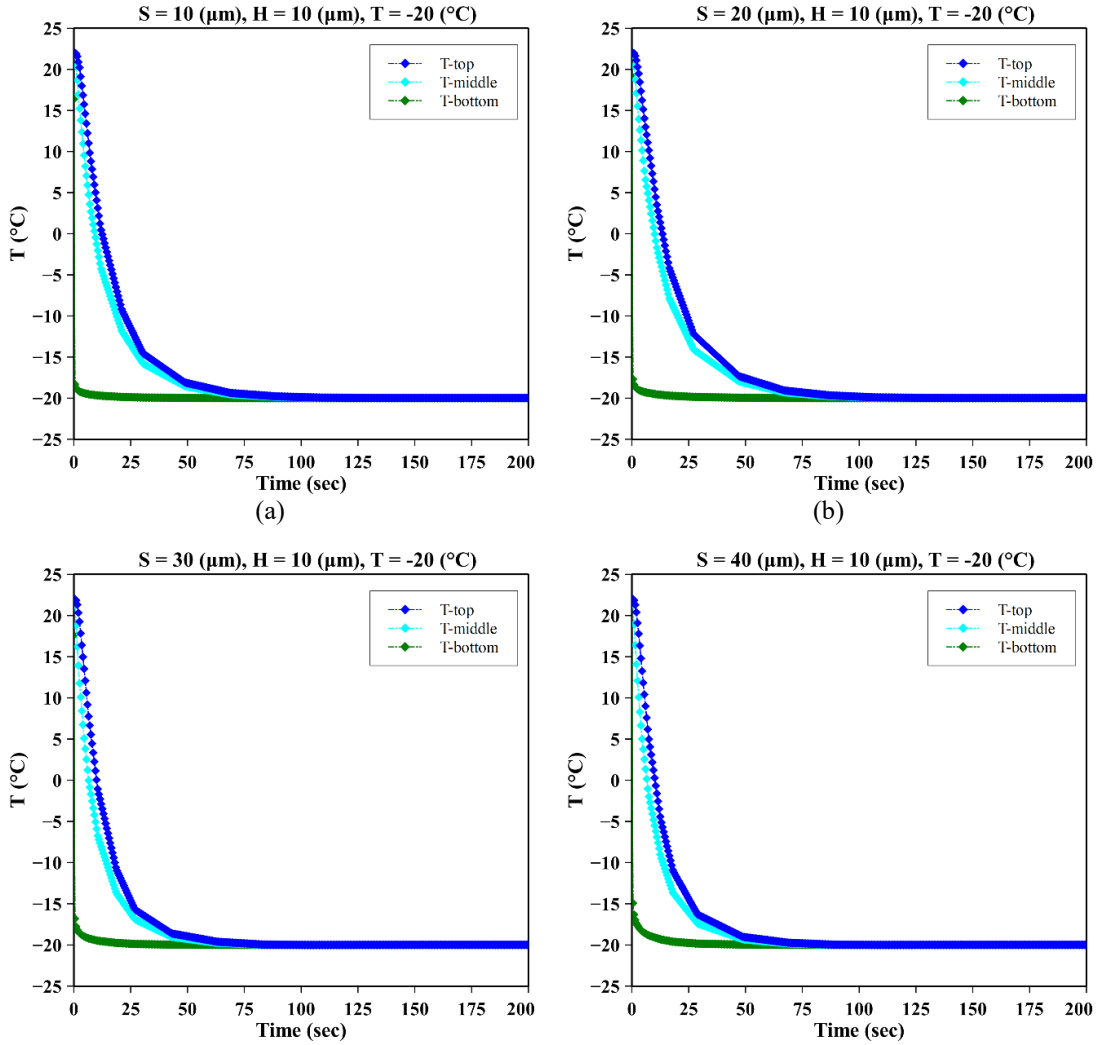

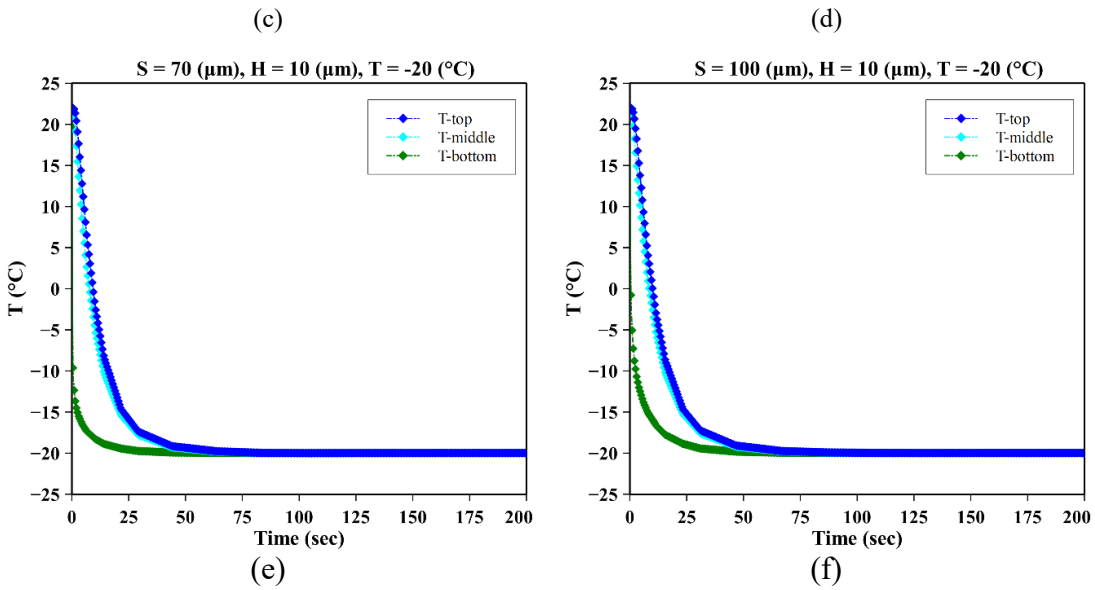

Figure A-II. 5: Temperature distribution profiles at different time instances for a micro-structured surface with H=10 µm at T = −20 ℃; (a) S = 10 µm, (b) S = 20 µm, (c) S = 30 µm, (d) S = 40 µm, (e) S = 70 µm, (f) S = 100 µm.

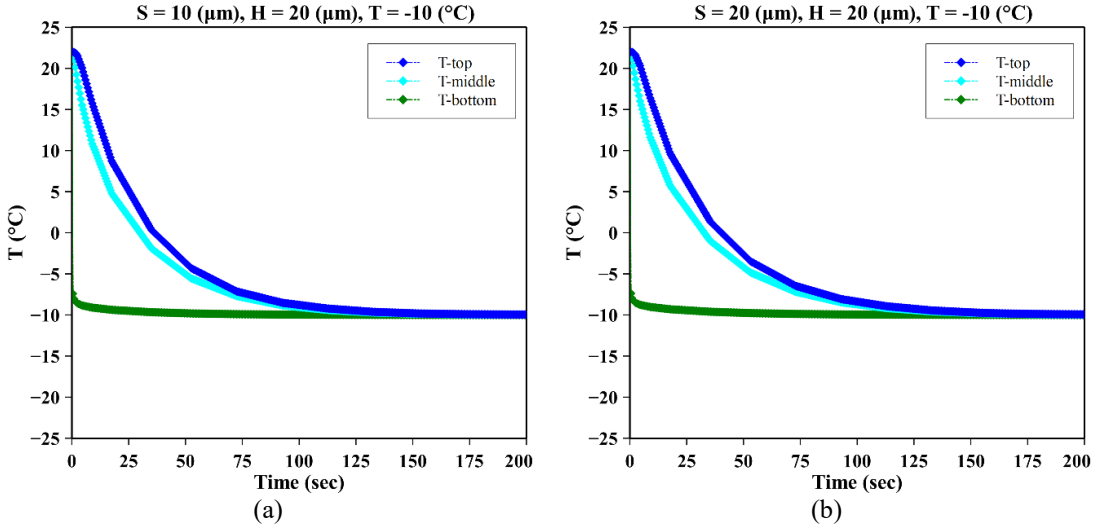

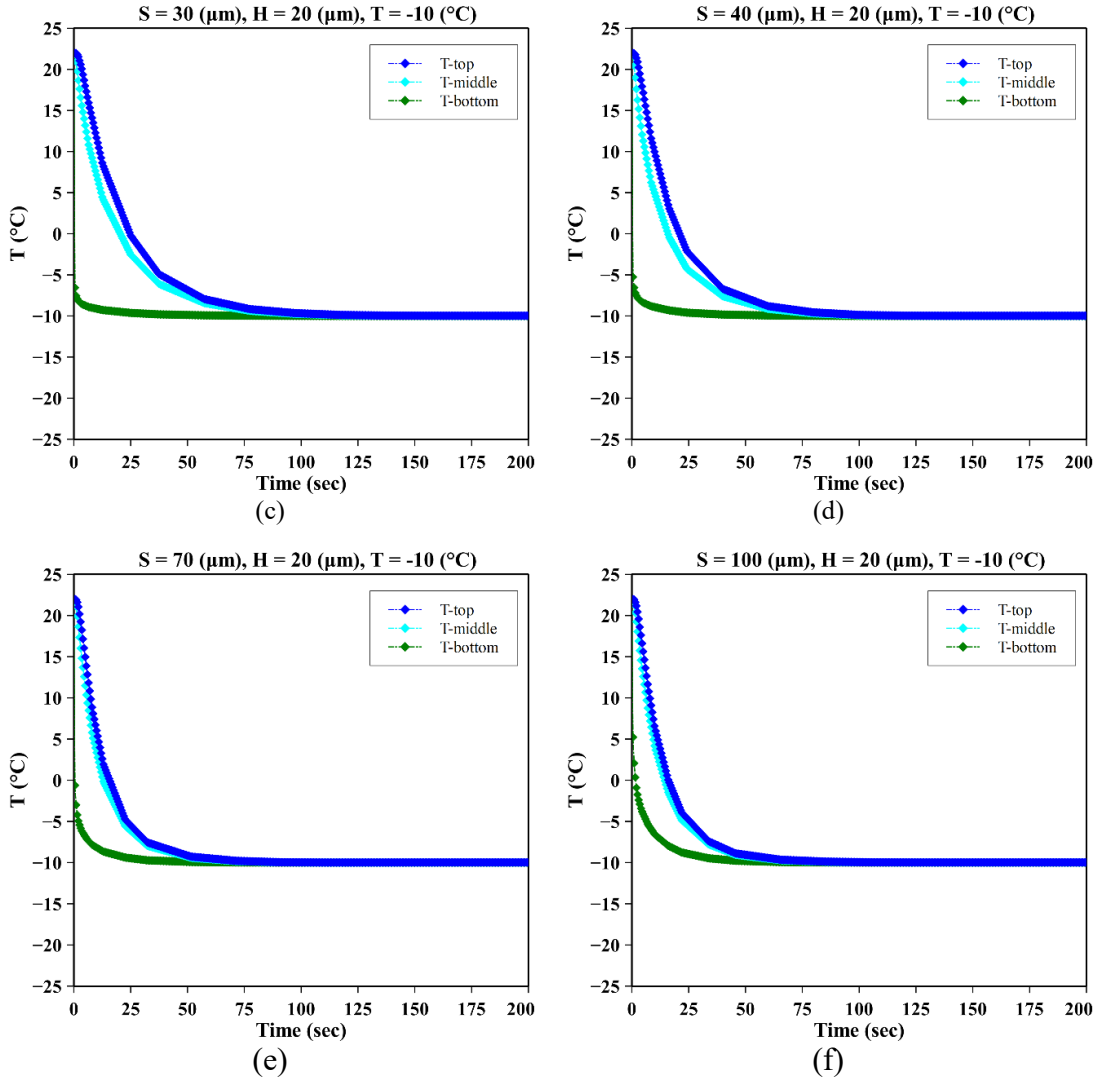

Figure A-II. 6: Temperature distribution profiles at different time instances for a micro-structured surface with H=20 µm at T = −10 ℃; (a) S = 10 µm, (b) S = 20 µm, (c) S = 30 µm, (d) S = 40 µm, (e) S = 70 µm, (f) S = 100 µm.

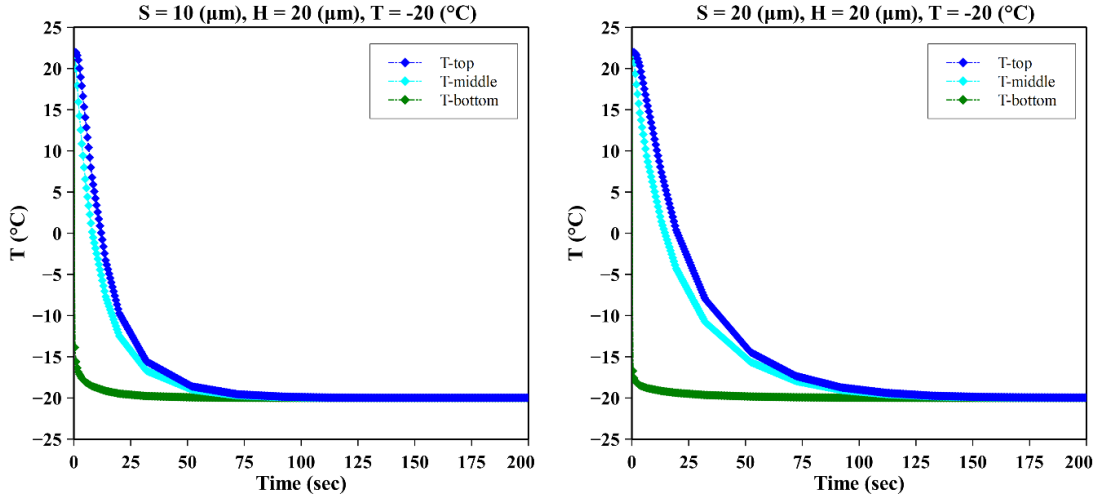

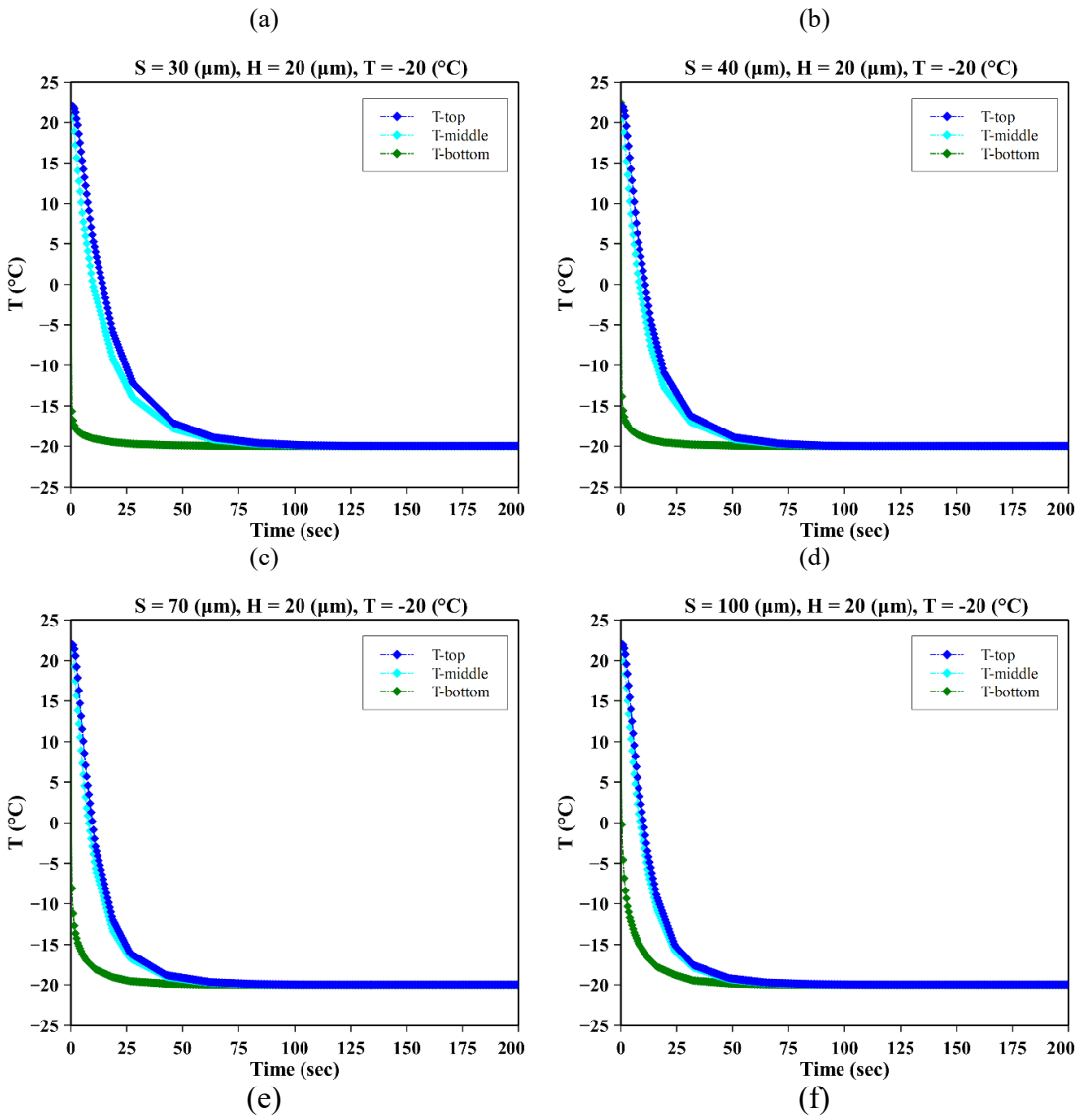

Figure A-II. 7: Temperature distribution profiles at different time instances for a micro-structured surface with H=20 µm at T = −20 °C; (a) S = 10 µm, (b) S = 20 µm, (c) S = 30 µm, (d) S = 40 µm, (e) S = 70 µm, (f) S = 100 µm.

Section 3. Ice nucleation delay time

The following equations provide additional details for the parameters mentioned in Equation 4-6.

In Equation 4-6, K(T) can be expressed as follows:

$$K(T) = \frac{K_B T}{h} \exp\left(\frac{-\frac{K_B T^2 E}{(T - T_R)^2}}{K_B T} \right) n \qquad \textit{Equation A-II. 6}$$

where k_B, h, and n are the Boltzmann constant ($1.38 \times 10^{-23}\, J/K$), Planck constant ($6.62 \times 10^{-34}\, J/S$), and the number density of water molecules at the ice nucleus/water interface (n $\approx 10^{19}\, m^{-2}$). In the temperature range of 150K to 273K, $T_R = 118\ K$ and $E = 892\ K$ have been determined experimentally for liquid water [140].

$$\gamma_{IW} = 28 + 0.25(T - 273.15) \qquad \textit{Equation A-II. 7}$$

$$\Delta G_V = \frac{T_m - T}{T_m} \Delta H_V \qquad \textit{Equation A-II. 8}$$

where T_m (K) $= 273.15$ is the melting point of ice at 1atm and ΔH_V (MJm^{-3}) = 278 is the enthalpy of fusion.

References

[1] Y. Cao, Z. Wu, Y. Su, Z. Xu, Aircraft flight characteristics in icing conditions, Prog. Aerosp. Sci. (2015). https://doi.org/10.1016/j.paerosci.2014.12.001.

[2] W.D. Hintz, R.A. Relyea, Impacts of road deicing salts on the early-life growth and development of a stream salmonid: Salt type matters, Environ. Pollut. (2017). https://doi.org/10.1016/j.envpol.2017.01.040.

[3] Z. Zhang, X.Y. Liu, Control of ice nucleation: Freezing and antifreeze strategies, Chem. Soc. Rev. 47 (2018) 7116–7139. https://doi.org/10.1039/c8cs00626a.

[4] M. Kerry, G. Kelk, D. Etkin, I. Burton, S. Kalhok, Glazed over: Canada copes with the ice storm of 1998, Environment. (1999). https://doi.org/10.1080/00139159909604608.

[5] C. Armenakis, N. Nirupama, Urban impacts of ice storms: Toronto December 2013, Nat. Hazards. (2014). https://doi.org/10.1007/s11069-014-1211-7.

[6] April ice storm cost Hydro-Quebec $14 million due to damage, overtime, (2019). https://www.thestar.com/news/canada/2019/06/15/april-ice-storm-cost-hydro-quebec-14-million-due-to-damage-overtime.html.

[7] G. Hou, K.K. Muraleetharan, V. Panchalogaranjan, P. Moses, A. Javid, H. Al-Dakheeli, R. Bulut, R. Campos, P.S. Harvey, G. Miller, K. Boldes, M. Narayanan, Resilience assessment and enhancement evaluation of power distribution systems subjected to ice storms, Reliab. Eng. Syst. Saf. (2023). https://doi.org/10.1016/j.ress.2022.108964.

[8] J.W. Busby, K. Baker, M.D. Bazilian, A.Q. Gilbert, E. Grubert, V. Rai, J.D. Rhodes, S. Shidore, C.A. Smith, M.E. Webber, Cascading risks: Understanding the 2021 winter blackout in Texas, Energy Res. Soc. Sci. (2021). https://doi.org/10.1016/j.erss.2021.102106.

[9] P. Irajizad, S. Nazifi, H. Ghasemi, Icephobic surfaces: Definition and figures of merit, Adv. Colloid Interface Sci. 269 (2019) 203–218. https://doi.org/10.1016/j.cis.2019.04.005.

[10] O. Parent, A. Ilinca, Anti-icing and de-icing techniques for wind turbines: Critical review, Cold Reg. Sci. Technol. 65 (2011) 88–96. https://doi.org/10.1016/j.coldregions.2010.01.005.

[11] Y. Yao, Y. Jiang, S. Deng, Z. Ma, A study on the performance of the airside heat exchanger under frosting in an air source heat pump water heater/chiller unit, Int. J. Heat Mass Transf. (2004). https://doi.org/10.1016/j.ijheatmasstransfer.2004.03.013.

[12] J.L. TULLIS, E.G. ROCHOW, Methods: Non-Wettable Surfaces, Blood. 7 (1952) 850–853. https://doi.org/10.1182/blood.V7.8.850.850.

[13] M. Farzaneh, C. Volat, A. Leblond, Anti-icing and de-icing techniques for overhead lines, in: Atmos. Icing Power Networks, 2008. https://doi.org/10.1007/978-1-4020-8531-4_6.

[14] W. Hou, Y. Shen, J. Tao, Y. Xu, J. Jiang, H. Chen, Z. Jia, Anti-icing performance of the superhydrophobic surface with micro-cubic array structures fabricated by plasma etching, Colloids Surfaces A Physicochem. Eng. Asp. 586 (2020) 124180. https://doi.org/10.1016/j.colsurfa.2019.124180.

[15] Y. Shen, X. Wu, J. Tao, C. Zhu, Y. Lai, Z. Chen, Progress in Materials Science Icephobic materials : Fundamentals , performance evaluation , and applications, Prog. Mater. Sci. 103 (2019) 509–557. https://doi.org/10.1016/j.pmatsci.2019.03.004.

[16] G. Wang, Y. Shen, J. Tao, X. Luo, L. Zhang, Y. Xia, RSC Advances Fabrication of a superhydrophobic surface with a hierarchical nano fl ake – micropit structure and its, (2017) 9981–9988. https://doi.org/10.1039/c6ra28298a.

[17] Z. He, H. Xie, M.I. Jamil, T. Li, Q. Zhang, Electro-/Photo-Thermal Promoted Anti-Icing Materials: A New Strategy Combined with Passive Anti-Icing and Active De-Icing, Adv. Mater. Interfaces. 9 (2022). https://doi.org/10.1002/admi.202200275.

[18] X. Huang, N. Tepylo, V. Pommier-Budinger, M. Budinger, E. Bonaccurso, P. Villedieu, L. Bennani, A survey of icephobic coatings and their potential use in a hybrid coating/active ice protection system for aerospace applications, Prog. Aerosp. Sci. (2019). https://doi.org/10.1016/j.paerosci.2019.01.002.

[19] T.M. Schutzius, S. Jung, T. Maitra, P. Eberle, C. Antonini, C. Stamatopoulos, D. Poulikakos, Physics of Icing and Rational Design of Surfaces with Extraordinary Icephobicity, Langmuir. 31 (2015) 4807–4821. https://doi.org/10.1021/la502586a.

[20] A.M. Robin H.A. Ras, Non-wettable Surfaces: Theory, Preparation and Applications, 2016.

[21] A. Azimi Yancheshme, G. Momen, R. Jafari Aminabadi, Mechanisms of ice formation and propagation on superhydrophobic surfaces: A review, Adv. Colloid Interface Sci. 279 (2020) 102155. https://doi.org/10.1016/j.cis.2020.102155.

[22] S. Heydarian, R. Jafari, G. Momen, Recent progress in the anti-icing performance of slippery liquid-infused surfaces, Prog. Org. Coatings. 151 (2021) 106096. https://doi.org/10.1016/j.porgcoat.2020.106096.

[23] X. Wu, X. Zhao, J.W.C. Ho, Z. Chen, Design and durability study of environmental-friendly room-temperature processable icephobic coatings, Chem. Eng. J. (2019). https://doi.org/10.1016/j.cej.2018.07.204.

[24] Y. Zhuo, S. Xiao, A. Amirfazli, J. He, Z. Zhang, Polysiloxane as icephobic materials – The past, present and the future, Chem. Eng. J. (2021). https://doi.org/10.1016/j.cej.2020.127088.

[25] P. Irajizad, S. Nazi, H. Ghasemi, Icephobic surfaces : De fi nition and fi gures of merit, 269 (2019) 203–218. https://doi.org/10.1016/j.cis.2019.04.005.

[26] M.J. Kreder, J. Alvarenga, P. Kim, J. Aizenberg, Design of anti-icing surfaces: Smooth, textured or slippery?, Nat. Rev. Mater. 1 (2016) 15003. https://doi.org/10.1038/natrevmats.2015.3.

[27] C.W. Lo, V. Sahoo, M.C. Lu, Control of Ice Formation, ACS Nano. (2017). https://doi.org/10.1021/acsnano.6b07348.

[28] S. Jung, M.K. Tiwari, N.V. Doan, D. Poulikakos, freezing on surfaces, Nat. Commun. (2012). https://doi.org/10.1038/ncomms1630.

[29] Y. Shen, X. Xie, Y. Xie, J. Tao, J. Jiang, H. Chen, Y. Lu, Y. Xu, Statistically understanding the roles of nanostructure features in interfacial ice nucleation for enhancing icing delay performance, Phys. Chem. Chem. Phys. 21 (2019) 19785–19794. https://doi.org/10.1039/C9CP04103F.

[30] J. Jiang, G.X.X. Li, Q. Sheng, G.H.H. Tang, Microscopic mechanism of ice nucleation: The effects of surface rough structure and wettability, Appl. Surf. Sci. 510 (2020) 145520. https://doi.org/10.1016/j.apsusc.2020.145520.

[31] Freezing delay of sessile drops : probing the impact of contact angle , surface roughness and thermal conductivity Highlights - Factors affecting the freezing delay of sessile drops on solid surfaces is still a matter of discussion and controversy . - Sur, (n.d.).

[32] T. Vasileiou, T.M. Schutzius, D. Poulikakos, Imparting Icephobicity with Substrate Flexibility, Langmuir. 33 (2017) 6708–6718. https://doi.org/10.1021/acs.langmuir.7b01412.

[33] M. Abolghasemibizaki, R. Mohammadi, Droplet impact on superhydrophobic surfaces fully decorated with cylindrical macrotextures, J. Colloid Interface Sci. 509 (2018) 422–431. https://doi.org/10.1016/j.jcis.2017.09.030.

[34] L. Boinovich, A.M. Emelyanenko, V. V. Korolev, A.S. Pashinin, Effect of wettability on sessile drop freezing: When superhydrophobicity stimulates an extreme freezing delay, Langmuir. 30 (2014) 1659–1668. https://doi.org/10.1021/la403796g.

[35] G. Wang, Y. Shen, J. Tao, X. Luo, L. Zhang, Y. Xia, Fabrication of a superhydrophobic surface with a hierarchical nanoflake-micropit structure and its anti-icing properties, RSC Adv. 7 (2017) 9981–9988. https://doi.org/10.1039/c6ra28298a.

[36] Y. Qi, Z. Yang, T. Chen, Y. Xi, J. Zhang, Fabrication of superhydrophobic surface

with desirable anti-icing performance based on micro/nano-structures and organosilane groups, Appl. Surf. Sci. 501 (2020) 144165. https://doi.org/10.1016/j.apsusc.2019.144165.

[37] S. Farhadi, M. Farzaneh, S.A. Kulinich, Anti-icing performance of superhydrophobic surfaces, Appl. Surf. Sci. (2011). https://doi.org/10.1016/j.apsusc.2011.02.057.

[38] III. An essay on the cohesion of fluids, Philos. Trans. R. Soc. London. 95 (1805) 65–87. https://doi.org/10.1098/rstl.1805.0005.

[39] R.D. Hazlett, Fractal applications: Wettability and contact angle, J. Colloid Interface Sci. (1990). https://doi.org/10.1016/0021-9797(90)90425-N.

[40] B. Mockenhaupt, H.J. Ensikat, M. Spaeth, W. Barthlott, Superhydrophobicity of biological and technical surfaces under moisture condensation: Stability in relation to surface structure, Langmuir. (2008). https://doi.org/10.1021/la802351h.

[41] A. Lafuma, D. Quéré, Superhydrophobic states, Nat. Mater. (2003). https://doi.org/10.1038/nmat924.

[42] K. Lum, D. Chandler, J.D. Weeks, Hydrophobicity at small and large length scales, J. Phys. Chem. B. (1999). https://doi.org/10.1021/jp984327m.

[43] R.N. Wenzel, Resistance of solid surfaces to wetting by water, Ind. Eng. Chem. (1936). https://doi.org/10.1021/ie50320a024.

[44] A.B.D. Cassie, S. Baxter, Wettability of porous surfaces, Trans. Faraday Soc. 40 (1944) 546. https://doi.org/10.1039/tf9444000546.

[45] G. Nagayama, D. Zhang, Intermediate wetting state at nano/microstructured surfaces, Soft Matter. (2020). https://doi.org/10.1039/c9sm02513h.

[46] Y. Yu, D. Zhang, G. Nagayama, Estimation of surface free energy at microstructured surface to investigate intermediate wetting state for partial wetting model, Soft Matter. 19 (2023) 1249–1257. https://doi.org/10.1039/D2SM01406H.

[47] R.E. Johnson, R.H. Dettre, Contact angle hysteresis. III. Study of an idealized heterogeneous surface, J. Phys. Chem. (1964). https://doi.org/10.1021/j100789a012.

[48] S. Wang, K. Liu, X. Yao, L. Jiang, Bioinspired surfaces with superwettability: New insight on theory, design, and applications, Chem. Rev. (2015). https://doi.org/10.1021/cr400083y.

[49] S. Keshavarzi, A. Entezari, K. Maghsoudi, G. Momen, R. Jafari, Ice nucleation on silicone rubber surfaces differing in roughness parameters and wettability: Experimental investigation and machine learning–based predictions, Cold Reg. Sci. Technol. 203 (2022) 103659. https://doi.org/10.1016/j.coldregions.2022.103659.

[50] S. Keshavarzi, B. Bouazara, G. Momen, R. Jafari, Hydrophobicity and icephobicity of micropillared silicone rubber surfaces fabricated by compression molding, Results in Surfaces and Interfaces. (2023). https://doi.org/10.1016/j.rsurfi.2023.100132.

[51] K. Ellinas, P. Dimitrakellis, P. Sarkiris, E. Gogolides, A Review of Fabrication Methods, Properties and Applications of Superhydrophobic Metals, Processes. 9 (2021) 666. https://doi.org/10.3390/pr9040666.

[52] E.S. Gadelmawla, M.M. Koura, T.M.A. Maksoud, I.M. Elewa, H.H. Soliman, Roughness parameters, J. Mater. Process. Technol. 123 (2002) 133–145. https://doi.org/10.1016/S0924-0136(02)00060-2.

[53] A.M. Worthington, A Study of Splashes, Longmans, Green Co. (1908).

[54] J. Kim, Spray cooling heat transfer: The state of the art, Int. J. Heat Fluid Flow. 28 (2007) 753–767. https://doi.org/10.1016/j.ijheatfluidflow.2006.09.003.

[55] H. Wijshoff, Drop dynamics in the inkjet printing process, Curr. Opin. Colloid Interface Sci. 36 (2018) 20–27. https://doi.org/10.1016/j.cocis.2017.11.004.

[56] S. Mashaghi, A. Abbaspourrad, D.A. Weitz, A.M. van Oijen, Droplet microfluidics: A tool for biology, chemistry and nanotechnology, TrAC Trends Anal. Chem. 82 (2016) 118–125. https://doi.org/10.1016/j.trac.2016.05.019.

[57] M.G. Potapczuk, Aircraft Icing Research at NASA Glenn Research Center, J. Aerosp. Eng. 26 (2013) 260–276. https://doi.org/10.1061/(ASCE)AS.1943-5525.0000322.

[58] S. Shi, C. Lv, Q. Zheng, Drop Impact on Two-Tier Monostable Superrepellent Surfaces, ACS Appl. Mater. Interfaces. 11 (2019) 43698–43707. https://doi.org/10.1021/acsami.9b14880.

[59] C. Antonini, M. Innocenti, T. Horn, M. Marengo, A. Amirfazli, Understanding the effect of superhydrophobic coatings on energy reduction in anti-icing systems, Cold Reg. Sci. Technol. 67 (2011) 58–67. https://doi.org/10.1016/j.coldregions.2011.02.006.

[60] D. Khojasteh, M. Kazerooni, S. Salarian, R. Kamali, Droplet impact on superhydrophobic surfaces: A review of recent developments, J. Ind. Eng. Chem. 42 (2016) 1–14. https://doi.org/10.1016/j.jiec.2016.07.027.

[61] A.L. Yarin, DROP IMPACT DYNAMICS: Splashing, Spreading, Receding, Bouncing…, Annu. Rev. Fluid Mech. 38 (2006) 159–192. https://doi.org/10.1146/annurev.fluid.38.050304.092144.

[62] Y. Pan, K. Shi, X. Duan, G.F. Naterer, Experimental investigation of water droplet impact and freezing on micropatterned stainless steel surfaces with varying wettabilities, Int. J. Heat Mass Transf. 129 (2019) 953–964. https://doi.org/10.1016/j.ijheatmasstransfer.2018.10.032.

[63] S. Moghtadernejad, C. Lee, M. Jadidi, An Introduction of Droplet Impact Dynamics to Engineering Students, Fluids. 5 (2020) 107. https://doi.org/10.3390/fluids5030107.

[64] M. Pasandideh-Fard, Y.M. Qiao, S. Chandra, J. Mostaghimi, M. Pasandideh-Fard, Y.M. Qiao, S. Chandra, J. Mostaghimi, Capillary effects during droplet impact on a solid surface, Phys. Fluids. 8 (1996) 650–659. https://doi.org/10.1063/1.868850.

[65] J. Madejski, Solidification of droplets on a cold surface, Int. J. Heat Mass Transf. 19 (1976) 1009–1013. https://doi.org/10.1016/0017-9310(76)90183-6.

[66] T. Bennett, D. Poulikakos, Splat-quench solidification: estimating the maximum spreading of a droplet impacting a solid surface, J. Mater. Sci. 28 (1993) 963–970. https://doi.org/10.1007/BF00400880.

[67] B.L. Scheller, D.W. Bousfield, Newtonian drop impact with a solid surface, AIChE J. 41 (1995) 1357–1367. https://doi.org/10.1002/aic.690410602.

[68] C. Clanet, C. Béguin, D. Richard, D. Quéré, Maximal deformation of an impacting drop, J. Fluid Mech. 517 (2004) 199–208. https://doi.org/10.1017/S0022112004000904.

[69] A. Rozhkov, B. Prunet–Foch, M. Vignes–Adler, Dynamics of a liquid lamella resulting from the impact of a water drop on a small target, Proc. R. Soc. London. Ser. A Math. Phys. Eng. Sci. 460 (2004) 2681–2704. https://doi.org/10.1098/rspa.2004.1293.

[70] C. Ukiwe, D.Y. Kwok, On the Maximum Spreading Diameter of Impacting Droplets on Well-Prepared Solid Surfaces, Langmuir. 21 (2005) 666–673. https://doi.org/10.1021/la0481288.

[71] I.S. BAYER, C.M. MEGARIDIS, Contact angle dynamics in droplets impacting on flat surfaces with different wetting characteristics, J. Fluid Mech. 558 (2006) 415. https://doi.org/10.1017/S0022112006000231.

[72] I. V. Roisman, Inertia dominated drop collisions. II. An analytical solution of the Navier–Stokes equations for a spreading viscous film, Phys. Fluids. 21 (2009) 052104. https://doi.org/10.1063/1.3129283.

[73] M. Budakli, Prediction of maximum spreading factor after drop impact: Development of a novel semi-analytical model incorporating effect of surface roughness, Colloid Interface Sci. Commun. 41 (2021) 100384. https://doi.org/10.1016/j.colcom.2021.100384.

[74] T. Mao, D.C.S. Kuhn, H. Tran, Spread and rebound of liquid droplets upon impact on flat surfaces, AIChE J. 43 (1997) 2169–2179. https://doi.org/10.1002/aic.690430903.

[75] Z. Jin, H. Zhang, Z. Yang, Experimental investigation of the impact and freezing processes of a water droplet on an ice surface, Int. J. Heat Mass Transf. (2017).

https://doi.org/10.1016/j.ijheatmasstransfer.2017.02.055.

[76] R. Zhang, P. Hao, X. Zhang, F. He, Supercooled water droplet impact on superhydrophobic surfaces with various roughness and temperature, Int. J. Heat Mass Transf. (2018). https://doi.org/10.1016/j.ijheatmasstransfer.2018.01.076.

[77] C. Tang, M. Qin, X. Weng, X. Zhang, P. Zhang, J. Li, Z. Huang, Dynamics of droplet impact on solid surface with different roughness, Int. J. Multiph. Flow. 96 (2017) 56–69. https://doi.org/10.1016/j.ijmultiphaseflow.2017.07.002.

[78] L. Xu, W.W. Zhang, S.R. Nagel, Drop splashing on a dry smooth surface, Phys. Rev. Lett. 94 (2005) 1–4. https://doi.org/10.1103/PhysRevLett.94.184505.

[79] X. Yan, L. Zhang, S. Sett, L. Feng, C. Zhao, Z. Huang, H. Vahabi, A.K. Kota, F. Chen, N. Miljkovic, Droplet Jumping: Effects of Droplet Size, Surface Structure, Pinning, and Liquid Properties, ACS Nano. 13 (2019) 1309–1323. https://doi.org/10.1021/acsnano.8b06677.

[80] R. Rioboo, C. Tropea, M. Marengo, Outcomes from a drop impact on solid surfaces, At. Sprays. (2001). https://doi.org/10.1615/atomizspr.v11.i2.40.

[81] C. Josserand, S.T. Thoroddsen, Drop Impact on a Solid Surface, Annu. Rev. Fluid Mech. 48 (2016) 365–391. https://doi.org/10.1146/annurev-fluid-122414-034401.

[82] P. Tsai, S. Pacheco, C. Pirat, L. Lefferts, D. Lohse, Drop impact upon micro- and nanostructured superhydrophobic surfaces, Langmuir. 25 (2009) 12293–12298. https://doi.org/10.1021/la900330q.

[83] F. Yeganehdoust, R. Attarzadeh, A. Dolatabadi, I. Karimfazli, A comparison of bioinspired slippery and superhydrophobic surfaces: Micro-droplet impact, Phys. Fluids. 33 (2021) 022105. https://doi.org/10.1063/5.0035556.

[84] N.D. Patil, R. Bhardwaj, A. Sharma, Droplet impact dynamics on micropillared hydrophobic surfaces, Exp. Therm. Fluid Sci. 74 (2016) 195–206. https://doi.org/10.1016/j.expthermflusci.2015.12.006.

[85] Z. Li, Q. Kong, X. Ma, D. Zang, X. Guan, X. Ren, Dynamic effects and adhesion of water droplet impact on hydrophobic surfaces: Bouncing or sticking, Nanoscale. (2017). https://doi.org/10.1039/c7nr02906c.

[86] C. Hao, J. Li, Y. Liu, X. Zhou, Y. Liu, R. Liu, L. Che, W. Zhou, D. Sun, L. Li, L. Xu, Z. Wang, Superhydrophobic-like tunable droplet bouncing on slippery liquid interfaces, Nat. Commun. (2015). https://doi.org/10.1038/ncomms8986.

[87] R. Rioboo, M. Marengo, C. Tropea, Time evolution of liquid drop impact onto solid, dry surfaces, Exp. Fluids. 33 (2002) 112–124. https://doi.org/10.1007/s00348-002-0431-x.

[88] B. Thesis, The influence of electrowetting on the behavior of impacting droplets on superhydrophobic surfaces, (2015).

[89] C. Antonini, A. Amirfazli, M. Marengo, Drop impact and wettability: From hydrophilic to superhydrophobic surfaces, Phys. Fluids. 24 (2012) 102104. https://doi.org/10.1063/1.4757122.

[90] P. Foltyn, D. Ribeiro, A. Silva, G. Lamanna, B. Weigand, Influence of wetting behavior on the morphology of droplet impacts onto dry smooth surfaces, Phys. Fluids. 33 (2021) 063305. https://doi.org/10.1063/5.0053539.

[91] P.G. Bange, R. Bhardwaj, Computational study of bouncing and non-bouncing droplets impacting on superhydrophobic surfaces, Theor. Comput. Fluid Dyn. 30 (2016) 211–235. https://doi.org/10.1007/s00162-015-0376-3.

[92] D. Khojasteh, A. Bordbar, R. Kamali, M. Marengo, Curvature effect on droplet impacting onto hydrophobic and superhydrophobic spheres, Int. J. Comut. Fluid Dyn. 31 (2017) 310–323. https://doi.org/10.1080/10618562.2017.1349312.

[93] M.A. Quetzeri-Santiago, A.A. Castrejón-Pita, J.R. Castrejón-Pita, The Effect of Surface Roughness on the Contact Line and Splashing Dynamics of Impacting Droplets, Sci. Rep. 9 (2019) 15030. https://doi.org/10.1038/s41598-019-51490-5.

[94] T. de Goede, K. de Bruin, N. Shahidzadeh, D. Bonn, Droplet splashing on rough surfaces, Phys. Rev. Fluids. 6 (2021) 043604. https://doi.org/10.1103/PhysRevFluids.6.043604.

[95] H. Zhang, X. Zhang, X. Yi, Y. Du, F. He, F. Niu, P. Hao, How surface roughness promotes or suppresses drop splash, Phys. Fluids. 34 (2022). https://doi.org/10.1063/5.0079494.

[96] Y. Bao, Z. Wang, Z. Shi, Y. Gan, A Modified Weber Number Capturing the Bouncing–Wetting Transition of Droplet Impact on Rough Surfaces, Adv. Mater. Interfaces. 10 (2023). https://doi.org/10.1002/admi.202201873.

[97] P.J. Cruz, P.-P. De Breuck, G.-M. Rignanese, K. Glinel, A.M. Jonas, Influence of roughness and coating on the rebound of droplets on fabrics, Surfaces and Interfaces. 36 (2023) 102524. https://doi.org/10.1016/j.surfin.2022.102524.

[98] L. Wang, A. Zhou, J. Zhou, L. Chen, Y. Yu, Soft Matter Droplet impact on pillar-arrayed non-wetting surfaces, (2021) 5932–5940. https://doi.org/10.1039/d1sm00354b.

[99] S. Process, Droplet Impact on the Super-Hydrophobic Surface with Micro-Pillar Arrays Fabricated by Hybrid Laser, (2019). https://doi.org/10.3390/ma12050765.

[100] N.S. Singh, T. Jitniyom, M. Navarro-Cía, N. Gao, Droplet impact on doubly re-entrant structures, Sci. Rep. 14 (2024) 2700. https://doi.org/10.1038/s41598-024-52951-2.

[101] L. Xia, Z. Yang, F. Chen, T. Liu, Y. Tian, D. Zhang, Droplet impacting on pillared hydrophobic surfaces with different solid fractions, J. Colloid Interface Sci. 658 (2024) 61–73. https://doi.org/10.1016/j.jcis.2023.12.053.

[102] H. Tan, Numerical study on splashing of high-speed microdroplet impact on dry microstructured surfaces, Comput. Fluids. 154 (2017) 142–166. https://doi.org/10.1016/j.compfluid.2017.05.014.

[103] M. Broom, G.R. Willmott, Water drop impacts on regular micropillar arrays: Asymmetric spreading, Phys. Fluids. 35 (2023). https://doi.org/10.1063/5.0153645.

[104] Z. Jin, H. Zhang, Z. Yang, The impact and freezing processes of a water droplet on a cold surface with different inclined angles, Int. J. Heat Mass Transf. (2016). https://doi.org/10.1016/j.ijheatmasstransfer.2016.08.012.

[105] T. Maitra, M.K. Tiwari, C. Antonini, P. Schoch, S. Jung, P. Eberle, D. Poulikakos, On the nanoengineering of superhydrophobic and impalement resistant surface textures below the freezing temperature, Nano Lett. (2014). https://doi.org/10.1021/nl4037092.

[106] T. Maitra, C. Antonini, M.K. Tiwari, A. Mularczyk, Z. Imeri, P. Schoch, D. Poulikakos, Supercooled Water Drops Impacting Superhydrophobic Textures, Langmuir. 30 (2014) 10855–10861. https://doi.org/10.1021/la502675a.

[107] K.R. Khedir, G.K. Kannarpady, H. Ishihara, J. Woo, M.P. Asar, C. Ryerson, A.S. Biris, Temperature-dependent bouncing of super-cooled water on teflon-coated superhydrophobic tungsten nanorods, Appl. Surf. Sci. 279 (2013) 76–84. https://doi.org/10.1016/j.apsusc.2013.04.038.

[108] A. Alizadeh, V. Bahadur, S. Zhong, W. Shang, R. Li, J. Ruud, M. Yamada, L. Ge, A. Dhinojwala, M. Sohal, Temperature dependent droplet impact dynamics on flat and textured surfaces, Appl. Phys. Lett. 100 (2012) 2010–2014. https://doi.org/10.1063/1.3692598.

[109] Y. Shang, Y. Zhang, Y. Hou, B. Bai, X. Zhong, Effects of surface subcooling on the spreading dynamics of an impact water droplet, Phys. Fluids. 32 (2020). https://doi.org/10.1063/5.0028081.

[110] X. Zhou, H. Wang, J. Wu, Q. Zhang, X. Zhu, Y. Ding, R. Chen, Q. Liao, Bounce behaviors of double droplets simultaneously impact cold superhydrophobic surface, Int. J. Heat Mass Transf. 208 (2023) 124075. https://doi.org/10.1016/j.ijheatmasstransfer.2023.124075.

[111] X. Zhang, K. Li, Z. Zhu, W.-Z. Fang, F.-Q. Zhu, C. Yang, Droplet impact and freezing dynamics on ultra-cold surfaces: A scaling analysis of central-concave pattern, Appl. Therm. Eng. 239 (2024) 122135. https://doi.org/10.1016/j.applthermaleng.2023.122135.

[112] H. Yu, X. Zhou, H. Wang, Q. Zhang, X. Zhu, Y.D. Ding, R. Chen, Q. Liao, Effect of temperature difference between impinging droplet and cold superhydrophobic surface on its dynamic behavior, Exp. Therm. Fluid Sci. 150 (2024) 111049. https://doi.org/10.1016/j.expthermflusci.2023.111049.

[113] Y. Yao, K. Wu, R. Yang, H. Zhang, W. Yang, C. Li, Effects of surface temperature and Weber number on the dynamic and freezing behavior of impacting water droplets on a superhydrophobic ultra-cold surface, Appl. Therm. Eng. 236 (2024) 121705. https://doi.org/10.1016/j.applthermaleng.2023.121705.

[114] C. Guo, L. Liu, R. Yang, J. Lu, S. Liu, Bouncing Regimes of Supercooled Water Droplets Impacting Superhydrophobic Surfaces with Controlled Temperature and Humidity, Langmuir. 39 (2023) 10199–10208. https://doi.org/10.1021/acs.langmuir.3c01099.

[115] P. Hao, C. Lv, X. Zhang, Freezing of sessile water droplets on surfaces with various roughness and wettability, Appl. Phys. Lett. 104 (2014) 161609. https://doi.org/10.1063/1.4873345.

[116] P. Guo, Y. Zheng, M. Wen, C. Song, Y. Lin, L. Jiang, Icephobic/anti-icing properties of micro/nanostructured surfaces, Adv. Mater. 24 (2012) 2642–2648. https://doi.org/10.1002/adma.201104412.

[117] C. Antonini, A. Amirfazli, M. Marengo, Superhydrophobicity or icephobicity for an effective icing mitigation strategy?, in: Proc. 15th Int. Heat Transf. Conf. IHTC 2014, 2014. https://doi.org/10.1615/ihtc15.nmt.009482.

[118] G. Dhanaraj, K. Byrappa, V. Prasad, M. Dudley, K. Schmetzer, Springer Handbook of Crystal Growth, Japanese Mag. Mineral. Petrol. Sci. (2010). https://doi.org/10.2465/gkk.39.193a.

[119] I. V Markov, Crystal Growth for Beginners, 2003. https://doi.org/10.1142/5172.

[120] J.W. Gibbs, H.A. Bumstead, W.R. Longley, Van Name, RG On the Equilibrium of Heterogeneous Substances, Collected Works, (1928).

[121] J.W. Gibbs, On the equilibrium of heterogeneous substances, Am. J. Sci. (1878). https://doi.org/10.2475/ajs.s3-16.96.441.

[122] D. Turnbull, J.C. Fisher, Rate of Nucleation in Condensed Systems, J. Chem. Phys. 17 (1949) 71–73. https://doi.org/10.1063/1.1747055.

[123] H.R. Pruppacher, J.D. Klett, Microphysics of Clouds and Precipitation, Springer Netherlands, Dordrecht, 2010. https://doi.org/10.1007/978-0-306-48100-0.

[124] Y. Bi, B. Cao, T. Li, Enhanced heterogeneous ice nucleation by special surface geometry, Nat. Commun. (2017). https://doi.org/10.1038/ncomms15372.

[125] J. Frenkel, A General Theory of Heterophase Fluctuations and Pretransition Phenomena, J. Chem. Phys. 7 (1939) 538–547. https://doi.org/10.1063/1.1750484.

[126] R. Becker, W. Döring, The Kinetic Treatment of Nuclear Formation in Supersaturated Vapors, Ann. Phys. (1935).

[127] A. Volmer, M.; Weber, Nucleus Formation in Supersaturated Systems, Z. Phys. Chem. (1926).

[128] J.Y. Yan, G.N. Patey, Molecular dynamics simulations of ice nucleation by electric fields, J. Phys. Chem. A. (2012). https://doi.org/10.1021/jp3039187.

[129] E.B. Moore, V. Molinero, Structural transformation in supercooled water controls the crystallization rate of ice, Nature. (2011). https://doi.org/10.1038/nature10586.

[130] E.J. Langham, B.J. Mason, The heterogeneous and homogeneous nucleation of supercooled water, Proc. R. Soc. London. Ser. A. Math. Phys. Sci. 247 (1958) 493–504. https://doi.org/10.1098/rspa.1958.0207.

[131] X.Y. Liu, Heterogeneous nucleation or homogeneous nucleation?, J. Chem. Phys. 112 (2000) 9949–9955. https://doi.org/10.1063/1.481644.

[132] I. V Markov, Crysta growth for beginners, 2003.

[133] F. Tancini, Y.-L. Wu, W.B. Schweizer, J.-P. Gisselbrecht, C. Boudon, P.D. Jarowski, M.T. Beels, I. Biaggio, F. Diederich, 1,1-Dicyano-4-[4-(diethylamino)phenyl]buta-1,3-dienes: Structure-Property Relationships, European J. Org. Chem. 2012 (2012) 2756–2765. https://doi.org/10.1002/ejoc.201200111.

[134] G. Vali, ICE NUCLEATION C THEORY, Molecules. (1999).

[135] T. Li, D. Donadio, L.M. Ghiringhelli, G. Galli, Surface-induced crystallization in supercooled tetrahedral liquids, Nat. Mater. 8 (2009) 726–730. https://doi.org/10.1038/nmat2508.

[136] K. Li, S. Xu, W. Shi, M. He, H. Li, S. Li, X. Zhou, J. Wang, Y. Song, Investigating the effects of solid surfaces on Ice nucleation, Langmuir. 28 (2012) 10749–10754. https://doi.org/10.1021/la3014915.

[137] Z. Guo, F. Yang, Introduction for Biomimetic Superhydrophobic Materials, in: Surfaces Interfaces Biomim. Superhydrophobic Mater., Wiley-VCH Verlag GmbH & Co. KGaA, Weinheim, Germany, 2018: pp. 1–24. https://doi.org/10.1002/9783527806720.ch1.

[138] N.H. Fletcher, Size effect in heterogeneous nucleation, J. Chem. Phys. 29 (1958) 572–576. https://doi.org/10.1063/1.1744540.

[139] B. Na, R.L. Webb, A fundamental understanding of factors affecting frost nucleation,

Int. J. Heat Mass Transf. 46 (2003) 3797–3808. https://doi.org/10.1016/S0017-9310(03)00194-7.

[140] R.S. Smith, B.D. Kay, The existence of supercooled liquid water at 150?K, Nature. 398 (1999) 788–791. https://doi.org/10.1038/19725.

[141] P. Eberle, M.K. Tiwari, T. Maitra, D. Poulikakos, Rational nanostructuring of surfaces for extraordinary icephobicity, Nanoscale. 6 (2014) 4874–4881. https://doi.org/10.1039/C3NR06644D.

[142] Y. Wang, Z. guo Wang, Sessile droplet freezing on polished and micro-micro-hierarchical silicon surfaces, Appl. Therm. Eng. 137 (2018) 66–73. https://doi.org/10.1016/j.applthermaleng.2018.03.068.

[143] A. Bodaghkhani, X. Duan, Water droplet freezing on cold surfaces with distinct wetabilities, Heat Mass Transf. 57 (2021) 1–10. https://doi.org/10.1007/s00231-020-02984-w.

[144] C. Li, R. Tao, S. Luo, X. Gao, K. Zhang, Z. Li, Enhancing and Impeding Heterogeneous Ice Nucleation through Nanogrooves, J. Phys. Chem. C. 122 (2018) 25992–25998. https://doi.org/10.1021/acs.jpcc.8b07779.

[145] L. Cao, A.K. Jones, V.K. Sikka, J. Wu, D. Gao, Anti-Icing Superhydrophobic Coatings, Langmuir. 25 (2009) 12444–12448. https://doi.org/10.1021/la902882b.

[146] S. Jung, M. Dorrestijn, D. Raps, A. Das, C.M. Megaridis, D. Poulikakos, Are superhydrophobic surfaces best for icephobicity?, Langmuir. 27 (2011) 3059–3066. https://doi.org/10.1021/la104762g.

[147] G. Heydari, E. Thormann, M. Järn, E. Tyrode, P.M. Claesson, Hydrophobic Surfaces: Topography Effects on Wetting by Supercooled Water and Freezing Delay, J. Phys. Chem. C. 117 (2013) 21752–21762. https://doi.org/10.1021/jp404396m.

[148] T.-B. Nguyen, S. Park, H. Lim, Effects of morphology parameters on anti-icing performance in superhydrophobic surfaces, Appl. Surf. Sci. 435 (2018) 585–591. https://doi.org/10.1016/j.apsusc.2017.11.137.

[149] S. Milles, M. Soldera, B. Voisiat, A.F. Lasagni, Fabrication of superhydrophobic and ice-repellent surfaces on pure aluminium using single and multiscaled periodic textures, Sci. Rep. 9 (2019) 13944. https://doi.org/10.1038/s41598-019-49615-x.

[150] A.K. Metya, J.K. Singh, F. Müller-Plathe, Ice nucleation on nanotextured surfaces: the influence of surface fraction, pillar height and wetting states, Phys. Chem. Chem. Phys. 18 (2016) 26796–26806. https://doi.org/10.1039/C6CP04382H.

[151] M. Rahimi, A. Afshari, E. Thormann, Effect of Aluminum Substrate Surface Modification on Wettability and Freezing Delay of Water Droplet at Subzero Temperatures, ACS Appl. Mater. Interfaces. 8 (2016) 11147–11153.

https://doi.org/10.1021/acsami.6b02321.

[152] S. Rønneberg, J. He, Z. Zhang, The need for standards in low ice adhesion surface research: a critical review, J. Adhes. Sci. Technol. (2020). https://doi.org/10.1080/01694243.2019.1679523.

[153] Z. He, S. Xiao, H. Gao, J. He, Z. Zhang, Multiscale crack initiator promoted super-low ice adhesion surfaces, Soft Matter. (2017). https://doi.org/10.1039/c7sm01511a.

[154] D.L. Beemer, W. Wang, A.K. Kota, Durable gels with ultra-low adhesion to ice, J. Mater. Chem. A. (2016). https://doi.org/10.1039/c6ta07262c.

[155] H. Sojoudi, G.H. McKinley, K.K. Gleason, Linker-free grafting of fluorinated polymeric cross-linked network bilayers for durable reduction of ice adhesion, Mater. Horizons. (2015). https://doi.org/10.1039/c4mh00162a.

[156] A. Work, Y. Lian, A critical review of the measurement of ice adhesion to solid substrates, Prog. Aerosp. Sci. (2018). https://doi.org/10.1016/j.paerosci.2018.03.001.

[157] L. Makkonen, Ice adhesion - Theory, measurements and countermeasures, J. Adhes. Sci. Technol. (2012). https://doi.org/10.1163/016942411X574583.

[158] L. Makkonen, Surface melting of ice, J. Phys. Chem. B. (1997). https://doi.org/10.1021/jp963248c.

[159] L. Gao, T.J. McCarthy, Teflon is hydrophilic. Comments on definitions of hydrophobic, shear versus tensile hydrophobicity, and wettability characterization, Langmuir. (2008). https://doi.org/10.1021/la8014578.

[160] L. Gao, T.J. McCarthy, Wetting 101°, Langmuir. (2009). https://doi.org/10.1021/la902206c.

[161] Y. He, C. Jiang, X. Cao, J. Chen, W. Tian, W. Yuan, Reducing ice adhesion by hierarchical micro-nano-pillars, Appl. Surf. Sci. 305 (2014) 589–595. https://doi.org/10.1016/j.apsusc.2014.03.139.

[162] T. Bharathidasan, S.V. Kumar, M.S. Bobji, R.P.S. Chakradhar, B.J. Basu, Effect of wettability and surface roughness on ice-adhesion strength of hydrophilic, hydrophobic and superhydrophobic surfaces, Appl. Surf. Sci. 314 (2014) 241–250. https://doi.org/10.1016/j.apsusc.2014.06.101.

[163] Z. Ghalmi, M. Farzaneh, Experimental investigation to evaluate the effect of PTFE nanostructured roughness on ice adhesion strength, Cold Reg. Sci. Technol. (2015). https://doi.org/10.1016/j.coldregions.2015.03.009.

[164] M. Zou, S. Beckford, R. Wei, C. Ellis, G. Hatton, M.A.A. Miller, Effects of surface roughness and energy on ice adhesion strength, Appl. Surf. Sci. 257 (2011) 3786–3792. https://doi.org/10.1016/j.apsusc.2010.11.149.

[165] G. Momen, R. Jafari, M. Farzaneh, Ice repellency behaviour of superhydrophobic surfaces: Effects of atmospheric icing conditions and surface roughness, Appl. Surf. Sci. 349 (2015) 211–218. https://doi.org/10.1016/j.apsusc.2015.04.180.

[166] A.J. Meuler, J.D. Smith, K.K. Varanasi, J.M. Mabry, G.H. McKinley, R.E. Cohen, Relationships between water wettability and ice adhesion, ACS Appl. Mater. Interfaces. (2010). https://doi.org/10.1021/am1006035.

[167] H. Sojoudi, M. Wang, N.D. Boscher, G.H. McKinley, K.K. Gleason, Durable and scalable icephobic surfaces: Similarities and distinctions from superhydrophobic surfaces, Soft Matter. (2016). https://doi.org/10.1039/c5sm02295a.

[168] X. Wu, V. V. Silberschmidt, Z.T. Hu, Z. Chen, When superhydrophobic coatings are icephobic: Role of surface topology, Surf. Coatings Technol. (2019). https://doi.org/10.1016/j.surfcoat.2018.11.039.

[169] J. Chen, J. Liu, M. He, K. Li, D. Cui, Q. Zhang, X. Zeng, Y. Zhang, J. Wang, Y. Song, Superhydrophobic surfaces cannot reduce ice adhesion, Appl. Phys. Lett. (2012). https://doi.org/10.1063/1.4752436.

[170] M. Nosonovsky, V. Hejazi, Why superhydrophobic surfaces are not always icephobic, ACS Nano. (2012). https://doi.org/10.1021/nn302138r.

[171] M.A. Sarshar, C. Swarctz, S. Hunter, J. Simpson, C.H. Choi, Effects of contact angle hysteresis on ice adhesion and growth on superhydrophobic surfaces under dynamic flow conditions, Colloid Polym. Sci. (2013). https://doi.org/10.1007/s00396-012-2753-4.

[172] K.K. Varanasi, T. Deng, J.D. Smith, M. Hsu, N. Bhate, Frost formation and ice adhesion on superhydrophobic surfaces, Appl. Phys. Lett. 97 (2010) 23–26. https://doi.org/10.1063/1.3524513.

[173] A. Dotan, H. Dodiuk, C. Laforte, S. Kenig, The relationship between water wetting and ice adhesion, J. Adhes. Sci. Technol. (2009). https://doi.org/10.1163/016942409X12510925843078.

[174] H. Memon, J. Liu, D.S.A. De Focatiis, K. Choi, X. Hou, Intrinsic dependence of ice adhesion strength on surface roughness, Surf. Coatings Technol. 385 (2020) 125382. https://doi.org/10.1016/j.surfcoat.2020.125382.

[175] E.J.Y. Ling, V. Uong, J.-S. Renault-Crispo, A.-M. Kietzig, P. Servio, Reducing Ice Adhesion on Nonsmooth Metallic Surfaces: Wettability and Topography Effects, ACS Appl. Mater. Interfaces. 8 (2016) 8789–8800. https://doi.org/10.1021/acsami.6b00187.

[176] H. Memon, J. Wang, X. Hou, Interdependence of Surface Roughness on Icephobic Performance: A Review, Materials (Basel). 16 (2023) 4607. https://doi.org/10.3390/ma16134607.

[177] B. McDonald, P. Patel, B. Zhao, Droplet freezing and ice adhesion strength measurement on super-cooled hydrophobic surfaces, J. Adhes. 93 (2017) 375–388. https://doi.org/10.1080/00218464.2015.1077329.

[178] J.F. Ou, Q.W. Shi, Z. Le Wang, F.J. Wang, M.S. Xue, W. Li, G.L. Yan, Sessile droplet freezing and ice adhesion on aluminum with different surface wettability and surface temperature, Sci. China Physics, Mech. Astron. 58 (2015) 1–8. https://doi.org/10.1007/s11433-015-5646-y.

[179] L.B. Boinovich, K.A. Emelyanenko, A.M. Emelyanenko, Superhydrophobic versus SLIPS: Temperature dependence and the stability of ice adhesion strength, J. Colloid Interface Sci. 606 (2022) 556–566. https://doi.org/10.1016/j.jcis.2021.08.030.

[180] I. El Naqa, M.J. Murphy, What Is Machine Learning?, in: Mach. Learn. Radiat. Oncol., Springer International Publishing, Cham, 2015: pp. 3–11. https://doi.org/10.1007/978-3-319-18305-3_1.

[181] Y. Reich, S.V. Barai, Evaluating machine learning models for engineering problems, Artif. Intell. Eng. 13 (1999) 257–272. https://doi.org/10.1016/S0954-1810(98)00021-1.

[182] Z. Hajjar, S. Tayyebi, M.H.E. Ahmadi, Application of AI in Chemical Engineering, in: Artif. Intell. - Emerg. Trends Appl., 2018. https://doi.org/10.5772/intechopen.76027.

[183] A. Ligeza, Artificial Intelligence: A Modern Approach, Neurocomputing. (1995). https://doi.org/10.1016/0925-2312(95)90020-9.

[184] S. Russel, P. Norvig, Artificial intelligence—a modern approach 3rd Edition, 2012. https://doi.org/10.1017/S0269888900007724.

[185] R.S. Defever, C. Targonski, S.W. Hall, M.C. Smith, S. Sarupria, A generalized deep learning approach for local structure identification in molecular simulations, Chem. Sci. (2019). https://doi.org/10.1039/c9sc02097g.

[186] D. mname Acemoglu, P. mname Restrepo, Artificial Intelligence, Automation and Work, SSRN Electron. J. (2018). https://doi.org/10.2139/ssrn.3098384.

[187] S. Li, J. Qin, M. He, R. Paoli, Fast Evaluation of Aircraft Icing Severity Using Machine Learning Based on XGBoost, Aerospace. 7 (2020) 36. https://doi.org/10.3390/aerospace7040036.

[188] S.B. Kotsiantis, Supervised machine learning: A review of classification techniques, Inform. (2007). https://doi.org/10.31449/inf.v31i3.148.

[189] L. Francis, Unsupervised learning, in: Predict. Model. Appl. Actuar. Sci. Vol. I Predict. Model. Tech., 2014. https://doi.org/10.1017/CBO9781139342674.012.

[190] M.S. Mazloom, F. Rezaei, A. Hemmati-Sarapardeh, M.M. Husein, S. Zendehboudi, A. Bemani, Artificial intelligence based methods for asphaltenes adsorption by nanocomposites: Application of group method of data handling, least squares support vector machine, and artificial neural networks, Nanomaterials. 10 (2020) 1–29. https://doi.org/10.3390/nano10050890.

[191] VA, Proceedings of ICRIC 2019 - Recent Innovations in Computing, 2019.

[192] D. Dhall, R. Kaur, M. Juneja, Machine Learning: A Review of the Algorithms and Its Applications, in: Lect. Notes Electr. Eng., 2020: pp. 47–63. https://doi.org/10.1007/978-3-030-29407-6_5.

[193] S. Ray, A Quick Review of Machine Learning Algorithms, in: 2019 Int. Conf. Mach. Learn. Big Data, Cloud Parallel Comput., IEEE, 2019: pp. 35–39. https://doi.org/10.1109/COMITCon.2019.8862451.

[194] V. Nasteski, An overview of the supervised machine learning methods, HORIZONS.B. 4 (2017) 51–62. https://doi.org/10.20544/HORIZONS.B.04.1.17.P05.

[195] A. Singh, N. Thakur, A. Sharma, A review of supervised machine learning algorithms, in: Proc. 10th INDIACom; 2016 3rd Int. Conf. Comput. Sustain. Glob. Dev. INDIACom 2016, 2016.

[196] J. Alzubi, A. Nayyar, A. Kumar, Machine Learning from Theory to Algorithms: An Overview, J. Phys. Conf. Ser. 1142 (2018) 012012. https://doi.org/10.1088/1742-6596/1142/1/012012.

[197] C. Li, D. Rubín De Celis Leal, S. Rana, S. Gupta, A. Sutti, S. Greenhill, T. Slezak, M. Height, S. Venkatesh, Rapid Bayesian optimisation for synthesis of short polymer fiber materials, Sci. Rep. 7 (2017) 1–10. https://doi.org/10.1038/s41598-017-05723-0.

[198] S. Ringdahl, S. Xiao, J. He, Z. Zhang, Machine Learning Based Prediction of Nanoscale Ice Adhesion on Rough Surfaces, Coatings. 11 (2020) 33. https://doi.org/10.3390/coatings11010033.

[199] A. Kordijazi, H.M. Roshan, A. Dhingra, M. Povolo, P.K. Rohatgi, M. Nosonovsky, Machine-learning methods to predict the wetting properties of iron-based composites, Surf. Innov. (2020). https://doi.org/10.1680/jsuin.20.00024.

[200] A. Azimi Yancheshme, S. Enayati, Y. Kashcooli, R. Jafari, H. Ezzaidi, G. Momen, Dynamic behavior of impinging drops on water repellent surfaces: Machine learning-assisted approach to predict maximum spreading, Exp. Therm. Fluid Sci. 139 (2022) 110743. https://doi.org/10.1016/j.expthermflusci.2022.110743.

[201] M. Tembely, D.C. Vadillo, A. Dolatabadi, A. Soucemarianadin, A Machine Learning Approach for Predicting the Maximum Spreading Factor of Droplets upon Impact on Surfaces with Various Wettabilities, Processes. 10 (2022) 1141.

https://doi.org/10.3390/pr10061141.

[202] J. Yee, D. Igarashi(五十嵐大地), S. Miyatake(宮武駿), Y. Tagawa(田川義之), Prediction of the morphological evolution of a splashing drop using an encoder–decoder, Mach. Learn. Sci. Technol. 4 (2023) 025002. https://doi.org/10.1088/2632-2153/acc727.

[203] X. Zhang, B. Ding, R. Cheng, S.C. Dixon, Y. Lu, Computational Intelligence-Assisted Understanding of Nature-Inspired Superhydrophobic Behavior, Adv. Sci. 5 (2018). https://doi.org/10.1002/advs.201700520.

[204] R. Ramachandran, Using neural networks to predict icephobic performance, (2020). http://arxiv.org/abs/2008.00966.

[205] M. Fitzner, P. Pedevilla, A. Michaelides, Predicting heterogeneous ice nucleation with a data-driven approach, Nat. Commun. 11 (2020) 4777. https://doi.org/10.1038/s41467-020-18605-3.

[206] R. Jafari, G. Momen, M. Farzaneh, Durability enhancement of icephobic fluoropolymer film, J. Coatings Technol. Res. 13 (2016) 405–412. https://doi.org/10.1007/s11998-015-9759-z.

[207] K. Maghsoudi, E. Vazirinasab, G. Momen, R. Jafari, Icephobicity and durability assessment of superhydrophobic surfaces: The role of surface roughness and the ice adhesion measurement technique, J. Mater. Process. Technol. 288 (2021) 116883. https://doi.org/10.1016/j.jmatprotec.2020.116883.

[208] Z. Jin, Z. Wang, D. Sui, Z. Yang, The impact and freezing processes of a water droplet on different inclined cold surfaces, Int. J. Heat Mass Transf. (2016). https://doi.org/10.1016/j.ijheatmasstransfer.2016.02.024.

[209] G. Yang, K. Guo, N. Li, Freezing mechanism of supercooled water droplet impinging on metal surfaces, in: Int. J. Refrig., 2011. https://doi.org/10.1016/j.ijrefrig.2011.07.001.

[210] H. Li, I. V. Roisman, C. Tropea, J. Li, S. Fu, Water Drop Impact on Cold Surfaces with Solidification, in: AIP Conf. Proc., 2011: pp. 451–453. https://doi.org/10.1063/1.3651944.

[211] Z. Jin, D. Sui, Z. Yang, The impact, freezing, and melting processes of a water droplet on an inclined cold surface, Int. J. Heat Mass Transf. (2015). https://doi.org/10.1016/j.ijheatmasstransfer.2015.06.086.

[212] X. Jiang, E. Xu, G. Wu, H.Z. Li, Drop impact on superhydrophobic surface with protrusions, Chem. Eng. Sci. 212 (2020) 115351. https://doi.org/10.1016/j.ces.2019.115351.

[213] B.J. Murray, D. O'sullivan, J.D. Atkinson, M.E. Webb, Ice nucleation by particles

immersed in supercooled cloud droplets, Chem. Soc. Rev. (2012). https://doi.org/10.1039/c2cs35200a.

[214] S. Kim, T. Wang, L. Zhang, Y. Jiang, Droplet impacting dynamics on wettable, rough and slippery oil-infuse surfaces, J. Mech. Sci. Technol. (2020). https://doi.org/10.1007/s12206-019-1223-z.

[215] T. Maitra, M.K. Tiwari, C. Antonini, P. Schoch, S. Jung, P. Eberle, D. Poulikakos, Erratum: Nanoengineering of superhydrophobic and impalement resistant surface textures below the freezing temperature (Nano Letters (2014) 14:1 (172-182) DOI: 10.1021/nl4037092), Nano Lett. 14 (2014) 1106. https://doi.org/10.1021/nl500297b.

[216] L. Mishchenko, B. Hatton, V. Bahadur, J.A. Taylor, T. Krupenkin, J. Aizenberg, Design of ice-free nanostructured surfaces based on repulsion of impacting water droplets, ACS Nano. (2010). https://doi.org/10.1021/nn102557p.

[217] B. Ding, H. Wang, X. Zhu, R. Chen, Q. Liao, Water droplet impact on superhydrophobic surfaces with various inclinations and supercooling degrees, Int. J. Heat Mass Transf. 138 (2019) 844–851. https://doi.org/10.1016/j.ijheatmasstransfer.2019.04.106.

[218] L. Zheng, Z. Li, S. Bourdo, K.R. Khedir, M.P. Asar, C.C. Ryerson, A.S. Biris, Exceptional superhydrophobicity and low velocity impact icephobicity of acetone-functionalized carbon nanotube films, Langmuir. 27 (2011) 9936–9943. https://doi.org/10.1021/la201548k.

[219] H. Li, I. V. Roisman, C. Tropea, Influence of solidification on the impact of supercooled water drops onto cold surfaces, Exp. Fluids. 56 (2015) 1–13. https://doi.org/10.1007/s00348-015-1999-2.

[220] V. Asghari, Y.F. Leung, S.-C. Hsu, Deep neural network based framework for complex correlations in engineering metrics, Adv. Eng. Informatics. 44 (2020) 101058. https://doi.org/10.1016/j.aei.2020.101058.

[221] A. Azimi Yancheshme, S. Hassantabar, K. Maghsoudi, S. Keshavarzi, R. Jafari, G. Momen, Integration of experimental analysis and machine learning to predict drop behavior on superhydrophobic surfaces, Chem. Eng. J. 417 (2021) 127898. https://doi.org/10.1016/j.cej.2020.127898.

[222] G.G. Moisen, Classification and Regression Trees, Elsevier, 2008. https://doi.org/10.1016/B978-008045405-4.00149-X.

[223] A. Criminisi, J. Shotton, E. Konukoglu, Decision Forests for Classification , Regression , Density Estimation , Manifold Learning and Semi-Supervised Learning, 2011.

[224] R.M. Neal, Pattern Recognition and Machine Learning, Springer US, 2007. https://doi.org/10.1198/tech.2007.s518.

[225] R. Tibshirani, Regression Shrinkage and Selection Via the Lasso, J. R. Stat. Soc. Ser. B. (1996). https://doi.org/10.1111/j.2517-6161.1996.tb02080.x.

[226] A.E. Hoerl, R.W. Kennard, Ridge Regression: Biased Estimation for Nonorthogonal Problems, Technometrics. (1970). https://doi.org/10.1080/00401706.1970.10488634.

[227] A. Latka, A. Strandburg-Peshkin, M.M. Driscoll, C.S. Stevens, S.R. Nagel, Creation of prompt and thin-sheet splashing by varying surface roughness or increasing air pressure, Phys. Rev. Lett. 109 (2012) 3–6. https://doi.org/10.1103/PhysRevLett.109.054501.

[228] D. Bartolo, F. Bouamrirene, É. Verneuil, A. Buguin, P. Silberzan, S. Moulinet, Bouncing or sticky droplets: Impalement transitions on superhydrophobic micropatterned surfaces, Europhys. Lett. 74 (2006) 299–305. https://doi.org/10.1209/epl/i2005-10522-3.

[229] X. Wang, Z. Tang, B. Xu, Z. Chen, Anti-freezing characteristics of water droplet impinging the superhydrophobic surface: An experimental and predictive study, Appl. Surf. Sci. (2021). https://doi.org/10.1016/j.apsusc.2021.150717.

[230] Z. Yuan, S. Gao, Z.F. Hu, L. Dai, H. Hou, F. Chu, X. Wu, Ultimate jumping of coalesced droplets on superhydrophobic surfaces, J. Colloid Interface Sci. (2021). https://doi.org/10.1016/j.jcis.2020.12.007.

[231] N. V. Chawla, K.W. Bowyer, L.O. Hall, W.P. Kegelmeyer, SMOTE: Synthetic minority over-sampling technique, J. Artif. Intell. Res. (2002). https://doi.org/10.1613/jair.953.

[232] R. Wang, V. Asghari, S.C. Hsu, C.J. Lee, J.H. Chen, Detecting corporate misconduct through random forest in China's construction industry, J. Clean. Prod. (2020). https://doi.org/10.1016/j.jclepro.2020.122266.

[233] M. Saarela, S. Jauhiainen, Comparison of feature importance measures as explanations for classification models, SN Appl. Sci. (2021). https://doi.org/10.1007/s42452-021-04148-9.

[234] T. RATVASKY, R. RANAUDO, Icing effects on aircraft stability and control determined from flight data - Preliminary results, in: 31st Aerosp. Sci. Meet., American Institute of Aeronautics and Astronautics, Reston, Virigina, 1993. https://doi.org/10.2514/6.1993-398.

[235] Y. Shen, X. Wu, J. Tao, C. Zhu, Y. Lai, Z. Chen, Icephobic materials: Fundamentals, performance evaluation, and applications, Prog. Mater. Sci. 103 (2019) 509–557. https://doi.org/10.1016/j.pmatsci.2019.03.004.

[236] F.J. Montes Ruiz-Cabello, S. Bermúdez-Romero, P.F. Ibáñez-Ibáñez, M.A. Cabrerizo-Vílchez, M.A. Rodríguez-Valverde, Freezing delay of sessile drops: Probing the impact of contact angle, surface roughness and thermal conductivity,

Appl. Surf. Sci. 537 (2021) 147964. https://doi.org/10.1016/j.apsusc.2020.147964.

[237] T. Bartkowiak, M. Mendak, K. Mrozek, M. Wieczorowski, Analysis of surface microgeometry created by electric discharge machining, Materials (Basel). (2020). https://doi.org/10.3390/ma13173830.

[238] K. Peta, T. Bartkowiak, P. Galek, M. Mendak, Contact angle analysis of surface topographies created by electric discharge machining, Tribol. Int. (2021). https://doi.org/10.1016/j.triboint.2021.107139.

[239] N.D. Boscher, V. Vaché, P. Carminati, P. Grysan, P. Choquet, A simple and scalable approach towards the preparation of superhydrophobic surfaces-importance of the surface roughness skewness, J. Mater. Chem. A. 2 (2014) 5744–5750. https://doi.org/10.1039/c4ta00366g.

[240] W.Z. Yuan, L.Z. Zhang, Lattice Boltzmann simulation of droplets impacting on superhydrophobic surfaces with randomly distributed rough structures, Langmuir. 33 (2017) 820–829. https://doi.org/10.1021/acs.langmuir.6b04041.

[241] L.Z. Zhang, W.Z. Yuan, A lattice Boltzmann simulation of coalescence-induced droplet jumping on superhydrophobic surfaces with randomly distributed structures, Appl. Surf. Sci. 436 (2018) 172–182. https://doi.org/10.1016/j.apsusc.2017.11.200.

[242] N. Sharifi, M. Pugh, C. Moreau, A. Dolatabadi, Developing hydrophobic and superhydrophobic TiO2 coatings by plasma spraying, Surf. Coatings Technol. 289 (2016) 29–36. https://doi.org/10.1016/j.surfcoat.2016.01.029.

[243] Y.H. Yeong, E. Loth, J. Sokhey, A. Lambourne, Ice adhesion strength on hydrophobic and superhydrophobic coatings, in: 6th AIAA Atmos. Sp. Environ. Conf., American Institute of Aeronautics and Astronautics, Reston, Virginia, 2013: pp. 1–19. https://doi.org/10.2514/6.2014-2063.

[244] A. Davis, Y.H. Yeong, A. Steele, I.S. Bayer, E. Loth, Superhydrophobic nanocomposite surface topography and ice adhesion, ACS Appl. Mater. Interfaces. 6 (2014) 9272–9279. https://doi.org/10.1021/am501640h.

[245] E. Vazirinasab, K. Maghsoudi, R. Jafari, G. Momen, A comparative study of the icephobic and self-cleaning properties of Teflon materials having different surface morphologies, J. Mater. Process. Technol. 276 (2020) 116415. https://doi.org/10.1016/j.jmatprotec.2019.116415.

[246] M. Psarski, D. Pawlak, J. Grobelny, G. Celichowski, Relationships between surface chemistry, nanotopography, wettability and ice adhesion in epoxy and SU-8 modified with fluoroalkylsilanes from the vapor phase, Appl. Surf. Sci. 479 (2019) 489–498. https://doi.org/10.1016/j.apsusc.2019.02.082.

[247] K. Maghsoudi, G. Momen, R. Jafari, M. Farzaneh, Direct replication of micro-nanostructures in the fabrication of superhydrophobic silicone rubber surfaces by

compression molding, Appl. Surf. Sci. 458 (2018) 619–628. https://doi.org/10.1016/j.apsusc.2018.07.099.

[248] M. Sedlaček, B. Podgornik, J. Vižintin, Correlation between standard roughness parameters skewness and kurtosis and tribological behaviour of contact surfaces, Tribol. Int. 48 (2012) 102–112. https://doi.org/10.1016/j.triboint.2011.11.008.

[249] M. Rahimi, A. Afshari, P. Fojan, L. Gurevich, The effect of surface modification on initial ice formation on aluminum surfaces, Appl. Surf. Sci. 355 (2015) 327–333. https://doi.org/10.1016/j.apsusc.2015.06.201.

[250] M.A. Rahman, A.M. Jacobi, Drainage of frost melt water from vertical brass surfaces with parallel microgrooves, Int. J. Heat Mass Transf. 55 (2012) 1596–1605. https://doi.org/10.1016/j.ijheatmasstransfer.2011.11.015.

[251] R.O. Piucco, C.J.L. Hermes, C. Melo, J.R. Barbosa, A study of frost nucleation on flat surfaces, Exp. Therm. Fluid Sci. 32 (2008) 1710–1715. https://doi.org/10.1016/j.expthermflusci.2008.06.004.

[252] X. Zhang, X. Liu, X. Wu, J. Min, Experimental investigation and statistical analysis of icing nucleation characteristics of sessile water droplets, Exp. Therm. Fluid Sci. 99 (2018) 26–34. https://doi.org/10.1016/j.expthermflusci.2018.07.027.

[253] Y. Bengio, Learning Deep Architectures for AI, Found. Trends® Mach. Learn. 2 (2009) 1–127. https://doi.org/10.1561/2200000006.

[254] T. Dozat, Incorporating Nesterov Momentum into Adam, ICLR Work. (2016) 2013–2016.

[255] S.M. Lundberg, P.G. Allen, S.-I. Lee, A Unified Approach to Interpreting Model Predictions, Adv. Neural Inf. Process. Syst. 2017-Decem (2017) 4766–4775. http://arxiv.org/abs/1705.07874 (accessed September 24, 2021).

[256] E. Mitridis, T.M. Schutzius, A. Sicher, C.U. Hail, H. Eghlidi, D. Poulikakos, Metasurfaces Leveraging Solar Energy for Icephobicity, ACS Nano. 12 (2018) 7009–7017. https://doi.org/10.1021/acsnano.8b02719.

[257] V. Singh, J. Zhang, J. Chen, C.G. Salzmann, M.K. Tiwari, Precision Covalent Organic Frameworks for Surface Nucleation Control, Adv. Mater. (2023). https://doi.org/10.1002/adma.202302466.

[258] Z. He, W.J. Xie, Z. Liu, G. Liu, Z. Wang, Y.Q. Gao, J. Wang, Tuning ice nucleation with counterions on polyelectrolyte brush surfaces, Sci. Adv. 2 (2016). https://doi.org/10.1126/sciadv.1600345.

[259] E. Bakhshandeh, S. Sobhani, R. Jafari, G. Momen, New insights into tailoring physicochemical properties for optimizing the anti-icing behavior of polyurethane coatings, J. Appl. Polym. Sci. (2023). https://doi.org/10.1002/app.54610.

[260] S. Bengaluru Subramanyam, V. Kondrashov, J. Rühe, K.K. Varanasi, Low Ice Adhesion on Nano-Textured Superhydrophobic Surfaces under Supersaturated Conditions, ACS Appl. Mater. Interfaces. 8 (2016) 12583–12587. https://doi.org/10.1021/acsami.6b01133.

[261] V.J. Rico, C. López-Santos, M. Villagrá, J.P. Espinós, G.F. de la Fuente, L.A. Angurel, A. Borrás, A.R. González-Elipe, Hydrophobicity, Freezing Delay, and Morphology of Laser-Treated Aluminum Surfaces, Langmuir. 35 (2019) 6483–6491. https://doi.org/10.1021/acs.langmuir.9b00457.

[262] A. Alizadeh, M. Yamada, R. Li, W. Shang, S. Otta, S. Zhong, L. Ge, A. Dhinojwala, K.R. Conway, V. Bahadur, A.J. Vinciquerra, B. Stephens, M.L. Blohm, Dynamics of ice nucleation on water repellent surfaces, Langmuir. 28 (2012) 3180–3186. https://doi.org/10.1021/la2045256.

[263] S. Jung, M.K. Tiwari, N.V. Doan, D. Poulikakos, Mechanism of supercooled droplet freezing on surfaces, Nat. Commun. (2012). https://doi.org/10.1038/ncomms1630.

[264] C. Antonini, F. Villa, I. Bernagozzi, A. Amirfazli, M. Marengo, Drop rebound after impact: The role of the receding contact angle, Langmuir. (2013). https://doi.org/10.1021/la4012372.

[265] D. Zhang, S. Takase, G. Nagayama, Measurement of effective wetting area at hydrophobic solid–liquid interface, J. Colloid Interface Sci. 591 (2021) 474–482. https://doi.org/10.1016/j.jcis.2021.01.056.

[266] P. Wang, L. He, Z. Wang, The effect of surface structure and arrangement on wettability of substrate surface, Colloids Surfaces A Physicochem. Eng. Asp. 614 (2021) 126165. https://doi.org/10.1016/j.colsurfa.2021.126165.

[267] X. Zhang, F. Shi, J. Niu, Y. Jiang, Z. Wang, Superhydrophobic surfaces: from structural control to functional application, J. Mater. Chem. 18 (2008) 621–633. https://doi.org/10.1039/B711226B.

[268] H. Lambley, G. Graeber, R. Vogt, L.C. Gaugler, E. Baumann, T.M. Schutzius, D. Poulikakos, Freezing-induced wetting transitions on superhydrophobic surfaces, Nat. Phys. (2023). https://doi.org/10.1038/s41567-023-01946-3.

[269] P. Papadopoulos, L. Mammen, X. Deng, D. Vollmer, H.-J. Butt, How superhydrophobicity breaks down, Proc. Natl. Acad. Sci. 110 (2013) 3254–3258. https://doi.org/10.1073/pnas.1218673110.

[270] C. Guo, M. Zhang, J. Hu, Icing delay of sessile water droplets on superhydrophobic titanium alloy surfaces, Colloids Surfaces A Physicochem. Eng. Asp. 621 (2021) 126587. https://doi.org/10.1016/j.colsurfa.2021.126587.

[271] W. Xing, Z. Li, H. Yang, X. Li, X. Wang, N. Li, Anti-icing aluminum alloy surface with multi-level micro-nano textures constructed by picosecond laser, Mater. Des. 183

(2019) 108156. https://doi.org/10.1016/j.matdes.2019.108156.

[272] X. Li, G. Wang, A.S. Moita, C. Zhang, S. Wang, Y. Liu, Fabrication of bio-inspired non-fluorinated superhydrophobic surfaces with anti-icing property and its wettability transformation analysis, Appl. Surf. Sci. (2020). https://doi.org/10.1016/j.apsusc.2019.144386.

[273] J. Li, Y. Zhou, W. Wang, C. Xu, L. Ren, Superhydrophobic Copper Surface Textured by Laser for Delayed Icing Phenomenon, Langmuir. (2020). https://doi.org/10.1021/acs.langmuir.9b02273.

[274] H.R. PRUPPACHER, J.D. KLETT, Microphysics of Clouds and Precipitation, Nature. 284 (1980) 88–88. https://doi.org/10.1038/284088b0.

[275] B. Zobrist, T. Koop, B.P. Luo, C. Marcolli, T. Peter, Heterogeneous Ice Nucleation Rate Coefficient of Water Droplets Coated by a Nonadecanol Monolayer, J. Phys. Chem. C. 111 (2007) 2149–2155. https://doi.org/10.1021/jp066080w.

[276] J. Jeevahan, M. Chandrasekaran, G. Britto Joseph, R.B. Durairaj, G. Mageshwaran, Superhydrophobic surfaces: a review on fundamentals, applications, and challenges, J. Coatings Technol. Res. 15 (2018) 231–250. https://doi.org/10.1007/s11998-017-0011-x.

[277] L. Ge, G. Ding, H. Wang, J. Yao, P. Cheng, Y. Wang, Anti-icing property of superhydrophobic octadecyltrichlorosilane film and its ice adhesion strength, J. Nanomater. (2013). https://doi.org/10.1155/2013/278936.

[278] Y. Xu, G. Zhang, L. Li, C. Xu, X. Lv, H. Zhang, W. Yao, Icephobic behaviors of superhydrophobic amorphous carbon nano-films synthesized from a flame process, J. Colloid Interface Sci. (2019). https://doi.org/10.1016/j.jcis.2019.05.096.

[279] M. Huré, P. Olivier, J. Garcia, Effect of Cassie-Baxter versus Wenzel states on ice adhesion: A fracture toughness approach, Cold Reg. Sci. Technol. 194 (2022) 103440. https://doi.org/10.1016/j.coldregions.2021.103440.

[280] M. Leshno, V.Y. Lin, A. Pinkus, S. Schocken, Multilayer feedforward networks with a nonpolynomial activation function can approximate any function, Neural Networks. 6 (1993) 861–867. https://doi.org/10.1016/S0893-6080(05)80131-5.

[281] M.J. Brown, L.A. Hutchinson, M.J. Rainbow, K.J. Deluzio, A.R. De Asha, A comparison of self-selected walking speeds and walking speed variability when data are collected during repeated discrete trials and during continuous walking, J. Appl. Biomech. 33 (2017) 384–387. https://doi.org/10.1123/jab.2016-0355.

[282] C. Nwankpa, W. Ijomah, A. Gachagan, S. Marshall, Activation Functions: Comparison of trends in Practice and Research for Deep Learning, (2018) 1–20. http://arxiv.org/abs/1811.03378.

[283] M.A. Cauchy, Méthode générale pour la résolution des systèmes d'équations simultanées, C. R. Hebd. Seances Acad. Sci. 25 (1847) 536–538. https://cs.uwaterloo.ca/~y328yu/classics/cauchy-en.pdf.

[284] M. Statistics, A Stochastic Approximation Method Author (s): Herbert Robbins and Sutton Monro Source : The Annals of Mathematical Statistics , Vol . 22 , No . 3 (Sep ., 1951), pp . 400-407 A STOCHASTIC APPROXIMATION METHOD ' x , then the method is irrespective of th, 22 (2014) 400–407.

[285] M. Statistics, Author (s): J . Wolfowitz Source : The Annals of Mathematical Statistics , Vol . 23 , No . 1 (Mar ., 1952), pp . 1-13 Published by : Institute of Mathematical Statistics Stable URL : http://www.jstor.org/stable/2236396, Ann. Math. Stat. 23 (1952) 1–13.

[286] S. Ruder, An overview of gradient descent optimization algorithms, (2016) 1–14. http://arxiv.org/abs/1609.04747.

[287] Y.N. Dauphin, R. Pascanu, C. Gulcehre, K. Cho, S. Ganguli, Y. Bengio, Identifying and attacking the saddle point problem in high-dimensional non-convex optimization, Adv. Neural Inf. Process. Syst. 4 (2014) 2933–2941.

[288] Y.E. Nesterov, A Method of Solving a Convex Programming Problem with Convergence Rate $\mathcal{O}(1/k^2)$, Sov. Math. Dokl. (1983).

[289] J.C. Duchi, P.L. Bartlett, M.J. Wainwright, Randomized smoothing for (parallel) stochastic optimization, Proc. IEEE Conf. Decis. Control. 12 (2012) 5442–5444. https://doi.org/10.1109/CDC.2012.6426698.

[290] M.D. Zeiler, ADADELTA: An Adaptive Learning Rate Method, (2012). http://arxiv.org/abs/1212.5701.

[291] D.P. Kingma, J.L. Ba, Adam: A method for stochastic optimization, 3rd Int. Conf. Learn. Represent. ICLR 2015 - Conf. Track Proc. (2015) 1–15.

[292] A. Choromanska, M. Henaff, M. Mathieu, G. Ben Arous, Y. Lecun, The loss surfaces of multilayer networks, J. Mach. Learn. Res. 38 (2015) 192–204.

[293] K. Maghsoudi, E. Vazirinasab, G. Momen, R. Jafari, Advances in the Fabrication of Superhydrophobic Polymeric Surfaces by Polymer Molding Processes, Ind. Eng. Chem. Res. 59 (2020) 9343–9363. https://doi.org/10.1021/acs.iecr.0c00508.